3D numerical modelling of dune formation and dynamics in inland waterways

Annalena Goll

Annalena Goll. 3D numerical modelling of dune formation and dynamics in inland waterways. Fluid mechanics [physics.class-ph]. Université Paris-Est, 2016. English. NNT : 2016PESC1119 . tel-01542852

HAL Id: tel-01542852
https://pastel.hal.science/tel-01542852

Submitted on 20 Jun 2017

BAW Bundesanstalt für Wasserbau
Federal Waterways Engineering and Research Institute

LABORATOIRE D'HYDRAULIQUE SAINT-VENANT

UNIVERSITÉ PARIS-EST

3D NUMERICAL MODELLING OF DUNE FORMATION AND DYNAMICS IN INLAND WATERWAYS

PhD thesis

by

Annalena Goll

Date of Defence: 14.10.2016

Ph.D. committee

Reporters	Prof. Peter Stansby, University of Manchester
	Prof. Richard Whitehouse, HR Wallingford
Director	Dr. Catherine Villaret, EDF
Co-director	Dr. Rebekka Kopmann, BAW
Examiner	Prof. Reinhard Hinkelmann, TU Berlin (President of the Committee)
	Dr. Pablo Tassi, EDF

3D NUMERICAL MODELLING OF DUNE FORMATION AND DYNAMICS IN INLAND WATERWAYS

PHD THESIS

BY

ANNALENA GOLL

Federal Waterways Engineering and Research Institute (BAW)
and Laboratoire Hydraulic St Venant (EDF)

A PERFECTLY REASONABLE JUDGEMENT,
BASED ON CURRENT KNOWLEDGE,
MAY PROVE TO BE WRONG IN THE FUTURE.

H.W. SHEN, *River Mechanics*, 1970

BUILDING BRIDGES AIN'T THE HARDEST PART,
IT'S TRYING TO SWIM ONCE THEY FALL APART.

ISRAEL NASH GRIPKA,
Barn Doors and Concrete Floors, 2011

Abstract

In this work the possibilities of modelling large scale bed forms in waterways are highlighted and analysed. It is motivated by the fact that in river modelling, uncertainties in predicting water depth and bed movement can often be attributed to bed forms. Those bed forms are the dominating factor for bed load transport in many river stretches, which need to be maintained by the responsible waterways authorities.

Hydrodynamic and morphodynamic experiments have been conducted at the Federal Waterways Engineering and Research Institute of Germany (BAW). High-resolution measurements have been performed over fixed, naturally formed three-dimensional sand dunes, which are at equilibrium with the surrounding flow field. Using these measured data sets, a hydrodynamic model is calibrated to simulate the complex flow situation over a train of several three-dimensional dunes. Simulation results show that it is possible to reproduce the measured turbulent flow field in the wake of the fixed dunes and that the measured and simulated water levels agree for the chosen configuration. Vertical and horizontal mesh resolution, roughness height, small scale bed forms and turbulence modelling are identified as most sensitive parameters during the calibration.

The second part of this thesis focuses on morphodynamic simulations of the same experimental flume but with a mobile bed. High resolution measured bottom scans of the dune forms, developing over time, are available for comparison. Dune height and length, as well as the distribution moments, skewness and kurtosis are used to compare the dimensions of the dunes and also their shape and spatial distribution. Bed load transport formulation, skewness and kurtosis formulae, boundary conditions and the consideration of sub-grid scale roughness elements are the parameters which influence the quality of the results the most. A particular focus during the study is the inclusion of turbulent fluctuations in bed shear stress calculation. A new, total bed shear stress calculation is proposed, which incorporates mean flow velocities and turbulent kinetic energy provided by the turbulence model. With this approach, the numerical model is able to reproduce both qualitatively and quantitatively the measured mean bed forms dimensions and the shape moments of the physical dunes. It proves to be the only way to also produce the right distribution moments (skewness and kurtosis) of the dune field.

Finally, the model is applied to field scale and tested on a stretch of the river Elbe, Germany. High resolution morphodynamic simulations coupled to 3D-hydrodynamics are conducted over several days for the chosen river stretch which is $4\,\mathrm{km}$ in length. The dune forms preserve form and shape parameters and the dune speed agrees with the measured one. The simulations show promising results concerning the possibility of operational use of the model in the future. Local problems and statements, e.g. maintenance strategies such as changes in flow cross section, groynes and revetments, are possible tasks that can be examined.

Résumé

Ce rapport présente et analyse les différentes possibilités de modélisation et de grande envergure de la forme du fond des voies naviguables. Cette étude est motivée par le fait que dans la modélisation de rivière, les incertitudes quant à la prédiction de la profondeur et du mouvement du lit, peuvent souvent être affectées par sa forme. La forme du fond constitue le facteur dominant dans le transport solide de nombreux cours d'eau qui nécessitent donc d'être entretenus par les autorités compétantes.

Des expériences hydrodynamiques et morphodynamiques ont été menées au sein de l'institut fédéral allemand de la recherche et de l'ingénieurie des cours d'eau (BAW). Des mesures en haute résolution ont été effectuées et ont révélé la formation naturelle de dunes tridimensionelles à l'équilibre avec le champ d'écoulement environnant. Le modèle hydrodynamique est calibré sur cette base de données pour modéliser le régime d'écoulement complexe à travers une suite de dunes tridimensionelles. Les résultats de la simulation montrent qu'il est possible de reproduire le champ d'écoulement turbulent mesuré dans la configuration précédemment citée et que le niveau d'eau mesuré et simulé est également en accord avec cette même configuration. La résolution verticale et horizontale du maillage, le coefficient de friction, la forme du lit à petite échelle et la modélisation turbulente sont identifiés comme paramètres sensibles durant le calibrage.

La seconde partie de cette thèse se concentre sur les simulations morphodynamiques de ce même canal expérimental mais cette fois avec un lit mobile. La numérisation du fond mesuré en haute résolution montrant la formation et le développement des dunes au fil du temps, est mis à disposition pour la comparaison. La hauteur et la largeur des dunes tout comme le moment de distribution, l'inclinaison et l'aplatissement sont utilisés pour comparer les dimensions des dunes ainsi que leur forme et leur distribution spatiale. Les formules du transport solide, de l'inclinaison, de l'aplatissement, les conditions aux limites et la considération des éléments de rugosité de sous échelle sont les paramètres qui influencent le plus la qualité des résultats. Durant cette étude, une attention toute particulière a été portée sur l'intégration des fluctuations turbulentes dans le calcul de la contrainte de cisaillement du fond. Un nouveau calcul total de cette contrainte est proposé et incorpore les vitesses d'écoulement principales et l'énergie cinétique turbulente fournit par le modèle turbulent.

Grâce à cette approche, le modèle numérique est capable de reproduire quantitativement et qualitativement les dimensions de la forme du lit principal mesurée et les moments de forme des dunes physiques. Cela s'avère être la seule façon de reproduire le bon moment de distribution (aplatissement) du champ de dunes.

Finalement, le modèle est appliqué à l'échelle du projet et testé sur une portion de l'Elbe (Allemagne). Les simulations morphodynamiques en haute résolution couplées à l'hydrodynamique-3D sont menées durant plusieurs jours sur la portion de rivière choisit d'une longueur de 4 kilomètres. Les formes des dunes préservent les paramètres de forme et la vitesse des dunes est en accord avec celle mesurée. La simulation montre des résultats prométeurs concernant la possibilité d'un usage opérationel du modèle dans l'avenir. Des problèmes locaux et communs comme les stratégies d'entretien tel que les changements dans les sections transversales d'écoulement, les brises lames et le revêtement sont des missions possibles qui peuvent être examinées.

Contents

List of symbols

Symbol (latin)	Dimension	Description
C_1,C_2	$-$	proportionality constants
C_d	$-$	drag coefficient
d, d_*	m	grain diameter
d_{50}	m	mean diameter at 50% of sieve line
d_{90}	m	mean diameter at 90% of sieve line
f_x, f_y, f_z	$\mathrm{m/s^2}$	source terms
g	m/s	gravitational acceleration
h	m	water depth
K	$-$	constant
k	$\mathrm{m^2/s^2}$	turbulent kinetic energy (TKE)
k_r	$\mathrm{m^2/s^2}$	unresolved turbulent kinetic energy
k^*	$\mathrm{m^2/s^2}$	resolved turbulent kinetic energy
k_s	m	bed roughness height
k_s^g	m	grain roughness height
k_s^r	m	ripple roughness height
k_s^d	m	dune roughness height
ku	$-$	kurtosis
l_m	m	mixing length (in turbulence model)
P	$\mathrm{m^2/s^3}$	production of turbulent kinetic energy
p	$\mathrm{N/m^2}$	pressure
p_d	$\mathrm{N/m^2}$	dynamic pressure
p_h	$\mathrm{N/m^2}$	hydrostatic pressure
q_s,Q_s	$\mathrm{m^3/s}$	sediment discharge
Q	$\mathrm{m^3/s}$	water discharge
r	$-$	proportionality constant
S	m	free surface
sk	$-$	skewness

Symbol (latin)	Dimension	Description
t	s	time
T_T	$-$	total load transport parameter
u, v, w	m/s	velocities in x, y, z-direction
$u_i(t)$	m/s	velocity in x, y, z-direction
u_*	m/s	friction velocity, effective grain shear velocity
$\overline{u_i}$	m/s	averaged velocities
$u_i'(t)$	m/s	fluctuating term of velocities
$\mathbf{u}$	m/s	vector of the velocities
$\overline{u_i'u_j'}$	m/s	Reynold's stress
u_{*c}	m/s	critical shear velocity for sediment movement
x, y	m	horizontal components of space
z	m	vertical component of space
z_o	m	(hypothetical) zero-velocity level
Z_f	m	height of bottom
$\mathrm{d}z$	m	$= (z_1 - z_0)$, thickness of lowermost σ-layer in 3D hydrodynamic model
Re	$-$	Reynolds number
Re_*	$-$	sedimentological Reynolds number
Fr	$-$	Froude number
Fr_*	$-$	sedimentological Froude number
$<>$	$-$	time average

Symbol (greek)	Dimension	Description
β	$-$	factor (Sisyphe)
γ, γ_s	$\mathrm{N/m^3}$	specific weight of water and sediment
γ_r	$-$	presence factor for ripples
γ_d	$-$	form factor for dunes
Δ	m	bed form height
ε	$\mathrm{m^2/s^3}$	energy dissipation
θ	$-$	Shields parameter
θ_c	$-$	critical Shields parameter
θ_s	$\mathrm{m^3/s}$	total bed load
Θ'	$-$	non-dimensional effective shear velocity
Θ_c	$-$	non-dimensional critical shear velocity
κ	$-$	von Kármán constant
λ	m	bed form length
ν	$\mathrm{m^2/s}$	kinematic viscosity
ν_t	$\mathrm{m^2/s}$	turbulent (eddy) viscosity
ρ_s, ρ	$\mathrm{kg/m^3}$	density of sediment and water
ρ_{dep}	$\mathrm{kg/m^3}$	density of deposition
σ^2	$\mathrm{m^2}$	variance
σ	m	standard deviation
τ, τ_o, τ_B	$\mathrm{N/m^2}$	bed shear stress
$\overline{\tau}$	$\mathrm{N/m^2}$	mean bed shear stress
τ'	$\mathrm{N/m^2}$	turbulent part of the bed shear stress
τ_{ij}	$\mathrm{N/m^2}$	Reynolds stress tensor
ϕ, ϕ_s	°	angle of repose, friction angle of sediment
Φ_m	$\mathrm{kg/m^2s}$	mass flux
Φ_s, Φ_b	$-$	non-dimensional sediment discharge
ω	1/s	specific turbulent dissipation rate
ω_g	m/s	grain settling velocity
$C_\mu, C_{1\varepsilon}, C_{2\varepsilon}$	$-$	constants of k-ε model
$\sigma_k, \sigma_\varepsilon$	$-$	constants of k-ε model
Ψ	$-$	dimensionless entrainment rate

1

Introduction

River dunes are three-dimensional bed forms that evolve on the bottom of streams. The comprehension of the mechanisms behind their formation and evolution has been named one of the main challenges in practical water engineering (Engelund and Fredsøe, 1982; Southard, 1991) and this classification is still valid today. The morphology of the river bed influences not only hydraulic resistance and sediment transport. It also affects habitat development for fish, macro- and microbenthos. It is dynamic in nature with most of the processes evading the critical eye of the engineer. A main reason for it being in the focus of research for many years, is that rivers have a long tradition of being used by men. Their history as transport routes can be traced back almost three thousand years. Nowadays 2.2 millon TEU containers (Twenty-foot Equivalent Unit, German standard container) are transported on German waterways each year (BMVI - Bundesministerium für Verkehr und digitale Infrastruktur, 2015) and 228 million tonnes of goods have been transported on German inland waterways in the year 2014 (Federal Statistical Office, 2015). When maintaining these waterways their water depth is a crucial parameter, which directly depends on the form of the bottom and sediment transport. Uncertainties in predicting water depth and bed movement can be accounted to the presence of bed forms, whose quantification is often difficult (ASCE, 2002).

During the last years there has been a great advance in understanding the dynamics that lead to and govern the complex processes of river dunes morphology. Improved measurement techniques have enabled more thorough experimental studies in recent times (e.g. Maddux et al., 2003b; Venditti, 2007; Singh and Foufoula-Georgiou, 2013). Similarly, availability of high performance computational resources have allowed more detailed simulations (e.g.

Nabi, 2012; Omidyeganeh and Piomelli, 2013a; Kidanemariam and Uhlmann, 2014; Schmeeckle, 2015). Despite of these achievements, it is still not possible to accurately predict dune growth rate, equilibrium shape and dimensions as well as migration rate for large river sections or forecast their long-term form development.

In practice bed forms in rivers have been parametrised through empirical formulations, for example using an equivalent dune height and length and changing the roughness height, presented by e.g. van Rijn (1993). In his formula the bed roughness height is composed from several individual factors

$$k_s = k_s^g + k_s^r + k_s^d \tag{1.1}$$

where k_s^g is the roughness height due to the sediment grain size and k_s^r and k_s^d are form roughnesses due to ripples and dunes, respectively. The form roughnesses are calculated from equilibrium heights and lengths of dunes and ripples. Total roughness predictors, such as proposed by van Rijn (2007), also decompose the roughness into small and large scale roughness. The roughness predictor of van Rijn (2007) calculates corresponding equilibrium dune and ripple heights based on the prevailing flow field and use these values to calculate a dynamic bottom roughness.

These sorts of formulae generate several problems. Firstly, they do not include time-lag effects. Dune fields are rarely in a state of equilibrium but are constantly adjusting to the changing flow field. Thus their heights and length 'lag' behind the flow field variables. This time lag-effect has been observed e.g. by Claude (2012) in the Loire river.

Secondly, dunes are large scale bed forms. Including these bed forms into a bed roughness coefficient is a mere approximation, as the notion of roughness coefficient is based on turbulent boundary layer concepts for flat beds. These concepts are only valid, if the bed roughness is much smaller than the water depth. In flow over dunes flow separation occurs at the lee side of bed forms and a new boundary layer needs to establish after reattachment (Best, 2005).

Thirdly, for practical engineering application the bed roughness coefficient is a spatially averaged value rather than representing an actual, local bottom geometry. The position of dunes and their movement is lost in this averaging procedure. Thus precise prognosis of dune forms and their changes due to impacts like groynes and maintenance structures in a dune regime can be a very important tool for improving the accuracy and reliability of the forecasts made using numerical models.

A computation of individual bed forms and their interactions with the surrounding hydrodynamic flow field promises better results than their parametrisation via empirical formulations. This thesis therefore outlines the possibilities and limits of explicit dunes modelling in practical waterways engineering. The dissertation examines the ability of a three-dimensional hydrodynamic model with classical turbulence models to simulate the flow above bed forms and the moving bed forms themselves using a morphodynamic model. Turbulence structures over naturally formed dunes in an experimental flume are examined and the sensitivity of numerical results to model parameters is highlighted. The effects of turbulence modelling are explored and a method to account for the influence of the fluctuating motion of the flow field onto sediment dynamics is presented. In the presented morphodynamic model large scale bed forms (dunes) are directly simulated, while only small scale bed forms (ripples) are parametrised. Finally, the numerical model is applied to an in situ application. In a large scale engineering application dune movement of dunes in the river Elbe in Germany is presented.

This document is the result of Ph.D. research conducted in the framework of the research and development project “Numerical modelling of bed forms (dunes) in inland waterways” (*Numerische Modellierung von Transportkörpern (Dünen) in Binnenwasserstraßen*) at the Federal Waterways Engineering and Research Institute of Germany (BAW). Chapter 2 is a review of the published material on dunes, their characteristic and formation. Dune measurements, techniques as well as an overview of past and recent dune modelling approaches and achievements are presented and discussed. Further it addresses the issue of morphodynamic modelling practice and bed shear stress calculation.

Chapter 3 describes the experimental flume which delivered the physical results for calibration of the numerical model. The data is presented and analysed.

Chapter 4 introduces the governing, hydrodynamic equations and the numerical frame work and the hydrodynamic numerical model.

Chapters 5 presents the validation of the numerical model. The fixed bed experiments are presented, analysed and discussed.

Chapter 6 introduces the morphodynamic, governing equations and a description of the morphodynamic model. The module is presented and as well as the numerical options developed during this work.

This model is used for morphodynamic simulations of the experimental flume. The results are presented and discussed in Chapter 7.

In Chapter 8 the complete set-up is tested at an in situ application at a reach of the river Elbe, Germany.

Chapter 9 summarises the results and gives final conclusions and recommendations.

2

Literature review

Contents

Dunes have been in the focus of physical, theoretical and numerical research for almost a century (e.g. Shields, 1936; Kennedy, 1963; Reynolds, 1965; Fredsøe, 1979; Engelund and Fredsøe, 1982; McLean, 1990).

During the last decade increasingly extensive experimental studies have been conducted (e.g. Maddux et al., 2003b,a; Balachandar et al., 2007; McLean et al., 2008; Naqshband et al., 2014b) and with growing computer capacities more and more detailed simulations have been made possible (e.g. Yue et al., 2006; Giri and Shimizu, 2006; Stoesser et al., 2008; Bhaganagar and Hsu, 2009; el Kheiashy et al., 2010; Nabi, 2012; Omidyeganeh and Piomelli, 2013a). The main reason for all these efforts is, that because of their dominating impact on sediment transport and flow resistance, dunes are one of the most important bed forms to be considered in practical river engineering (Engelund and Fredsøe, 1982).

2.1 Dunes

2.1.1 Dunes as bed forms

Bed forms can be divided into ripples, dunes, anti-dunes and bars. The main difference between dunes and ripples is that former interact with the free surface and latter do not. Hence, ripples are much smaller than dunes compared to the water depth (Zanke, 1982). Bars can be distinguished from dunes by their greater length and less frequent occurrence: whereas bars can also appear as single features, dunes mostly appear periodically and in trains (Kennedy, 1963). Anti-dunes arise under higher velocities and Froude numbers and differ in orientation of their crest form towards the mean flow direction. A main characteristic is that they mostly migrate slowly upstream (Kennedy, 1963; Colombini, 2004).

A longitudinal section through a dune is approximately triangular in shape. The upstream slope is gentle and slightly convex, the lee side is steep and forms a deep trough, see Figure 2.1. This steep lee slope will reach approximately the angle of repose of the sediment.

Dunes are spatially periodic structures and thus their periodicity (wave length λ) and amplitude (wave height Δ) are their main characteristics. Dune length is the distance from crest to crest or trough to trough, see Fig. 2.1. Dune height is the vertical distance from crest to trough. Literature supplies a vast number of dune formulae, calculating dune height as a function

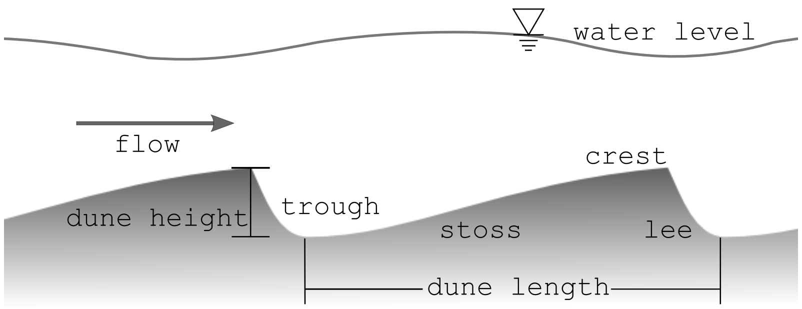

Figure 2.1: Definition of dune length, height and locations along dune forms

of water depth, bottom shear stress or Froude number as governing, hydrodynamic parameters, e.g. by Gill (1971), Yalin (1964, 1992), Engelund and Fredsøe (1982) and van Rijn (1984b). The dune length has been parametrised e.g. by Flemming (1988) or Yalin and Ferreira da Silva (2001), who link dune length to dune height in a proportional way. The formula of van Rijn (1984a) relates dune length and water depth following the relation $\lambda/h = 7.3$. Other evaluations show that the length of dunes further depends on the presence of suspended sediment, with relative dune length increasing with increasing suspended sediment (Naqshband et al., 2014a).

Dunes are generally distinguished as two-dimensional and three-dimensional bed forms. Length and height of these three-dimensional bed forms vary in space and time. Thus calculated length and height are spatially averaged values, calculated rather for a dune field than for single bed forms. If three-dimensional bed forms are regarded, superimposed forms also need to be separated from underlying ones (Coleman and Nikora, 2010). The crest lines of two-dimensional dunes are straight, whereas three-dimensional dunes have a sinuous crest line, which is often additionally non-uniform (Venditti et al., 2005). Size and arrangement of three-dimensional dunes is random for individual dunes and only uniform in the statistical sense (Kennedy, 1963). Being characterised through permanently changing shape, three-dimensional dunes are less stable than two-dimensional dunes. But even though two-dimensional bed forms are considered more stable, they will change to three-dimensional bed forms over time (Baas et al., 1993; Baas, 1994; Venditti et al., 2005).

Following this, dunes in natural rivers are generally not two- but three-dimensional and it is thus not surprising that theories in which dunes are described by a single height and length do not deliver qualitatively good results for river prognosis (Mertens, 1995). As most of these approaches are based on laboratory results, they will produce more accurate results for experimental flumes than for natural rivers (Karim, 1998).

The shape of the bed(-form) is a product of interaction between flow and river bottom. Therefore, it depends not only on flow characteristics such as water depth and flow velocity, but also on properties of sediment and fluid, e.g. grain diameter and fluid density (Kennedy, 1963). A diagram of this interaction has been originally presented by Shields (1936) in his thesis and has been modified and optimised by many authors (e.g. Chabert and Chauvin, 1963; Raudkivi, 1967; Zanke, 1982), see e.g. Figure 2.2. This so-called Shields diagram sets the sedimentological Reynolds number Re_* in relation to the sedimentological Froude number Fr_*, also called Shields parameter θ. They are calculated as follows

$$Re_* = \frac{u_* d}{\nu} \tag{2.1}$$

$$Fr_* = \theta = \frac{\rho u_*^2}{(\rho_s - \rho) g d} \tag{2.2}$$

where u_* is the friction velocity in [m/s]

$$u_* = \sqrt{\frac{\tau_o}{\rho}} \tag{2.3}$$

with:	d	grain diameter [m]
	ν	kinematic viscosity [$\mathrm{m^2/s}$]
	ρ	density of water [$\mathrm{kg/m^3}$]
	ρ_s	density of sediment [$\mathrm{kg/m^3}$]
	g	gravitational acceleration [m/s]
	τ_o	bed shear stress [$\mathrm{N/m^2}$].

The Shields diagram illustrates that ripples will appear as a first bed form at subcritical flow and from a flat bed. Their size is mainly dependent on the mean diameter of the sediments. As the rate of flow increases, dunes as well as dunes superimposed by ripples will form (Zanke, 1982). The diagram – based on a vast number of experiments – shows that the transition from ripples to dunes is smooth and can not be determined exactly.

Equilibrium dunes are in balance with the surrounding flow field. They might still undergo morphodynamic changes, but average values of the complete dune field, such as mean dune height and mean dune length, remain constant. In natural surroundings this state only exists when averaging over long time periods. Over short time scales dunes in rivers are exposed to varying boundary conditions in water discharge and are therefore in a constant state of adjustment. In flume experiments equilibrium dunes can be generated. A steady state is characterised by maximum dune height $\Delta \approx 1/3\ h$ at corresponding water depth h in free surface flow. In this situation, the phase lag δ between the point of maximum velocity and the maximum bed shear stress disappears (Kennedy, 1963). This equilibrium state can be easily disturbed.

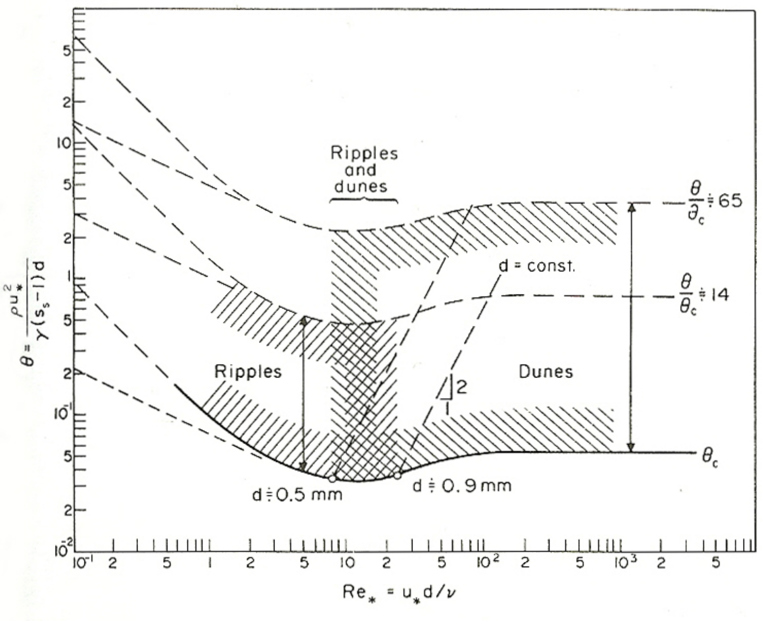

Figure 2.2: Formation of dunes and ripples in the Shields diagram, Shields parameter θ over sedimentological Reynolds number Re_*, in Raudkivi (1967)

2.1.2 Flow over dunes, occurrence and development

Flow over dunes can be categorised through five regions, shown in Figure 2.3 (after e.g. Engelund and Fredsøe, 1982; Nelson et al., 1993; McLean, 1990; Bennett and Best, 1995; Maddux et al., 2003b; Best, 2005; Balachandar and Reddy, 2011). Behind the crest of the dune a *separation zone* is formed that reattaches to the dune after 4–6 times the dune height following the point of separation (Engel, 1981). In and below the separation zone, the flow recirculates. Over the separation zone a *shear layer* develops that divides the recirculation zone from the free flow above. This zone expands and dissipates further downstream. Also it gradually merges into the zone of *expanding flow* that characterises the flow field at the lee side of the dune. At the bottom, a new *internal boundary layer* forms after the point of reattachment. Here the flow interacts with the wake region above, but it is mainly characterised by the re-establishment of logarithmic velocity profiles. The zone of *maximum (horizontal) velocity* is at the crest of the dunes. The point of maximum bed shear stress is located upstream of this zone, creating a phase lag. It determines the quantity of sediment transported towards the lee side of the dune. It is widely agreed that flow separation, turbulence production and transport as well as shear layer formation are the governing flow features for morphodynamics of dunes (e.g. Nelson et al., 1993; Bennett and Best, 1995; ASCE, 2002; Sumer et al., 2003; Best, 2005; Paarlberg, 2008; Nabi, 2012).

An initial perturbation of the bottom will trigger the emergence of dunes. This may be caused by several reasons. Coleman and Nikora (2008) name three phenomena that can be held responsible for initiation of dunes from a flat bed: first is the turbulent fluid motion (e.g. Jackson, 1976; Yalin, 1992), second is an instability of the fluid-sediment flow configuration which reacts to a disturbance, discussed for example by Kennedy (1969); Fredsøe (1974); Colombini (2004), and third granular transport mechanics, also discussed by e.g. Raudkivi (1966) and Venditti et al. (2005). After initiation of movement the perturbed bottom will react with a phase of re-formation and furthermore, in interaction with the flow, dunes might form.

Transport of sediment is often decomposed into bed load and suspended load. The transport is catagorised as bed load, if the sediment particles move in sliding and rolling mode in a thin layer. If the sediment particles enter the free flow field and return to the bed surface, the transport mode is called saltation, which is often included in the definition of bed load. In suspension, sediment grains are dispersed through the complete water column. This happens, if the order of fluid velocity fluctuations is comparable to the order of settling velocity (Charru et al., 2013). Even with this definition there is often no sharp distinction between suspended and bed load transport in natural flows. Then both modes are interchangeable, and sediment is transported as bed load at one instance and as suspension at the next (Yang and Lim, 2003). Over dunes sediment grains are transported close to the bed over the stoss side of the dune. At the point where the flow detaches itself from the bottom

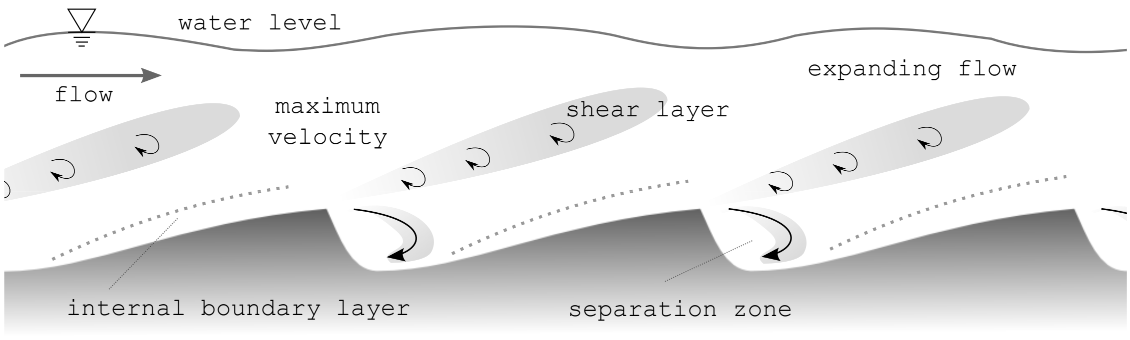

Figure 2.3: Flow regions of river dunes

form (point of separation), they either roll down at the lee side and come to rest in the trough. Alternatively they enter the state of suspension in the turbulent fluid flow after the point of separation. These sediment particles can be transported back to the dune trough or further on to the following stoss side of the next bed form (Wilbers, 2004).

The effect of suspension on dune dynamics depends on flow and sediment characteristics. With weak separation zones, suspension was found to have no consequences on the dune form and their dynamics (Carling et al., 2000a). If medium and coarse sediment is responsible for the bed form movement, the sediment is generally transported as bed load (Yalin, 1972). If the sediment is fine, it will be accumulated in the troughs of the bed forms and can play a crucial part in the transport process (van den Berg, 1987). Experimentally, Schmeeckle (2014) found that the hydraulic roughness increases abruptly at the transition from bed load transport to suspended load. Thus the presence of suspended sediment can influence the transport governing flow structures, even if it is irrelevant for the mass of the bed form. Concerning dune shape it has been mentioned above, that the relative dune length increases with increasing suspended sediment (Naqshband et al., 2014a).

The time for dunes and ripples to reach equilibrium dimensions has been intensively studied (Kennedy, 1963; Baas et al., 1993). Studies of this category need to be carried out under laboratory conditions, as natural boundary conditions vary and results are not independent of these. The time t^* to reach equilibrium dimensions is independent of water depth for ripples, as they do not interact with the free surface, whereas for dunes it is typically independent of viscosity effects. For dunes the equilibrium state is reached after time $t^* = f(\theta, h/d)$, being a function of dimensionless bed shear stress θ, water depth h and representative grain size d (Coleman et al., 2005).

2.1.3 Simulation of flow over dunes

Most coupled hydro-morphodynamic simulations are RANS (Reynolds-Averaged Navier-Stokes) simulations, thus only the mean, time averaged flow is calculated. Turbulent fluctuations of the flow stay unknown – with these being calculated only by Direct Numerical Simulation (DNS). Large Eddy Simulation (LES) calculates the larger turbulence structures (Pope, 2004); the limiting size will depend on mesh resolution. Effects of turbulent structures below mesh resolution are captured by turbulence models, which use empiric formulations that account for small scale, fluctuating parts of the flow.

Algebraic turbulence models, where no additional differential equation is solved, are often applied in river modelling, as this approach allows to save computational time. This explicit approach can be sufficient, if the model area and its water body is very large, thus turbulence is of minor importance or does not need to be examined in detail. In this case, the turbulent viscosity ν_t, which is needed for closing the Navier-Stokes Equations (see Section 4.1) can be calculated by an algebraic equation. The simplest form is a constant. The value is either obtained from physical experiments or calibration. Another classical approach is the widely used *mixing-length-hypothesis* of Prandtl (1925). It relates the turbulent viscosity to the gradients of the velocity and the mixing length l_m, which can be calculated by empirical formulations for simple flows. The *Smagorinsky model* (1963), also used in LES for sub-grid scale turbulence modelling, calculates a turbulent viscosity from the local mesh size and the derivatives of the velocity field.

The simulation of more complex flows also requires a more complex representation of the turbulent viscosity. *Two-equation turbulence models* additionally describe the transport of characteristic turbulence parameters (turbulent velocity scale and length scale) with two additional differential equations. The most popular is the k-ε model, which includes the turbulent kinetic energy k as characteristic velocity gradient scale, see Section 4.1 (Launder and Sharma, 1974; Rodi, 1993). It has been used in various dune applications (e.g. Tjerry and Fredsøe, 2005; Giri and Shimizu, 2006; Dimas et al., 2008; Amoudry and Souza, 2011). The k-ω model also finds wide application (e.g. Lyn, 2008; Niemann et al., 2011; Khosronejad et al., 2015). It includes the calculation of the turbulent kinetic energy as well as the characteristic frequency ω of the energy dissipating eddies (Wilcox, 1993).

2.2 Dune experiments for the calibration of numerical models

2.2.1 Measurements of dunes

Various experiments form the basis for bed load transport description in fluvial systems as it finds application in modern numerical systems (e.g. Einstein, 1950; Kennedy, 1963; Shen, 1970; Yalin, 1972; Raudkivi, 1967; Zanke, 1982; Engelund and Fredsøe, 1982). Additionally there are experiments and studies with focus on suspended sediment (e.g. Talmon, 1992; McLean et al., 2008; Kostaschuk et al., 2009; Naqshband et al., 2014b), which is not part of this work.

For hydrodynamic measurements over dunes – for example in the experiments of Venditti (2007) – often only a rigid, non-erodible dune bed is used. This has some practical reasons: not only do the bed forms of a mobile bed migrate downstream, they are also constantly in a state of adjustment in height and length as well as in position of maximum sediment transport. High resolution measurements over a sufficiently long period of time are hardly feasible upon a highly dynamic bottom. Therefore, almost no high resolution measurements above moving bed exist for comparison. An exception so far is the work of Naqshband et al. (2014b), who conducted high resolution measurements over mobile sand dunes with an acoustic system (Acoustic Concentration and Velocity Profiler). They measured the velocity field, turbulence and the suspended sediment field and showed that the mean and turbulent flow evolution over mobile beds greatly differ from experiments by other authors, where the measurements were conducted over fixed beds.

Sumer et al. (2003) also conducted experiments in a flume with mobile bed. They described the influence of turbulence on bed load transport in their experimental study by evaluating the resulting bottom evolution. In their experiments they added external turbulence generated by different devices into their open channel flume and compared sediment transport rates with and without externally added, singled out, turbulence. They found that the sediment transport rate increased considerably at points of increased turbulence level for ripple-covered as well as for flat bed.

2.2.2 Morphodynamic simulations

For numerical investigations of morphodynamic processes at a river scale Reynolds-Averaged Navier-Stokes (RANS) simulations are still the only practical alternative. LES and DNS will provide higher mesh resolutions and generate more information. Nowadays, RANS simulations for larger river sections already reach the limits of growing computer capacities. For an adequate mesh resolution in RANS simulations parallelisation (splitting the work load on different processors) becomes necessary. For long term simulations, parallelisation scales not with the amount of 'real' time simulated, but with model extent. Thus parallelisation is also limited. LES and DNS calculations for large river sections, with even higher mesh resolutions, are not feasible. It is therefore useful to test RANS models for their applicability to dune simulation.

In the past, RANS models have been successfully used for dune simulations. Paarlberg (2008) used a RANS model in which the separation zone created by dunes was parametrised. As dunes extend into the flow, they induce flow resistance and by doing so generate mixing patterns and turbulence. Through these effects the flow is slowed down and higher free surface levels are generated. Therefore a numerical model needs to compute all mixing patterns at all associated scales to incorporate all flow resistances directly. These scales might range from short time Kolmogorov scale to complete river reaches (Paarlberg, 2008). The author still did not find this approach feasible for his project work on river reach scale, due to necessary computational effort and also due to lacking knowledge about flow around dunes. Paarlberg (2008) therefore used a parametrisation of the separation zone to account for the effects mentioned above. He used a two-dimensional laterally-averaged model, which was able to realistically simulate river dune evolution (Paarlberg et al., 2009).

Giri and Shimizu (2006) applied an Eulerian stochastic formulation of sediment transport in their morphodynamic model, which was coupled to a two-dimensional (in a vertical plane) hydrodynamic model. They used an empirical model for pick-up and deposition of sediment, where the step length of the sediment particle (distance of its travel in water column before returning to bottom) was calculated through a formulation of Einstein (1942, see Giri and Shimizu, 2006). Their simulations of a laboratory experiment showed promising results, but the dune length strongly depended on definition of the sediment step length.

Niemann et al. (2011) presented results of a hydrodynamic RANS model with a k-ω turbulence closure (see Chapter 4.1 for details on turbulence models) coupled to morphodynamics. An individual dune was modelled. They successfully predicted dune evolution from an initial perturbation with their RANS model.

Main difference between DNS and LES compared to RANS models is the simulation of turbulence. Turbulence has been identified as a dominant factor for dune emergence, development and movement (Jackson, 1976; Nelson et al., 1993; Bennett and Best, 1995). This is the case even though morphodynamic processes are of a different time scale as the formation of turbulence.

Turbulent flow structures consist of short-term flow fluctuations of all spatial scales, ranging from the size of water depth down to the Kologmorov scale. Tjerry and Fredsøe (2005) were able to create realistic dune shape patterns when using turbulence-averaged bed shear stress for sediment transport. In agreement with Nelson et al. (1995) they state the need of including the local fluctuation term of the bed shear stress and their characteristics into the sediment transport description. This should lead to a local increase of sediment transport and result in a more pronounced sediment transport peak.

Three-dimensionality of dunes further changes the flow field, making it more complex and less repetitive. This was shown by Omidyeganeh and Piomelli (2013a,b), who presented Large Eddy Simulations (LES) over fixed, three-dimensional dunes. They successfully captured the formation of vortex structures behind the 3D bed forms and also their transport further down the dune field and towards the surface. Nevertheless, as previously discussed, the range of applicability in morphological simulations of this kind of models is limited. Nabi (2012); Nabi et al. (2012, 2013a,b) presented LES results on a locally refined Cartesian grid. Bed evolutions were calculated as net result of pick-up and deposition of sediment particles, which were assumed as rigid spheres moving in the water under the influence of gravitational and flow-induced forces. Furthermore, Nabi (2012) showed successful simulation of emergence and movement of three-dimensional dunes. Because of the highly complex and time-consuming nature of the computational model, he also used his findings to develop parametric models which can be used efficiently at larger spatial and temporal scales.

Schmeeckle (2015) presented numerical investigations with a LES model, where the influence of turbulence on individual sediment grains and its influence on bed shear stress after a backward-facing step was investigated. Schmeeckle (2015) concluded, that using bed shear stress that is averaged over time, is not sufficient to calculate the bed load transport rate downstream of separated flows. His investigations were also motivated by the findings of Nelson et al. (1995), who 20 years earlier had already stated that there was no simple relation between near-bed Reynold stress and bed load transport. Moreover, the magnitude of turbulent structures showed significant spatial variations, which in turn caused significant peaks in bed load transport. Flow events of high stress resulted in a change of sediment flux. Schmeeckle (2015) logically came to the conclusion that these peaks need to be included in bed load models, if transport over dunes and ripples is simulated.

In their papers Khosronejad and Sotiropoulos (2014) and Khosronejad et al. (2015) presented morphodynamic simulations of dunes with LES on laboratory scale, as well as URANS (Unsteady Reynolds-Averaged Navier-Stokes) on project scale. They used a dynamic Smagorinski subgrid scale model in which the LES and the URANS simulations equations are closed with a k-ω turbulence model. They were able to translate their URANS model to a practical engineering scale, where they applied it to a $27\,\mathrm{m}$ wide river and showed first promising morphodynamic results concerning overall sediment phenomena with characteristic bed feature positions. They stated that the URANS simulations seem sufficient to capture flow structures responsible for morphological processes on this scale.

2.3 Calculation of bed shear stress

Sediment transport is related to the flow field by the bed shear stress τ_B. It expresses the force that acts on the bed as well as the resistance the bottom opposes the flow. As it is the link between flow and moving bed for morphodynamic simulations, special attention needs to be given to this parameter. The shear exerted over a surface is calculated by projecting the tensor of the internal stresses in a fluid **P** to the direction of the normal unit vector of the bottom $\mathbf{n}_B$

$$\tau_B = -\mathbf{P}\,\mathbf{n}_B\,. \tag{2.4}$$

with the components $(n_B^x,\ n_B^y)$ along the x- and y-Cartesian system, respectively. Over a flat bottom in laminar flows, the shear stress of Newtonian fluids at point z will be therefore

$$\tau_B(z) = \mu\frac{\partial u}{\partial z} \tag{2.5}$$

with: μ dynamic viscosity of the fluid $[\mathrm{Pas}]$
u velocity of the fluid along the bottom $[\mathrm{m/s}]$
z height above the bottom $[\mathrm{m}]$.

Thus for the bed shear stress directly at the bottom, the velocity field at this point needs to be known. This velocity field is generally difficult to measure, especially in field conditions. Therefore various approaches to estimate the bed shear stress exist.

Most simply, the bed shear stress is calculated using the skin friction at the bottom. The bottom is then considered to be flat and the skin friction depends on the prevailing sediment (diameters). It finds application in one-dimensional flow calculations, where the velocities are regarded depth-averaged and also averaged over the cross section of a channel. Wide application find the formulas of e.g. Chezy, Darcy-Weisbach and Manning-Strickler (see DVWK, 1991; Naudascher, 1992). These approaches simply assume that the bottom is flat and thus the bed shear stress can be calculated from the energy slope of the flow.

In three-dimensional flow simulations velocity profiles are resolved over the complete water depth. In this case the bed shear stress can be calculated from velocities close to the bottom, delivering a more accurate representation of the local, sediment movement governing flow situation. It was found that this bed shear stress calculated from velocity profiles is valid for flat beds with steady and uniform flow, where the boundary layer is well-developed (Nelson et al., 1995). Over non uniform topography, where the flow is characterised by turbulent motions, the bed shear stress is additionally dependent on the turbulence and cannot be calculated from the velocities only (Nelson et al., 1995; Biron et al., 2004).

Over dunes, turbulent flow features have been identified as crucial for morphodynamic processes. The calculation of bed shear stress from turbulent parameters is an established approach and different methods exist. Reynolds stress models include the velocity fluctuations of streamwise (u') and vertical (w') velocity components (Pope, 2000)

$$\tau_o \;=\; -\rho < u'w' > \tag{2.6}$$

where $<>$ represents a time average and ρ is the water density. All three components of the velocity (v' is the crosswise velocity component) are used in the turbulent kinetic energy (TKE) method, presented e.g. by Soulsby (1983),

$$\tau_o \;=\; C_1\,\frac{1}{2}\,\rho\,(< u'^2 > + < v'^2 > + < w'^2 >) \;=\; C_1\,\rho\,k\;, \tag{2.7}$$

basically using the turbulent kinetic energy k and the proportionality constant $C_1 = 0.19$ (Soulsby, 1983). A vertical turbulent kinetic energy (TKE-w') approach is presented by Kim et al. (2000), which only uses the vertical components of the velocity fluctuations

$$\tau_o \;=\; C_2\,\rho < w'^2 > \tag{2.8}$$

with $C_2 = 0.9$. This approach can be chosen to exclude noise errors of horizontal velocity fluctuation measurements, which are generally higher than the vertical ones.

Biron et al. (2004) compared the above approaches along with the logarithmic relation of velocity and bed shear stress (Eq. 2.9)

$$\tau_o \;=\; \rho u_*^2 \quad ; \quad \frac{u}{u_*} \;=\; \frac{1}{\kappa}\ln\left(\frac{h}{z_o}\right) \tag{2.9}$$

where κ is the von Kármán constant and z_o is the hypothetical level where the velocity is zero, and the quadratic stress law (Eq. 2.10)

$$\tau_o \;=\; \rho\,C_d\,\mathbf{U}|\mathbf{U}| \tag{2.10}$$

with U being the average fluid velocity and C_d a drag coefficient. They found that for complex flow fields the TKE method (Eq. 2.7) produces the best match with a bed topography of two scour zones, whereas the bed shear stress calculated with Eqs. 2.9 and 2.10 produced less satisfying results. The shear stress calculated with the TKE method followed the turbulence pattern, which increased notably in the scour zones. The TKE-w' method failed to follow this pattern, even though it gave good results for a simple boundary layer set-up. Biron et al. (2004) reasoned that for shear stress production, the streamwise fluctuations must be more relevant than the vertical ones. They still advise to re-estimated the constant C_1 for natural river applications.

Hoan et al. (2011) conducted an analysis on integration of turbulence into shear calculations over a stone bed. They presented their own (Eq. 2.13) and two existing formulae, by Jongeling et al. (2003) (Eq. 2.11) and Hofland (2005) (Eq. 2.12), in their comparison:

$$\Psi_{WL} = \frac{\langle(\overline{u}+\alpha\sqrt{k})^2\rangle_{hm}}{\Delta g d} \tag{2.11}$$

with:	Ψ	dimensionless entrainment rate $[-]$
	$\overline{u}$	mean velocity $[\mathrm{m/s}]$
	k	turbulent kinetic energy $[\mathrm{m^2/s^2}]$
	α	$= 6$, empirical turbulence magnification factor
	hm	$= 5d + 0.2h$, distance above the bed $[\mathrm{m}]$
	$\langle ... \rangle_{hm}$	spatial average over distance hm
	h	water depth $[\mathrm{m}]$
	Δ	$= \rho_s/\rho_w - 1$ $[-]$
	d	sediment diameter $[\mathrm{m}]$,

$$\Psi_{Lm} = \frac{\max\left[\langle\overline{u}+\alpha\sqrt{k}\rangle_{Lm}\frac{Lm}{z}\right]^2}{\Delta g d} \tag{2.12}$$

with:	max	(vertical spatial) maximum of the (temporal) maximum velocity
	Lm	$= \kappa\, z\sqrt{1 - z/h}$, Bakhmetev mixing length $[\mathrm{m}]$
	$\langle ... \rangle_{Lm}$	moving average with filter length Lm
	z	distance from the bed $[\mathrm{m}]$.

These approaches integrate the turbulence (k) as well as the velocity into the bed shear stress. The calculations of the existing formulae differ in extraction height (z) and the averaging process of k and the u-, v- and w-velocity components through the water column. The formula of Hoan et al. (2011) uses a similar approach and is deduced from measurements via correlation analysis:

$$\Psi_{u-\sigma[u]} = \frac{\langle [\overline{u} + \alpha\sigma(u)]^2 \; x \; \sqrt{1 - z/h}\rangle_h}{\Delta g d} \tag{2.13}$$

Here $\sigma(u)$ [m/s] is a parameter calculated from the fluctuating velocity component u' in the form of $\sigma(u) = \sqrt{\overline{u}'^2}$ and $\alpha = 3$ is also a turbulence magnification factor. The parameter for comparison is the dimensionless entrainment rate Ψ, which is common in calculations of stone beds, where the force on a single stone (and for example in revetments) is the crucial parameter for bed movements. Hoan et al. (2011) found that for non-uniform flow there is no clear correlation between Shields parameter and dimensionless entrainment rate. Following this, in non-uniform flow conditions, it is not sufficient to calculate the quantity of flow impact onto the bed through the Shields parameter alone (Hoan et al., 2011).

2.4 Synthesis

The maintenance of waterways is mostly motivated by economic interests. Bed load needs to be transported and minimum water depths need to be guaranteed for a safe passageway of ships. Dunes are the most common bed forms of waterways (Engelund and Fredsøe, 1982). Their analysis and prognosis is therefore of interest for the responsible shipping authorities. It has been shown, that dunes can be present as two- but in nature mostly three-dimensional structures. They cover a broad range of size and dimension depending on boundary conditions, flow field and sediment composition. Thus in their analysis different aspects need to be regarded: form and shape, distribution on the river bottom, time scale as well as spatial scale (flume or field scale bed forms). In this complex setting, measurements on dunes have long been focused on fixed, two-dimensional dunes, especially in experiments concerning the turbulent flow field. The last decades have brought more detailed experiments, as measurement equipment was enhanced and computer capacities have been growing. In the last years the main focus has been on numerical experiments. River simulations used for in situ prognosis of water levels and also bed movement are nonetheless mostly RANS (Reynolds-Averaged Navier-Stokes) simulations. LES or DNS (Large-Eddy and Direct Numerical Simulation) are still not applicable for long-term field scale simulations.

If sediment transport by three-dimensional bed forms is simulated, special attention has to be given to the calculation of bed shear stress. Various approaches of calculating bed shear stress from the surrounding flow field have been presented. It shows that for complex flow fields the use of turbulent kinetic energy for bed shear stress calculation enhances the distribution of bed shear stress over characteristic bed deformations, e.g. scour zones (Biron et al., 2004).

This thesis therefore presents morphodynamic RANS simulations, on laboratory and in situ scale, where the turbulent kinetic energy is included into bed shear stress calculation and its effect on dune forms is evaluated. For validation of the hydrodynamic model, the turbulent flow field is measured over naturally formed, three-dimensional dunes, as the hydrodynamic model provides the input variables for the bed shear stress calculation. With these adaptations a morphodynamic model for the behaviour of river dunes can be provided for maintenance strategies.

3

Physical Model

Contents

River engineering combines various fields that are in close interaction with each other. Nowadays the hydraulics of waterways are not only influenced by natural processes, e.g. the runoff regime or climate change, but also dominated by man-made structures. Morphodynamic processes, and as well their reactions to external influences, are amongst the most difficult to be predicted. Therefore, river engineering is often an inexact science. Thus, detailed hydrodynamic and morphological measurements form the groundwork of all validation and verification for the simulation of waterways. New numerical developments may be derived from physical experiments, field measurements or from mathematical considerations.

The experimental data sets used in this thesis are part of a morphological experimental series that has been conducted within the scope of a research and development project, “Hydraulic response towards structures of river regulation”, conducted at the German Federal Waterways Engineering and Research Institute (BAW). A thorough statistical analysis of some of the experiments of this experimental series is also presented in the thesis of M. Henning (2013), “Multidimensional statistic analysis of spatial and temporal high-resolution dune fields” (*Mehrdimensionale statistische Analyse räumlich und zeitlich hoch aufgelöster Oberflächen von Dünenfeldern*).

The laboratory experiments serve to examine bed load transport with focus on the movement of bed forms in a dynamic, but morphologically steady state. No suspended sediment is considered. Additional to morphodynamic experiments, hydrodynamic measurements over a fixed dune bed have been conducted in the scope of this Ph.D. study, in order to improve the understanding of the processes happening inside the hydro-morphological system and to enhance the comprehension of numerical transport models.

3.1 Experimental facility

The hydrodynamic and morphodynamic physical experiments that form the basis for verification of the simulations performed during this work were conducted in an experimental flume situated at the German Federal Waterways Engineering and Research Institute (BAW) in Karlsruhe, Germany (Figure 3.1). Further detailed descriptions of the flume concept can be found in LWI (2004). The flume is $32\,\mathrm{m}$ long and $5\,\mathrm{m}$ wide and has a rectangular cross section with variable intermediate walls, which divide it into two identical halves, each $2\,\mathrm{m}$ in width. The outer walls are made of glass with vertical metal bars. The inner, dividing wall is made of plastic material. In one half, the morphodynamic experiments with moving bottom are conducted, while the other half contains a fixed dune bed.

From x = $2\,\mathrm{m}$ to $30\,\mathrm{m}$ deformations of the movable bottom of the flume can be recorded and analysed. The first non-measurable $2\,\mathrm{m}$ of the inflow zone have a paved, fixed bottom, while the last $2\,\mathrm{m}$ are allotted to the flow-governed weir. Along the analysable length of $28\,\mathrm{m}$ the water depth is measured at 15 points based on the principle of communicating vessels. The water depth is regulated by a flow-governed weir at the outlet, using the last of the measuring points before the weir as reference. Figure 3.2 (top) shows a sketch of the experimental flume with the orientation of the x- and y-axis as well as the position of the 15 measurement points including reference point P15, at $29.15\,\mathrm{m}$ along the x-axis. Figure 3.2 (bottom) shows a vertical longitudinal section of

Figure 3.1: Experimental flume for morphodynamic experiments at the Federal Waterways Engineering and Research Institute in Karlsruhe, BAW Bildarchiv

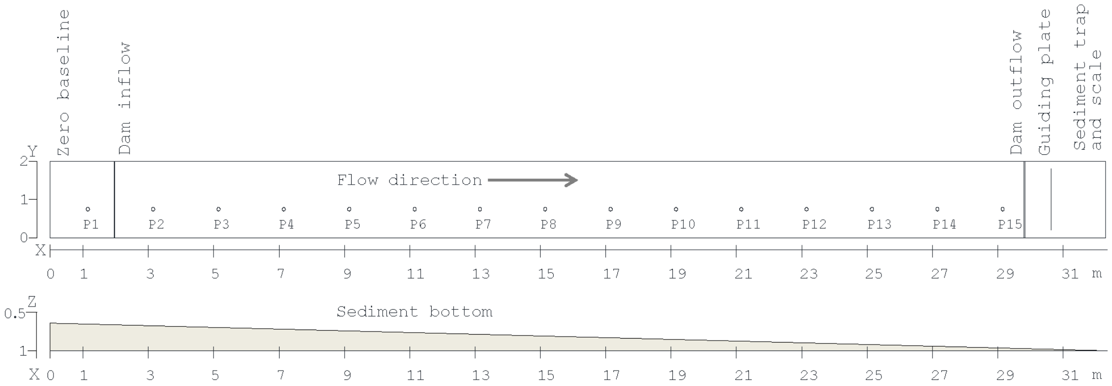

Figure 3.2: Orientation of x-, y-, and z-axis of one halve of the experimental flume, position of the 15 water level measurement points, inflow and outflow dam. Flow is from left to right

the flume with orientation of the x- and z-axis. The solid, non-erodible flume bottom has a height of z = $1.0\,\mathrm{m}$ above zero-level. The bottom of the flume above this level is constantly covered with sediment which has an average thickness of $0.2\,\mathrm{m}$. Both flume halves have an identical set-up and produce the same hydrodynamics.

3.2 Hydrodynamic measurements

For the hydrodynamic runs in one half of the experimental flume a fixed dune bed was installed. To create dunes, morphodynamic runs (described in Section 3.3) were conducted until stable bed forms for a discharge of $240\,\mathrm{l/s}$ were established (see Fig. 3.3). These dunes were fixed with a glue mixture of a wood glue powder without accelerator (KAURIT 234) and formic acid. The mixture enters the sand in liquid form and only hardens when the acid is added. Through this a 0.01 m to 0.02 m thick, firm coating consisting of sand and glue in the top layer of the sandy dune bottom is produced. For details of the process see LWI (2012b). Recordings of the bottom before and after the fixing showed no significant changes. Extensive bottom deformations were smaller than 1 mm. Close to the side of the flume measurement resolution coarsened due to the camera position of the recording system (see Section 3.3.2). Here differences reached 2 mm, see Fig. 3.4. Considering that the sand used in the experiments has a mean diameter of 0.94 mm (see Table 3.2), this corresponds to twice the grain size. During the measurement programme monitoring recordings of the bottom were done regularly. After four weeks of experimental operation, minimal results of settling process could be detected, but they also remained below the 2 mm threshold.

Test runs were conducted to verify the hydrodynamic similarity of fixed dunes and mobile bed. At the same discharge water levels measured before the fixation were in average 1 mm higher than water levels over the fixed dune forms. An explanation for this can be found in the changed roughness of the sand structures due to the coating (see Figure 3.5): the surface of the fixed sand has fewer pores and is smoother than the mobile sand. Additionally no energy is needed for the transport of bed load any more. This leads to higher velocities and a reduced water level (LWI, 2012b).

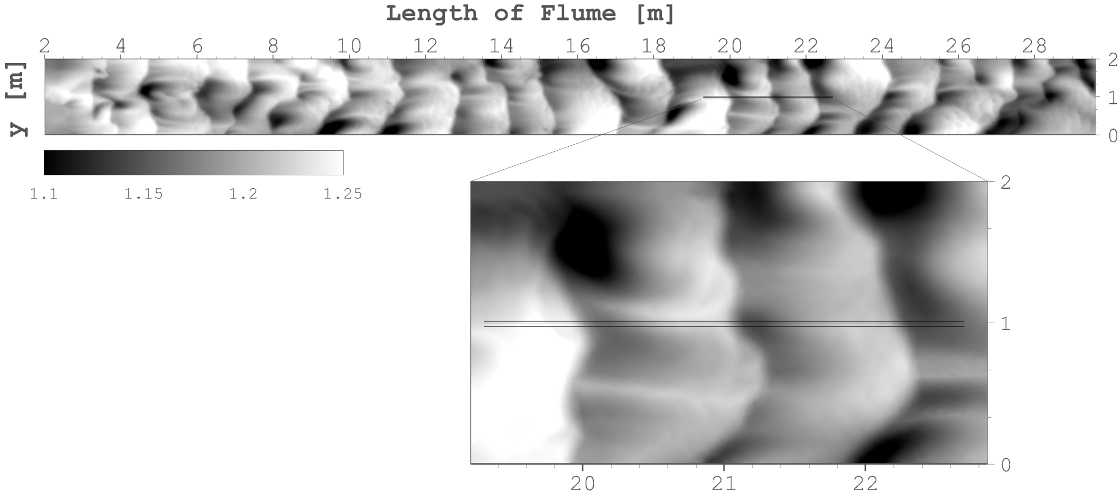

Figure 3.3: Bottom scan of fixed dune bed with position of longitudinal, hydrodynamic measuring points (detail). The bottom height is shown above the non-erodible bottom of the flume at z = 1.0 m. Flow is from left to right

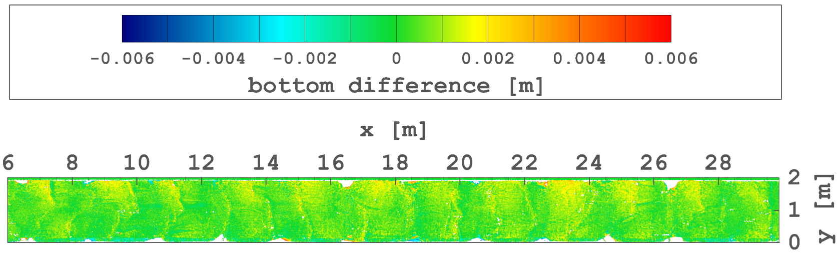

Figure 3.4: Difference in bottom elevation before and after fixation of the created dunes

Figure 3.5: Fixed (left) and unfixed sand in the experimental flume (LWI, 2012b)

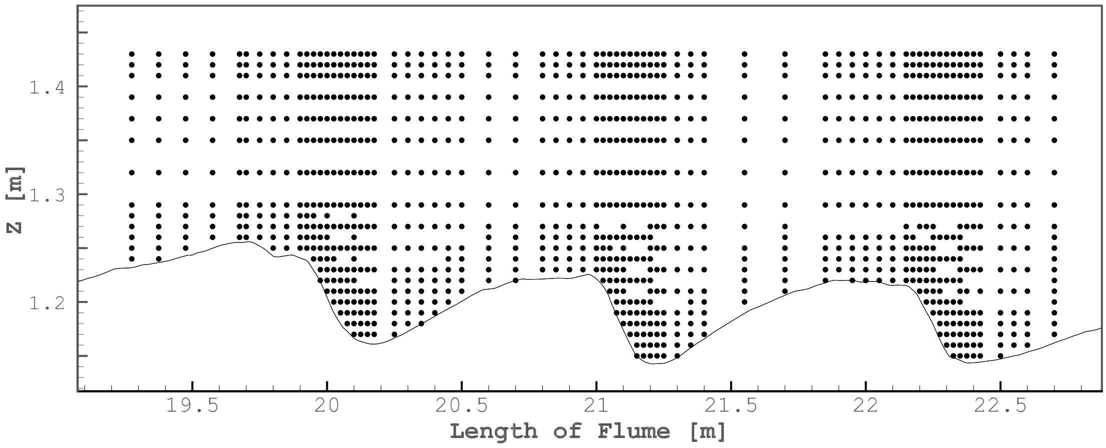

Figure 3.6: Measuring grid at longitudinal section y = $0.9725\,\mathrm{m}$

The presented hydrodynamic experiments were designed and evaluated in the scope of this thesis. The measurements over the fixed dunes were conducted as part of a Bachelor thesis at BAW by Steffen Thielmann (2013). They were conducted with a VECTRINO II probe (Nortek) which uses Acoustic Doppler Velocimetry (ADV). Following a very fine 3D measurement grid with 3000 measuring points in total, the velocities and standard deviations over three dunes (flume section x = $19.2\,\mathrm{m}$ to $22.7\,\mathrm{m}$) were measured in 3 longitudinal sections (y = $0.9725\,\mathrm{m}$, $0.9925\,\mathrm{m}$, $1.0125\,\mathrm{m}$, see Figure 3.3). Close to the bottom and in the recirculation zones of the dunes, the measuring grid is refined, see Figure 3.6.

The point measurements of velocities $u_i(t)$ ($i = 1...3$, $u_1 = u, u_2 = v, u_3 = w$) have been conducted over a time period of $100\,\mathrm{s}$. From these instantaneous flow velocities average velocities of the flow field are calculated

$$\overline{u_i} = \frac{1}{n} \sum_{j=1}^{n} u_{i,j} \tag{3.1}$$

where $i = 1...3$ for the the three velocity components and $j = 1...n$ presents the number of measurements in the averaging time frame. With Reynolds averaging

$$u_i(t) = \overline{u_i} + u_i'(t) \tag{3.2}$$

the fluctuating term $u_i'(t)$ can be extracted. The correlation terms $\overline{u_i'u_j'}$, which can be described as the exchange of momentum by the turbulent fluctuating movement of the flow, often exceed their laminar counterpart in practical flow situations (Kallenberg, 2014).

Figure 3.7 shows an example time series at x = $21.0\,\mathrm{m}$ of the flume and $0.04\,\mathrm{m}$ above the bed, displaying the complete time series $u(t)$ and the average velocity $\overline{u}$. Note that for further evaluations the outliers that can be identified as measurement errors by crossing a threshold have been removed from the data sets.

In Figure 3.8 vectors of $\overline{u}$ and $\overline{w}$ from the longitudinal section at $y = 0.9725\,\mathrm{m}$ are shown. The velocities were averaged over a time frame of $100\,\mathrm{s}$. This time frame for averaging has been established during the physical experiments. The recirculation zones of the average velocities is clearly displayed. Velocity fluctuations have been extracted from the complete time series in form of the standard deviations $u'(t)$, $v'(t)$ and $w'(t)$. From these the turbulent kinetic energy of the flow field can be calculated as

$$k = \frac{1}{2}\langle u_i' u_i' \rangle = \frac{1}{2}\langle u'u' + v'v' + w'w' \rangle = \frac{1}{2}\langle u'^2 + v'^2 + w'^2 \rangle \qquad (3.3)$$

This turbulent kinetic energy (TKE) is displayed in Figures 3.9 (a) and (b).

In Figure 3.9 (a) the turbulent kinetic energy is shown at the location of

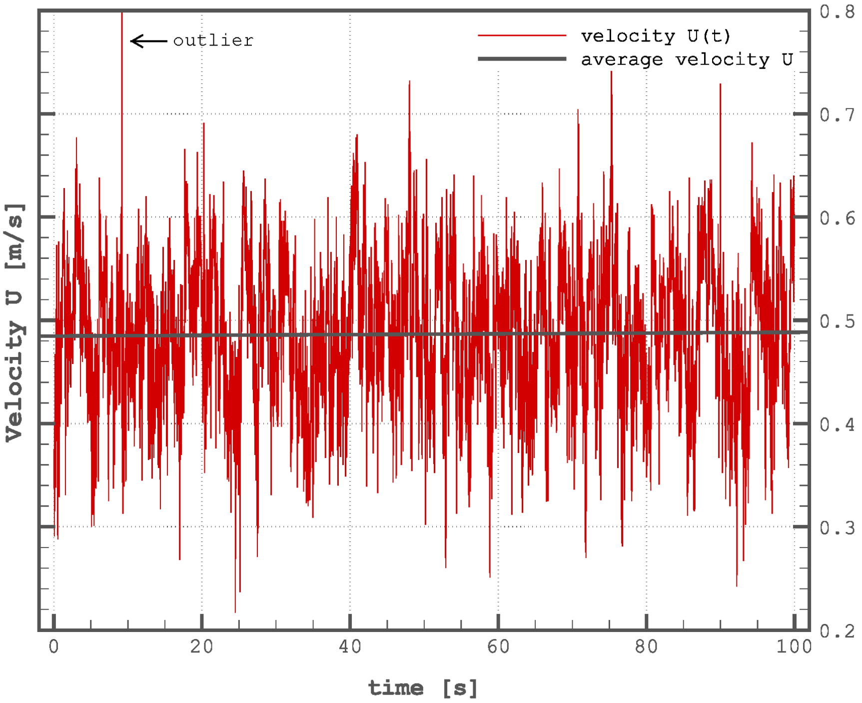

Figure 3.7: Example of time series of hydrodynamic measurements over 100 s. The graph shows the entire time series and the average velocity $\overline{u}$ at one single point in the measured domain ($x = 21\,\mathrm{m}$, $z = 0.04\,\mathrm{m}$ above the bed)

the point measurements in colour code. Figure 3.9 (b) shows the same measurements but interpolated for the areas between the measurement points through linear interpolation. Due to the fineness of the measuring grid, this display method is chosen for further comparisons between measurements and calculation.

Figure 3.10 shows measured profiles of streamwise and vertical velocities, and turbulent kinetic energy over two dunes in one of the longitudinal section. The profiles are displayed at their original measurement position over the course of the dunes. Maximum and minimum values of the parameters are given as reference. The vertical and streamwise velocities display the recirculation zone behind the dunes. The maximum values of the turbulent kinetic energy too are found here in the lee-side zone.

Figure 3.12 shows selected profiles of Fig. 3.10 in more detail, the positions are shown in Fig. 3.11. These results also show that in the recirculation zone, Fig. 3.12 (c) and (d), the turbulent kinetic energy peaks, whereas the velocity $\overline{u}$ is reduced towards the bottom. The profiles are always measured as close to the bottom as possible ($0.005\,\mathrm{m}$ to $0.01\,\mathrm{m}$ above the bottom and $0.02\,\mathrm{m}$ below the surface).

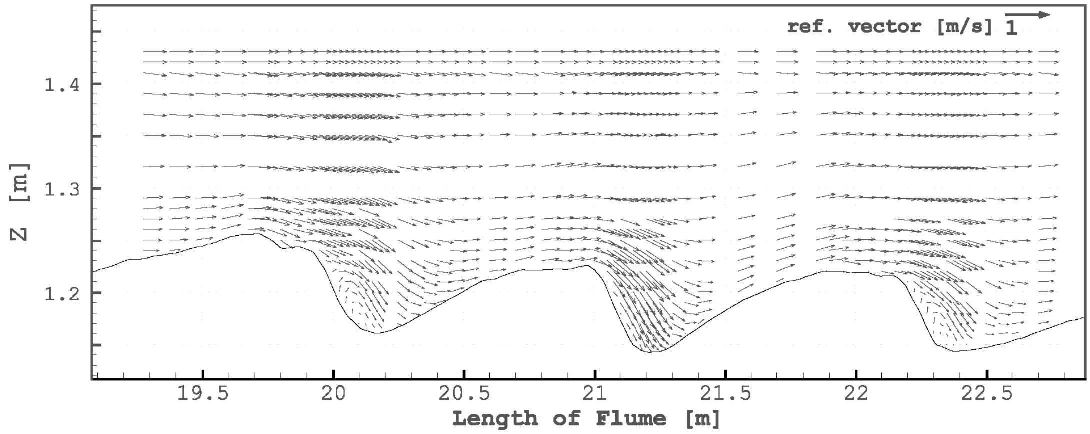

Figure 3.8: Vectors of the measured velocities ($\overline{u}, \overline{v}$) at longitudinal section y = 0.9725 m, averaged over $100\,\mathrm{s}$

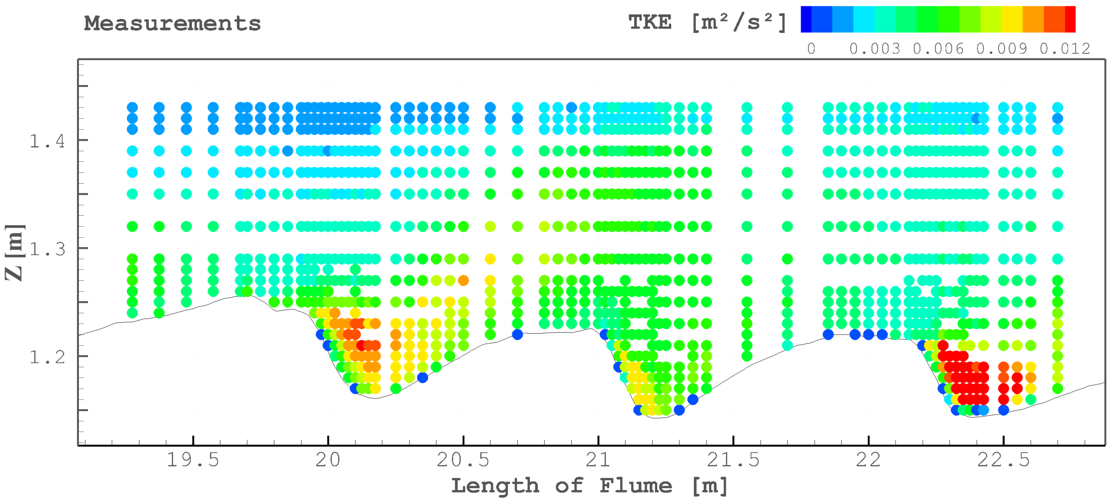

(a) TKE at the location of the point measurements

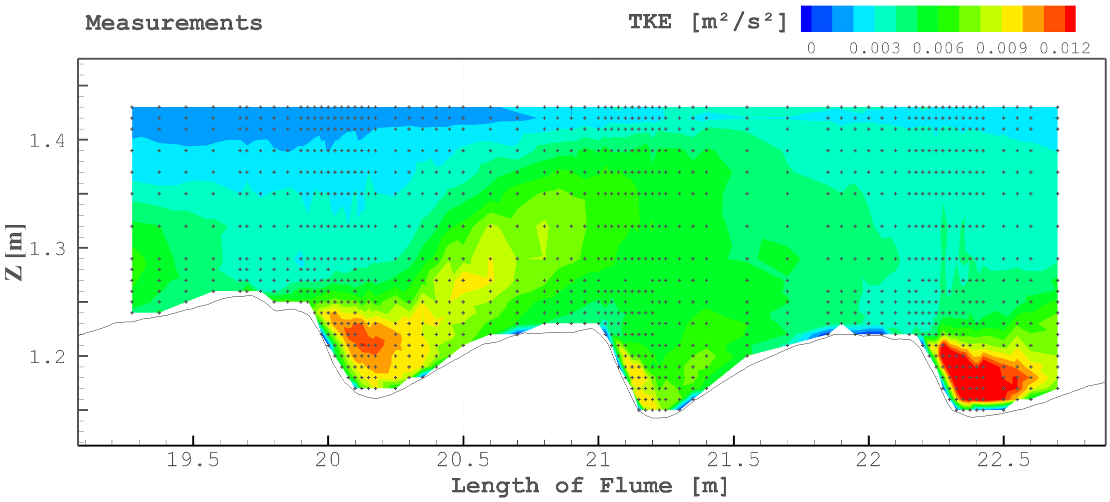

(b) TKE interpolated from marked measurement points over complete water column

Figure 3.9: Turbulent kinetic energy (TKE) [$\mathrm{m}^2/\mathrm{s}^2$] at longitudinal section $y = 0.9725\,\mathrm{m}$, averaged over $100\,\mathrm{s}$. Flow is from left to right

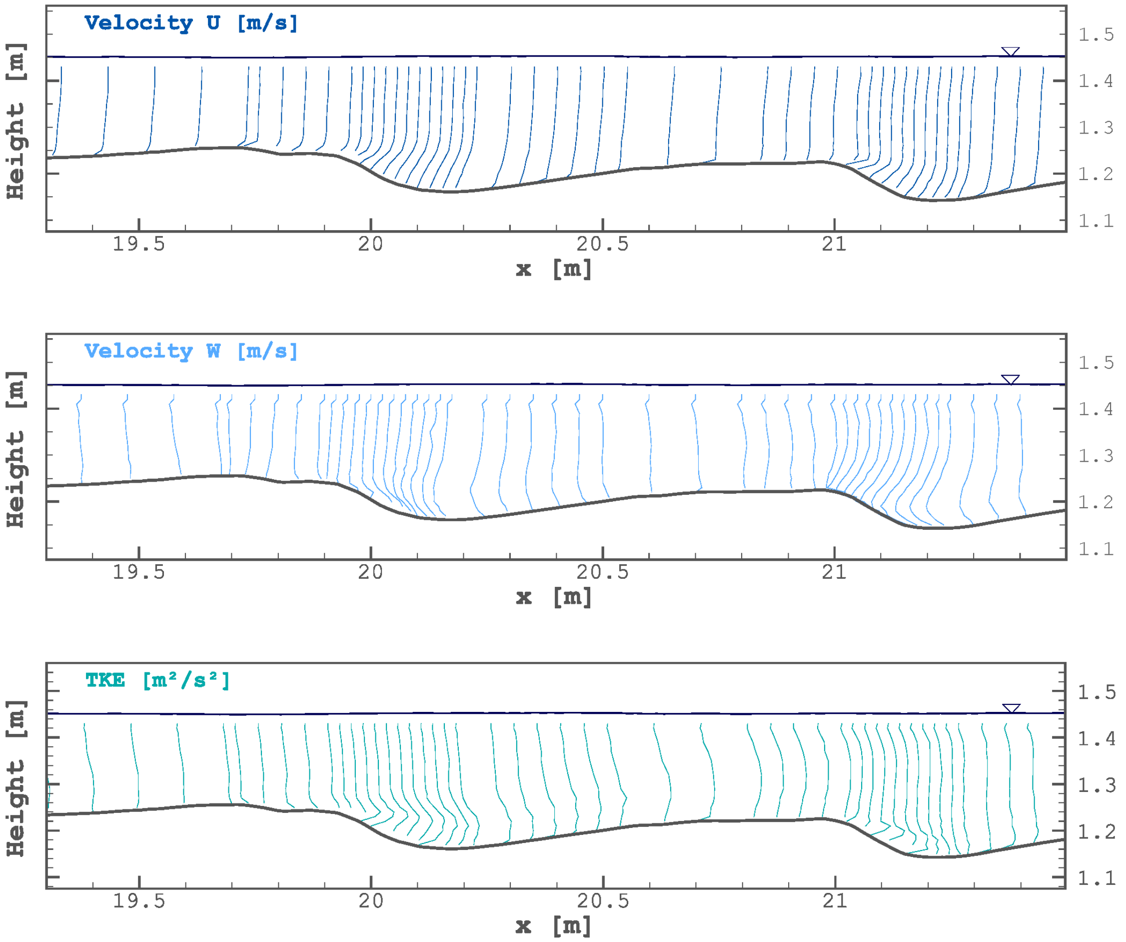

Figure 3.10: Velocities u and w [m/s] and turbulent kinetic energy (TKE) [$\mathrm{m}^2/\mathrm{s}^2$] over the course of two dunes. Reference values: $u_{max} = 0.61\,\mathrm{m/s}$, $u_{min} = -0.003\,\mathrm{m/s}$; $w_{max} = 0.0243\,\mathrm{m/s}$, $w_{min} = -0.151\,\mathrm{m/s}$; $\mathrm{TKE}_{max} = 0.012\,\mathrm{m}^2/\mathrm{s}^2$, $\mathrm{TKE}_{min} = 0.0\,\mathrm{m}^2/\mathrm{s}^2$

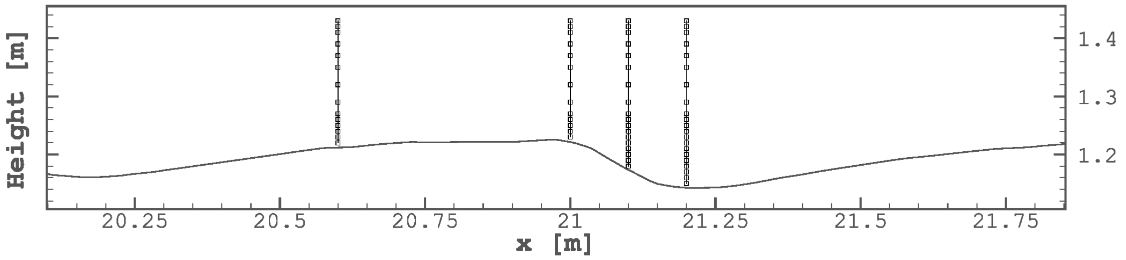

Figure 3.11: Position of selected, measured profiles over the course of a dune. Profile plots see Figure 3.12

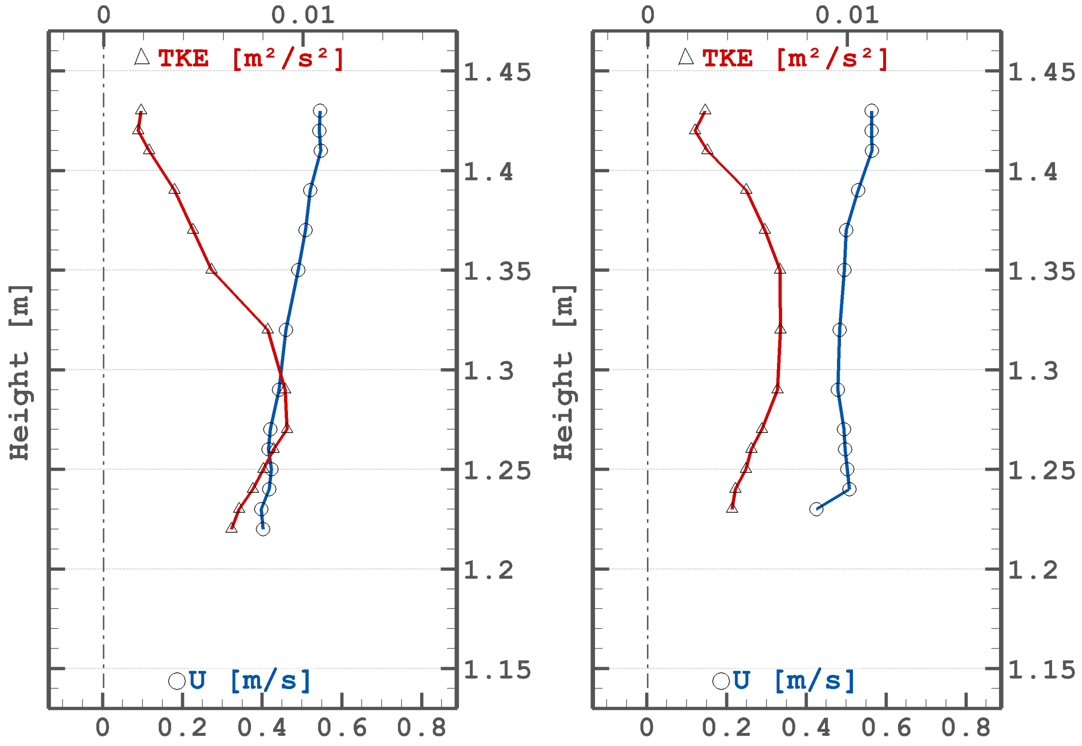

(a) Profile at x = 20.6 m

(b) Profile at x = 21.0 m

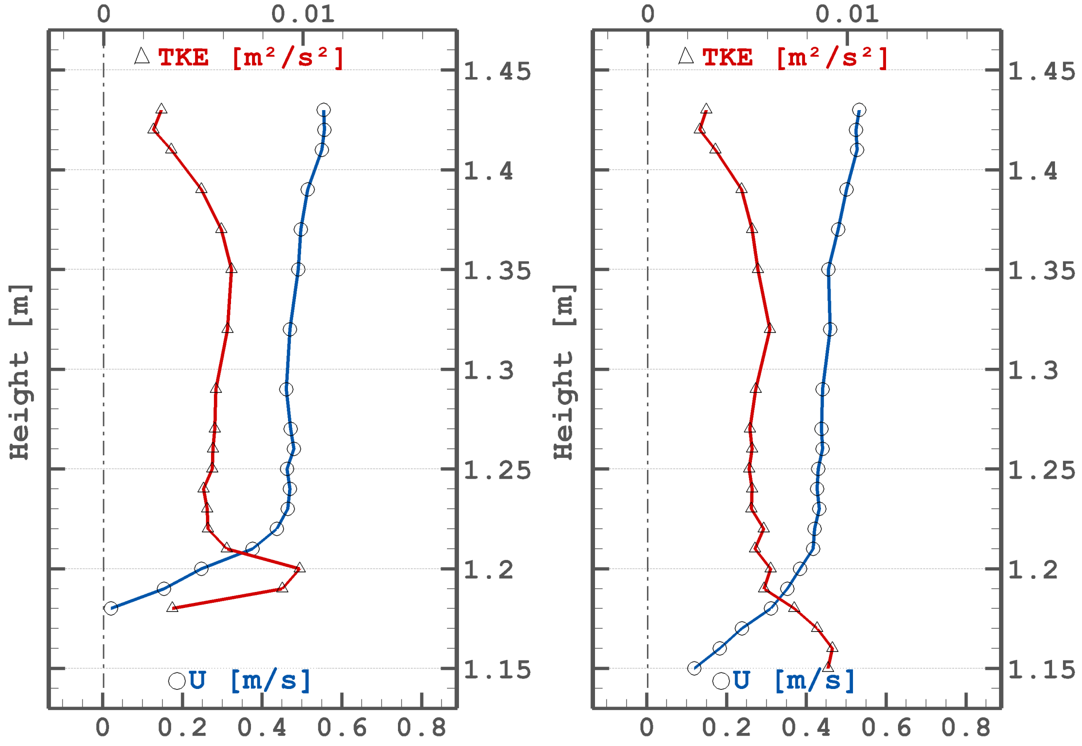

(c) Profile at x = 21.1 m

(d) Profile at x = 21.2 m

Figure 3.12: Selected profiles of measurements: average velocity ($\overline{u}$) [m/s] and turbulent kinetic energy (TKE) [m^2/s^2]

3.3 Morphodynamic measurements

During the study different morphological experiments were conducted in the experimental flume, by installing different maintenance measurements, e.g. partially fixed bed and groyne variations. Despite obtaining single, characteristic shapes, several runs of each configuration were carried out, as morphodynamic processes are subject to strong fluctuations. This work focuses on the experimental runs of the first, basic configuration with no installation of maintenance measurements. Of all other configurations the same, high-resolution data sets are available and offer the possibility to continue the work started during the research project which forms the basis of this thesis.

For this work 3 experiments (referenced as S6, S9, S10 in Haber et al. (2014)) have been used for evaluation and comparison with numerical results. Each of these experiments consists of 10 sub-experiments (runs), with a duration of 6 h each. An experiment starts with a so-called 'pre-run' (VV) of 6 h, where discharge is raised slowly ($145\,\mathrm{l/s}$ to $155\,\mathrm{l/s}$) to establish equilibrium dunes forming from a flat bed. This pre-run is followed by 18 h (3 runs of 6 h) of discharge Q_1 ($140\,\mathrm{l/s}$, with a mean water level of $0.17\,\mathrm{m}$), 18 h (3 runs of 6 h) of discharge Q_2 ($185\,\mathrm{l/s}$, with a mean water level of $0.22\,\mathrm{m}$) and 18 h (3 runs of 6 h) of discharge Q_3 ($240\,\mathrm{l/s}$, with a mean water level of $0.27\,\mathrm{m}$). An overview of discharge (Q), water levels (h_{out}, h_{mean}) and sediment discharge (G_s) is given in Table 3.1. Dune forms were analysed every 6 h, after which the experiment was continued, resulting in 30 analysed bottom scans. Description of the measuring device can be found in Section 3.3.2.

Table 3.1: Settings of experiments S6, S9, S10, each with a total duration of 60 h. One experiment can be divided in sub-experiments (runs) according to changing discharge Q. h_{out} is the water level at the outflow, h_{mean} is the mean water level over the total flume. G_s is the solid discharge rate of the sediment

name	t [hh:mm]	dur. [h]	Q [l/s]	G_s [kg/h]	h_{out} [m]	h_{mean} [m]
VV	00:00–06:00	6	145 – 155	37	0.141	0.17
W1	06:00–24:00	18	140	37	0.141	0.17
W2	24:00–42:00	18	185	47	0.191	0.22
W3	42:00–60:00	18	240	60	0.241	0.27

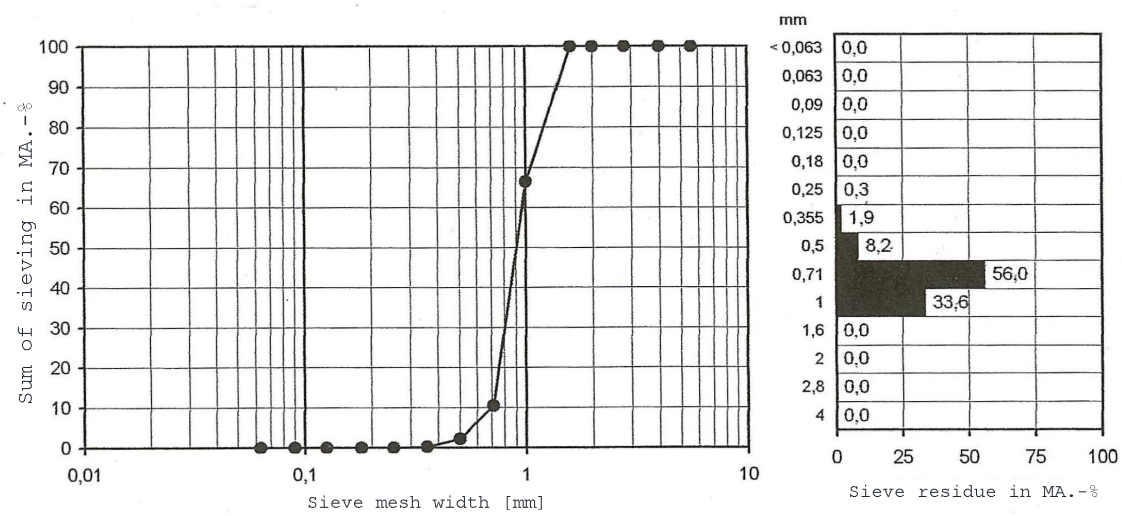

Figure 3.13: Granulometry curve of the sediment used in the morphodynamic experiments (BAW). Mean diameter is $0.94\,\mathrm{mm}$

3.3.1 Sediment composition and discharge

For morphodynamic experiments the bottom is constantly covered with sediment, see also Figure 3.2. The sediment has a steep grading curve with a total mean diameter of d_m =$0.94\,\mathrm{mm}$ and is classified as 'sand'. It can be subdivided in 4 grading classes, of which the class of $0.71\,\mathrm{mm}$ to $1.0\,\mathrm{mm}$ has a weight per cent of 64, see Table 3.2. Figure 3.13 shows a granulometry curve of the sediment. Further analysis of the sediment can be found in Appendix 1.

Sediment is introduced into the flume discontinuously at the inflow boundary. The bed load is re-introduced via a specially designed device, which steadily and slowly trickles a desired amount of sand into the flume. This

Table 3.2: Grain size distribution of the sediment, with grading class, mass per cent and mean diameter of 50% (D_{50}) and 90% (D_{90}) of the sediment volume

grading class [mm]	mass [%]	D_{50} [mm]	D_{90} [mm]
1.0 – 1.4	32%	1.2	1.36
0.71 – 1.0	64%	0.855	0.971
0.5 – 0.71	3%	0.605	0.689
0.355 – 0.5	1%	0.4275	0.486

approach ensures a minimal dispersion of the sand during the input. The bed load material is inserted once every hour over a period of 5 – 10 minutes, alternating between the right and left half of the flume. Until the next input interval the added material has progressed from the paved input zone to the moveable part of the flume. This input method ensures a development of three-dimensional dunes over the length of the flume. Established dunes, providing a form roughness throughout the flume, will result in an equilibrium of free surface elevation over the length of the flume (Henning, 2013).

At the outflow of the flume the sediment is constantly weighted, collected, dried and introduced into the flume via the above mentioned installation at the top of the flume. Record of sediment output over time is available for calibration. Sediment equilibrium between in- and output is not reached for any individual discharge (Q). Due to the design of the experiment, which contains 3 different, consecutive discharges with appendant water levels, a total sediment equilibrium is reached only after the completion of the experimental series after 60 h.

The slope of the flume is not adjustable, therefore the mobile bed is levelled to a certain slope before each run. For the start of each new series it is set to a slope of 0.6‰.

The average flow velocities are the same for all runs: $0.46\,\mathrm{m/s}$ to $0.48\,\mathrm{m/s}$. Moderate hydraulic conditions were chosen (*Fr* < 0.4) to ensure correct functioning of the photogrammetric measurement advice, which is described in the next section (Henning et al., 2009). The Froude and Reynolds number of the bed load material (sedimentological Froude and Reynolds number, Fr_* and Re_*, see 2.1 and Eq. 2.2) were chosen to correspond with the values of German lowland rivers (like the Elbe or Danube). The chosen diameter also ensures the absence of suspended material. Figure 3.14 shows the position of the experiments in the Shields diagram presented in Chapter 2, using the sedimentological Froude and Reynolds number. Table 3.3 presents sedimentological as well as hydraulic Froude and Reynolds numbers of the low (W1) and high (W3) water level experiments.

3.3.2 General information about measuring system

For measurement of the dune bottom a special, three-dimensional, photogrammetric measurement system has been developed by BAW in cooperation with AICON 3D System GmbH (Henning, 2008; Henning et al., 2009). It is a

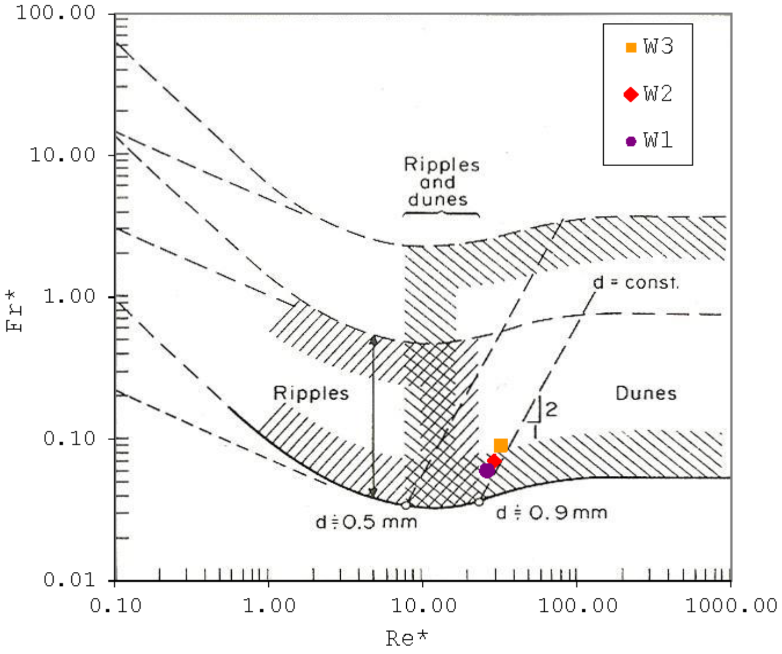

Figure 3.14: Position of the three different discharges (W1 = $140\,\mathrm{l/s}$, W2 = $185\,\mathrm{l/s}$, W3 = $240\,\mathrm{l/s}$) of the experiments in the Shields diagram, Raudkivi (1967, modified)

Table 3.3: Sedimentological Froude and Reynolds number (Fr_*, Re_*), Froude and Reynolds number (Fr, Re) of the three applied discharges in the experiments

Discharge	Fr_*	Re_*	Fr	Re
W1 = 140 l/s	0.06	26	0.35	6100
W2 = 185 l/s	0.07	29	0.36	8700
W3 = 240 l/s	0.09	32	0.37	11500

laboratory based photogrammetric system for monitoring alluvial bed topography and allowing repeated, instantaneous recording of dune beds during water flow. Initially designed to measure dry channel surfaces, it has been enhanced for subaqueous surfaces as well. The system consists of an automated camera orientation unit (Fig. 3.15 number 1–3) and is based on bar coded markers and a grid ($0.02\,\mathrm{m}$ to $0.02\,\mathrm{m}$) projection unit for identification of bed topography (Fig. 3.15 number 4). Figure 3.16 shows the projected grid on a dune bottom with conventionalised groyne installations. Achievable vertical accuracies for bed elevation measurements are $1\,\mathrm{mm}$ for subaqueous measurements and $0.1\,\mathrm{mm}$ for dry bed model measurements. Further details can be found in Henning (2008).

The advantage of this system over existing measuring advices is the possibility to record continuously and instantaneously through the water surface, instead of emptying the flume to be able to record the dry bed topography. For the presented morphodynamic flume results the water discharge was reduced to a minimum discharge of $2\,\mathrm{l/s}$ after every 6 h. By doing this, the dune movement was stopped and the forms were preserved. The complete bottom of the flume was recorded and the experiment continued.

Surface velocities were recorded using the same installation via 3D-PTV (3D-Particle Tracking Velocimetry) at regular intervals. These 3D velocity measurements also included elevations, thus delivering additional free surface elevations. Free surface levels where also continuously measured at 15 measuring points, their positions are shown in Fig. 3.2.

Figure 3.17 shows bottom scans of one complete experiment. The experiments start from a flat bed (0 h). The initial bottom is provided with streaks in order to accelerate the dune development during the first hours. It can be seen that after a development stage over the first 6 h, the dunes reach a quasi-steady state for each of the three discharges. Note that for one discharge no solid discharge steady state is reached. This is only established over the complete experimental cycle of 60 h, compare Section 3.3.5 as well. For all experiments the bottom is constantly covered with sediment and the floor of the flume is never exposed.

3.3.3 Dune analysis

Length and height are the main geometrical characteristics of dunes. These quantities have been used extensively in dune analysis (e.g. van Rijn, 1984b;

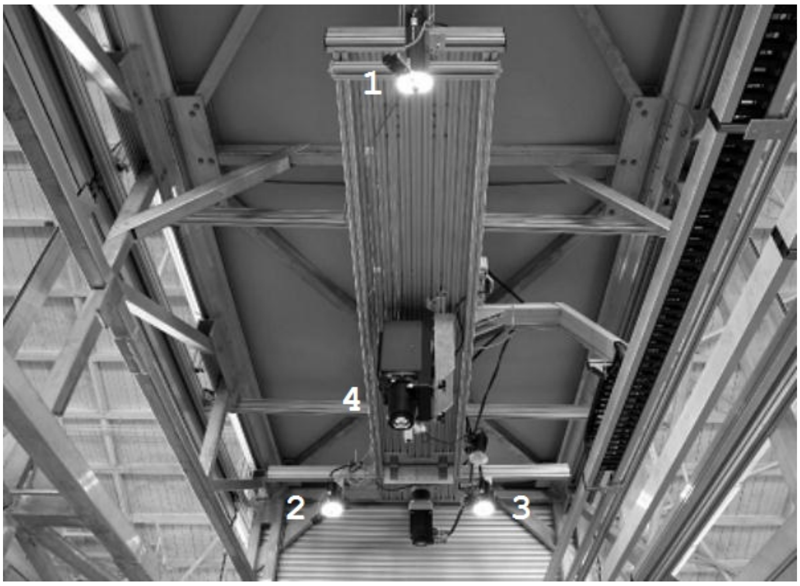

Figure 3.15: Photogrammetric measurement system with cameras with ring-lamps (1–3) and projector (4), picture by Bernd Hentschel (BAW)

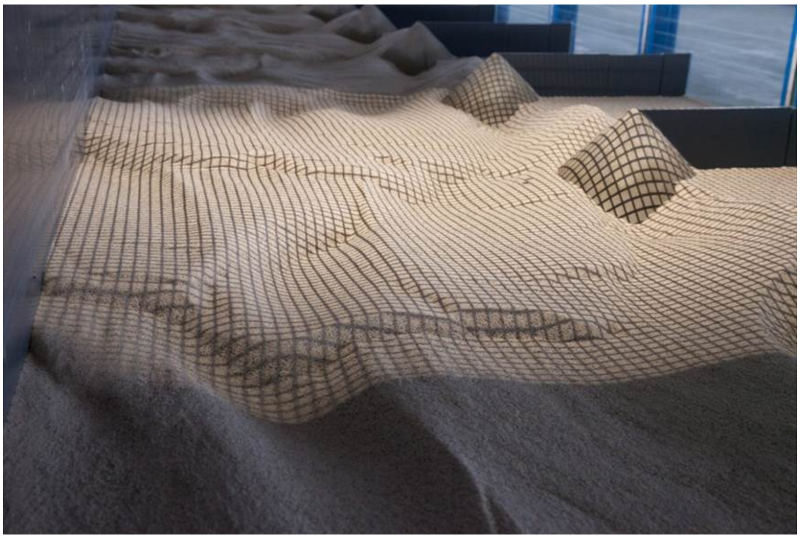

Figure 3.16: Projected grid on dune surface in an experimental configuration with conventionalised groynes. Grid distance is $0.02\,\mathrm{m}$ to $0.02\,\mathrm{m}$, picture by Bernd Hentschel (BAW)

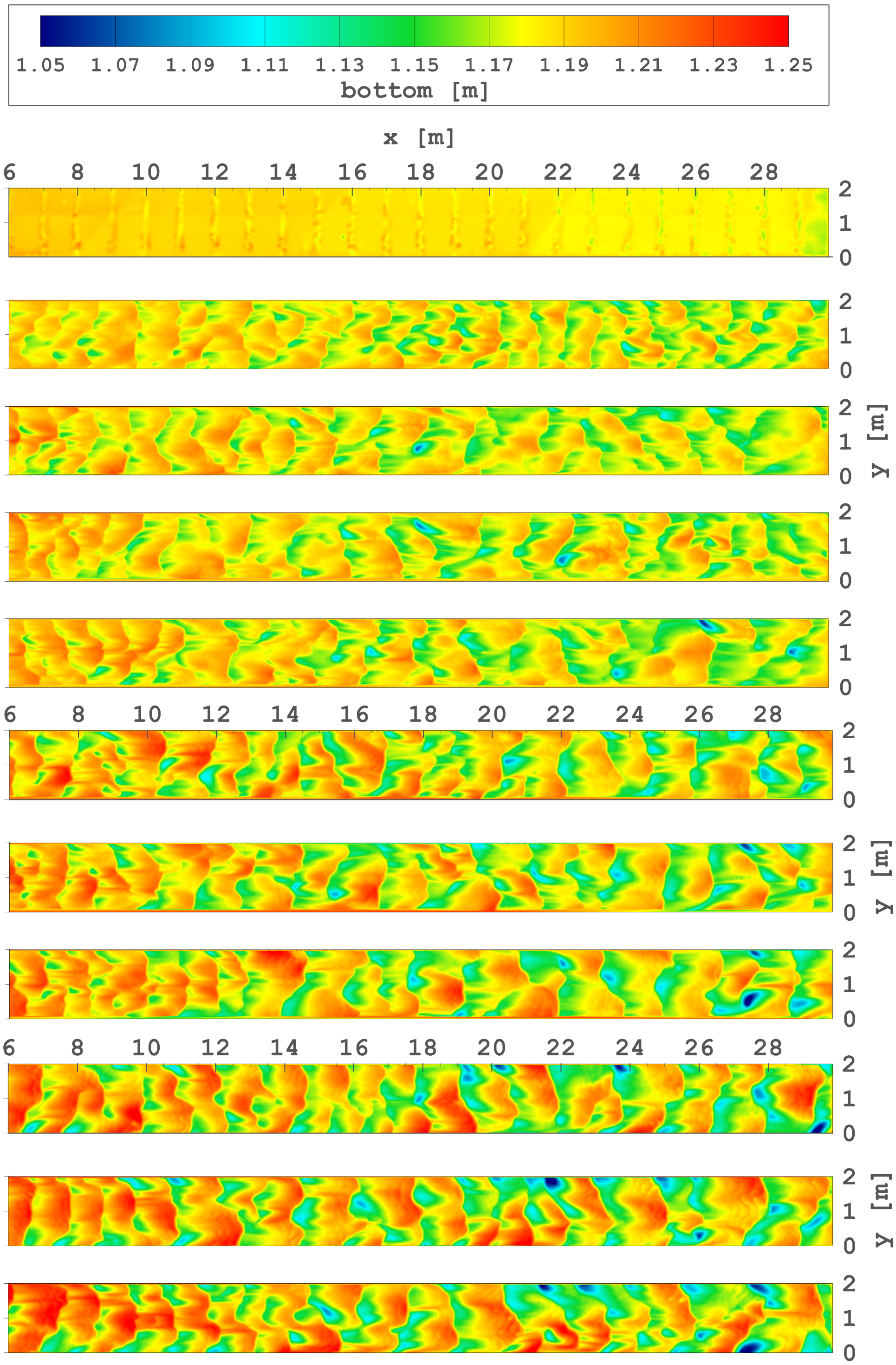

Figure 3.17: Bottom scans, 0 – 24 h: W1 = 140 l/s, 30 – 42 h: W2 = 185 l/s, 48 – 60 h: W3 = 240 l/s, in total 60 h of experimental time. Flow is from left to right

Allen, 1968; Gill, 1971; Engelund and Fredsøe, 1982; Yalin and Ferreira da Silva, 2001; Coleman and Nikora, 2010). In addition three other parameters can be used to further evaluate dune fields: standard deviation, skewness and kurtosis (Coleman et al., 2011). Skewness and kurtosis are third- and fourth-order distribution moments normalised by the variance. Using distribution moments implies that results are independent of the mean of a bed-form profile series, as well as the resolution of recording (Friedrich et al., 2006).

Elevation α of bed surface can be expressed as $\alpha(x, y, t = t_1)$ with variance σ^2 of this data set being the 2nd order moment of this spatial series

$$\sigma^2 = \int_{-\infty}^{\infty} \alpha'^2 f(\alpha)\mathrm{d}\alpha = \langle \alpha'^2 \rangle \tag{3.4}$$

with $f(\alpha)$ is the probability density function of the variable α (with $\int_{-\infty}^{\infty} f(\alpha)\mathrm{d}\alpha = 1$) and $\langle\rangle$ represent spatial averaging over the bed surface (Coleman et al., 2011). Standard deviation σ of a spatial series is a characteristic vertical roughness scale for bed surface, even though dunes with their specific heights are resolved (Aberle and Smart, 2003; Coleman et al., 2011). As the standard deviation has the same unit as the dune height, it is a more descriptive measure for roughness of a dune bed than the variance.

Skewness is the 3rd order moment divided by the cube of the standard deviation σ:

$$Sk = \langle \alpha'^3 \rangle / \sigma^3 \tag{3.5}$$

It is a measure for symmetry of a spatial series relative to the normal distribution. If the skewness is zero, distribution around a sample mean is symmetric. Data which is spread more to the right of the mean has a positive skewness value and vice versa (Friedrich et al., 2006). The general shape or form of the bed surface can be taken from its skewness value. Dune fields are associated with a negative skewness, which might represent flattened crests and steep, distinct troughs (Coleman et al., 2011). A negative skewness also represents long, convex upwards stoss-side slopes and relatively steep and short lee-side faces which are characteristic for dunes (Friedrich et al., 2006).

Kurtosis is the 4th order moment divided by the standard deviation to the power of 4:

$$Ku = \langle \alpha'^4 \rangle / \sigma^4 - 3 \tag{3.6}$$

It is a measure for peakedness or tailedness of a spatial series distribution, as it is the variation of the variance. Data with a high kurtosis value is distributed around the mean with single, steep peak, which tails off slowly. A low kurtosis value represents a distribution with a plateau near the mean (Friedrich et al., 2006). The kurtosis value of a normal distribution is 3, thus normally this value is corrected by -3 to receive a value of zero for a normal distribution. A positive value then means more extreme fluctuations of the data set, whereas a negative kurtosis is result of flat data with less extreme values (Friedrich et al., 2006). Bed waves that are widely spread on a flat bed have a large and positive kurtosis. A train of triangular, identical waves following each other will have a negative kurtosis (Coleman et al., 2011).

The graph of Friedrich et al. (2006) (Fig. 3.18) shows values of skewness and kurtosis of coarse (green diamonds) and fine (red crosses) sand dunes and ripples (black dots) plotted against each other. One can see that results vary, but that a characteristic region can be assigned to each category of coarse and fine sand dunes and ripples.

The parameters described above can be extracted with discrete and statistical methods. The discrete approach of zero crossing analysis is used for the

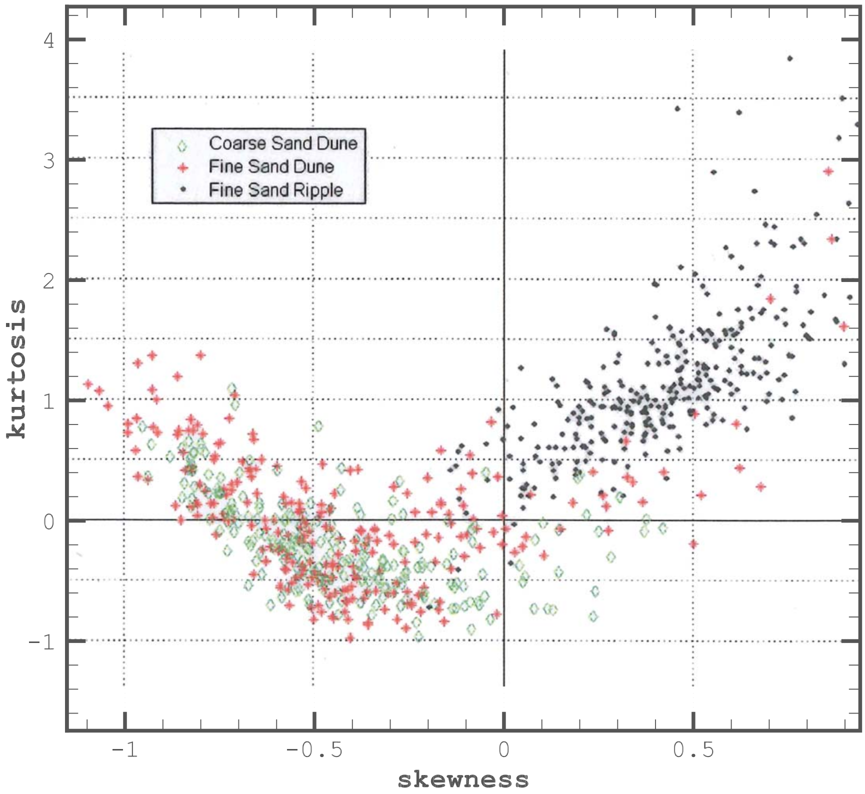

Figure 3.18: Collection of skewness and kurtosis values of coarse (green diamonds) and fine (red crosses) sand dunes and ripples (black dots) in flume experiments by Friedrich et al. (2006; modified)

evaluation of this work and is described in the next section. Statistical methods on the other hand are based on analysis of extensive alluvial bed surfaces. The surfaces are described in the form of a moving random field of bed heights $z(x, y, t)$, opposed to zero crossing analysis, which considers longitudinal sections in the form of $z(x, y = 0, t)$.

3.3.4 Zero crossing analysis

The zero crossing analysis (Nordin, 1971) is a discrete approach for the evaluation of dune heights and lengths. It is based on the identification of zero-crossings (crossings with the mean bed level) of longitudinal cross sections or time series in the form of $z(x, y = 0, t)$. This approach is best used for 2D dunes – individual 3D dunes cannot be described – but sufficient sections over a three-dimensional dune can yield a set of average parameters representing the characteristic form (Henning, 2013). This is especially valid as the extraction of single, individual dunes is neither the aim of the present study and nor representative for a complete river section.

To prepare the data sets presented here, longitudinal cross sections $\alpha(x, y = 0, t = t_1)$ are extracted from the topography and for each resulting profile the slope is deducted. Afterwards an individual partial regression line is plotted for each profile and from the crossings of the profiles with these regression lines (see Figure 3.19), a mean dune length and a mean dune height is calculated. The height of a bed form is the distance between the absolute maximum and minimum between two upwards directed zero-crossings of the bottom profile with the regression line. The length of a bed form is calculated accordingly from the horizontal distance between the zero-crossings. A total mean for the complete dune field can be calculated from the sum of all profiles.

To exclude small superimposing forms (e.g. ripples), which might also stem from random noise, a minimum threshold for dune height is defined. Similarly, bed forms with large wave lengths (e.g. bars) can be excluded with a high pass filter, meaning a maximum critical value.

As these minimum and maximum values depend on user input, zero crossing analysis is partly subjective. Hence, reference values for dune length and height (length about six times the water depth and height about 1/3 of water depth) should be used (Yalin, 1972; Paarlberg, 2008; LWI, 2012a).

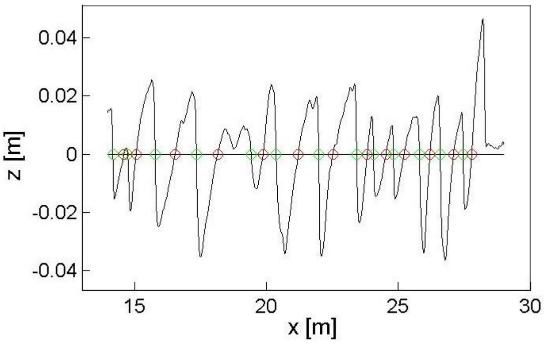

Figure 3.19: Schematic diagram of the zero-crossing approach. Green are downwards and red are upwards directed zero-crossings of a longitudinal profile

3.3.5 Results

For comparison with numerical simulations, the physical data sets are analysed. Three experiments (S6, S9, S10), each offering in total 60 h of running time with a complete, high-resolution bottom scan every 6 h, have been analysed. A focus has been laid on the first 24 h of each experiment (in total 12 data sets), with a constant discharge of $140\,\mathrm{l/s}$.

The average minimum of dune length, height, skewness and kurtosis, as well as the average maximum, calculated from these 12 data sets are given in Table 3.4. Additionally the values are plotted into a length vs height diagram (diagram 3.20) and skewness vs kurtosis (diagram 3.21), which are compared to experimental data sets of Friedrich et al. (2006). Figure 3.22 displays resulting bottom scans of the first 24 h of experiment S6.

As described in Section 3.3, sediment output was continuously measured

Table 3.4: Dune parameters of the physical experiments (S6, S9, S10, first 24 h). min_{EXP} is the average, minimum value of all experiments, max_{EXP} is the average, maximum value

	height $[\mathrm{m}]$	length $[\mathrm{m}]$	skewness	kurtosis	steepness
min_{EXP}	0.035	1.03	-0.73	-0.057	0.023*
max_{EXP}	0.047	1.51	-0.445	+1.336	0.046*

*The steepness is calculated from minimum height over maximum length, maximum height over minimum length respectively

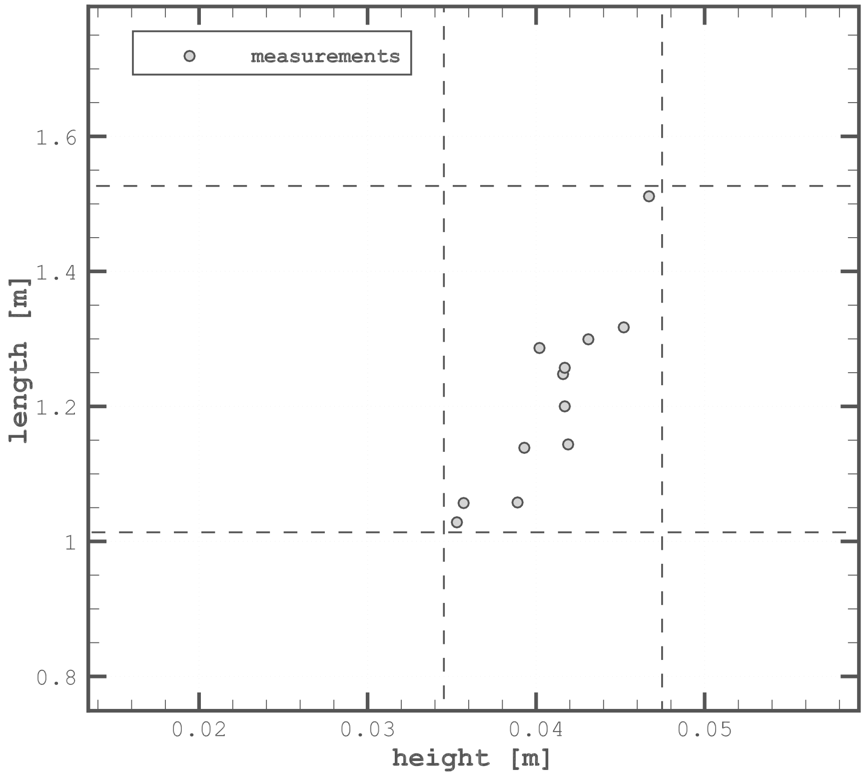

Figure 3.20: Collection of average lengths and heights of the experimental data sets (S6, S9, S10, after 6, 12 18 and 24 h)

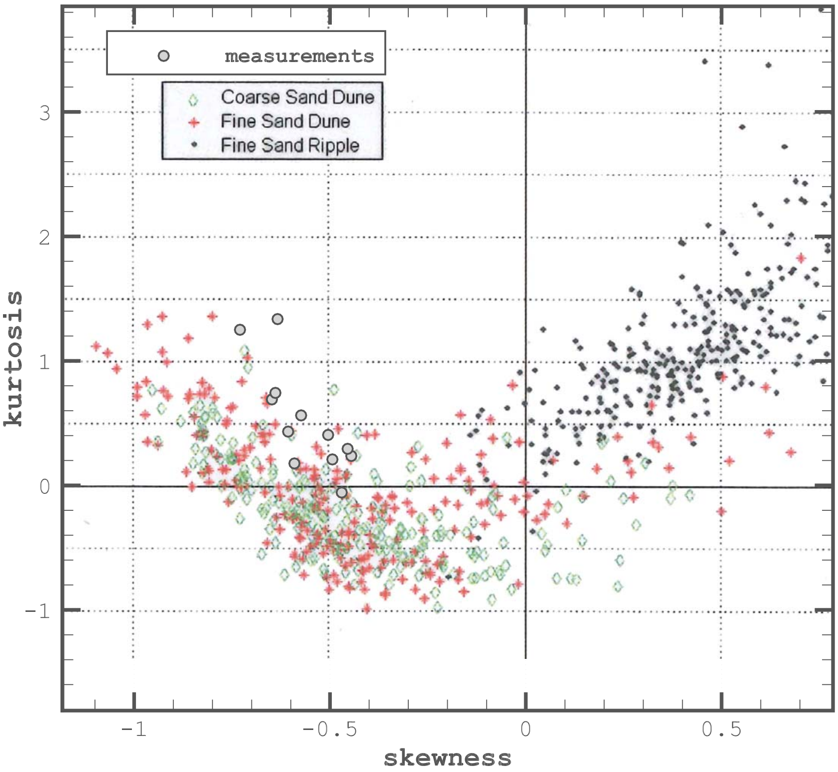

Figure 3.21: Collection of skewness and kurtosis values of the experimental data sets (grey circles; S6, S9, S10, after 6, 12 18 and 24 h) compared to coarse and fine sand dunes and ripples (green diamonds, red crosses, black dots) of flume experiments by Friedrich et al. (2006; modified), see as well Fig. 3.18

after the weir at the outflow. Table 3.5 gives an overview of the solid discharge rates of runs at lowest discharge W1 = 140 l/s, which are used for comparison with the numerical results. The mean for the pre-runs (VV) differs from the subsequent runs of each experiment. This can be attributed to dune fields that are in the process of getting established from a flat bed towards equilibrium dunes. Hence, an additional mean (**Mean W1**) is calculated, excluding the pre-runs. **Mean W1** is therefore a value of equilibrium dune fields.

The variation of the solid discharge rates at discharge W1 = 140 l/s in the experiments is illustrated in Figure 3.23. In this plot long wave lengths stem from large dune forms leaving the flume over a time frame of 0.5 h to 1.0 h. Those wave lengths are notably smaller for the pre-run, when dunes are still establishing. Solid discharge rate varies not only over time but also between runs at same discharge (W1). For future comparison between physical and numerical experiments, an average value, marked **Mean W1** in Table 3.5, has been calculated. This value, combined with the range of the solid discharge rates, will provide a reference for comparison with the numerical results of the simulations.

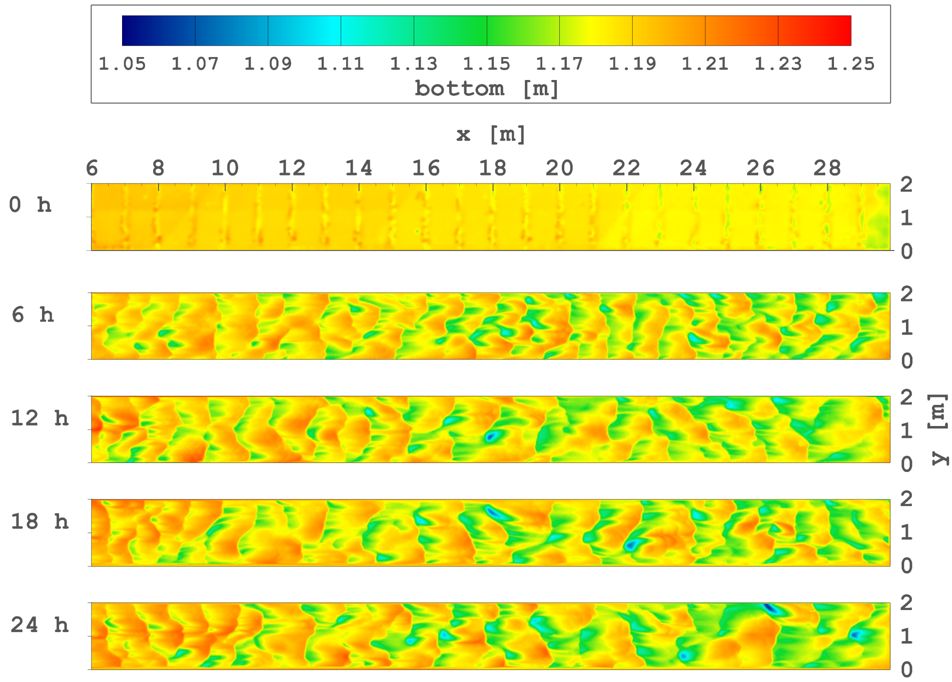

Figure 3.22: Bottom scans of experiments (S6), discharge 140 l/s, after 0 h, 6 h, 12 h, 18 h and 24 h of experimental time

Table 3.5: Average solid discharge rates Q_s in [kg/s], [kg/h] over the flume width (2 m) and summed amount in [kg] of the physical experiments (S6, S9, S10) at lowest discharge W1, including the pre-runs. **Mean W1** is a mean for equilibrium dunes, excluding the pre-runs

Run	Q_s [kg/s]	Q_s [kg/h]	$\sum Q_s$ kg in 6 h
S6 0-6h	8.48E-03	30.5	183.2
S6 6-12h	5.08E-03	18.1	108.9
S6 12-18h	4.34E-03	15.6	93.4
S6 18-24h	5.98E-03	21.4	128.4
S9 0-6h	1.03E-02	35.4	212.2
S9 6-12h	7.58E-03	27.4	164.2
S9 12-18h	4.81E-03	17.2	103.4
S9 18-24h	5.26E-03	18.8	113.0
S10 0-6h	1.16E-02	41.7	250.2
S10 6-12h	6.04E-03	21.8	130.7
S10 12-18h	5.64E-03	21.1	120.8
S10 18-24h	5.81E-03	21.0	125.7
Mean	6.74E-03	24.1	144.51
Mean W1	**5.61E-03**	**20.2**	**120.95**
Range W1 from	4.34E-03	15.6	93.35
to	7.58E-03	27.4	164.21

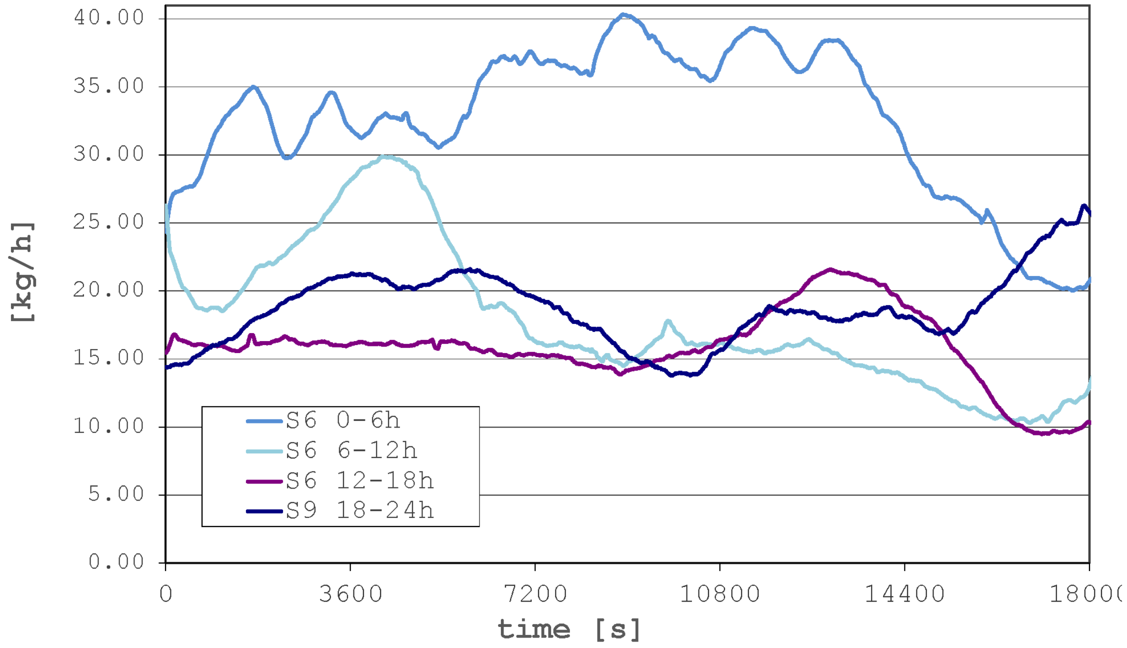

Figure 3.23: Solid discharge rates of selected experiments discharge W1 and pre-run VV (140 l/s) in kg/h (averaged over the consecutive next 1 h at every time step) per flume width 2 m, experiments see Tbl. 3.5

4

Hydrodynamic Model

Contents

In this work the open-source finite-element Telemac-Mascaret system is used for hydro- and morphodynamic calculations. The system is developed by a consortium of core organisations: Artelia (formerly Sogreah, France), Bundesanstalt für Wasserbau (BAW, Germany), Centre d'Etudes Techniques Maritimes et Fluviales (CEREMA, France), Daresbury Laboratory (United Kingdom), Electricité de France R&D (EDF, France) and HR Wallingford (United Kingdom). The code is available at www.opentelemac.org .

4.1 Numerical framework

The advantage of the Telemac-Mascaret system over similar comprehensive modelling systems e.g. Flow3D by Deltares (Lesser et al., 2004), Mike3-TR by DHI (Tjerry and Fredsøe, 2005) and UnTRIM (Casulli and Lang, 2004) is the adaptivity of the finite elements, which are combined with highly developed sediment transport modules (Villaret et al., 2013; Mendoza et al., 2015). These sediment modules distinguish it from other finite element systems like e.g. OpenFOAM (Hirt and Nichols, 1981). The Telemac-Mascaret system is very efficient and its massive parallelism allows its use in computationally intensive applications, e.g. studies on the river and ocean scale or those involving small scale features with high resolutions. These components predestine it for the applications presented in this work, where sophisticated bed load transport is regarded on experimental and project scale.

The Telemac-3D module of the Telemac-Mascaret system solves the Reynolds-Averaged Navier-stokes equations. It is a finite-element solver module, which delivers results of the computation of three-dimensional equations for free surface flow and the transport-diffusion equations for velocity in all three directions, water depth and concentrations of transported quantities. This can be done with or without hydrostatic pressure assumption. Detailed description of the numerical system can be found in Hervouet (2007) and in Jankowski (1999). Hydrodynamic results can be coupled to the morphodynamic module Sisyphe, described in Chapter 6.

4.2 Hydrodynamic model

Telemac-3D solves the Navier-Stokes-Equations, which describe the conservation of momentum

$$\frac{\partial \mathbf{u}}{\partial t} + (\mathbf{u} \cdot \nabla) \cdot \mathbf{u} = -\frac{1}{\rho}\nabla p + \nabla \cdot (\nu \nabla \mathbf{u}) + f \tag{4.1}$$

Mass conservation is provided by the continuity equation

$$\nabla \cdot \mathbf{u} = 0 , \tag{4.2}$$

with:		
	$\mathbf{u}$	three-dimensional velocity vector [m/s]
	p	pressure $[\mathrm{N/m^2}]$
	ρ	characteristic density of fluid [kg/m^3]
	ν	viscosity of fluid $[\mathrm{m^2/s}]$
	f	source term $[\mathrm{m/s^2}]$.

Equations 4.1 and 4.2 describe the distribution of velocity and pressure in time and space, assuming that the fluid is incompressible. Time variation of each of the velocity components is subject to advection, diffusion (viscosity), change of pressure and, if applicable, various source terms. Reynolds-Averaging is applied, thus velocities and the pressure term are divided in an averaged and a fluctuating part

$$u_i = \overline{u_i} + u_i' , \quad i = 1, 2, 3$$

$$p = \overline{p} + p' \tag{4.3}$$

By introducing Eq. 4.3 into Eq.s 4.1 and 4.2 and by using index notation, the following equations are gained

$$\frac{\partial(\overline{u_i} + u'_i)}{\partial t} + (\overline{u_i} + u'_i)\frac{\partial(\overline{u_i} + u'_i)}{\partial x_j} = -\frac{1}{\rho}\frac{\partial(\overline{p} + p')}{\partial x_i} + \nu\frac{\partial^2(\overline{u_i} + u'_i)}{\partial x_j \partial x_i} + f_i \quad (4.4)$$

$$\nabla \cdot (\overline{u_i} + u'_i) = 0 \,, \quad (4.5)$$

for $i = 1, 2, 3$. If now both sides of the equation are averaged over time, the fluctuating velocity parts in the partial time derivative and the viscous term on the right hand side vanish. The following terms remain

$$\frac{\partial \overline{u_i}}{\partial t} + \overline{(\overline{u_j} + u'_j)\frac{\partial(\overline{u_i} + u'_i)}{\partial x_j}} = -\frac{1}{\rho}\frac{\partial \overline{p}}{\partial x_i} + \nu\frac{\partial^2 \overline{u_i}}{\partial x_j \partial x_i} + \overline{f_i} \,, \quad (4.6)$$

where the advective term on the left hand side can be further transformed

$$\begin{aligned}\overline{(\overline{u_i} + u'_i)\frac{\partial(\overline{u_i} + u'_i)}{\partial x_j}} &= \overline{u_j}\frac{\partial \overline{u_i}}{\partial x_j} + \overline{u'_j\frac{\partial u'_i}{\partial x_j}} = \overline{u_j}\frac{\partial \overline{u_i}}{\partial x_j} + \underbrace{\overline{u'_i\frac{\partial u'_j}{\partial x_j}}}_{=0} + \overline{u'_j\frac{\partial u'_i}{\partial x_j}} \\ &= \overline{u_j}\frac{\partial \overline{u_i}}{\partial x_j} + \frac{\partial \overline{u'_i u'_j}}{\partial x_j} \,. \end{aligned} \quad (4.7)$$

Inserting Eq. 4.7 into Eq. 4.6 the Reynolds-Averaged Navier-Stokes (RANS) equations are

$$\frac{\partial \overline{u_i}}{\partial t} + \underbrace{\overline{u_j}\frac{\partial \overline{u_i}}{\partial x_j}}_{advection} = \underbrace{-\frac{1}{\rho}\frac{\partial \overline{p}}{\partial x_i}}_{pressure} + \underbrace{\frac{\partial}{\partial x_j}(\nu\frac{\partial \overline{u_i}}{\partial x_j} - \overline{u'_i u'_j})}_{diffusion} + \underbrace{\overline{f_i}}_{sourceterms} \quad . \quad (4.8)$$

It contains the correlated, fluctuating term $-\overline{u'_i u'_j}$ called the Reynolds stress. This can approximated by the Boussinesq eddy-viscosity approach (Boussinesq, 1877)

$$-\overline{u'_i u'_j} = \nu_t \left(\frac{\partial \overline{u_i}}{\partial x_j} + \frac{\partial \overline{u_j}}{\partial x_i}\right) \,. \quad (4.9)$$

The turbulent viscosity, ν_t, which is now part of the formulation, needs to be provided by a suitable turbulence model, see below.

Telemac-3D offers the possibility to calculate hydrostatic as well as non-hydrostatic RANS-equations. The first assumes a pressure that only increases with water depth, whereas the second approach will solve an additional equation for the vertical velocities. Calculation of the non-hydrostatic pressure is decomposed into a hydrostatic p_h and a 'dynamic' pressure term p_d, in order to use a common core of computation as much as possible (EDF, 2013)

$$p = p_h \; + \; p_d \; . \tag{4.10}$$

The hydrostatic pressure term is solved by integrating over the water depth

$$p_h \; = \; \int_z^{Z_s} (\rho + \Delta\rho) g \mathrm{d}z \; = \; g\rho_o(Z_s - z) + g\rho_o \int_z^{Z_s} \frac{\Delta\rho}{\rho_o} \mathrm{d}z \; , \tag{4.11}$$

whereZ_s is the free surface elevation, ρ_o is the reference density and $\Delta\rho$ is the variation of density (EDF, 2013). Thus the pressure term p of Eq. 4.8 changes to

$$\frac{\partial p}{\partial x} \; = \; g\rho_o(Z_s - z) + g\rho_o \frac{g}{\partial x} \int_z^{Z_s} \frac{\Delta\rho}{\rho_o} \mathrm{d}z \; + \; \frac{\partial p_d}{\partial x} \tag{4.12}$$

for x- and y-direction. In vertical direction only the dynamic pressure term remains. The dynamic pressure term p_d is solved in the three Cartesian directions through a Poisson pressure equation. Through the non-hydrostatic pressure approach vertical accelerations are taken into account as well, thus allowing calculations of short waves and steeper slopes. Implementation and details of the non-hydrostatic approach can be found in Jankowski (1999).

As the equations are used for an incompressible fluid (water), there is no variation of density inside the water/fluid column. The Boussinesq (1903) approximation states that the variations in density are small compared to the reference density. Thus they are only accounted for in terms of Eq. 4.1, where they give rise to buoyancy forces. In the free surface calculation, where the density only describes fluid inertia, its variation can be ignored (Spiegel and Veronis, 1960).

The Reynolds stress tensor, see Eq. 4.9, contains a three-dimensional turbulent eddy viscosity ν_t, which can either be defined by the user or be determined by an algebraic turbulence model, like the mixing length model. Moreover, the turbulent eddy viscosity can be calculated from a two-equation turbulence model, e.g. the k-ε model. Here additional differential equations need to solved and this model is therefore a time-consuming procedure. Telemac-3D offers the possibility to define a constant viscosity. Available algebraic models are mixing length models e.g by Prandtl (1925) or Nezu and Nakagawa (1993) (EDF, 2013). For two-equation models the choice is between the k-ε model (Launder and Sharma, 1974; Rodi, 1993) and the k-ω model (Wilcox, 1993; Weilbeer, 2001).

Turbulence is a key feature of flow over dunes (Jackson, 1976; Nelson et al., 1993; Bennett and Best, 1995). Thus proper representation of these flow patterns with a sophisticated turbulence model becomes necessary when modelling flow over dunes. The k-ε model is one of the most commonly used turbulence models. It contains one equation for the transport of kinetic energy and a second for the dissipation of energy. The transport equation for k, the turbulent kinetic energy, is

$$\frac{\partial k}{\partial t} + \mathbf{u} \cdot \nabla k \;=\; \nabla \left(\nu + \frac{\nu_t}{\sigma_k} \right) \nabla k + P - \varepsilon \; . \tag{4.13}$$

It is accompanied by the equation of energy dissipation ε

$$\frac{\partial \varepsilon}{\partial t} + \mathbf{u} \cdot \nabla \varepsilon \;=\; \nabla \left(\nu + \frac{\nu_t}{\sigma} \right) \nabla \varepsilon + C_{1\varepsilon} \frac{\varepsilon}{k} P - C_{2\varepsilon} \frac{\varepsilon^2}{k} \; . \tag{4.14}$$

Equation 4.13 and 4.14 contain the term of turbulent energy production P

$$P \;=\; \nu_t \left(\frac{\partial u_i}{\partial x_j} + \frac{\partial u_j}{\partial x_i} \right) \frac{\partial u_i}{\partial x_j} \; , \tag{4.15}$$

and the eddy viscosity ν_t is computed as

$$\nu_t \;=\; C_\mu \frac{k^2}{\varepsilon} \; . \tag{4.16}$$

The standard values of the model constants can be taken from Table 4.1.

The three-dimensional system of Telemac gives several options to calculate advection: the method of characteristics, the Streamline-Upwind Petrov-Galerkin (SUPG) method, the Multidimensional Upwind Residual Distribution (MURD) scheme as well as N- and Psi-schemes. For details see Hervouet (2007). In this study the Streamline-Upwind Petrov-Galerkin (SUPG) method is used, which is of first order accuracy, like the widely used method of characteristics. The SUPG method is more time consuming and less stable, but the method of characteristics tends to generate more numerical diffusion. This smoothens results on the one hand, but would suppress turbulent structures on the other. Due to importance of turbulent flow features in the presented study, the SUPG method is chosen for calculations.

Table 4.1: Standard values of the constants of the k-ε model

C_μ	$C_{1\varepsilon}$	$C_{2\varepsilon}$	σ_k	σ_ε
0.09	1.44	1.92	1.0	1.3

In Telemac-3D the RANS equations are solved on an unstructured mesh of triangles. The 3D-mesh is gained from a two-dimensional mesh by superimposition. In the vertical the mesh adapts to the bottom by σ-transformation (Decoene and Gerbeau, 2008), where the spacing of the layers may be defined by the user. Through this method a refinement of the resolution near the bed is possible, allowing for better accuracy of the turbulence models (Villaret et al., 2013).

5

Numerical Fixed Bed Experiments

Contents

In this chapter results from the physical experiments introduced in Section 3 are compared to simulations with Telemac-3D. The hydrodynamic simulations are summarised in Table 5.1. Reference will be given to these simulations in the following chapter. A complete list of parameters can be found in Appendix 5. Computing times of the runs with the fine mesh are 4.5 h for a simulated time period of 15 minutes. These simulations are performed on 64 processors. The computing time for the medium mesh is 1 h on 16 processors for the same time period. The coarse mesh has computing times of 2 minutes on 16 processors. Simulations are performed on the high-performance cluster of BAW, a bullx blade B510 series, containing 126 nodes with 2 CPUs each. Each CPU contains 16 processors.

A large number of simulations have been conducted with Telemac-3D resulting in the determination of some key parameters of the numerical set-up and their influence on the results. In this chapter, these parameters, their effects, specific features, properties and influences will be presented and discussed. It will be shown, that the mesh resolution is a key parameter when modelling complex, turbulent flows. Meshes with different spatial resolution will require new calibration, and the applicability of the chosen combination of turbulence model, mesh resolution, roughness height and pressure approach needs to be reassessed. Furthermore, it will be demonstrated that even though qualitatively good results can be obtained for the flow structures, they lack in quantity of turbulent kinetic energy provided by the turbulence model. This needs to be considered when coupling the hydro- to the morphodynamic module (Chapter 7).

Table 5.1: Overview of hydrodynamic calculations presented in this chapter - data set number (No.) with corresponding parameter configuration

No.	mesh	t [s] [1]	k_s [m] [2]	NHS [3]	σ-layer [4]	turb. model [5]
1	fine	0.01	0.00395	yes	13	k-ε model
2	fine	0.01	0.005	yes	13	k-ε model
3	fine	0.01	0.01	yes	13	k-ε model
4	medium	0.1	0.00395	yes	13	k-ε model
5	medium	0.1	0.005	yes	13	k-ε model
6	medium	0.1	0.01	yes	13	k-ε model
7	coarse	0.5	0.00395	yes	13	k-ε model
8	coarse	0.5	0.005	yes	13	k-ε model
9	coarse	0.5	0.01	yes	13	k-ε model
10	medium	0.1	0.00395	no	13	k-ε model
11	medium	0.1	0.00395	no	10 adj.	k-ε model
12	medium	0.1	0.00395	no	10	k-ε model
13	medium	0.1	0.00395	yes	13	k-ε model
14	medium	0.1	0.00395	yes	10 adj.	k-ε model
15	medium	0.1	0.00395	yes	10	k-ε model
16	medium	0.1	0.00395	yes	13	Prandtl, const. viscosity
17	medium	0.1	0.00395	yes	13	Prandtl, Smagorisnky

[1] time step

[2] roughness height

[3] Non-hydrostatic pressure assumption

[4] number of σ-layers in the vertical

[5] turbulence model in vertical and horizontal direction

5.1 Horizontal mesh resolution

Mesh resolution is a key variable in numerical RANS simulations. The resolution will define which flow features will be directly represented on the mesh and which flow features need to be parametrised.

Three different mesh resolutions were compared for this preliminary study. The main characteristics of the meshes are summarised in Table 5.2. The finest mesh (ID 1) has a mean edge length of $0.014\,\mathrm{m}$, the medium one (ID 2) has a mean edge length of $0.065\,\mathrm{m}$, whereas the coarsest of the meshes (ID 3) has elements with a mean edge length of $0.11\,\mathrm{m}$. With these configurations the three mesh structures have about $360\,000$, $32\,000$ and 6000 nodes respectively, in the two-dimensional, horizontal $x - y$ plane.

Figure 5.1 shows the free surface elevation $[\mathrm{m}]$ calculated with the three meshes described in Table 5.2, using the same numerical configuration. The time step length for the different meshes is adapted to receive the same Courant number for all calculations. With the roughness height used in these computations ($k_s = 0.005\,\mathrm{m}$) the water levels of the two coarser meshes reach qualitative and quantitative agreement with the measurements. The free surface of the finest mesh is up to 3 mm lower at the inflow of the flume, while all water levels are equal at the outflow, where the water level is controlled by the boundary condition or the weir in the experimental flume respectively.

The dune bottom height (z) of all three meshes is linearly interpolated from the measured data sets, which have a higher resolution than each of the applied meshes. Thus, the finest mesh might contain more detailed bottom patterns than the coarse and medium one. In contrast, bottom differences between fine and medium mesh (1 and 2 in Table 5.2) are only in a range of

Table 5.2: Characteristics of the different meshes used for the hydrodynamic simulations: minimum, maximum and mean edge length $\mathrm{d}x$, number of nodes, number of elements (total mesh dimensions $2\,\mathrm{m} \times 30\,\mathrm{m}$)

name	ID	min $\mathrm{d}x$ $[\mathrm{m}]$	max $\mathrm{d}x$ $[\mathrm{m}]$	mean $\mathrm{d}x$ $[\mathrm{m}]$	nodes	elements
fine	1	0.01	0.02	0.014	359 129	711 855
medium	2	0.05	0.07	0.065	31 901	61 666
coarse	3	0.07	0.15	0.11	5 752	10 916

$\pm 0.01\,\mathrm{m}$, punctual and lie mostly at the boundaries of the flume, where the resolution of the measurements decreases and more interpolation is necessary, when computing the bottom heights at the mesh nodes. The form roughness of the fine mesh is therefore not considered higher than the one of the medium mesh.

Calculations have been conducted with the same roughness height for the three mesh resolutions. The results differ in free surface elevation, if the same roughness height is used in the simulations. Only the medium and coarse mesh (Table 5.2) produce the same free surface levels. For morphodynamic simulations these two meshes will be used, allowing to save computational time and enabling further comparison. See Section 5.3 for further discussions on roughness height and mesh resolution.

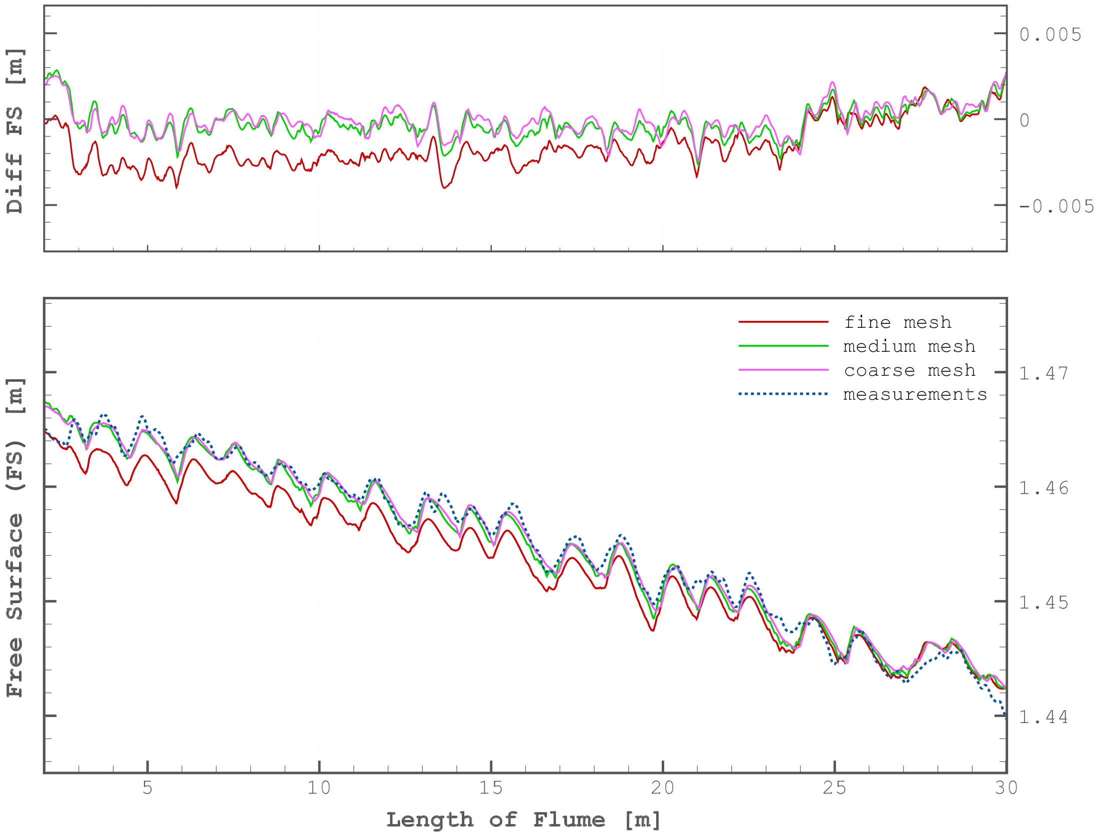

Figure 5.1: Free surface levels of fine (1), medium (2) and coarse mesh (3) and differences to measurements (top). Data sets No. 2, 5 and 8 of Table 5.1

5.2 Vertical mesh resolution

In Telemac-3D the vertical resolution of the mesh is implemented in form of σ-layers (Decoene and Gerbeau, 2008; Hervouet, 2007). The use of a σ-coordinate system offers the possibility to accurately define bed and surface boundaries in time and space. It further allows to incorporate bottom and surface boundary layers and increasing their resolution (Decoene and Gerbeau, 2008). In Telemac-3D users can either define specific σ-layer heights, distribute a chosen amount of layers evenly or define the layer distribution using their own algorithm. This allows for example to chose a resolution which refines in the are of interest. Figure 5.2 shows the schematics of vertical resolution over a smooth dune. The first sketch shows 10 σ-layers with a thin layer at the bottom, which has a predefined height of 1.5% of the water depth. The second displays 10 σ-layers refining logarithmically towards the bottom. Due to this the layer closest to the bottom has a height of 3% of the water depth. The last sketch shows 10 evenly distributed layers for comparison.

In this section, different vertical resolutions are tested. Firstly a layer distribution with a freely adjustable number of layers distributed logarithmically is chosen with the refinement with water depth defined as follows

$$for \;\; i \; = \; 1 \ldots n \quad : \quad z(i) \; = \; \frac{1 - r^{i-1}}{1 - r^{n-1}} \, h \tag{5.1}$$

where n is the desired number of layers and $z(i)$ gives the height of the layer between 0 to 1 multiplied by the water depth h above the bottom. r is the growth factor of the height from one layer to the next. Setting it close to

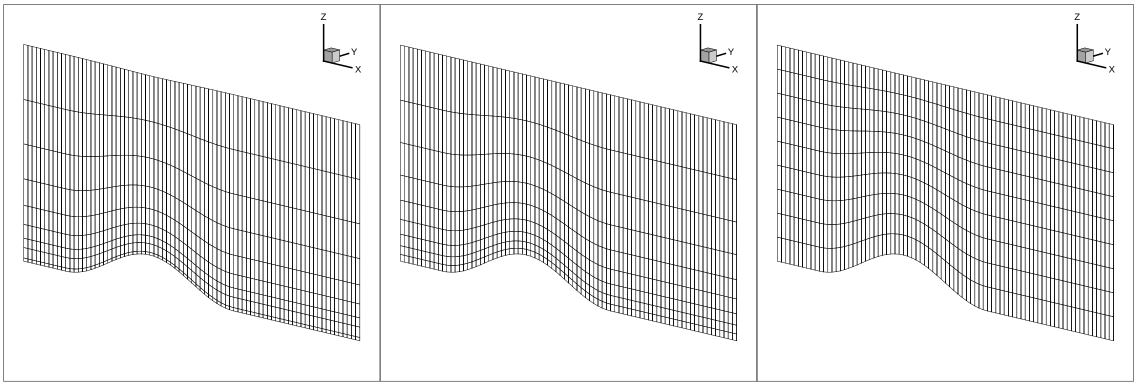

Figure 5.2: Schematic of vertical σ-layer distribution. A: 10 σ-layers with a fine one at the bottom – B: 10 σ-layers refining logarithmically towards the bottom – C: 10 evenly distributed σ-layers

1.0 would result in an almost even distribution of the layers over the water column. For this mesh the growth factor is chosen to $r = 1.3$.

Two different σ-layers numbers, 10 and 13, are tested. Further settings with 15 and 20 σ-layers do not result in different or better results than the calculations with 13 σ-layers. Thus, for the sake of saving calculation time, these calculations have not been pursued. Secondly an "adjusted" distribution, also with 10 σ-layers, is tested. Here the first "adjusted" σ-layer has 50% of the height of the first layer of the log-distributed 10 σ-layers and approximately the same height as the corresponding layer of the 13 logarithmically distributed σ-layers. The layer heights relative to the water depth are summarised in Table 5.3. Simulations with the vertical mesh configurations of Table 5.3 show no significant differences in the water level results (see Figure 5.3).

Results of the simulations are analysed in a 2D-vertical slice in flow direction. They are compared to the high resolution velocity measurements performed with a Vectrino II probe (Section 3.2). Comparing the velocity distributions for u, v and w only slight differences can be noticed between the

Table 5.3: Layer positions for 10 manually adjusted and 10 and 13 log-distributed σ-layers. Refer to A and B in Figure 5.2

no.	10 adjust.	10 log	13 log
01	0.0000	0.0000	0.0000
02	0.0150	0.0312	0.0135
03	0.0630	0.0718	0.0309
04	0.1060	0.1246	0.0537
05	0.1700	0.1933	0.0832
06	0.2580	0.2825	0.1217
07	0.3800	0.3984	0.1716
08	0.5410	0.5492	0.2366
09	0.7460	0.7452	0.3210
10	1.0000	1.0000	0.4307
11			0.5734
12			0.7589
13			1.0000

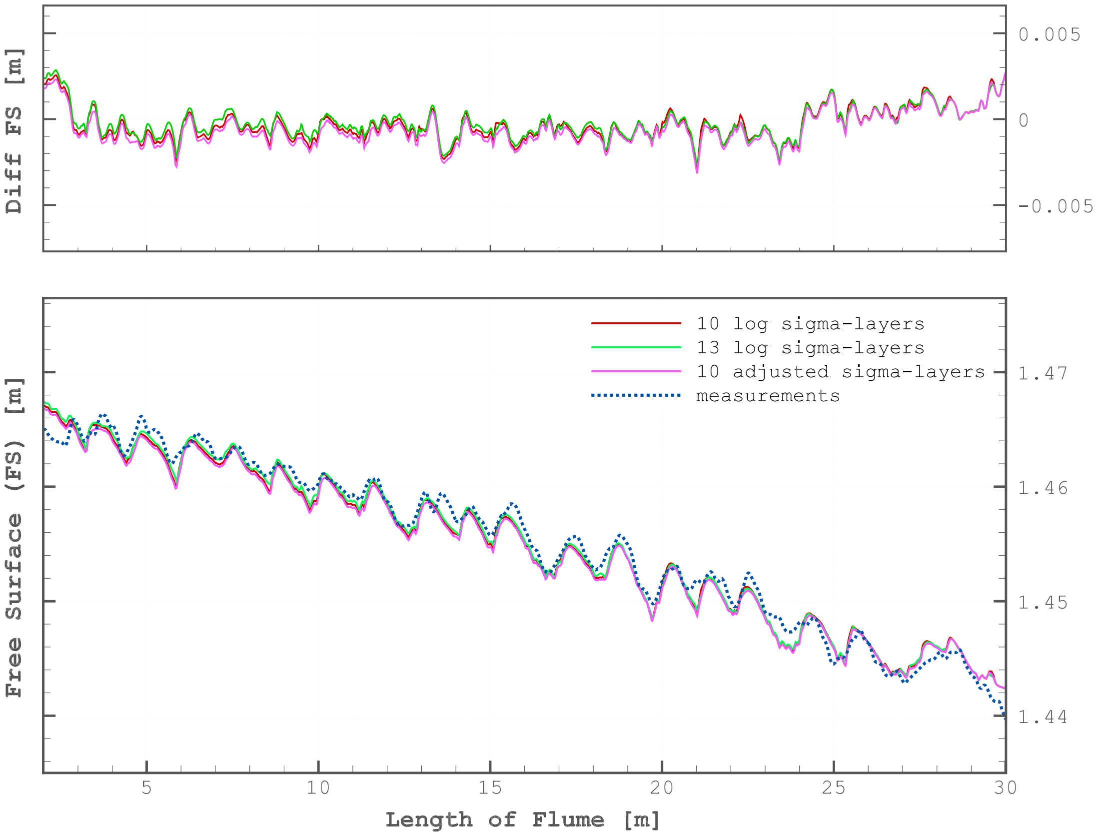

Figure 5.3: Free surface levels with 10 and 13 σ-layers, and 10 adjusted σ-layers and differences to measurements (top), $k_s = 0.003\,95\,\mathrm{m}$. Data sets No. 5, 14 and 15 of Table 5.1

simulation results and the measurements. For example the region of maximum u velocity over the dune crests reaches deeper (about half the water depth) in the simulations. Opposed to this the regions of lower u velocities up to $0.3\,\mathrm{m/s}$ in the lee side of the dunes measurements and simulations agree well. Vertical w velocities below $-0.1\,\mathrm{m/s}$ have a tendency to be wider distributed over the water depth. Figures 5.4 and 5.5 show a result where the stream-wise and vertical velocities of calculations with 10 logarithmic and adjusted σ-layers are compared to measurements. For all cases (13, 10 logarithmic and adjusted vertical layers) the flow velocities is qualitatively and quantitatively in agreement with the measurements in stream-wise direction, as well as cross-wise and vertical to the flow direction.

For morphodynamic simulations with Telemac-3D the bed shear stress is calculated from the velocities at the first σ-layer above the bed (Tassi and Villaret, 2014)

$$\tau_o \;=\; \rho \left(\frac{1}{\kappa} \ln \frac{z'}{z_o} \right)^{-2} u(z')^2 \tag{5.2}$$

with:		
	κ	von Kármán constant $[-]$
	z'	lowermost σ-layer height $[\mathrm{m}]$
	z_o	hypothetical level where the velocity is zero ($z_o \;=\; k_s/30$) $[\mathrm{m}]$
	$u(z')$	velocity at layer above the bed $[\mathrm{m/s}]$

according to the von Kármán (1930) log-law. Thus different bed shear stresses are expected from simulations, if the calculated velocity profiles differ. This can be seen in Figure 5.6, where slight differences in the calculated bed shear stress, resulting from the previous three vertical mesh resolutions, can be seen. Differences in bed shear stress might occur due to the fact that the velocity profiles over the topography of a dune are not logarithmic, as assumed by the log law.

For the finest vertical resolution (presented in Tbl. 5.3), the z+ criteria has been calculated. The law of the wall by von Kármán (1930) can only applied if the lowest σ-layer is positioned above the viscous sublayer (Jankowski, 1999). The non-dimensional number z+ is calculated according to

$$z+ \;=\; \frac{y\,u^*}{\nu} \tag{5.3}$$

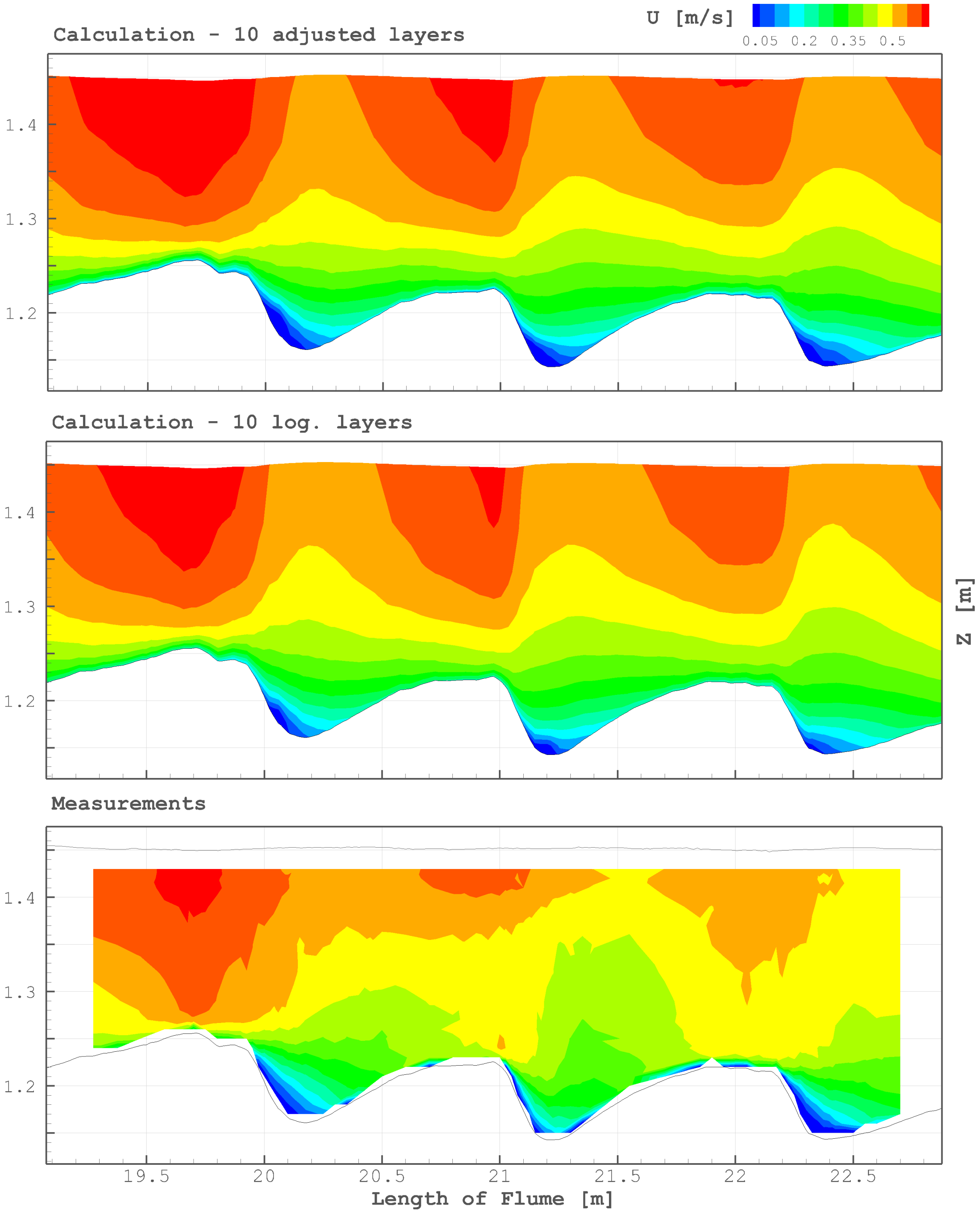

Figure 5.4: 2D-vertical slice of stream-wise velocity [m/s] calculated with 10 adjusted σ-layers (top) and 10 logarithmic σ-layers (middle) in comparison to measurements (bottom). Data sets No. 11 and 12 of Table 5.1

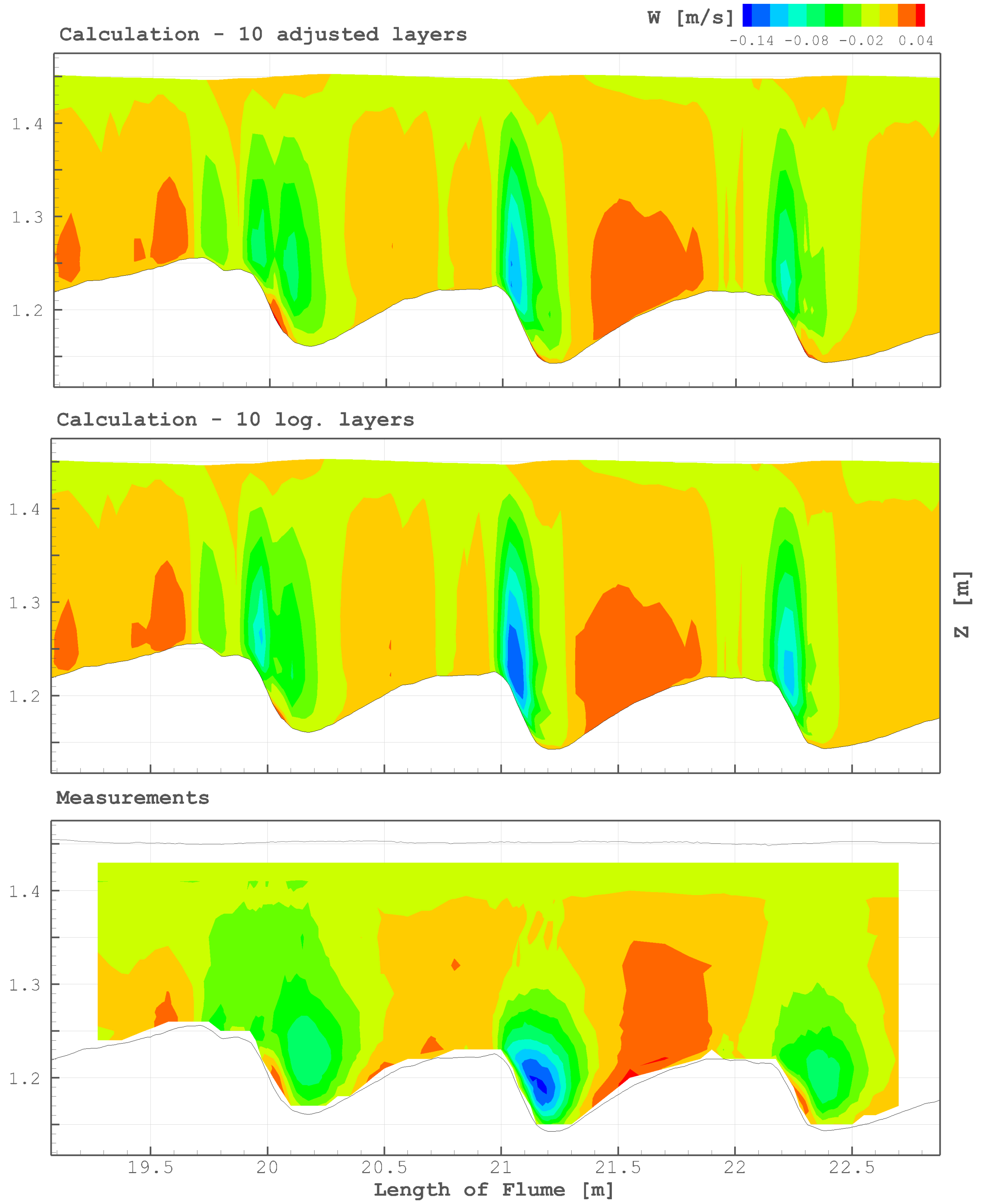

Figure 5.5: 2D-vertical slice of vertical velocity [m/s] calculated with 10 adjusted σ-layers (top) and 10 logarithmic σ-layers (middle) in comparison to measurements (bottom). Data sets No. 11 and 12 of Table 5.1

Table 5.4: Percentage of the area of the flume (A), for which the z+ criteria is valid

	z+ $\geq$ 30	z+ $\geq$ 60	z+ $\geq$ 80	z+ $\geq$ 90	z+ $\geq$ 100
A %	100	99.95	90.73	60.95	26.70

with:		
	y	height of extraction above the bottom $[\mathrm{m}]$
	u^*	friction velocity $[\mathrm{m/s}]$
	ν	cinematic viscosity $[\mathrm{m^2/s}]$

A position above the viscous sublayer and the buffer layer can be assumed, if z+ $\geq$30 (Patel, 2007). For the presented calculations, the chosen vertical resolution yields a flume area of 99.95% where z+ $\geq$ 30, and an area of 90.73% where z+ $\geq$ 60. The criteria of z+ $\geq$ 100 is reached for 26.7% of the flume area. The values are summarised in Table 5.4. Following this the extraction point of the applied velocity for bed shear stress calculation should be in the zone of fully turbulent flow. In this region a logarithmic velocity profile can be rightly assumed and the wall friction law of von Kármán (1930) is valid.

A vertical refinement, such as from simulation A $\rightarrow$ B in Figure 5.6 (where simulation A has 10 σ-layers in the vertical and B has 13), should generate the same results – merely with more computational time. Nonetheless the area of simulation B, in which the bed shear stress is higher than $1.25\,\mathrm{N/m^2}$, is reduced by 25% compared to A. The sensitivity of model results towards mesh refinement must kept in mind – and the same (vertical) resolution needs to be used when comparing numerical results. Calibration with measurements allows to find the correct resolution. It needs to be stated though, that when calculating morphodynamic processes with σ-layers, an influence of the layering can not always be completely ruled out, as the layer resolution changes as dynamically as the bottom itself (Decoene and Gerbeau, 2008).

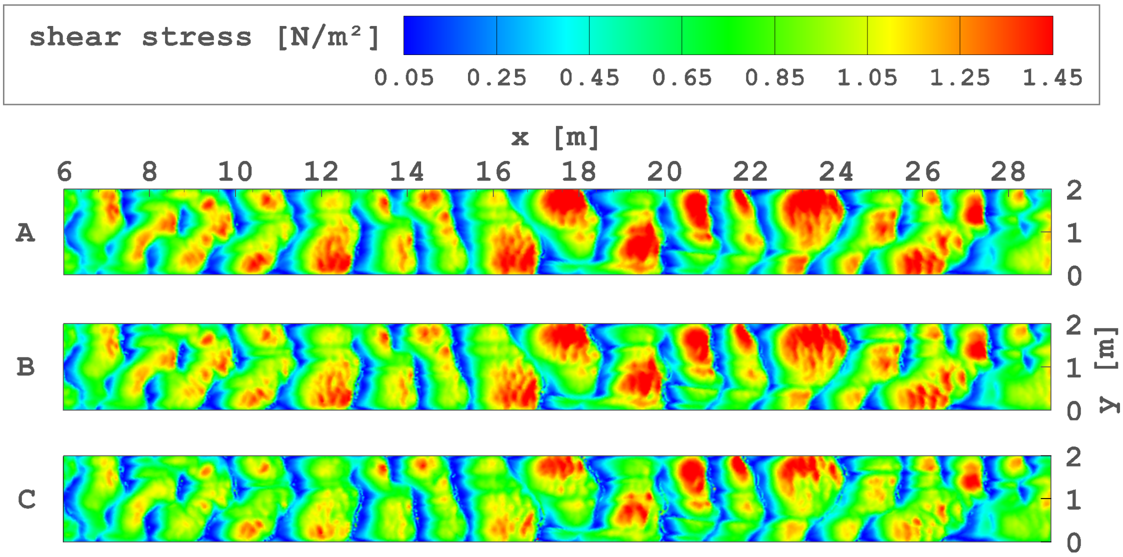

Figure 5.6: Bottom shear stress $[\mathrm{N/m^2}]$ over fixed bed, calculated from log law approach, with A: 10 logarithmic σ-layers – B: 13 logarithmic σ-layers – C: 10 adjusted σ-layers, k_s = 0.00395 m

5.3 Small scale bed elements

In 2D or 3D river flow models, the friction is the main calibration parameter for the hydrodynamics. A roughness height simply calculated from the sand mean diameter ($k_s = 3d_{50}$) is not sufficient, as the meshes are too coarse to include all bed forms. If they are smaller than the mesh size, they are not directly represented and their friction must thus be parametrised. This is also known as the topographic subgrid scale effect (Platzek et al., 2016). According to van Rijn (1993) the bed friction is composed from several individual factors

$$k_s = k_s^g + k_s^r + k_s^d \tag{1.1}$$

where k_s^g is a grain roughness and k_s^r and k_s^d a form roughness for ripples and dunes respectively. The grain roughness is calculated from the mean grain diameter d_{50} as

$$k_s^g = 3d_{50} \tag{5.4}$$

The form roughness of ripples is calculated as

$$k_s^r = 20\gamma_r \Delta_r \frac{\Delta_r}{\lambda_r} \ , \tag{5.5}$$

and the dune form roughness is calculated as

$$k_s^d = 1.1\gamma_d \Delta_d (1 - exp^{-25\frac{\Delta_d}{\lambda_d}}) \ , \tag{5.6}$$

with:	$\Delta_{r/d}$	ripple/dune height $[\mathrm{m}]$
	$\lambda_{r/d}$	ripple/dune length $[\mathrm{m}]$
	γ_r	presence factor: 1.0 for ripples alone, 0.7 for ripples superimposing dunes or sand waves
	γ_d	form factor: 0.7 for dunes in field condition.

For the presented experimental flume, a calculation of bed roughness from the mean diameter of the sediment results in a roughness height of $k_s = k_s^g = 3d_{50} = 0.002\,82\,\mathrm{m}$ according to the formula of van Rijn (1993). Preliminary tests have shown that it is necessary to adjust the roughness height k_s to gain quantitative and qualitative agreement of the water levels of simulation and measurements over fixed dunes (Goll, 2011).

From the analysis of the bottom scans, small-scale bottom forms can be observed. The extent to which the forms can be distinguished is the resolution of the recording. Accuracy for bed elevation measurements are of the order of $1\,\mathrm{mm}$ for subaqueous measurements used in this context (Henning, 2008). In x-y-direction the available data has a resolution of $0.02\,\mathrm{m} \times 0.02\,\mathrm{m}$. The numerical meshes of the hydrodynamic simulations have a coarser resolution except for the finest mesh, which lies lower with a mean edge length of $0.014\,\mathrm{m}$ (see Table 5.2).

The existence of these small, superceding bed forms, namely sand-sheets, in the data sets used in this Ph.d. study, has been analysed in a previous work (Henning, 2013). Other authors found similar structures during their experiments. Naqshband et al. (2014b) noted that these small, secondary bed forms migrated on the stoss side of the dune and had local effects on the flow near the bed and also the sediment transport. In the experimental study of Carling et al. (2000b) it was shown that this sort of secondary bed forms have an important influence on the velocity distribution not only near the bed, but throughout the water column. The presence of secondary bed forms not only resulted in a reduction of velocities near the bed, but also altered the mean velocity of the flow and the form of the velocity profile.

It has to be expect that small scale structures – smaller than the numerical mesh resolution, or the resolution of the photogrammetric recording – will not be represented in the mesh and, as a result, will not be captured in the calculation. These bottom deformations will not interact with the free surface. Due to their height compared to the water depth they can be placed in the same bed form category as ripples. To characterise these ripple forms, the following observations can be made:

1. The ripples will result in a form roughness of the bottom.
2. If a corresponding roughness height is calculated with the ripple formula of Van Rijn (Eq. 5.5), the maximum length of a bed form that cannot be resolved on a mesh will be the mesh/recording resolution.
3. The maximum slope of the ripples will not exceed the angle of repose of the sediment (35°).
4. As we expect a range of ripples, average approximations should be applied to receive an representative roughness height.
5. The roughness height for ripples k_s^r needs to be added to the grain friction to calculate the total roughness height.

Three values for an expected angle α of the stoss/lee side of the ripples (see Figure 5.7) are chosen: 7°, 10°and 18°. This is in accordance with Best (2005), who found that in large rivers the average lee side slope of dunes is often lower than 8°, thus ranging clearly below the angle of repose. With these values we can calculate the height h_r of the expected ripples from the following equation

$$\tan\alpha = \frac{h_r}{1/2\,\mathrm{d}x} \tag{5.7}$$

where $\mathrm{d}x$ the length of the ripple. The resolution of the bottom measurements is considered the minimum ripple length, that can resolved: $\mathrm{d}x = 0.02\,\mathrm{m}$. This is also the maximum mesh width of the finest mesh. This results in ripple heights h_r of $0.0012\,\mathrm{m}$, $0.0017\,\mathrm{m}$ and $0.0032\,\mathrm{m}$.

With ripple height and length, form-roughness heights k_s^r for the expected ripples are calculated according to the formula of van Rijn (1993), Eq. 5.5. It treats ripples as two-dimensional bed forms, characterized only by their height and wave length. This methods agrees with ripple predictors proposed by other authors, (e.g. Soulsby et al., 2012). The calculated roughness heights k_s^r for the ripples are $0.0011\,\mathrm{m}$, $0.0022\,\mathrm{m}$ and $0.0073\,\mathrm{m}$. These ripple form-frictions are 60% and 20% lower ($0.0011\,\mathrm{m}$, $0.0022\,\mathrm{m}$) and 160% higher ($0.0073\,\mathrm{m}$) than the grain roughness height k_s^g ($0.002\,82\,\mathrm{m}$) of the sand.

The ripple roughness height is added to the grain friction, and one receives three roughness heights $k_s = 0.003\,95\,\mathrm{m}$, $0.005\,\mathrm{m}$ and $0.01\,\mathrm{m}$. Simulations with these three roughness heights for the medium and coarse meshes are present in Figures 5.9 and 5.8 respectively.

Calculations with the medium mesh (Fig. 5.8), with an average mesh-width of $0.065\,\mathrm{m}$, have very similar free surface levels for roughness heights of $0.003\,95\,\mathrm{m}$ and $0.05\,\mathrm{m}$, as the roughness heights do not differ greatly. A roughness height of $0.01\,\mathrm{m}$ on the other hand will result in a too strong influence on the free surface levels: the free surface level is in average $1\,\mathrm{mm}$ too high at the inflow of the flume. This corresponds to 0.37% of the water depth. Obviously the size of ripples or sand-sheets that are included in this roughness

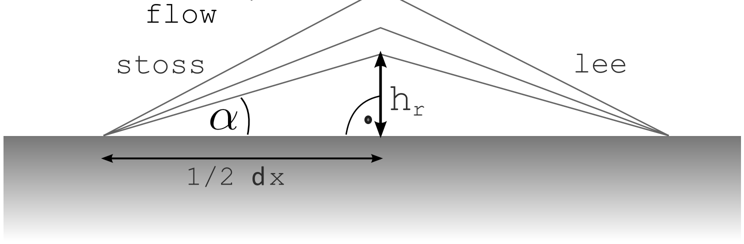

Figure 5.7: Calculation of the ripple height based on ripple slope, limited by the mesh width $\mathrm{d}x$

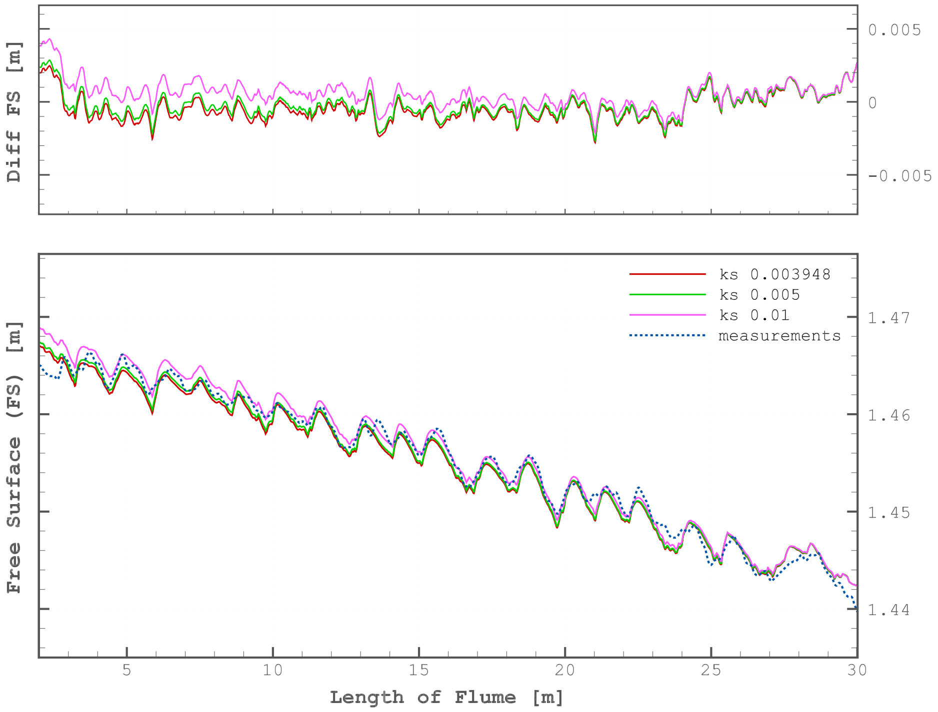

Figure 5.8: Free surface levels with $k_s = 0.003\,95\,\mathrm{m}$, $0.005\,\mathrm{m}$ and $0.01\,\mathrm{m}$ and differences to measurements (top), medium mesh. Data sets No. 4, 5, 6 of Tbl. 5.1

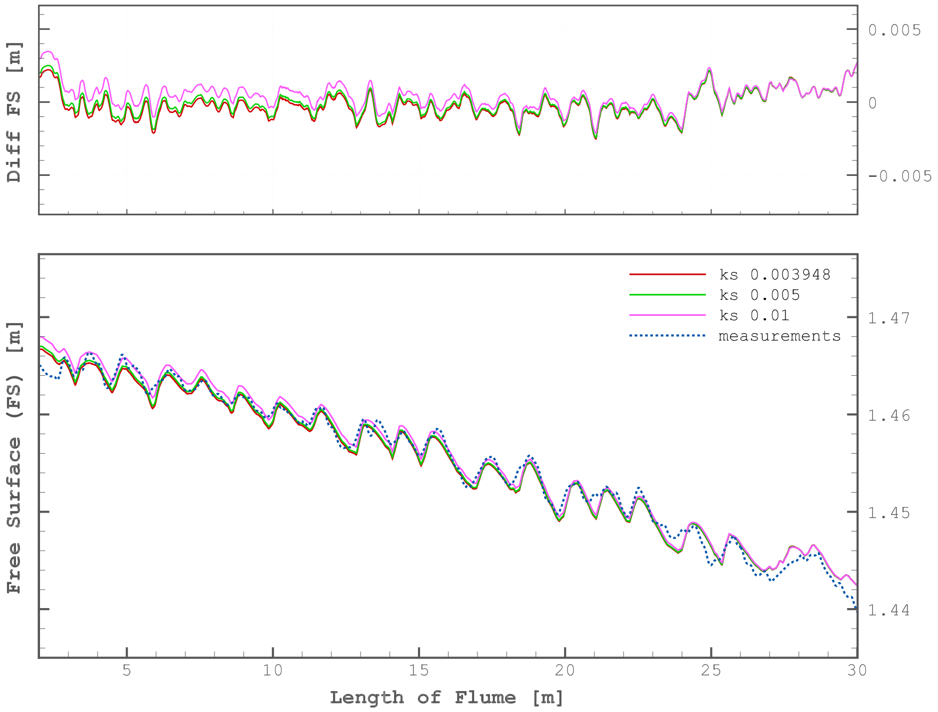

Figure 5.9: Free surface levels with $k_s = 0.003\,95\,\mathrm{m}$, $0.005\,\mathrm{m}$ and $0.01\,\mathrm{m}$ and differences to measurements (top), coarse mesh. Data sets No. 7, 8, 9 of Tbl. 5.1

height can already be represented on this mesh directly. The coarse mesh (Fig. 5.9), with an average mesh-width of $0.11\,\mathrm{m}$, will produce similar water levels with all three roughness heights. With the roughness height of $0.01\,\mathrm{m}$ the water level is slightly higher than the measurements ($<0.5\,\mathrm{mm}$ at the inflow, this corresponds to differences <0.18% of the water depth) than with the two lower roughness heights. Thus, the numerical system reacts in the expected way: a higher roughness height produces higher water levels. Overall, a roughness height of $k_s = 0.005\,\mathrm{m}$ (corresponding with a ripple height of $0.0022\,\mathrm{m}$) generates the best fit with the measurements.

Comparing the finest of the three meshes, with an average mesh-width of $0.014\,\mathrm{m}$, a very different result is obtained (Fig. 5.10). Here free surface levels only agree with the measurements, if the highest roughness height of $k_s = 0.01\,\mathrm{m}$ is applied. For the lowest value of friction, the water levels are distinctively lower than the measurements (in average $8\,\mathrm{mm}$) at the outflow which are about 3% of the water depth. All small scale bed forms (at least the smallest ones that are available in the recording) are included in the finest mesh, as its resolution is on average below the resolution of the photogrammetric recording. Due to this, only additional resulting roughness heights calculated from form roughnesses, which are *smaller* than the recording, should be included in the roughness heights. The ripples of the highest value of ripple form friction $k_s^r = 0.0073\,\mathrm{m}$, which yields a total roughness height $k_s = 0.01\,\mathrm{m}$, exceed these limits.

Bed level differences between the medium and fine mesh are in the range of $\pm 0.01\,\mathrm{m}$, not extensive and also found mostly close to the model boundaries (this is due to the distribution of the recorded data, which thins out towards the outer boundaries). However, this does not explain the differences between the free surface levels that lie in the range of half of the size of this difference of $\pm 0.01\,\mathrm{m}$.

Numerical diffusion is generally lower, if the mesh is refined (Bastian, 2008; Malcherek, 2013). The numerical combination used in this work with SUPG as advection scheme tends to produce less numerical diffusion than calculations with the classical scheme of characteristics. Less numerical diffusion is expected from the fine mesh – which should lead to a lower free surface elevation and higher mean velocities. The results for the free surface elevation obtained for the fine mesh resolution do reflect this, providing lower free surface levels as the coarse and medium mesh (Fig. 5.8 and 5.9). Numerical diffusion therefore provides a sort of additional roughness to the flow.

Further discussion will be provided in Section 5.6.

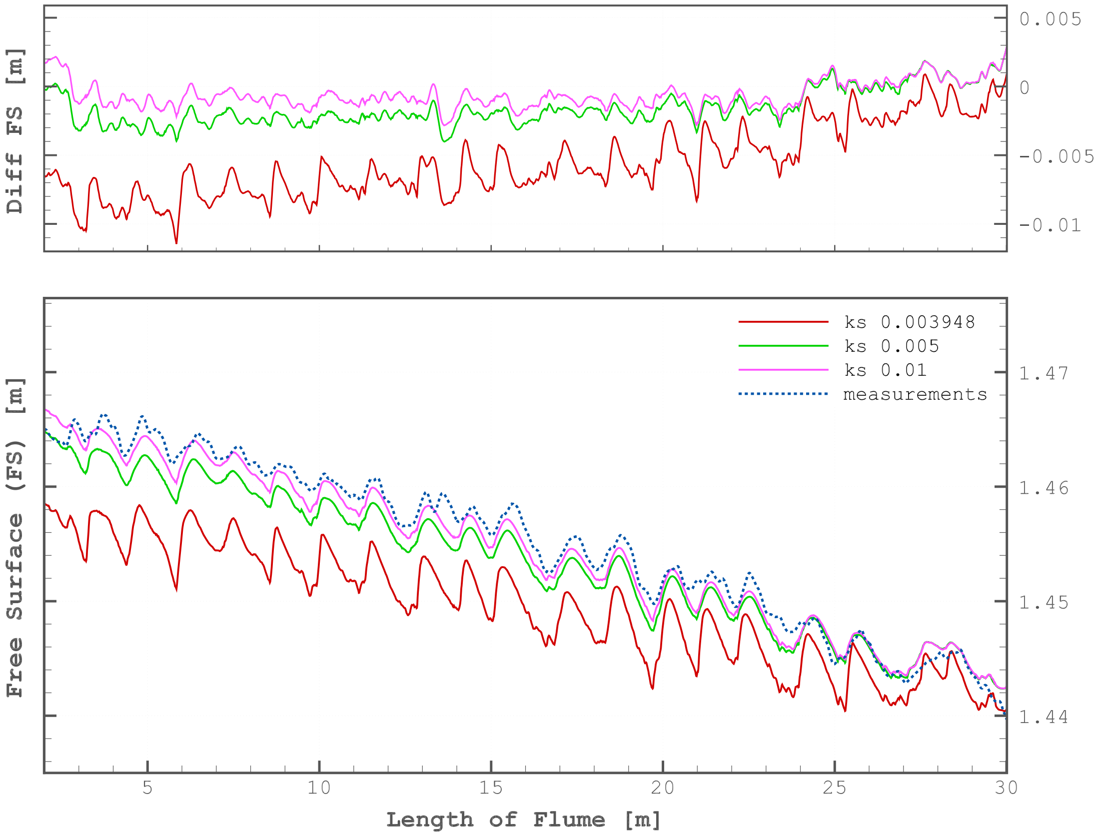

Figure 5.10: Free surface levels obtained with k_s of $0.003\,95\,\mathrm{m}$, $0.005\,\mathrm{m}$ and $0.01\,\mathrm{m}$ and differences to measurements (top), calculations with fine mesh. Data sets No. 1, 2, 3 of Tbl. 5.1

5.4 Pressure distribution

In shallow water flows, vertical velocity components are smaller than horizontal velocities by orders of magnitude and a hydrostatic pressure approach can be chosen (see Section 4.2). Pressure gradients are then sole represented by the slope of the free water surface.

In the case of dunes the eligibility of this approach must be insistently questioned. A reference value for maximal slope, where a hydrostatic pressure approach can be sufficient, is 1:10 in flow direction (Stansby and Zhou, 1998; Wenka and Schröder, 2004). A reason for this is, that non-hydrostatic pressure components can only be neglected, if no vertical acceleration is present (Jankowski, 1999). Vertical accelerations occur, for example, over suddenly changing bottom topography or in strong vertical circulations, meaning that the flow over dunes is prone to contain such accelerations. Using the non-hydrostatic option in the RANS code of the module Telemac-3D, an additional equation is solved for the w-component of the velocity, similar to the u- and v-equations which contains the gravity term (Hervouet, 2007), see Section 4.2.

A comparison of water levels with and without hydrostatic pressure approach shows, that it is not possible to reach qualitative and quantitative agreement of measured and simulated water levels with the simple hydrostatic pressure approach (see Fig. 5.11). Figures 5.12 to 5.14 show comparisons of the three velocity components u, v, w calculated with and without the hydrostatic pressure approach. The results are also compared to the measurements. Main differences are found for the vertical velocity components, but for all velocity distributions u, v, w good qualitative and quantitative agreement can be obtained. The differences of free surface levels obtained based on the hydrostatic pressure approach, shown in Fig. 5.11, must be thus due to summed-up differences in the velocity distributions over the complete water body – not only in longitudinal but also in transverse direction. It must be noted though, that at the position of the measured velocities above the dunes (flume meter x = $19.2\,\mathrm{m}$ to $22.7\,\mathrm{m}$), the free surface levels presented in Figure 5.11 are still very similar due to the fixed boundary conditions at the outflow. In the flume section of the measurements, the hydrostatic free surface levels are in average less than $1\,\mathrm{mm}$ lower than the non-hydrostatic ones and the ones of the measurements. The discrepancy in water levels increases towards the inflow of the flume.

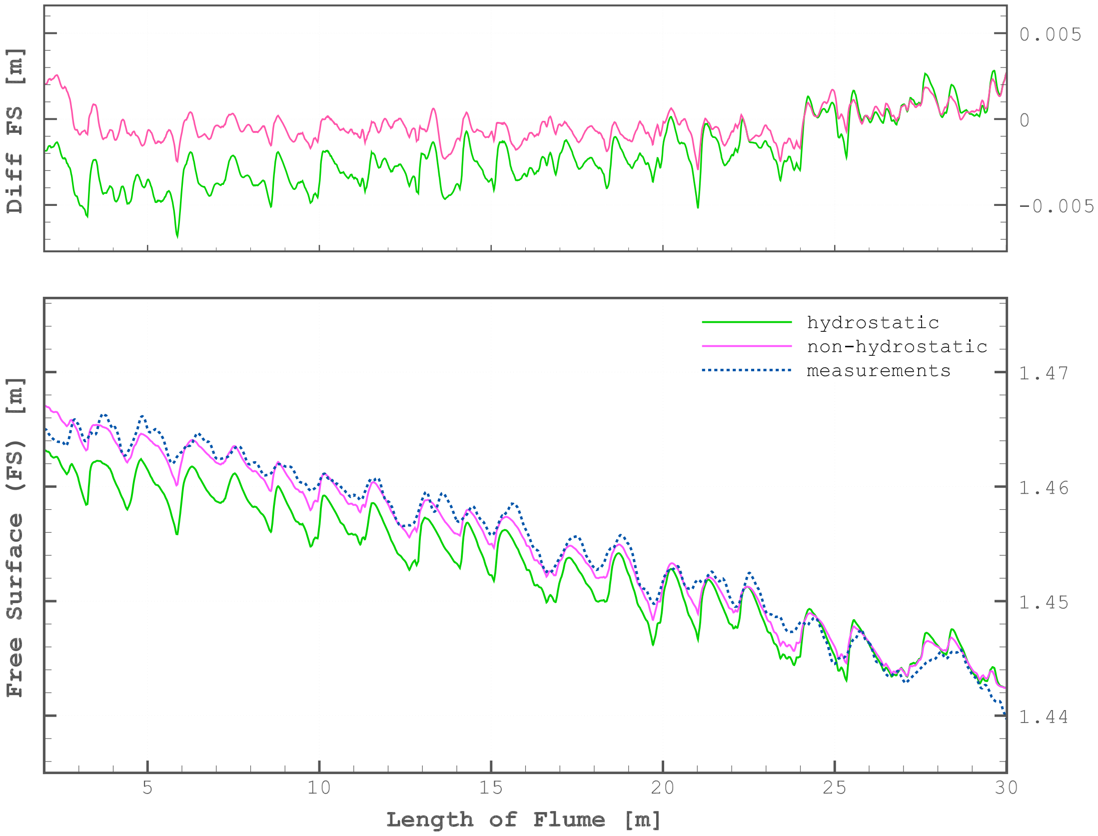

Figure 5.11: Free surface levels obtained with hydrostatic and non-hydrostatic pressure approach. $k_s = 0.003\,95\,\mathrm{m}$ and differences to measurements (top), calculations with medium mesh resolution. Data sets No. 12, 14 and 15 of Table 5.1

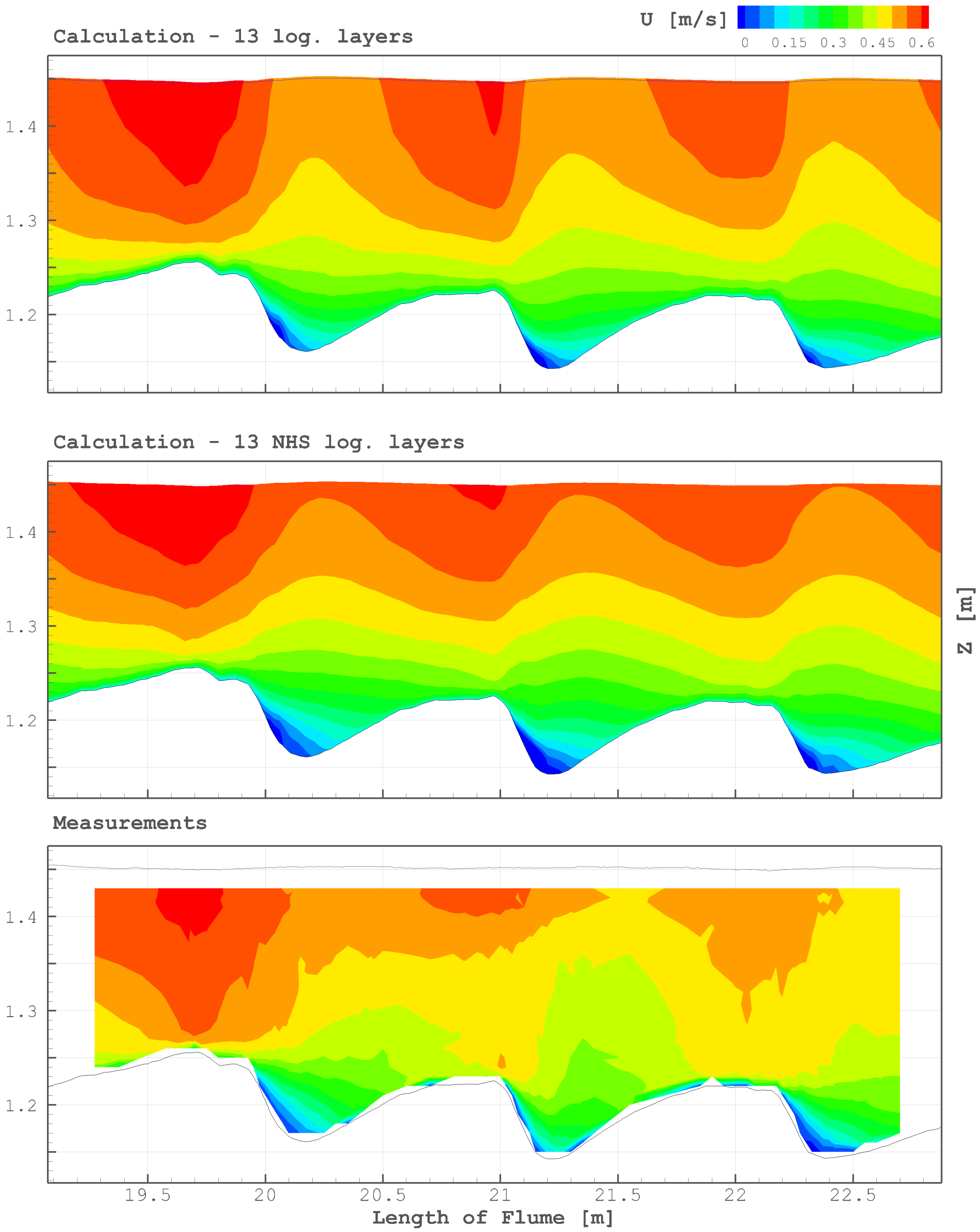

Figure 5.12: Comparison of velocity u [m/s] obtained with hydrostatic pressure approach (top) and non-hydrostatic pressure approach (NHS) (middle) to measurements (bottom). Data sets No. 10 and 13 of Table 5.1

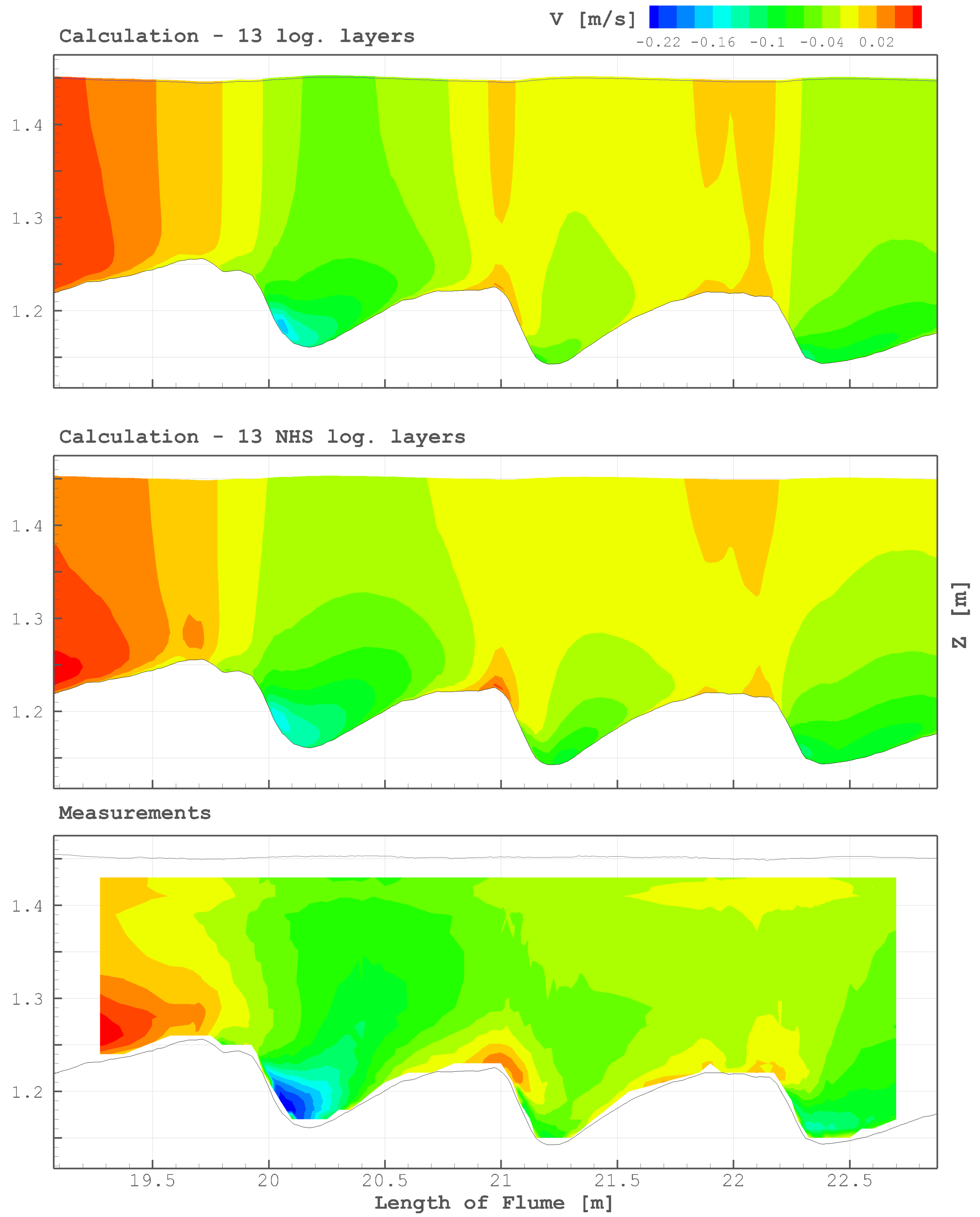

Figure 5.13: Comparison of velocity v [m/s] obtained with hydrostatic pressure approach (top) and non-hydrostatic pressure approach (NHS) (middle) to measurements (bottom). Data sets No. 10 and 13 of Table 5.1

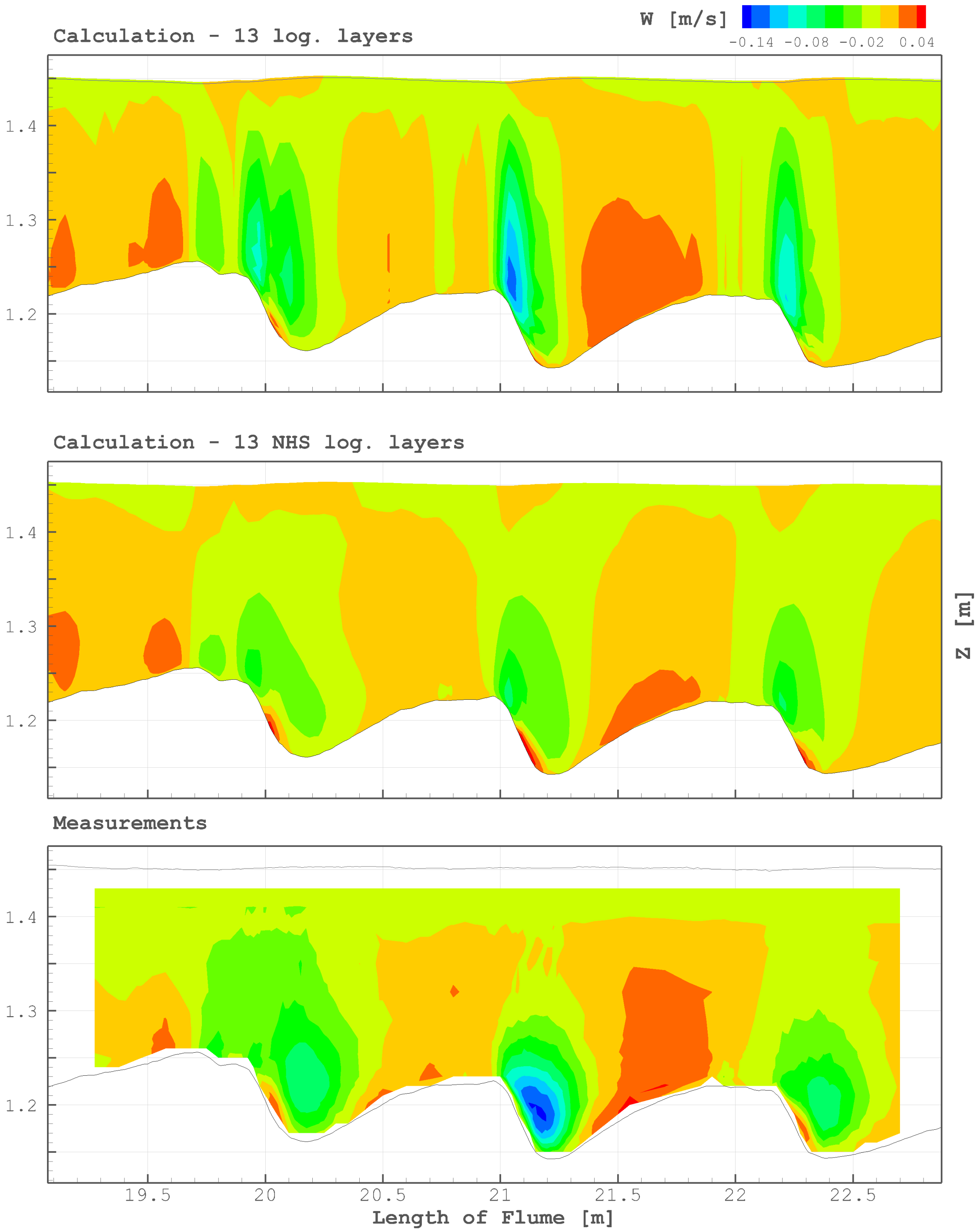

Figure 5.14: Comparison of velocity w [m/s] obtained with hydrostatic pressure approach (top) and non-hydrostatic pressure approach (NHS) (middle) to measurements (bottom). Data sets No. 10 and 13 of Table 5.1

5.5 Turbulence model

A key feature of flow over dunes is the pronounced presence of turbulence (Jackson, 1976; Nelson et al., 1993; Bennett and Best, 1995). Especially the region behind the dune crest up to the reattachment point (see also Figure 2.3) can be categorised as highly turbulent. Thus a proper representation of this flow pattern is essential to obtain a quantitative and qualitative agreement between experimental results and hydrodynamic simulations.

In Chapter 2 the close link between turbulence and dunes has been presented. This literature study has also shown, that all models satisfactorily representing the flow field over two- and three-dimensional dunes have either been Direct Numerical or Large Eddy Simulations, or have at least applied a two-equation turbulence model.

A study conducted by the Leichtweiß Institute for Hydraulic Engineering, TU Braunschweig, Germany (LWI, 2006) compared different turbulence models (Elder, k-ε and k-ω) in the Telemac system and their own code against measurements conducted at two BAW experimental models: a contraction flume and a model with installed groynes. They found that that only the two-equation turbulence models (k-ε and k-ω) were able to reproduce the flow features adequately. The experiments showed that in order to reproduce highly three-dimensional flows, algebraic models are not sufficient, as they simplify the physical processes too far. Flow over three-dimensional dunes possesses most of the features present in the LWI study. Thus the recommendations given in the study are also applicable for the dune processes. Most recently Stansby et al. (2016) presented a study of recirculation zone around headlands, where they used Telemac-3D in combination with the k-ε model. They performed experiments in an experimental facility to validate their numerical simulations. Stansby et al. (2016) reported good qualitative agreement for the recirculation patterns and associated velocities using the model configuration.

Figure 5.15 shows a comparison of velocity vectors between measurements and hydrodynamic simulations done with the k-ε model on the top left and algebraic models (top right: mixing-length model of Prandtl for the vertical, Smagorinsky model for the horizontal components; bottom right: mixing-length model of Prandtl for the vertical, constant viscosity for the horizontal components) on the right hand side. The plot shows the vectors of u- and w-velocities in order to capture the recirculation zone. One can clearly see the shortcomings of the algebraic models: in the recirculation zone, the area

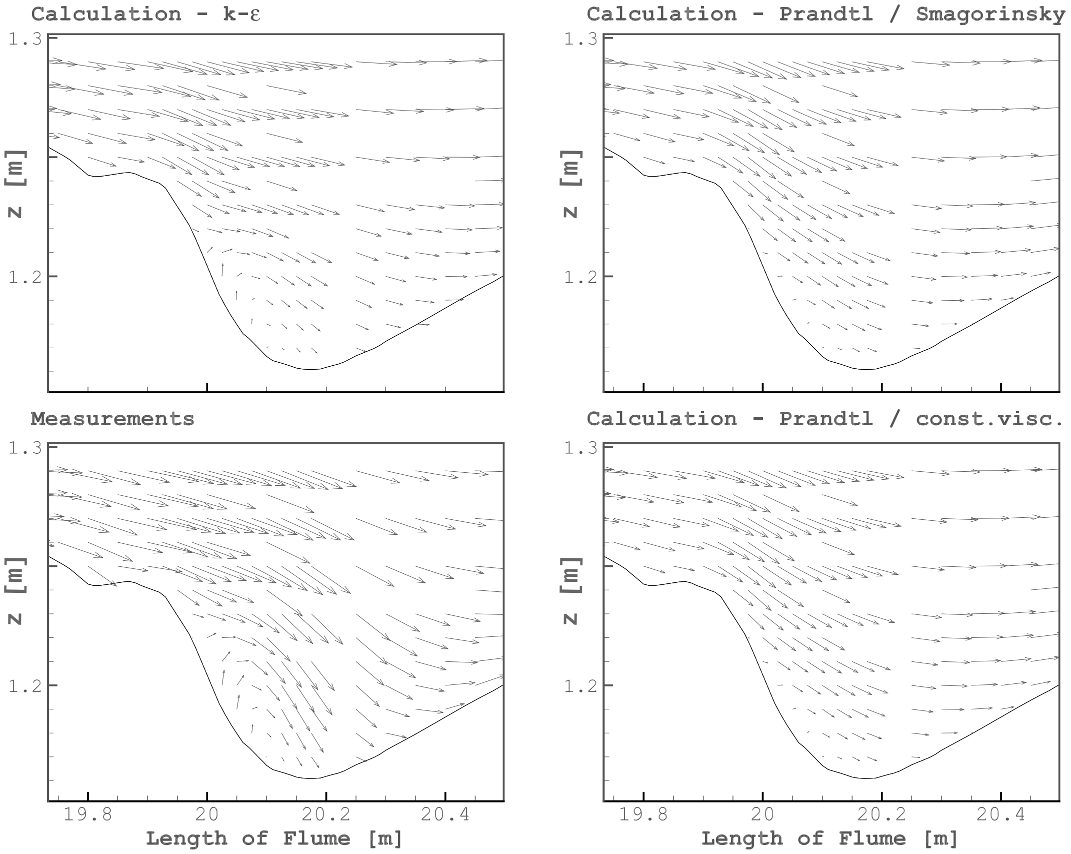

(a) k-ε model (b) Prandtl / Smagorinsky model

Figure 5.15: Details of velocity vectors (u, w) calculated with different turbulence models. Data sets No. 13, 16 and 17 of Table 5.1

most crucial for dune movement and preservation, no agreement with measurements can be obtained. The k-ε model on the other hand captures the recirculation zone.

Figure 5.16 displays a comparison of the turbulent kinetic energy distribution calculated with and without the hydrostatic pressure approach. The simulated turbulent kinetic energy is underestimated by a factor of 2.5. For further discussion on this topic see Section 5.6. Differences can be detected between simulations with hydrostatic and non-hydrostatic pressure approach. In the vertical, as well as in selected characteristic regions (recirculation zones behind the second and third dune and wider wake region behind the first dune), the distribution of turbulent kinetic energy of the non-hydrostatic simulation offers a qualitatively better agreement with the measurements.

For simulations with the algebraic models no turbulent kinetic energy is calculated and hence not available for comparison. Calculations with the k-ω turbulence model implemented in Telemac-3D showed the same tendency, overall producing an even lower turbulent kinetic energy throughout the water column.

Lyn (2008) as part of the collection "*Sedimentation Engineering – Processes, Measurements, Modelling and Practice*" also states that even though the k-ε model has proved itself through extensive tests and application as the standard model in flow calculation, one should not take its results as the unquestionable truth. The author found that even though the k-ε model is useful for providing engineering predictions, localised, possibly important flow details might not be captured (Lyn, 2008).

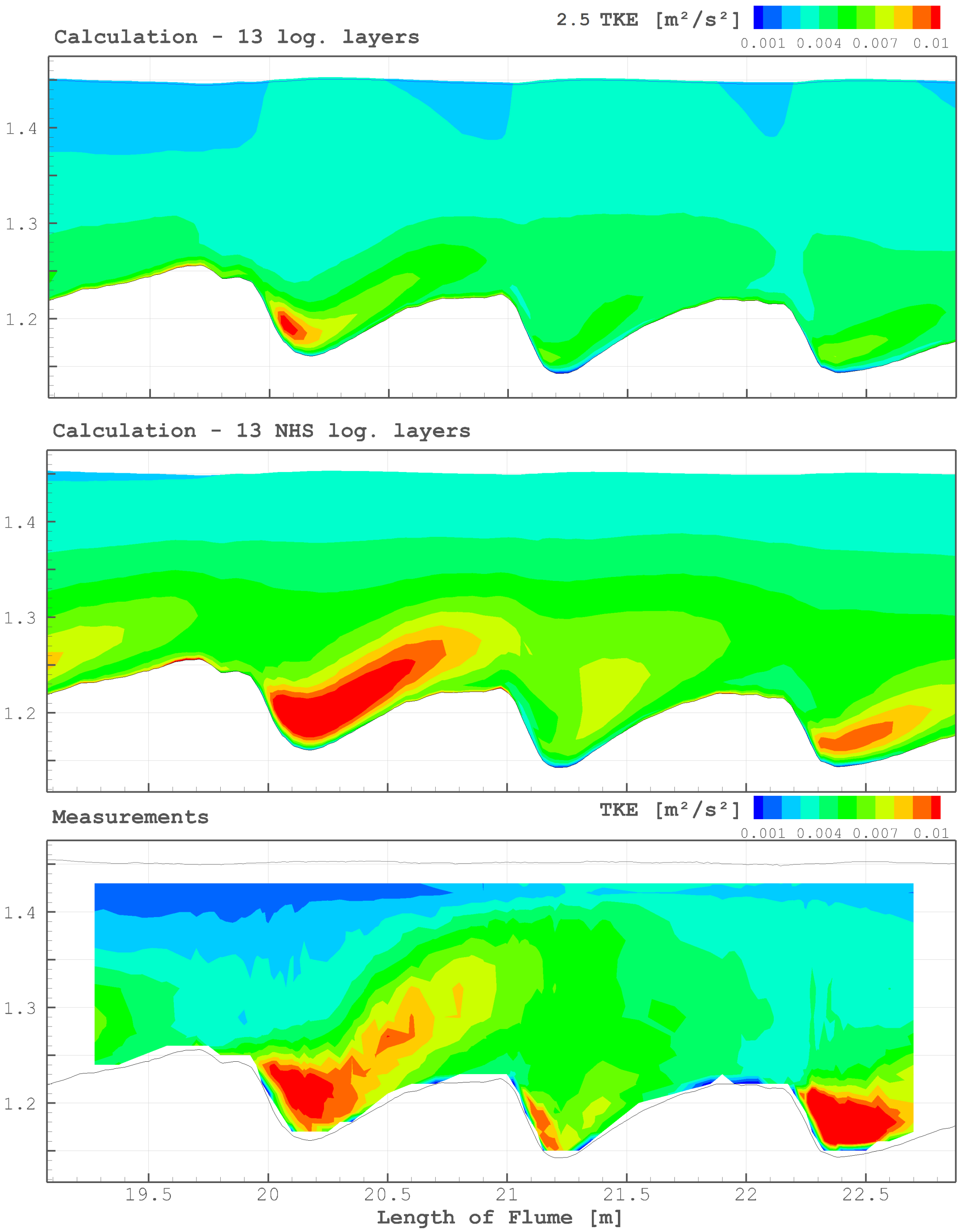

Figure 5.16: Comparison of the turbulent kinetic energy (TKE) [m^2/s^2] with hydrostatic pressure approach (top) and non-hydrostatic pressure approach (NHS) (middle) to measurements (bottom). Both calculations are rescaled with a factor of 2.5 in order to be in the same range as the measurements. Data sets No. 10 and 13 of Table 5.1

5.6 Discussion

The previous chapters show that various parameters of the numerical model influence the results obtained for the presented hydrodynamic experiments. Several influencing variables are extracted, which influence the numerical results concerning quantitative and qualitative agreement with measurements of free surface levels and flow structures.

Firstly it is shown, that it is necessary to apply the **non-hydrostatic pressure approach** to reach an agreement with the hydrodynamic measurements, see Figure 5.11. Considering the complex flow situation on the lee side of three-dimensional, natural dunes, this is not a surprising result.

The **mesh resolution** influences the quantity of flow features that is either directly modelled on the mesh or reproduced indirectly via a turbulence model. The different meshes studied in this section produce differences in free surface levels (Section 5.1). Examining the flow features which are created by different meshes, an explanation for the differences in the free surface levels can be found. Figure 5.17 displays the turbulent kinetic energy, Figure 5.18 shows the velocity vectors of the fine ($\mathrm{d}x$ = $0.014\,\mathrm{m}$) and medium mesh ($\mathrm{d}x$ = $0.065\,\mathrm{m}$) over dunes with a length of $1.2\,\mathrm{m}$ to $1.4\,\mathrm{m}$. Obviously the turbulent zones behind the dunes are displayed quite differently for the two meshes. The calculated recirculation – displayed through the u- and w-vectors – is more intense on the mesh with medium resolution (Fig. 5.18); this is a direct representation of flow features. The fine mesh on the other hand features more turbulent kinetic energy calculated by the turbulence model in the same region (Fig. 5.17), thus more turbulent flow features are parametrised. The less pronounced recirculation zone of the fine mesh can explain the lower free surface levels of the calculation, because of the lack of supporting flow characteristics. The lower free surface levels of the fine mesh also show, that the slightly higher turbulent kinetic energy provided by the turbulence model does not compensate for the missing recirculation.

It can be reasoned, that the diminution of the edge length of the cells by 80% (equals 11 times more nodes in the mesh, see Table 5.2) will lead to numerical effects that will make the results not comparable or scalable any more. Changing the roughness height does not compensate this lack in flow structures representation. Applying the same advection schemes and **turbulence models** that use a length scale of the mesh (such as the k-ε model, see Section 5.5) proves not to be feasible in highly three-dimensional flows,

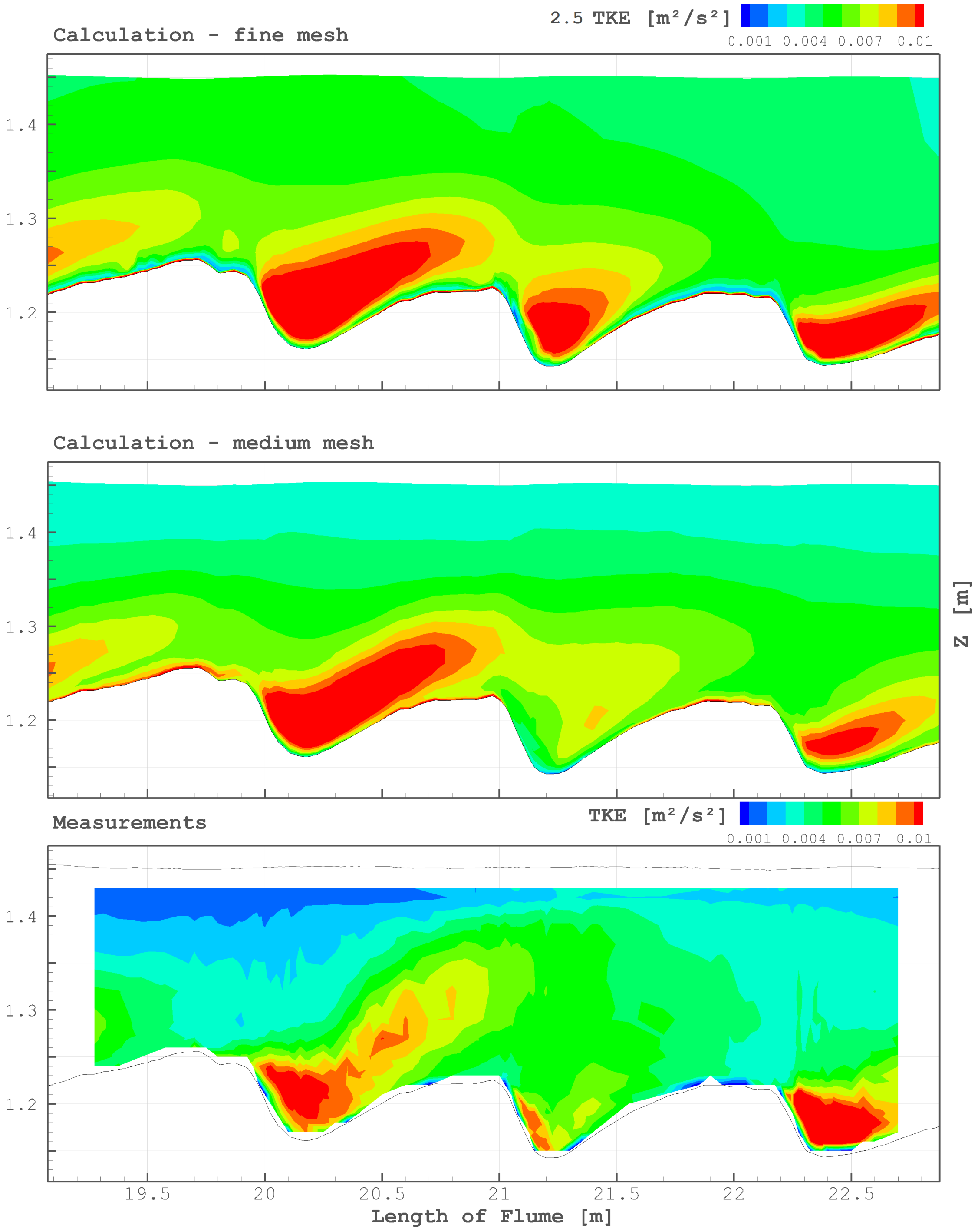

Figure 5.17: Turbulent kinetic energy (TKE) calculated by the fine (top) and the medium mesh (middle) in comparison to measurements (bottom). $k_s = 0.01\,\mathrm{m}$, the calculations are factored by 2.5. Data sets No. 1 and 6 of Table 5.1

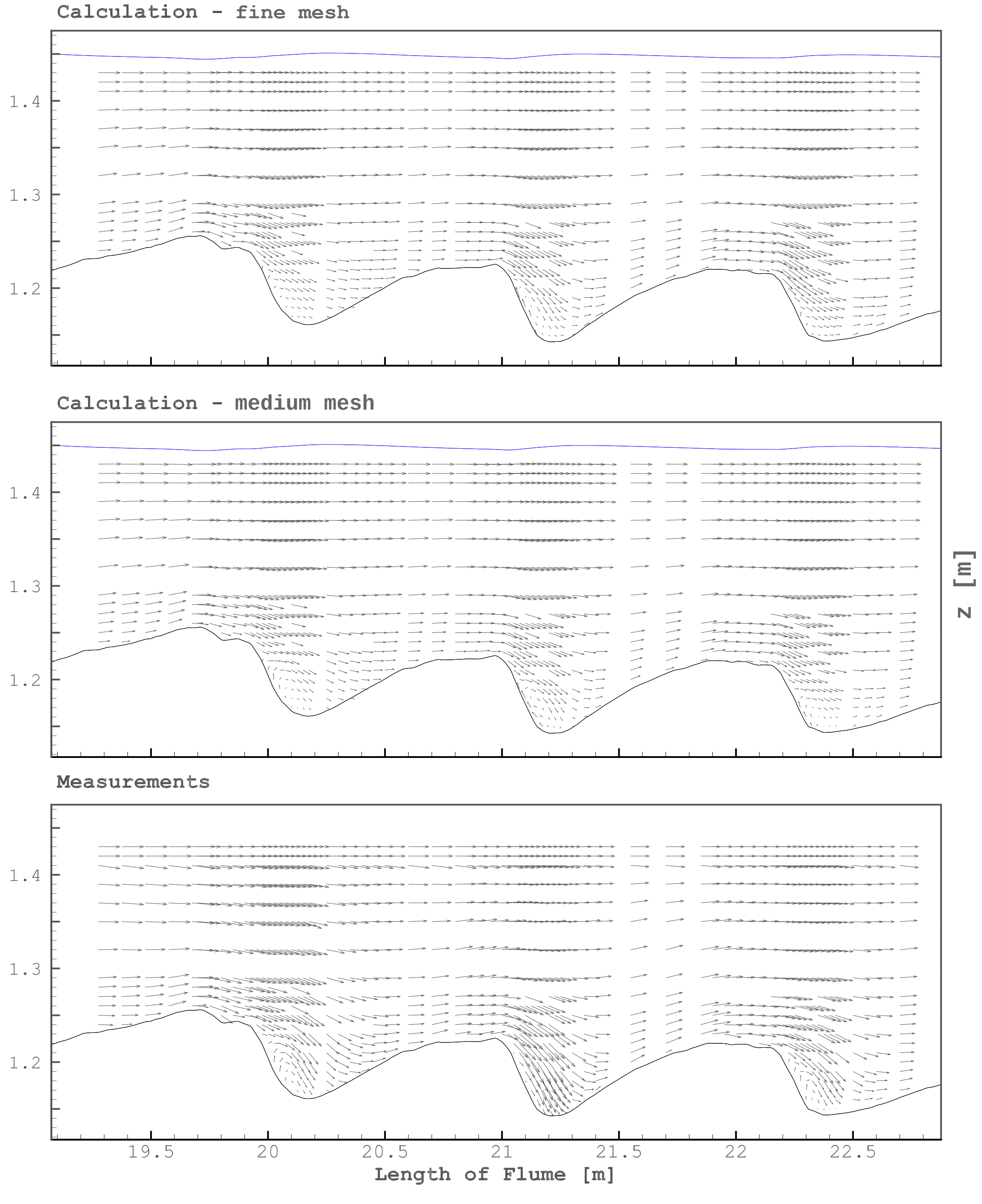

Figure 5.18: Details of velocity vectors (u, w) calculated with the fine mesh (top) and the medium mesh (middle) in comparison to measurements (bottom), k_s = 0.01 m. Data sets No. 1 and 6 of Table 5.1

when changing the mesh resolution. Thus new calibration as well as new considerations become necessary when leaving the range of similar modelled turbulence structures.

The amount of calculated turbulent kinetic energy is also sensitive to the amount of vertical σ-layers. With logarithmically distributed σ-layers, the chosen number of layers will change the height of each layer, depending on the water depth (compare Table 5.3). Figure 5.19 shows, that the different vertical resolutions influence the quantity of the turbulent kinetic energy calculated by the turbulence model. The change in numbers of σ-layers is similar to the change between fine and medium (horizontal) mesh resolution: the computational mesh is refined – only in this case it is in the vertical direction. Here also the finer σ-mesh produces more turbulent kinetic energy through the turbulence model. The considerations of the grid-size dependence of the k-ε model stated above are also valid for the vertical layering presented here. Anyhow, the lack of turbulent kinetic energy should lead to a compensation through other flow features. This is the case for the vertical layering, as it is shown in Section 5.2, where the independence of the free surface level from the chosen number of σ-layers is presented.

A main shortcoming of the numerical model is the quantity of calculated turbulent kinetic energy (k). As presented in Figures 5.16, 5.17 and 5.19, the simulated turbulent kinetic energy is underestimated compared to the measured turbulent kinetic energy by a factor of about 2.5. Considering the fact, that k is depended on the velocity fluctuations squared ($(u_i')^2$, see Eq. 3.3), this is a close agreement with the measurements nonetheless. It has been shown (Kallenberg, 2014), that the measured turbulent kinetic energy has to be seen as a minimal level of the turbulent fluctuations, which are actually present in the flume. The simulated amount of turbulent kinetic energy lies even below this minimal level of the measurements. It lacks in quantity, although the distribution (quality) of the modelled turbulence structures are good. Velocity distributions and water levels on the other hand reach quantitative and qualitative agreement with the measured data set.

The **roughness height** is derived from ripple forms that fall below the mesh resolution k_s^r (see Section 5.3) and grain roughness k_s^g

$$k_s = k_s^g + k_s^r \ . \tag{5.8}$$

k_s is assumed constant (uniform in space and time) and is a calibrated coefficient even though it has been derived from grain size and form parameters

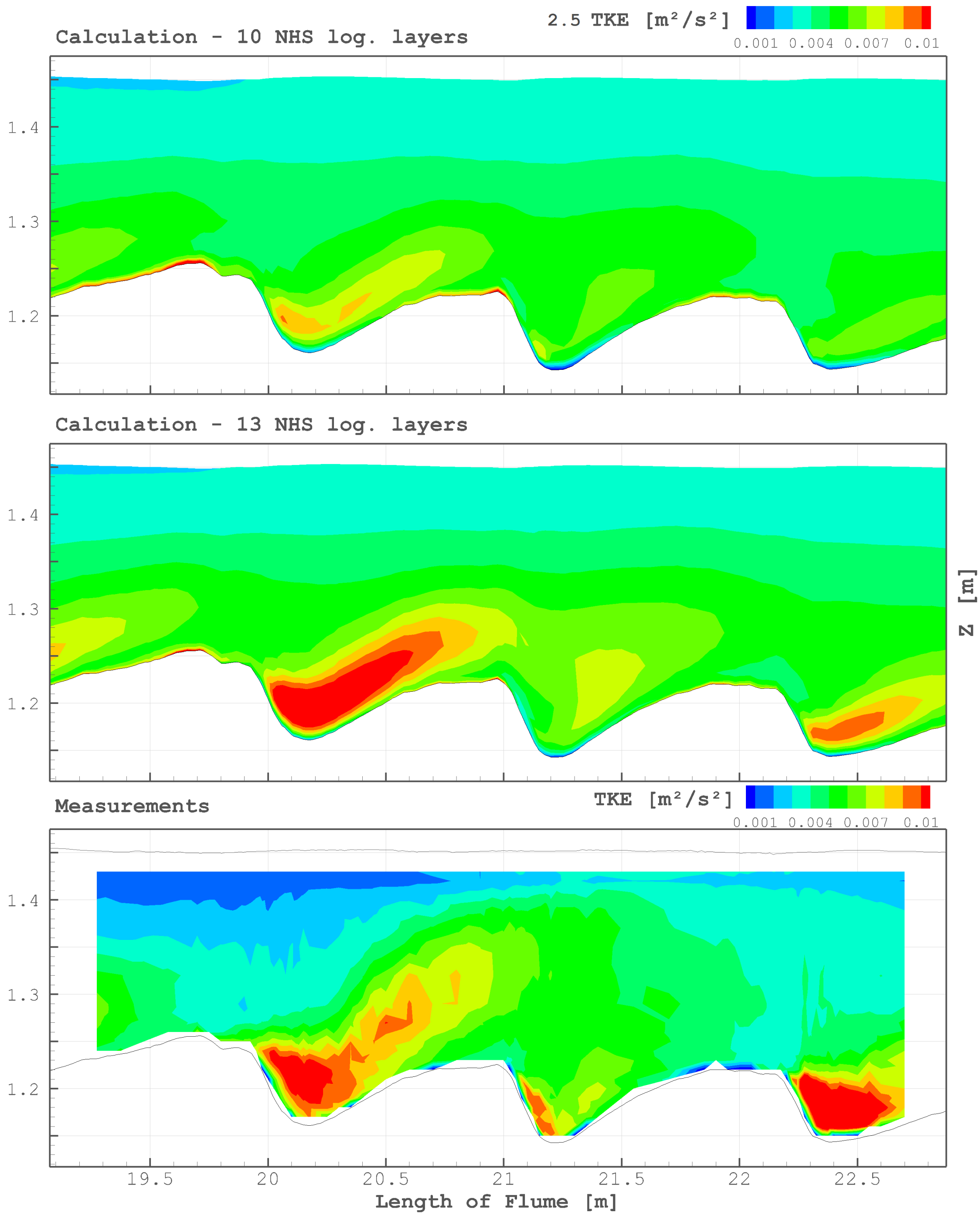

Figure 5.19: Comparison of the turbulent kinetic energy (TKE) [$\mathrm{m}^2/\mathrm{s}^2$] with 10 vertical σ-layers (top) and 13 vertical σ-layers (middle), calculations are factored by 2.5, $k_s = 0.003\,95\,\mathrm{m}$. Data sets No. 13 and 15 of Table 5.1

of superceeding ripple forms. As the simulations lag in turbulent flow features, these effects might be substitute by an elevated roughness height and its influence on the velocity profile.

The hydrodynamic model is tested extensively in this study. It can be concluded, that it is possible to reproduce the turbulent flow field behind a series of natural, three-dimensional dunes. Free surface levels of the chosen configuration agree well with the measurements. The only shortcoming is found in the amount of calculated turbulent kinetic energy, which is underestimated by a factor of 2.5. For the simulation the two-equation k-ε model is used. It is a stable, robust solution, as well as computationally cheap in comparison to other more-equation turbulence models. On the downside, it is basically only valid for fully turbulent flows and it lacks in the reproduction of severe pressure gradients and strong streamline curvatures. It has also been found that it lacks sensitivity towards adverse pressure gradients (Menter, 1993, 1994). Nonetheless it has been successfully applied in various dune applications including sediment transport (e.g. Tjerry and Fredsøe, 2005; Giri and Shimizu, 2006; Dimas et al., 2008; Amoudry and Souza, 2011) and the quality of the reproduced flow field presented in this chapter recommends it for further morphodynamic simulations.

It can be summarised that apart form the k-ε turbulence model, it is recommended to use the medium or coarse mesh (Table 5.2) for the morphodynamic simulations, which will be presented in Chapter 7. Both mesh sizes are able to represent the main flow features such as recirculation zones and free surface levels. The hydrodynamic results prove to be invariant to vertical resolution (σ-layers), if a logarithmic distribution is chosen which refines towards the bottom. The non-hydrostatic pressure approach needs to be used to gain a quantitatively and qualitatively good match with measured flow field and free surface levels. The roughness height k_s will need to represent grain roughness and small scale bed forms which fall below mesh resolution. It is calculated from grain and ripple form roughness according to van Rijn (1993) to $k_s = 0.003\,95\,\mathrm{m}$ to $0.005\,\mathrm{m}$.

All numerical parameters of the steering file used for the hydrodynamic calculations can be found in Appendix 5.

6

Morphodynamic Model

Contents

The hydrodynamic Telemac-Mascaret modelling system (described in Chapter 4) can be coupled to the morphodynamic module, **Sisyphe**, which calculates bottom evolution via solution of the Exner (1925) equation (Eq. 6.1), as well as sediment transport rates (decomposed into bed load and suspended load). Sisyphe includes various flow and sediment parameters in these calculations (flow velocity, water depth, wave height, grain diameter, relative density, settling velocity, etc.) and also offers a variety of additional effects of physical processes to be included, such as bottom slope, rigid beds, secondary currents and slope failure. A description of the sediment module Sisyphe is given in Weilbeer (2001), Goethel (2008) and Villaret et al. (2013).

6.1 Morphodynamic model

The response of the bottom to the prevailing flow field is of great importance when modelling waterways. Depending on sediment characteristics and soil composition, the bottom is deformed and in return will influence the flow field. The interface between hydro- and morphodynamic systems is the bottom shear stress.

The morphodynamic model of the Telemac system is called Sisyphe. It can be coupled either to Telemac-2D or Telemac-3D or used as a stand-alone programme with imposed hydrodynamic variables. It computes bed-load and suspended-load transport induced by currents, waves and current/waves interaction. Sediment transport rates are decomposed into $x-$ and $y-$direction. They are calculated at each grid point as a function of flow (flow velocity, water depth, wave height, etc.) and sediment parameters (grain diameter, relative density, settling velocity, etc.) (Tassi and Villaret, 2014). The model solves the Exner (1925) bed-evolution equation

$$\frac{\partial z_B}{\partial t} + \nabla \cdot \mathbf{q}_s = \frac{\Phi_m}{\rho_{dep}} \tag{6.1}$$

with:	$\partial z_B / \partial t$	local change of bottom elevation over time
	$\mathbf{q}_s$	sediment transport per meter width $[\mathrm{m}^3/\mathrm{ms}]$
	Φ_m	mass flux between river bed and water column $[\mathrm{kg}/\mathrm{m}^2/\mathrm{s}]$
	ρ_{dep}	density of deposit $[\mathrm{kg}/\mathrm{m}^3]$,

and an additional advection-diffusion equation for the suspended load concentration, if cohesive sediment is calculated. Exner's equation describes the mass conservation of sediment in an infinitesimal small control volume and during an infinitesimally small time step.

The parameter that relates sediment transport to the prevailing flow field is the bed shear stress $\boldsymbol{\tau}_B$. It is calculated from local flow parameters and expresses the force that acts on the bed as well as the resistance the bottom opposes towards the flow. Special attention needs to be given to its calculation, as it is the main link between numerical modules, discussed extensively in 2.2. Inclusion of turbulence into the morphologically relevant bed shear stress is presented in Section 6.2.

Sisyphe further offers the possibility to include the effects of rigid beds, secondary currents, slope failure, etc. via additional formulations. For cohesive sediments, bed consolidation can be taken into account.

One of the main effects on a river bottom with dunes is the effect of sloping bottoms. Most of the bed load formulae have been developed for horizontal bottoms, thus a correction is needed if they are applied in dune environments. A sloping bottom does influence not only the amount but also the direction of sediment transport, mainly due to gravity forces. In Sisyphe the effects are treated separately. Firstly, the transport rate is increased in direction of a downwards slope. This is done by analysing the present angle of longitudinal and transverse slope and calculation of a correction of direction. Secondly, the critical Shields parameter is corrected, as it was found that this threshold changes on sloping beds. It is adjusted based on the direction of the shear velocity, decreasing the amount of sediment transport if the direction of shear velocity points uphill, and increasing the transported amount of sediment on downhill slopes. A third effect, avalanching, accounts for slopes steeper than a critical angle, mostly the angle of repose of the sediment. Exceeding this critical value will trigger sediment displacement in down-slope direction even if the shear velocity is below the limit sediment transport initiation.

6.2 Inclusion of turbulence into bed load transport

The link between hydrodynamic and morphodynamic processes – the stress which the flow exerts onto the bottom – is expressed via the bottom or bed shear stress $\boldsymbol{\tau}$. It is calculated as

$$\boldsymbol{\tau} = \rho \, r \, |\mathbf{u}| \mathbf{u} \tag{6.2}$$

where u is the vector of the velocity u and | | denotes the norm of the vector. Eq. 6.2 is known as the Newton-Taylor law or simply Taylor law (Taylor, 1920; Malcherek, 2009a). r is a proportionality coefficient called Newton-Taylor coefficient.

Coupling Sisyphe to the three-dimensional flow calculation of Telemac, which uses σ-layering, the bottom shear stress is aligned with the near bed velocities. The magnitude of the bed shear stress is related to the near bed velocity

$$u(z') = \frac{u_*}{\kappa} \ln \left(\frac{z'}{z_o} \right) \tag{6.3}$$

where u_* is the friction velocity or shear velocity, z' is the distance of the first vertical σ-layer from the bed level and $\kappa = 0.4$ is the von Kármán constant. $u(z')$ is the velocity at the corresponding first vertical σ-layer above bed level. In this equation z_o is the hypothetical level where the velocity is zero, expressed as a function of the equivalent Nikuradse roughness height k_s

$$z_o = k_s/30 \; . \tag{6.4}$$

For flat beds, it has been shown to be approximately $k_s = 3d_{50}$. In Sisyphe the magnitude of the bed shear stress, τ_o, is calculated from the shear velocity u^* (Villaret et al., 2009), according to

$$\tau_o \;=\; \rho\, u_*^2 \tag{6.5}$$

Inserting Eq. 6.3, Eq. 6.5 transforms to

$$\tau_o \;=\; \rho\; \left(\frac{1}{\kappa}\ln\frac{z'}{z_o}\right)^{-2}\; u(z')^2 \;=\; \rho\, r\, u(z')^2 \tag{6.6}$$

where the coefficient r is

$$r \;=\; \left(\frac{1}{\kappa}\ln\frac{z'}{z_o}\right)^{-2} \tag{6.7}$$

See also Section 2.3 for further details on bed shear stress calculation.

Dunes create a highly turbulent flow field in their wake region. Experiments examining the influence of turbulence on bed load sediment transport, e.g. Sumer et al. (2003), found that the bed shear stress calculated from profiles of averaged velocities, referred to as mean bed shear stress $\overline{\tau}$, is not in accordance with the spatial distribution of sediment transport. In some regions, for example close to the point of reattachment, the mean bed shear stress remains below the critical shear stress for sediment movement – nonetheless sediment movement is recorded. According to Sumer et al. (2003), this must be due to the presence of turbulence. They reasoned that sediment motion was induced not only as a function of the mean bed shear stress due to skin friction (Section 2.3), but also depended on near-bed turbulence. In their experiments Sumer et al. (2003) inserted additional, external turbulence to their experimental flume with a moving bed. The mean bed shear stress, which was calculated from the mean velocities, was maintained the same for the two compared experiments – one with turbulence generators and a second, undisturbed case. Sumer et al. (2003) concluded, that any change of sediment transport must be related to turbulence change added by the turbulence generator. They recorded a remarkable correlation between sediment transport and turbulence in the bed shear stress: with an increase of turbulence by about 20 % the sediment transport was increased by a factor up to 6 for flat bed experiments. For ripple covered experiments the sediment transport increased by factors of 2 - 5 (Sumer et al., 2003). It needs to be noted though, that for higher transport rates and higher velocities they recorded smaller effects on sediment transport by increased turbulence than at lower mean bed shear stress values. But for all experiments the mean bed shear stress needed to be corrected to match the sediment transport rates, if turbulence was added to the experiments.

The hydrodynamics over the dune field have been correctly reproduced (Chapter 5). For morphodynamics it is now necessary to include the effects of unsteadiness of the flow in the highly turbulent flow field around dunes. The velocity field around the dunes is composed of Reynolds-Averaged velocities (see Section 4.2), thus the turbulent motion is not included. In RANS the turbulence of the flow field is contained in the turbulence model. Therefore, in order to receive a total bed shear stress, τ_{tot} needs to be calculated according to

$$\tau_{tot} \;=\; \overline{\tau_o} \;+\; \tau_o' \tag{6.8}$$

The total bed shear stress is now composed of a mean $\overline{\tau_o}$ and a turbulent part τ_o'. The turbulent kinetic energy k

$$k \;=\; \frac{1}{2}\langle u_i' u_i' \rangle \;=\; \frac{1}{2}\langle u'u' \;+\; v'v' \;+\; w'w' \rangle \;=\; \frac{1}{2}\langle u'^2 \;+\; v'^2 \;+\; w'^2 \rangle \tag{3.3}$$

of the flow field contains the flow fluctuations missing in the calculation of tau_o in Eq. 6.6. If they are added according to Eq. 6.8, the following equation is gained

$$\tau_{tot} \;=\; \rho u_*^2 \;+\; \rho\, r\, C\, k\;, \tag{6.9}$$

where $C \,=\, 2.0$ according to Eq. 3.3, where $k \,=\, \frac{1}{2}\langle u_i' u_i' \rangle$. This re-written formulation states that the total bed shear stress is calculated from two components: the first (ρu_*^2) is calculated according to Eq. 6.5 from the mean velocities of the flow field. The second term ($\rho\, r\, 2\, k$) is calculated from the turbulent kinetic energy of the flow field to include the effects of the unsteady flow in the highly turbulent flow field of the dunes.

Other approaches considering the turbulent kinetic energy of the flow field to calculate the bed shear stress also use coefficients or proportionality factors for the turbulent kinetic energy, see Section 2.3. An example is the approach of Soulsby (1983), Eq. 2.7, which considers k as the only flow induced variable. The formulation uses the proportionality constant $C_1 = 0.19$. This TKE method of Soulsby (1983) has found its application mostly in oceanography (Biron et al., 2004) and tests to obtain a u_* using this formulation have been conducted as well (McLelland and Nicholas, 2000). Chapter 7 will provide further discussion and tests of the dimensions of the proportionality coefficient, also comparing the dimension of r with C_1. Also see Appendix 2 for more details.

6.3 Bed load formula

The fundamental equation to describe bottom evolution is the equation of Exner (1925) (Eq. 6.1). Discussions on usefulness and stability of this hyperbolic equation have been presented (e.g. Kubatko and Westerink, 2007) and other approaches applying the Exner equation on the scale of single grains claim to be more effective (Coleman and Nikora, 2009). Recently a pre-study for a stochastic application has been presented by Audusse et al. (2015). Nonetheless in the Telemac-Sisyphe suite no option other than the classic formulation of the Exner equation is available. Various extensions, such as slope and deviations effects, can be incorporated. Also a the variation of bed load (and suspended load) transport formulae is possible.

Bed load formulae can be categorised in four groups (Marburger, 1999): (1) *stochastic approaches and regression models*, (2) *formulae of regime theory*, (3) *energy models* and (4) *shear stress or threshold formulae*. The most famous formula of Meyer-Peter and Müller (1948) falls, for example, into the threshold formula category.

The formula of Meyer-Peter and Müller is widely used but it was found that it over-predicts the transport capacity for sediment with grain size smaller than gravel (d < 2 mm) (Henning, 2008; Malcherek, 2009a). Also one has to keep in mind that it is an empiric formulation – similar to all transport formulae implemented into the Telemac-Mascaret system – based on certainly numerous but nonetheless physically artificial experiments.

No satisfactory results were obtained with this transport formula for the dune experiments in this thesis. Instead the formulation of Engelund and Hansen (1967) proved to be successful when modelling the movement of the dunes. The formula is a total load formula (it computes bed load and suspended load) and recommended for rivers (including those with dunes) and fine sediments ($0.2\,\mathrm{mm} < d_{50} < 1\,\mathrm{mm}$). The model can be assigned to the family of energy models: it is based on an energy balance analysis for bed and suspended load. It is assumed that the sediment is transported in a characteristic height Δ and over a certain length λ, and also over bed forms such as ripples and dunes. Thus the energy needed to lift the sediment up to height Δ is calculated (Malcherek, 2009b). It is one of the few sediment transport formulae that does not include any sort of critical value for the initiation of sediment transport. Even though this formula indirectly includes all sorts of bed forms using this approach, it should be noted that generally the total load formulae should only be used in quasi steady and uniform flow (Tassi and Villaret, 2014).

Implementation of the total load formula of Yang and Lim (2003)

An additional transport formula has been implemented into Sisyphe and proved successful when modelling dunes. The bed load formula of Yang and Lim (2003) is also a total load formula, based on the concept that under natural flow conditions there is often no sharp distinction between suspended and bed load transport. Hence, both types of load are computed together and expressed in a total load transport parameter T_T. This ensures that threshold fractions, and their movement, are not disregarded in the transition from bed to suspended load. As presented in their paper T_T reads

$$\theta_s \;=\; K \left(\frac{\gamma_s}{\gamma_s - \gamma}\right) \tau \left(\frac{u_*^2 - u_{*c}^2}{\omega_g}\right) \;=\; K\, T_T \tag{6.10}$$

with:		
	θ_s	total bed load $[\mathrm{m^3/s}]$
	K	constant equal to 12.5
	γ_s, γ	specific weight of sediment and water $[\mathrm{N/m^3}]$
	τ	bed shear stress $[\mathrm{N/m^2}]$
	u_*	effective grain shear velocity $[\mathrm{m/s}]$
	u_{*c}	critical shear velocity for sediment movement $[\mathrm{m/s}]$
	ω_g	grain settling velocity as proposed by Cheng (1997) $[\mathrm{m/s}]$
	T_T	total transport parameter.

ω_g, the grain settling velocity, is presented by Cheng (1997) in his paper as

$$\omega_g \;=\; \frac{\nu}{d} \left(\sqrt{25 + 1.2 d_*^2} - 5\right)^{1.5} \tag{6.11}$$

with:		
	ν	kinematic viscosity $[\mathrm{m^2/s}]$
	d	particle diameter $[\mathrm{m}]$
	d_*	dimensionless particle diameter [-].

Transforming Eq. 6.10 to a notation conformal with the Sisyphe manual and code structure, the transport formula takes the following form

$$\Phi_b \;=\; 12.5\, \frac{d}{\rho_s \omega_g}\, \tau \, (\Theta' - \Theta_c) \tag{6.12}$$

with: d grain diameter $[\mathrm{m}]$
ρ_s density of the sediment $[\mathrm{kg/m^3}]$
ω_g grain settling velocity $[\mathrm{m/s}]$
Θ' non-dimensional effective shear velocity [-]
Θ_c non-dimensional critical shear velocity [-].

The formula proved successful when modelling dunes in the settings of this work. Both applied formulae of sediment transport do not include a threshold (fraction) and consider gravitational factors such as lift-energy and settling velocity. Through this the smooth transition between bed and suspended load is regarded. See Appendix 3 and Section 7.2 for further details.

6.4 Slope and deviation formula

Classically bed load and total load formulae are designed for flat beds. For transport over bed forms, where bed slopes are higher, correction factors can be applied. These corrections are supposed to adjust the transport in such a way as to reduce it in up-slope direction and increase it in the down-slope direction. This correction happens on the solid transport rate, before the bed evolution equation (Eq. 6.1) is solved. The changes can be directed towards the magnitude (*slope*) as well as the direction (*deviation*) of the solid transport rate. The following section gives an overview of existing deviation correction formulae of Sisyphe.

Slope effect formula

Koch and Flokstra (1981)
With this correction method, the intensity of the solid transport Q_{so} rate is multiplied by a coefficient $c_{\texttt{coef}}$

$$Q_s = c_{\texttt{coef}} Q_{so} \tag{6.13}$$

to receive the corrected intensity of sediment discharge Q_s. $c_{\texttt{coef}}$ is calculated according to

$$c_{\texttt{coef}} = 1 - \beta \frac{\partial z}{\partial s} \tag{6.14}$$

with: β empirical factor (default value 1.3) $[-]$
$\partial z / \partial s$ change of bottom slope in flow direction $[-]$.

This procedure tends to reduce instabilities and smooths the results (Tassi and Villaret, 2014).

Deviation formula

The deviation correction, the coefficient T, changes the calculation of direction of solid transport in relation to the flow direction, α, following the relation

$$\tan\alpha \;=\; \tan\delta \;-\; T\frac{\partial z}{\partial n} \tag{6.20}$$

with:		
	δ	direction of bottom stress in relation to the flow direction $[-]$
	z	bottom height $[\mathrm{m}]$
	n	coordinate along the axis perpendicular to the flow $[-]$.

See Tassi and Villaret (2014) for further details.

Koch and Flokstra (1981)

According to this formulation the deviation coefficient T applied in Eq. 6.20 depends on the Shields parameter θ in the following way

$$T \;=\; \frac{4}{6\theta} \tag{6.15}$$

Implementation of the slope effect and deviation correction formula of Apsley and Stansby (2008)

The slope effect and deviation model proposed by Apsley and Stansby (2008), which was adapted by Stansby et al. (2009) for depth-averaged shallow water equation models, is based on the concept of “effective” shear stress, which is a modified shear stress that includes a bed slope contribution. The formulation has also been presented by Chini (2009).

The new “effective” shear stress in x- and y-direction is calculated as

$$\theta_x \;=\; \theta\cos(\delta) \;-\; \lambda\frac{\partial z_B}{\partial x}\cos^2(\beta) \tag{6.16}$$

$$\theta_y \;=\; \theta\cos(\delta) \;-\; \lambda\frac{\partial z_B}{\partial y}\cos^2(\beta) \tag{6.17}$$

where $\theta_{x,y}$ is the Shields parameter in x- and y-direction, δ is the direction of the bed shear stress and z_B is the bottom elevation. The factor λ is calculated from the critical Shields parameter θ_c and the angle of repose ϕ

$$\lambda = \frac{\theta_c}{\tan\phi} \tag{6.18}$$

The slope angle $cos\beta$ is calculated from the x- and y-components of the bed gradient as

$$\cos\beta = 1/\sqrt{1 + (\partial z/\partial x)^2 + (\partial z/\partial y)^2} \tag{6.19}$$

In Sisyphe, deviation and slope effect are changed separately by calculating individual coefficients – one for direction and one for magnitude of shear stress (or critical shear stress, respectively). In the notation used in the Sisyphe manual (Tassi and Villaret, 2014) the deviation $\tan\alpha$ takes the form of

$$\tan\alpha = \tan\delta - T\frac{\partial z_B}{\partial n} \tag{6.20}$$

where α is the direction of solid transport in relation to the flow direction, δ is the direction of bottom stress in relation to the flow direction and n is the coordinate along the axis perpendicular to the flow. In this notation the deviation change proposed by Apsley and Stansby (2008) is

$$T = \frac{\theta_c \cos^2\beta}{\tan\phi} \tag{6.21}$$

The change of magnitude (slope effect) has the magnitude $\cos\ \beta$.

Details of the implementation into the Telemac-Mascaret system can be found in Appendix 4. Apsley and Stansby (2008) and Stansby et al. (2009) also presented an avalanche model, which has been included into the code as well. Sisyphe already posses an avalanching model in the existing code. As tests have shown no improvement in results when using the avalanching model of Apsley and Stansby (2008) instead of the formula implemented in Sisyphe, it is not used in the presented calculations. Results of the implementation of the slope and deviation formula by Apsley and Stansby (2008) can be found in Section 7.4.

7

Numerical Movable Bed Experiments

Contents

Engelund and Fredsøe (1982) said “It has been a continuous challenge to scientists to determine why the bed forms grow and change from one form to another and yet remain stable for a given set of flow and sediment conditions”. Southard (1991) stated “Generations of scientists and engineers have marvelled at the rich and confusing variety of these features”. These two quotes still describe the challenge that bed forms present engineers and modellers.

Thus, this chapter summarises the knowledge gained during the hydrodynamic part of the research project in Chapter 5 and applies it to morphological studies. It is expected that a flow field, agreeing with the physical experiments, which interacts with a moveable bottom, will produce equally correct, morphodynamic results. To enable the coupling process, the bed shear stress is used as the link between hydro- and morphodynamic processes. This chapter will be used to investigate, which hydrodynamic parts of a complex, numerical system are actually responsible for producing dune forms in a moving bottom.

Numerical simulations of dunes in an experimental flume presented in Section 3.3 are conducted. Results of dune shape analysis have been presented in Section 3.3.3. These are now used for comparison with morphodynamic simulations, where Telemac3D is used in combination with the morphodynamic module Sisyphe. Several key-parameters are selected. A focus is on the inclusion of turbulent kinetic energy of the flow into bed shear calculation (Section 7.5). The last Section 7.6 summarises and evaluates the morphodynamic model results and the best parameter combination is chosen for the following river model simulations in Chapter 8.

The morphological experimental data used for this thesis has been gained in the same experimental flume as the experiments of Chapter 5. They were conducted at BAW in cooperation with the Leichtweiß Institute of the University of Braunschweig, Martin Henning through the Ph.D. thesis 2013. This work showed "... the benefits of statistical analysis for a practical description of dune surfaces and at developing a suitable methodology to contribute to the understanding of three-dimensional transport processes over dunes". The morphological measurements have been provided for comparison with the numerical results in this thesis.

The morphodynamic simulations presented in this thesis are summarised in Table 7.1. Computing times for the medium mesh are 86 h for a simulated time period of 24 h. The calculations were performed on 96 processors. The coarse mesh has computing times of 30 h for 24 h of simulated time on 32 processors. Simulations are performed on the high-performance cluster of BAW, a bullx blade B510 series, containing 126 nodes with 2 CPUs each. Each CPU contains 16 processors.

All morphodynamic simulations start from a flat bed, taken from photogrammetric measurements, see time step $0\,\mathrm{h}$ in Fig. 3.17. Inflow into the flume is the same as in the physical experiments discussed in Chapter 3.

Morphodynamic boundary conditions are discussed in Section 7.2.1, hydrodynamic boundary conditions in Section 7.3.

Table 7.1: Overview of calculations presented in this chapter - data set number (No.) with corresponding parameter configuration

No.	bed load[1]	slope eff.[2]	deviation eff.[3]	k incl.[4]	k fact.[5]	mesh[6]
1	Engl.-Hans.	Koch-Flok.	Apsl.-Stans.	no	no	coarse
2	Engl.-Hans., Yang	Koch-Flok., Soulsby, Apsl.-Stans.	Koch-Flok., Talmon, Apsl.-Stans.	no	no	coarse
3	Engl.-Hans.	Koch-Flok.	Talmon	no	no	coarse
4	Yang	Koch-Flok.	Apsl.-Stans.	no	no	coarse
5	Engl.-Hans.	Koch-Flok.	Apsl.-Stans.	yes	no	coarse
6	Engl.-Hans.	Koch-Flok.	Apsl.-Stans.	yes	no	medium
7	Engl.-Hans.	Koch-Flok.	Apsl.-Stans.	yes	yes	coarse

[1] bed load formulae of: Engelund and Hansen (1967) and Yang and Lim (2003)

[2] slope effect formulae of: Koch and Flokstra (1981), Soulsby (1997), Apsley and Stansby (2008)

[3] deviation effect formulae of: Koch and Flokstra (1981), Talmon (1992), Apsley and Stansby (2008)

[4] inclusion of turbulent kinetic energy into bed shear stress calculation, see Section 7.5

[5] factorised turbulent kinetic energy in bed shear stress calculation, see Section 7.5

[6] coarse or medium mesh resolution (Section 7.3)

7.1 General results

7.1.1 Free surface elevation

As previously mentioned in Chapter 5, a comparison of the water levels, continuously measured during the physical experiments, can be used for the verification of the accuracy and forecasting ability of the numerical results at predicting observed values. Figure 7.1 shows water levels of the physical moving bed experiments. The water levels were recorded at 15 water level measuring points (compare also Figure 3.2). The graphs show values for water levels of nine runs (referenced as S6, S9, S10 in Haber et al. (2014), first 6–24 h), each averaged over the course of 6 h. Additionally, the minimum and maximum values for each run are displayed (grey), marking the expected range of results from the numerical model. These minimum and maximum values provide a confidence interval of $\pm 0.004\,\mathrm{m}$.

In the graphs of the free surface measurements over a fixed bed, which were displayed in Chapter 5, one notices the absence of bed forms tracing onto the free surface. This can easily be explained by the length of the averaging time period: in Figure 7.1 each line represents a time frame of 6 h. During this time several bed forms have passed each measuring point with an average speed of about $1.5 \times 10^{-4}\,\mathrm{m/s}$ (Henning, 2013), thus providing a smoothed, mean result. The small outliers at measuring point P11 and P13 ($x = 21.15\,\mathrm{m}$ and $x = 25.15\,\mathrm{m}$) arise from inaccuracies in the measurements and problems with the devices at these points. These can be safely ignored.

Figure 7.2 (top and bottom) shows free surface levels of morphodynamic simulations in comparison to selected free surface level measurements. For comparison the global maximum and minimum of all measured free surfaces have been selected (grey dashed). Additionally, an average measured free surface level is displayed (blue dashed). The free surface levels of the numerical, morphodynamic results are extracted at the middle of the flume at y=$1\,\mathrm{m}$ and

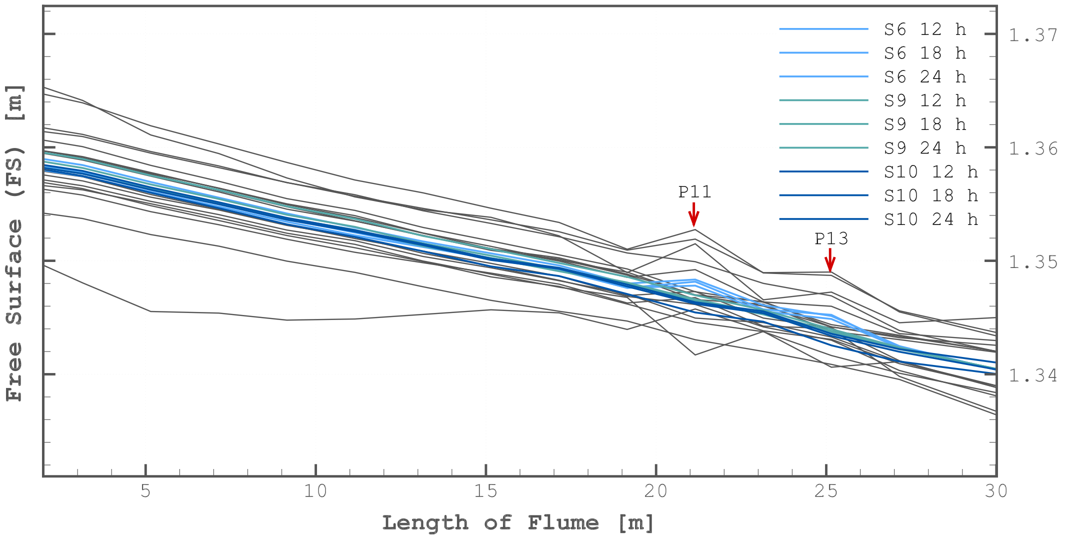

Figure 7.1: Average measured free surface elevation [m] of measurement series S6, S9 and S10 (each after 6, 18, 24 h) in Haber et al. (2014), see also Tbl. 3.1. The grey lines display the maximum and minimum values of each run, providing a range for comparison with numerical results

dune forms trace to the free surface. The straight lines are a linear fit of the same results and represent the mean free surface slope.

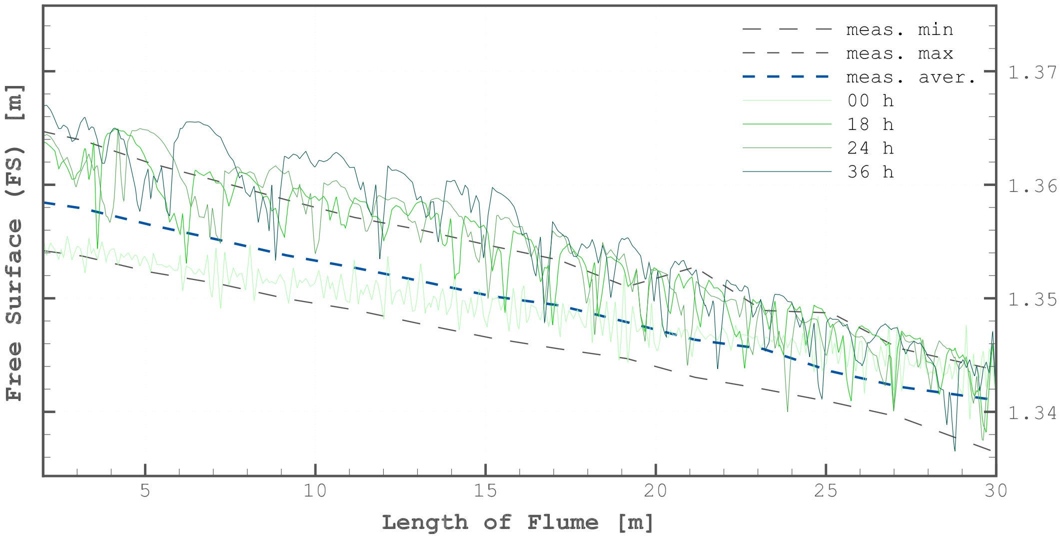

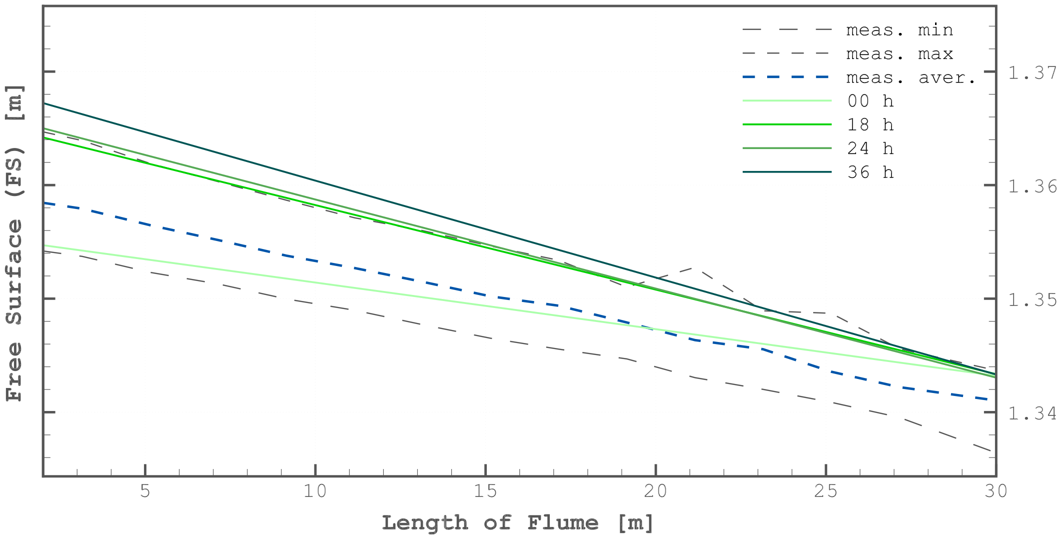

Figure 7.2: Average measured free surface elevation (meas. aver.) and minimal and maximal extents (meas. min/max) [m] of selected measurements of Fig. 7.1 (dashed), in comparison to simulations after 0, 18, 24 and 36 h (no additional bed load factor). Top figure shows non-smoothed free surface levels, where dunes trace to the free surface; bottom figure shows a linear fit of the same results and represent the mean free surface slope. Data set No. 1 of Table 7.1

For a clearer arrangement, only the mean free surface levels of the simulations are displayed in Figure 7.2 (bottom). It shows that at the beginning of the simulation a bottom without dune forms produces a different slope of the water level as the physical experiments, which already contain dunes. After 18 h of simulation, the numerical dunes have grown, and the free surface level is raised. The calculated free surface slope matches the measured values, the level is similar to top range of the measurements. The free surface level at the outflow boundary is set to $z = 1.341\,\mathrm{m}$, which corresponds to the setting of the physical experiment. The non-smoothened free surface levels (top) agree with the measurements at the outflow ($x = 30\,\mathrm{m}$). The roughness height is calculated from the mean diameter d_{50}, see Section 3.3.1, according to $k_s = 0.002\,82\,\mathrm{m} = 3 \cdot d_{50}$. It is slightly lower as the one established in Chapter 5. Nonetheless, a free surface elevation is produced which reaches quantitative and qualitative agreement with the highest free surface levels of the measurements. After the dunes are established, this elevation remains constant. In order to lower the simulated free surface level to the medium level of the measurements, a drastic lowering of the outflow level or roughness height would be necessary. Both procedures are out of range of physical values and are thus not feasible.

It can be summarised that the water levels of the experiments remain constant during the presented time frame, whereas the water levels of the numerical simulations rise to a higher level. This behaviour is related to an increasing roughness of the bottom.

7.1.2 Analysis of dune parameters

Mean length, height, skewness and kurtosis are standard parameters for evaluating dune fields (Coleman et al., 2011). The skewness of a dune field is the 3rd order moment of a spatial series divided by the cube of the standard deviation σ

$$Sk = \langle \alpha'^3 \rangle / \sigma^3 \tag{3.5}$$

It is a measure for the symmetry of a spatial series relative to the normal distribution. The general shape or form of the bed surface is represented by the skewness value (Friedrich et al., 2006; Coleman et al., 2011). Dune fields are associated with a negative skewness and these dunes will have a long, convex upwards stoss-side slope and a relatively steep and short lee-side face, see also Section 3.3.3.

The kurtosis is the 4th order moment divided by the standard deviation to the power of 4

$$Ku = \langle \alpha'^4 \rangle / \sigma^4 - 3 \tag{3.6}$$

A calculated kurtosis value is normally corrected by subtracting 3, so that a normal distribution has a value of zero. A train of triangular, identical waves following each other will have a negative kurtosis, whereas bed waves that are widely spread on a flat bed have a large and positive kurtosis (Coleman et al., 2011).

Figure 7.3 shows a plot of skewness and kurtosis values calculated from experimental runs and selected numerical results against results of data sets by Friedrich et al. (2006). It is clear that the simulated dune parameters do not generally follow the ones of the experimental results, but tend to gather in a region of coarser sand dunes and of fine sand ripples. The simulated

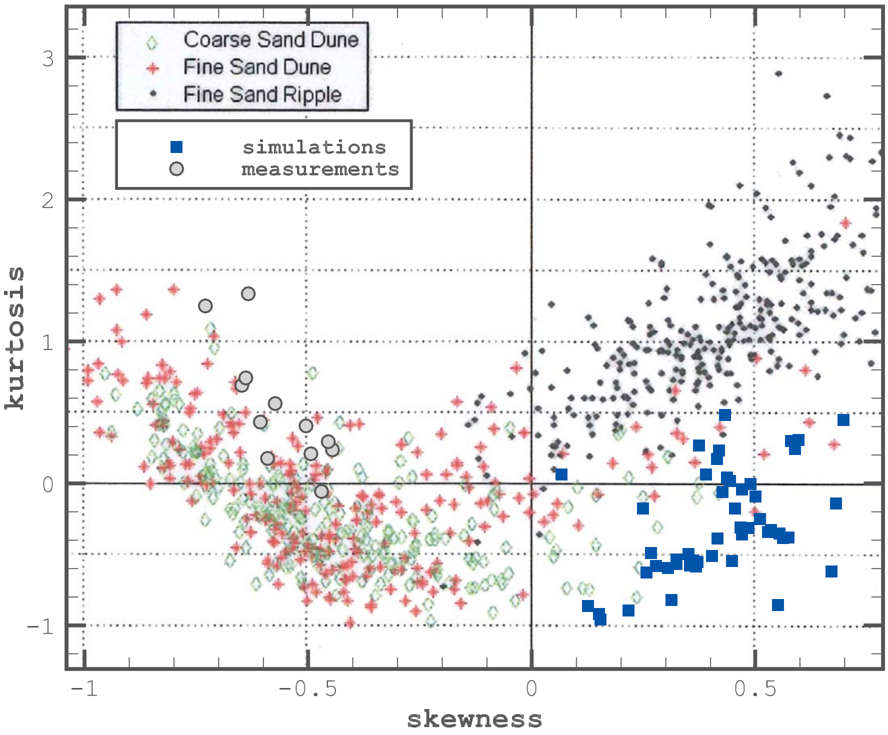

Figure 7.3: Skewness and kurtosis values of morphodynamic calculations with a variety of bed load, slope and deviation formulae, compared to values of the experimental data sets as well as to data sets of coarse and fine sand dunes and ripples by Friedrich et al. (2006; modified). Data sets No. 2 of Table 7.1

dunes have a skewness values afflicted with a positive algebraic sign, where as the experimental dunes have a negative one. Only absolute value is the same. As discussed in Section 5.3, the data sets of the physical experiments contain small scale bed forms: small ripples or sand sheets, that ride on the stoss-sides of the dunes and are too small to be represented on the numerical mesh used for morphodynamic calculations. They are parametrised in the hydrodynamic model only through the roughness height. But these small scale, superimposing bed forms are part of the total bed form shape, providing the bed form with its convex shape on its stoss-side. If the forms are not displayed directly on the mesh, these volume and shape-giving additional forms are missing in the overall shape and their volume is not included when calculating the bed form parameters. Their absence therefore might provide an explanation for the off-set of the skewness values of the numerical results.

Comparing mean dune heights and lengths of the simulations with the experimental ones (Fig. 7.4), only for some results a better quantitative and qualitative agreement can be reached. The numerical results presented in Figure 7.4 have been obtained through a choice of different bed load formulae, slope and deviation formulae, and other minor parameter variations (see Table 7.1). All simulations were conducted over 18 h. The created bed forms reach 66 % of the mean height of the experimental ones. They have a tendency to be elongated: in average they are 9 % longer as their experimental counterparts.

The difference in free surface elevation compared to the experimental results is attributed to different dune forms in the simulations, as for the hydrodynamic tests over fixed, naturally formed dunes a good agreement with the water level of the physical experiments has been reached (Chapter 5). The simulated dunes have different dune-form characteristics, such as skewness and kurtosis, which might be attributed to the numerical process necessary when forcing natural forms onto a (finite element) mesh. Further, no data of the flow field is available over the moving dunes. Hence it cannot be ruled out that the experiments with a moving bottom produce locally different velocity profiles compared to the fixed dune experiments. Several studies (e.g. Sumer et al., 2003; Schindler and Robert, 2005; Naqshband et al., 2014a) have shown the existence of a feedback between flow field and a moving bottom. Nonetheless, the provided numerical morphodynamic system offers variable combinations, where the two main characteristic dune parameters can be successfully matched with the physical experiments. In the following sections these combinations are used for further improvements.

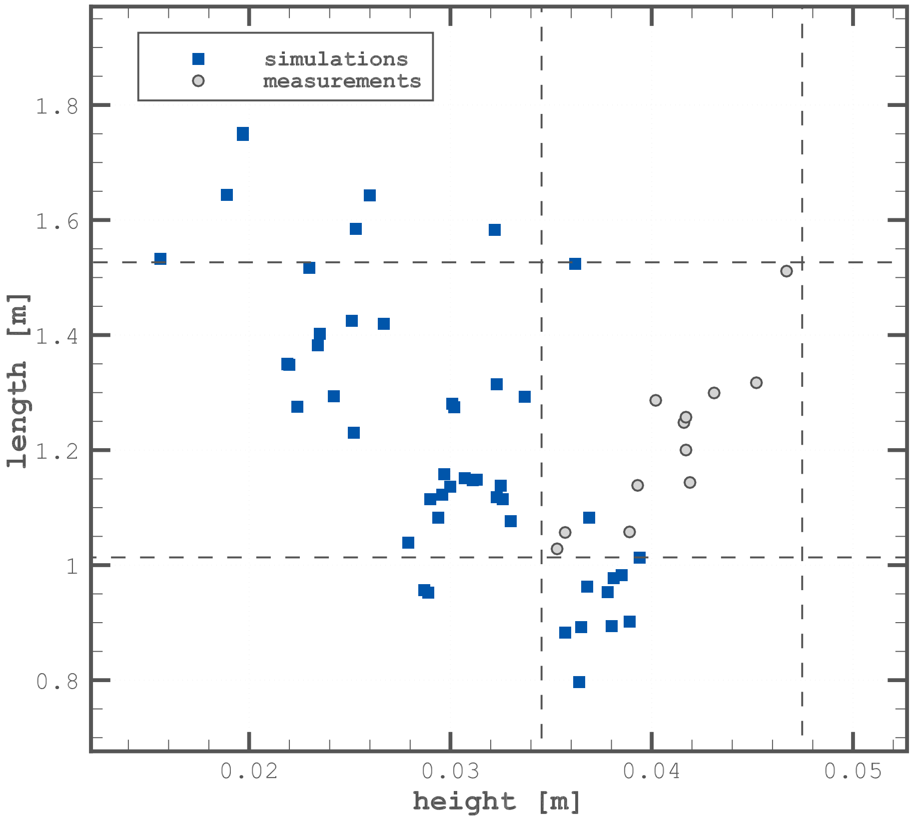

Figure 7.4: Average lengths and heights of morphodynamic calculations with a variety of bed load, slope and deviation formulae (squares), compared to values of the experimental data sets (circles). Data sets No. 2 of Table 7.1

7.2 Bed load formula

Several transport formulae exist, most of them are semi-empirical, and ten are implemented in Sisyphe (release v6p3): Meyer-Peter and Müller (1948), Engelund and Hansen (1967) plus a version modified by Chollet and Cunge (1979), Einstein-Brown (1950), Soulsby (1997), van Rijn (1984a), Hunziker (1995), Bijker (1968), Bailard (1984) and Dibajnia and Watanabe (1992). As the Telemac-Sisyphe system covers a broad spectrum of applications, not all of these formulae can be used for the purpose of modelling dunes in rivers.

The formulation of Engelund and Hansen (1967) is effective when modelling dune development and movement. It is a total load formula (bed load and suspended load in one formula) recommended for rivers and fine sediments, which might also contain dunes. The formula of Yang and Lim (2003) is a total load formula as well, thus not containing a threshold (fraction) and additionally considering grain settling velocity. For further details see Section 6.3.

7.2.1 Bed load discharge and input

In the numerical model, two different approaches are used to simulate the sediment input into the model. Sediment is inserted discontinuously over a time frame of 5 – 10 minutes every hour in the experimental flume (see Section 3.3). For a correct representation in the simulations, for a first approach the bottom is raised over a defined time frame and at defined nodes of the mesh, until a given sediment volume is added to the flume. With this method, sediment mounds are created at the inflow zone, which are transported into the flume over time (Goll, 2011). As a second approach, continuous sediment input is simulated by applying an equilibrium boundary condition for the bottom at the inflow boundary. The added sediment has the same properties as the bed material of the flume.

The numerical model is sensitive to the different sediment input methods. This is not surprising: Mendoza et al. (2015) analysed the influence of sediment transport boundary conditions on the results of numerical modelling of bed morphodynamics. They conducted their tests with Telemac-2D and

Sisyphe and showed that the sediment transport conditions on the boundary strongly influenced the numerical results. Khosronejad and Sotiropoulos (2014) also found that boundary conditions, such as sediment recirculation, influenced the form and development-period of the dunes in their experiments. Numerical models of straight and simple experimental flumes are strongly influenced by the boundary conditions. Installations such as groynes or revetments will dominate the flow field and boundary conditions will lose their influence. Also – proportionally – the zone in the vicinity of boundaries is much larger in experimental flumes than in a field scale river model. Thus, the influence of the boundary conditions in an application of river scale (see Chapter 8) is much less than for a flume model. For the flume experiments it was essential to represent the physical experiments as closely as possible to obtain comparable results. For the upstream part of the flume, which also influences the subsequent part, the discontinuous input method delivers the best results.

Dune bed migration, or the movement of the mean bed respectively, can be validated by comparing the total sediment discharge at the end of the flume. The sediment balance is analysed over 36 h of simulation time. It shows that the mean sediment output, averaged over 36 h, differs depending on the numerical configuration. For a run with the total load formula of Engelund and Hansen (1967) the mean sediment discharge is $10\,\mathrm{kg/h}$ averaged over 36 h of simulation time. The added amount of sediment (recorded at a cross section located $2\,\mathrm{m}$ downstream of the inflow of the flume) is $18.6\,\mathrm{kg/h}$ with the discontinuous sediment input method.

For their total load formula, Engelund and Hansen (1967) calculate the non-dimensional sediment discharge Φ_s in relation to the non-dimensional Shields stress θ in the form of

$$\Phi_s \sim \theta^{5/2}$$

They obtained a proportionality factor from experiments that is comprised of dunes, transition, standing waves, anti-dunes and chute-and-pool flow. The proportionality factor was found to be 0.1, thus giving

$$\Phi_s = 0.1\,\theta^{5/2} \tag{7.1}$$

and this formulation is implemented in Sisyphe (Tassi and Villaret, 2014).

Sediment discharge rates calculated with the formula of Engelund and Hansen (1967) are compared to mean discharge rates of the physical experiments (see Table 3.5 for values of the physical experiments). It shows that the calculated sediment output as well as input are under-predicted by factor 2.0. Following this, the bed load discharge formulation of Engelund and Hansen is corrected, similar to the coefficient that is used in the formulation of Meyer-Peter and Müller (1948), and multiplied by 2.0. This results in a corrected formulation given in Eq. 7.2.

$$\Phi_s \;=\; 0.2\,\theta^{5/2} \tag{7.2}$$

The justification of this approach is that the proportionality factor of 0.1 is not valid for the dune regime in this experimental flume. Figure 7.5 displays the bottom topography calculated with the bed load formula of Engelund and Hansen (1967) after 18 and 36 h. The first one (top, after 18 h) is calculated with an additional bed load proportionality factor of 2.0. The second one (bottom, after 36 h) is calculated without a bed load factor correction. Figure 7.6 shows a differential plot of the two runs. From this it follows that the dunes are similar in dimension and that the position of the dune crests is changed only by $0.1\,\mathrm{m}$ to $0.3\,\mathrm{m}$ in flow direction. Thus, either the transport formulae can be corrected by multiplying it with an additional proportionality factor, or the simulation-time can be corrected by the same factor. The runs of Fig. 7.5 can be compared to the experimental run after 18 h in Fig. 3.17.

Calculation with Eq. 7.2 results in a sediment output of $19.4\,\mathrm{kg/h}$, which is the expected doubling of the amount. The system records an input of $20.6\,\mathrm{kg/h}$ using the discontinuous sediment input method. If a continuous sediment input method is chosen, the output is in the same range ($23.6\,\mathrm{kg/h}$), but the

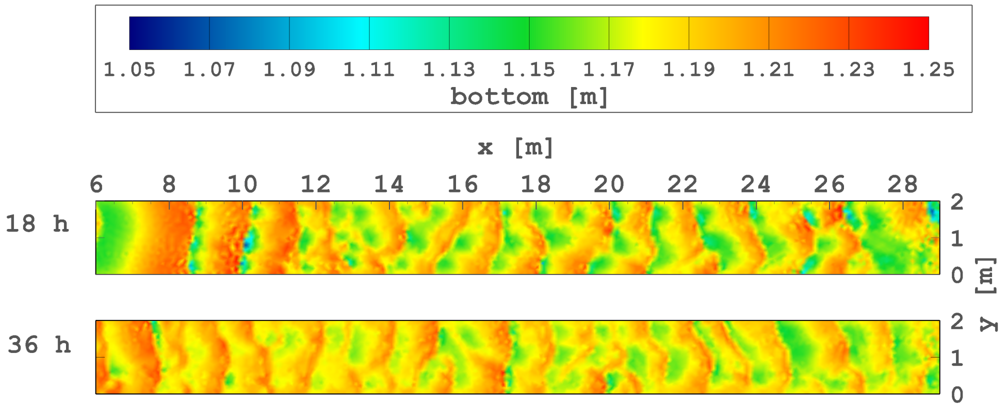

Figure 7.5: Bed load simulation after 36 h (bottom) and after 18 h, where the bed load formulation is corrected with a proportionality factor of 2.0 (top). Compare to experimental run after 18 h in Fig. 3.17. Data set No. 5 of Table 7.1

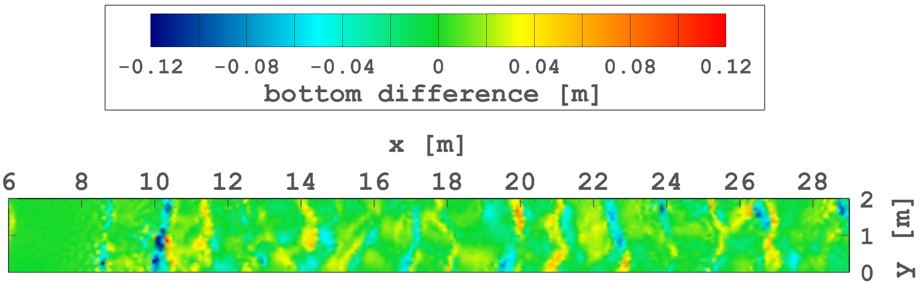

Figure 7.6: Differential plot of the runs shown in Fig. 7.5

input drops to $15.4\,\mathrm{kg/h}$. This means, that the discontinuous sediment input method does not correspond with a sediment equilibrium at the inflow boundary. Using the discontinuous sediment input method, similar to the one used in the experimental flume, will provide better comparability with experimental results.

For a correct output, the original formulation of Yang and Lim (2003) needs to be fitted with a proportionality factor of 1.75. This results in a mean output of $23.4\,\mathrm{kg/h}$. Following this, the formula of Yang and Lim (2003) (Eq. 6.12) is changed to

$$\Phi_b \;=\; 22\,\frac{d}{\rho_s \omega}\,\tau\,\left(\Theta' - \Theta_c\right)\;. \tag{7.3}$$

One has to note though, that both formulations deliver bed load discharges that lie in the broad range of the physical experiments (see Table 7.2), even without a correction of the transport formula through a proportionality factor.

Further the validating comparison, presented in Figures 7.5 and 7.6, allows to either correct the proportionality factor of the bed load formula or the simulation-time of results calculated without a corrected proportionality factor in the bed load transport formula. Unless mentioned otherwise, the results presented in the following sections have been gained with the standard formulation. Adjusted formulations will be referenced.

Table 7.2: Bed load discharges rates in [kg/h], Q_s without and Q_s^* with factorised transport formula in the simulation

	Q_s [kg/h]	Q_s^* [kg/h]
Englund & Hansen	10.0	19.4
Yang & Lim	13.4	23.4
measurements mean (range)	20.0 (15.6 - 27.4)	

7.2.2 Analysis of dune parameters

Figures 7.7 and 7.8 show the bottom of the flume generated with the formula of Engelund and Hansen (1967) and Yang and Lim (2003). The calculations are performed without an additional proportionality factor in the transport formulae. Flow is from left to right. From a flat bed the bottom starts to develop ripple-like structures, that soon form to have a more dune-like shape. After approximately 15 h a steady state is reached, where the dunes move continuously through the length of the flume. For comparison measurements are shown after 6 h (corresponding to 12 h of simulation time) and 12 h (corresponding to 24 h of simulation time). The initial state of the bottom (0 h) is the same as the experimental dune bottom at the start of the experimental runs (see Fig. 3.17). It does not influence the final dune forms, simply speeds-up the process of development. The differences between the two bed load formulae are apparent: the formula of Engelund and Hansen (1967) (Fig. 7.7) creates shorter dunes, whereas with the formula of Yang and Lim (2003) the flume has larger zones where the dunes are slightly more disordered. Visually the bottom created with the transport formula of Engelund and Hansen (1967) agrees better with the measured dune bottom after 12 h of measured time (24 h of simulation). Tables 7.3 and 7.4 show the development of the dune parameters in the simulations of Figure 7.7 and 7.8.

In Table 7.5 the mean length and height, steepness, skewness and kurtosis of the simulated dunes after 24 h are compared to results of the physical experiment. It clearly shows as well that the results obtained with the formula of Engelund and Hansen (1967) are in the range of the measurements for the dune length and height. The dunes obtained with the formula of Yang and Lim (2003) are flatter and longer than their physical counterparts and their steepness is too low. The differences in length and height obtained with both formulae can also be seen in Figures 7.7 and 7.8. Both dune form parameters of the calculated dune fields, skewness and kurtosis, show some shortcomings. The kurtosis values calculated using the bed load formulae of Engelund and Hansen (1967) as well as Yang and Lim (2003) are lower than the minimum value of the measured data sets (Table 7.5). Thus the simulated dunes are too regularly distributed, and single dune forms of the simulation do not differ greatly from each other. The kurtosis values of the simulated dune fields are values of two-dimensional dunes. Three-dimensional dunes have a wider form spectrum in a dune field and thus would produce a higher kurtosis value. The opposite algebraic signs (positive instead of negative) of the skewness values

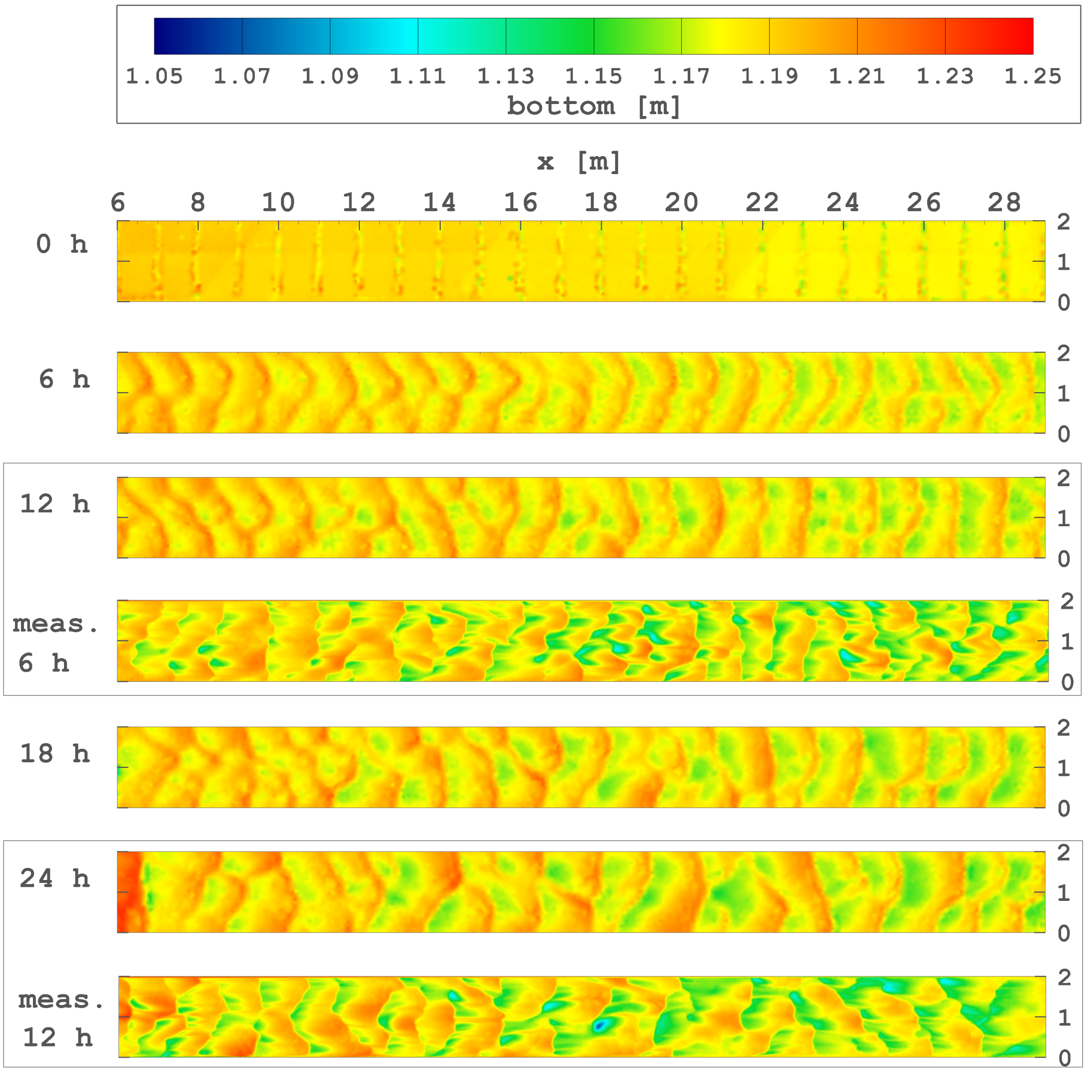

Figure 7.7: Bottom elevation of simulation with total load formula of Engelund and Hansen (1967), 0–24 h and corresponding measurements (connected with boxes). The flow is from left to right. Data set No. 1 of Table 7.1

which exist for both transport formulae denote that the bed forms have a lee-side, that is too weakly developed and might have a more concave stoss-side instead of a convex, upwards one. The displacement in skewness and kurtosis values has been already displayed in Figure 7.3. It has previously been discussed that one reason for this shortcoming might be the missing small scale bed forms, which are not directly displayed on the numerical mesh, but need to be parametrised in the roughness height.

Table 7.3: Dune parameters of simulations with formula of Engelund and Hansen (1967) after 6, 12, 18, 24 h, no correction of bed load formula

	height [m]	length [m]	skewness	kurtosis	steepness
6 h	0.023	0.964	0.285	-0.807	0.024
12 h	0.028	1.071	0.323	-0.733	0.026
18 h	0.030	1.122	0.304	-0.595	0.027
24 h	0.033	1.237	0.269	-0.659	0.027

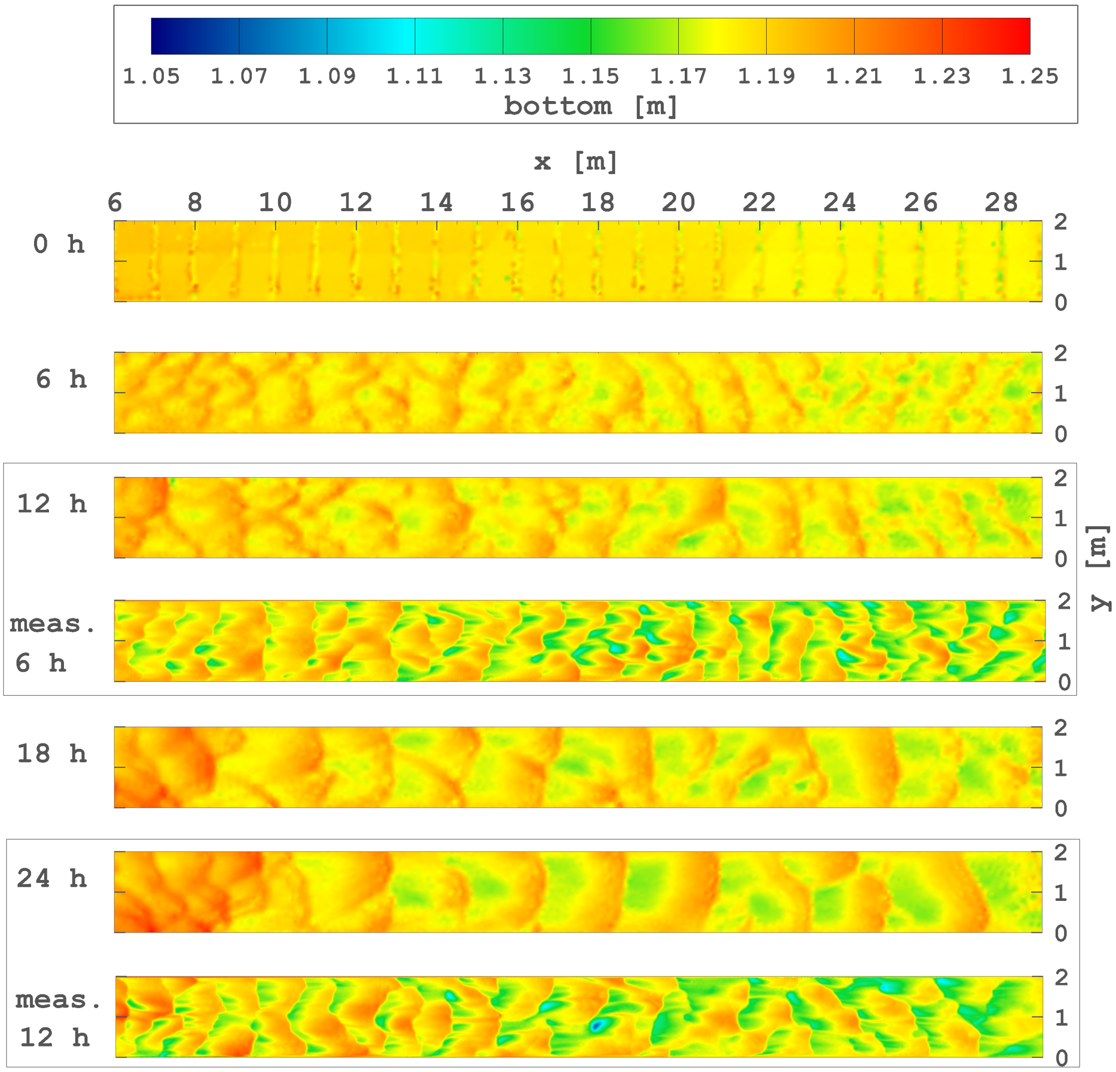

Figure 7.8: Bottom elevation of simulation with total load formula of Yang and Lim (2003), 0–24 h and corresponding measurements (connected with boxes). The flow is from left to right. Data set No. 4 of Table 7.1

Table 7.4: Dune parameters of simulations with formula of Yang and Lim (2003) after 6, 12, 18, 24 h, no correction of bed load formula

	height [m]	length [m]	skewness	kurtosis	steepness
6 h	0.018	1.104	0.490	-0.244	0.016
12 h	0.022	1.367	0.455	-0.351	0.016
18 h	0.025	1.584	0.554	-0.353	0.016
24 h	0.028	1.836	0.463	-0.402	0.015

Table 7.5: Dune parameters of simulations with formula of Engelund and Hansen (1967), and Yang and Lim (2003) after 24 h, no correction of bed load formula, compared to physical experiments (mean minimum and maximum of experiments S6, S9, S10)

Experi. after 24 h	height [m]	length [m]	skewness	kurtosis	steepness
Engelund and Hansen (1967)	0.033	1.237	0.269	-0.6585	0.027
Yang and Lim (2003)	0.028	1.836	0.463	-0.4021	0.015
$\min_{EXP}$	0.035	1.03	-0.73	-0.057	0.023*
$\max_{EXP}$	0.047	1.51	-0.445	+1.336	0.046*

*The dune steepness of the experiments is calculated from minimum height over maximum length, maximum height over minimum length respectively

7.3 Mesh resolution, hydrodynamic boundary conditions

All of the presented calculations have been conducted with the coarse mesh, which has a mean edge length of $0.11\,\mathrm{m}$ (see Table 5.2 of the hydrodynamic calculations). With this resolution, a dune form is represented by about 10 mesh elements in average. Additionally, calculations have been performed using the medium mesh with a mean edge length of $0.065\,\mathrm{m}$. Figure 7.9 shows a plot of the bed surface calculated with the two resolutions. It can be seen that similar bed forms develop at the same positions of the flume. The corresponding dune parameters after 11 h are compared in Table 7.6. It can be concluded that the mesh resolution influences the results due to local refinement, but that the main dune parameters remain the same. There are no major differences between dune characteristics such as skewness and kurtosis calculated from results gained with the two mesh resolutions. Therefore, three-dimensionality, form and distribution of the dunes are the same.

Hydro- and morphodynamic boundary conditions will influence the results of the simulations. Morphodynamic effects, governed by the applied boundary conditions, have been reported by different authors (Khosronejad and Sotiropoulos, 2014; Mendoza et al., 2015). These effects might be stronger for straight flumes with no installations. The same is valid for the hydrodynamic boundary conditions: if the flow field, that establishes over dune forms, differs greatly from the parameters presented at the boundary, a stable state might not be reached over the length of the experimental (numerical) flume. In the flume used for the physical experiments, the upstream inflow tank is blocked with a wall of hollow (perforated) bricks, which provide a partial calming of the highly turbulent flow close to the inlet from the deep tank. Nonetheless, the flow can be characterised as turbulent when entering the evaluation area.

Table 7.6: Dune parameters of simulations with coarse and medium mesh resolution after 11 h

mesh	height [m]	length [m]	skewness	kurtosis	steepness
coarse	0.033	1.03	0.218	-0.734	0.032
medium	0.029	0.96	0.225	-0.879	0.03

Thus a turbulent flow field distributed over the water depth needs to be prescribed at the inflow boundary of the numerical model.

It is imposed via two different formulae, either of Burchard (2002) or Nezu and Nakagawa (1993) respectively, for k and ε. With the imposed boundary conditions, the model does not need to establish the turbulent flow field, which might take about half of the length of the flume. With the mentioned boundary conditions, the flow field establishes already after about 1/4 of the flume. This fact is irrelevant for the mere hydrodynamic simulations, as the physically measured sections for comparison are positioned in the last third of the flume, but important for dune morphodynamics. The two boundary conditions do not produce different results compared to each other, but results are enhanced compared to simulations without added turbulence at the inflow boundary.

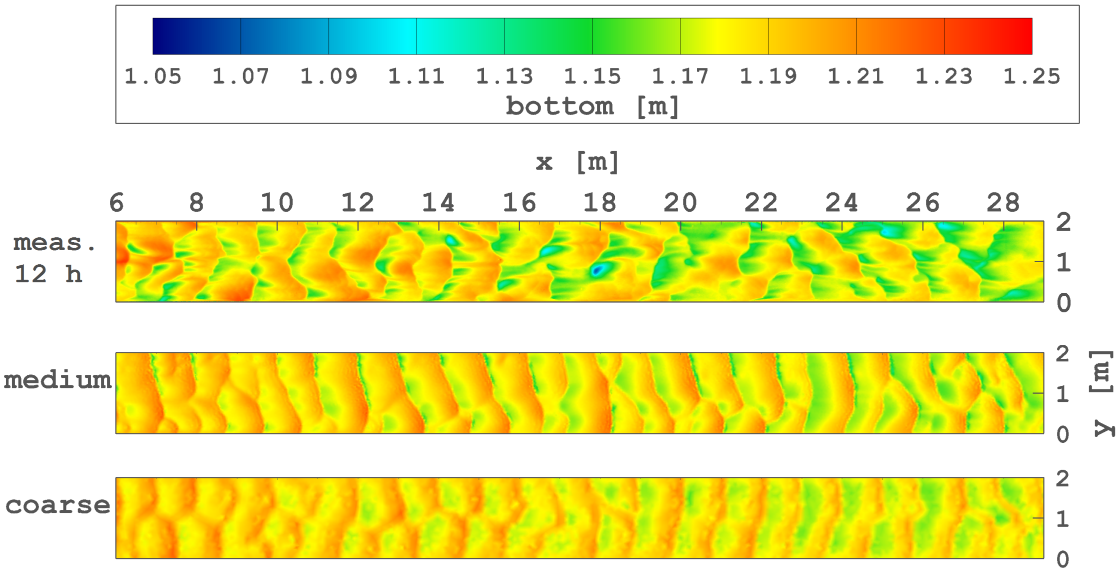

Figure 7.9: Dune development with medium and coarse mesh after 11 h. Data set No. 6 of Table 7.1

7.4 Slope effect and deviation

The formulae chosen for slope effect (change of magnitude of bed load transport) and deviation (change of direction of bed load transport) correction will profoundly influence the resulting form of the mobile bed. The shape of the dunes will affect the dynamics of the surrounding flow field, which in turn will determine the bottom form. Low-angle dunes will produce a different flow field without a separation zone (Best et al., 2004; Motamedi et al., 2014), an important stabilizing factor for a dynamic dune field (e.g. Bennett and Best, 1995; ASCE, 2002) (see also Chapter 2).

Apart from the actual choice of bed load formula, the formulae of slope and deviation correction are identified as primarily responsible for the shape and form of the resulting bed forms. The formulae available in Sisyphe as well as the additional formula presented in Section 6.4 have been tested and their effects were evaluated against the measured data. The runs presented previously in this chapter have been mainly calculated with the slope correction of Koch and Flokstra (1981) and the deviation correction of Apsley and Stansby (2008). Only in the runs presented in Section 7.1.2, plotted in Fig. 7.4 and 7.3, various slope and deviation corrections have been used (data sets No. 2 of Table 7.1).

Without slope and deviation corrections, no satisfying results were obtained. The use of these corrective formulae is a prerequisite for dune development. It has been discussed in Chapter 4.1 that slope and deviation correction formulae are necessary, as the bed load formulae have been developed for flat beds. Removing the correcting slope and deviation formulae, the resulting bed forms loose their dune shapes, no distinct difference between stoss- and lee-side develops and the simulation crashes due to the instability of these bed forms.

Slope and deviation corrections are generally obtained from an analysis of the forces acting on a sediment particle. These include the weight-force of the particle underwater, the angle between the bed shear stress and the bottom slope or channel axis, and the bed shear stress itself which acts on the sediment particle. The frictional force of a sediment particle is opposite to the resulting force and does not change the transport direction.

The choice of slope and deviation correction can be crucial. Figure 7.10 shows a plot of the flume after 18 h with slope correction of Koch and Flokstra (1981), Eq. 6.14. The results plotted in 7.10 (A) have been obtained in combination with the deviation correction of Koch and Flokstra (1981) (Eq. 6.15) too, and for (B) the deviation correction of Apsley and Stansby (2008) (Eq. 6.19) has been applied. The different behaviours of the dunes can be clearly seen. The deviation correction formula of Apsley and Stansby (2008) results in more variation in the dune field – the distribution of dunes is more scattered, whereas in (A) they are clearly more two-dimensional. Crest replacement is supposed to play a crucial role in dune dynamics (Fredsøe and Deigaard, 1992). Still none of the available avalanching routines, neither the one of Apsley and Stansby (2008) nor the one already implemented in the Sisyphe module, influenced the results in any apparent way. The routines would be triggered, if a critical angle of repose, which is set to 30°, is exceeded. The value of 30° has been obtained through sediment analysis of the bed load material of the physical experimental flume, see Appendix 1. This leads to the conclusion that the dunes in the experiment have a lower angle of repose then the critical value set in the routines.

The best match with the physical experiments is obtained with the bed load formula of Engelund and Hansen (1967), in combination with the slope correction formula of Koch and Flokstra (1981) and the deviation correction by Apsley and Stansby (2008). After 24 h (without additional bed load proportionality factor) the dunes have an average length of $1.24\,\mathrm{m}$ and a height of $0.033\,\mathrm{m}$. This corresponds with values of the experimental data sets (see Table 3.4). The skewness of the simulated dune field is 0.269 and the kurtosis is -0.659. Dune parameters can be also found in Table 7.3.

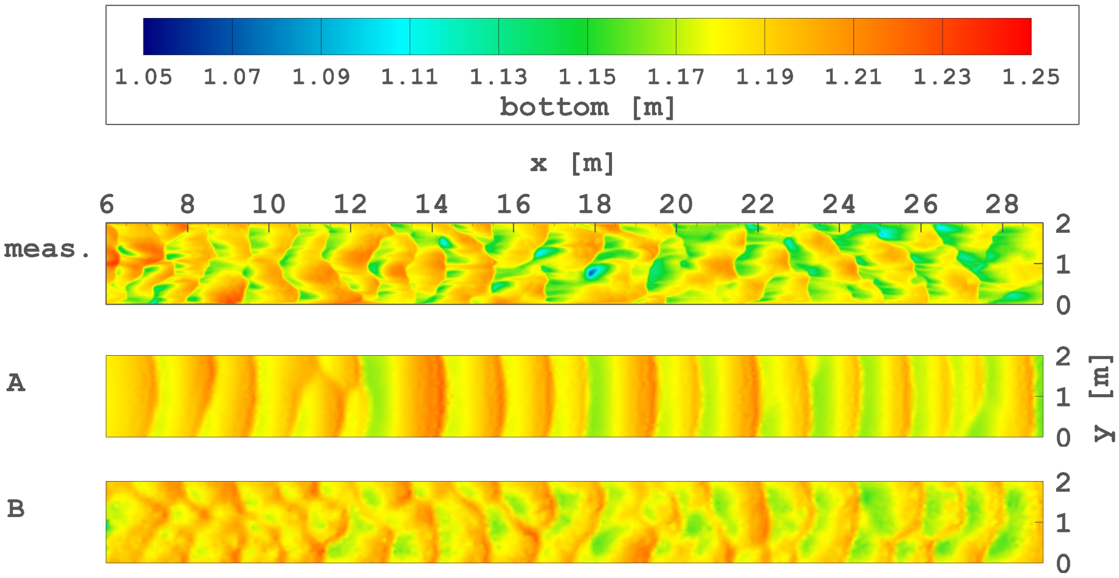

Figure 7.10: Dunes with slope effect correction formula of Koch and Flokstra (1981) in combination with deviation correction formula of (A) Koch and Flokstra and (B) Apsley and Stansby (2008) after 18 h in comparison to measurements. Data sets No. 3 and 1 of Table 7.1

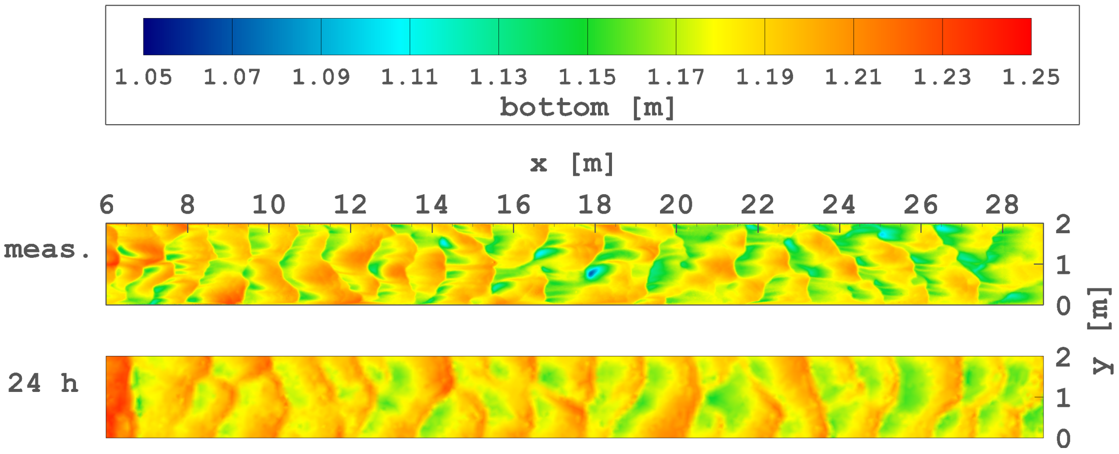

Figure 7.11: Dunes with slope effect correction formula of Koch and Flokstra (1981) in combination with deviation correction formula of Apsley and Stansby (2008) after 24 h (without additional bed load proportionality factor, hence corresponding to 12 h in the measurements) in comparison to measurements after 12 h. Data set No. 1 of Table 7.1

7.5 Inclusion of turbulence into bed shear stress

A moving bottom will influence the hydrodynamic flow field and vice versa. Naqshband et al. (2014b) conducted high resolution measurements over mobile sand dunes, where they measured the velocity field, turbulence and suspended sediment. They showed that the mean and turbulent flow evolution over mobile beds greatly differed from experiments where the measurements were conducted over fixed bed (e.g. Bennett and Best, 1995; Maddux et al., 2003b; Venditti, 2007). Naqshband et al. (2014b) attributed this to a dense sediment layer, that was present close to the bed and to the influence of secondary bed forms migrating over the moving sand dunes (see also Section 5.3). The differences were mainly found in the vicinity of the bed. Further within the water column the flow patterns matched the observations in studies involving fixed beds. In the experimental flume of BAW the hydrodynamic experiments have shown that for the same discharge a fixed bottom results in a marginally lower water level than over moving dunes. An explanation can be the lowered pore ratio of the surface due to the used glue mixture (see Section 3.2). The phenomena described by Naqshband et al. (2014b) would also create a lowered water level as soon as the dunes are fixed, because firstly the dense sediment layer just above the bottom, which removes energy, is missing and secondly no small scale bed forms migrate over the stoss-side of the dunes anymore.

Thus simply matching the flow field in the water column, as done in Chapter 5, is not sufficient, when calculating bed movement and bed shear stress. Additionally the inclusion of turbulent fluid motion into sediment transport near the bed becomes necessary. This is important, as previous studies have shown that the bed shear stress calculated from the mean velocities is not in agreement with the distribution of sediment transport (Sumer et al., 2003). Recently Schmeeckle (2015), while investigating the influence of turbulence on single grains and bed shear stress using a LES model, stated as well that for calculation of exact rates of bed load transport downstream of separated flow it is not sufficient to use time averaged bed shear stresses.

In accordance with these experiments, the addition of turbulent fluctuations to the mean bed shear stress derived from only velocities needs to be carried out for calculations with Telemac-Sisyphe as well.

In the numerical RANS model almost all of the turbulence is represented through the turbulence model only. If a total sediment transport capacity is to be calculated, the part of the turbulence-triggered transport needs to be included as well. Thus, as it has been presented in Section 6.2, in addition to the valid assumption of bed shear stress calculated from the flow field (Eq. 6.6), the turbulent part is included in form of Eq. 6.9

$$\tau_{tot} = \rho u_*^2 + \rho \, r \, 2 \, k \qquad (6.9)$$

with:

r	proportionality coefficient
$\mathbf{u}$	vector of velocity u [m/s]
k	turbulent kinetic energy [$\mathrm{m^2/s^2}$]
u_*	friction velocity [m/s]

The turbulent kinetic energy k is calculated from the turbulence model. What still needs to be validated is the proportionality constant r assigned to the turbulent term. Thus, it is necessary to compare the quantity of u_*^2 and k in the morphodynamic simulations. This is done in Table 7.7. It shows that even though the average values of the variables (average minimum and maximum, av$_{min}$ and av$_{max}$, as well as an average value over 18 h, av$_{18\ h}$, extracted at the σ-layer above the bed) are in the same range, their maximum and minimal values (max, min) do not follow this pattern. The maximum values of the turbulent kinetic energy are significantly higher, reinforcing the theory that turbulent flow events play a significant role in bed load transport of dunes (Nelson et al., 1995; Schmeeckle, 2015).

The factor between maximum turbulent kinetic energy and shear velocity is $(k/u_*^2)_{av} = 1.64$ (see as well Figure 7.12). It is lower over developing dunes and stabilises around 1.68 during the end of the run with stable dunes. Additionally, it needs to be kept in mind that k is underestimated by a factor of 2.5 in comparison to the measurements (see Section 5.5), which would increase the average factor up to 4.25. At points with maximum differences k exceeds u_*^2 up to factor max$_{tot} = 55$. Most interestingly, there are points with virtually no k compared to u_*^2. Figure 7.12 shows the factor k/u_*^2 over a formed bed. For orientation the bottom is shown as well (top). A higher value of k compared to u_*^2 is found on the crest of the dunes and at the steep lee-sides. In the troughs k/u_*^2 is close to zero or lower, which results from a high u_*^2 compared to k.

To decide on the dimensions of r assigned to the turbulent term, it has to be kept in mind that in the previous calculations, the correct dunes – concerning length and height – have been created. The aim of correcting the bed shear stress formulation is to take into account turbulence events, which are

Table 7.7: Comparison of dimension of simulated shear velocity (u_*^2) and turbulent kinetic energy (k), average values over 18 h ($\mathrm{av}_{18\ h}$), average maximum and minimum values, as well as total minimum and maximum

variable	$\mathrm{av}_{18\ h}$	av_{max}	av_{min}	min_{tot}	max_{tot}
u_*^2 [m^2/s^2]	$1.26{\cdot}10^{-3}$	$1.48{\cdot}10^{-3}$	$1.24{\cdot}10^{-3}$	$1.43{\cdot}10^{-4}$	$3.3{\cdot}10^{-3}$
k [m^2/s^2]	$1.97{\cdot}10^{-3}$	$2.12{\cdot}10^{-3}$	$1.95{\cdot}10^{-3}$	$1.48{\cdot}10^{-7}$	$1.15{\cdot}10^{-2}$
k/u_*^2 [-]	1.64	1.699	1.477	$< 10^{-10}$	22
$(2.5\ k)/u_*^2$ [-]	4.1	4.25	3.69	$< 10^{-10}$	55

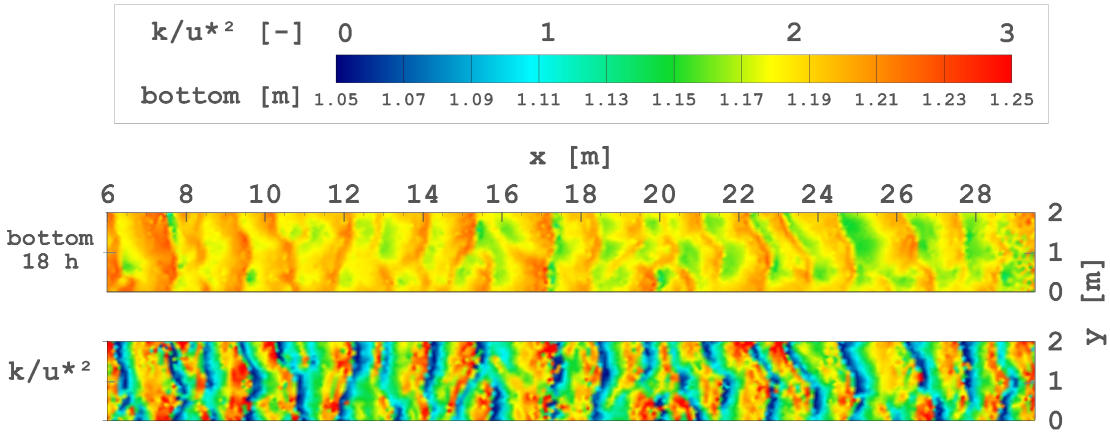

Figure 7.12: Factor k/u_*^2 in simulation, the bottom is shown for orientation. Data set No. 5 of Table 7.1

supposed to be governing features for the shape of dunes, expressed through skewness and kurtosis values. It is thus assumed, that the mean quantity of bed shear stress is correct but that peaks of bed shear stress due to the increased presence of turbulence are missing. The coefficient of the turbulent kinetic energy model of Soulsby (1983), see Eq. 2.7 in Section 6.2, is $C_1 = 0.19$. The coefficient r

$$r = \frac{\kappa^2}{\left(\ln \frac{\Delta z}{z_o}\right)^2} = \kappa^2 \left(\ln \frac{\Delta z}{z_o}\right)^{-2} \tag{7.4}$$

where Δz is the height of the σ-layer closest to the bottom, is included in the shear velocity $u_*^2 = r|\mathbf{u}|\mathbf{u}$, in order to extract **u** from the velocity profile at a specific height and interpolate it to the bottom. The turbulent kinetic energy cannot be extracted at the bottom due to the boundary conditions, thus it is extracted at the same point as **u**. The values of the coefficients are compared in Table 7.8.

The calculated coefficients stem from morphological, numerical experiments as presented earlier. The dynamically calculated coefficient r is not in the range of the coefficient found by Soulsby (1983). The coefficient $C_1 = 0.19$ [-] would need to be multiplied by a value of 12.25 to 16 to match the total maximal and minimal average of the coefficient r. This difference is close to the peaks (max$_{tot}$) presented in Table 7.7. The dimension of this coefficient has been evaluated before: In their paper, Biron et al. (2004) have already advised to re-estimate the constant C_1 for a natural river application.

For the forthcoming calculations, both factors r are calculated in the same way (Eq. 7.4), with k being extracted at the nodes above the bed, at the same position as u_*^2. Additionally, the factor 2.0 of the turbulent term of Eq. 6.9 and the underestimation of k by 2.5 are considered for the factor assigned to the

Table 7.8: Dimensional analysis for coefficient r for the inclusion of turbulent kinetic energy into the bed shear stress, average minimum and maximum value, as well as total maximum

coefficient	C_1 (Soulsby, 1983) [-]	$r = \kappa^2 \left(\ln \frac{\mathrm{d}z}{z_o}\right)^{-2}$ [-]
av$_{min}$	0.19	0.0119
av$_{max}$	0.19	0.0122
max$_{tot}$	0.19	0.0155

turbulent term

$$r = 2.0\,2.5\,\kappa^2 \left(\ln \frac{\Delta z}{z_o}\right)^{-2} \tag{7.5}$$

where Δz is the height of the bottom most σ-layer.

Figure 7.13 shows a comparison of calculated bottom shear stresses without the correction by turbulence (A) and the bottom shear stresses corrected by turbulence (B). The results are presented for a fixed bed (compare also Fig. 5.6). The change in magnitude is dominant at the top of the dunes, whereas the through-zones retain their low bottom shear stress values. Using Eq. 7.8 and 7.5 to calculate the coefficient r, the amount of bed shear stress calculated from k has the same range as the one calculated from u_*^2. The calculated τ_{tot} (Eq. 6.9) is enhanced at points with maximum turbulent kinetic energy k.

Figure 7.14 shows free surface levels for simulations which include turbulence in comparison to selected measured free surface levels. For comparison, the physical experiments producing a confidence interval of ±0.004 m are plotted. Morphodynamic results are shown as an extract in the middle

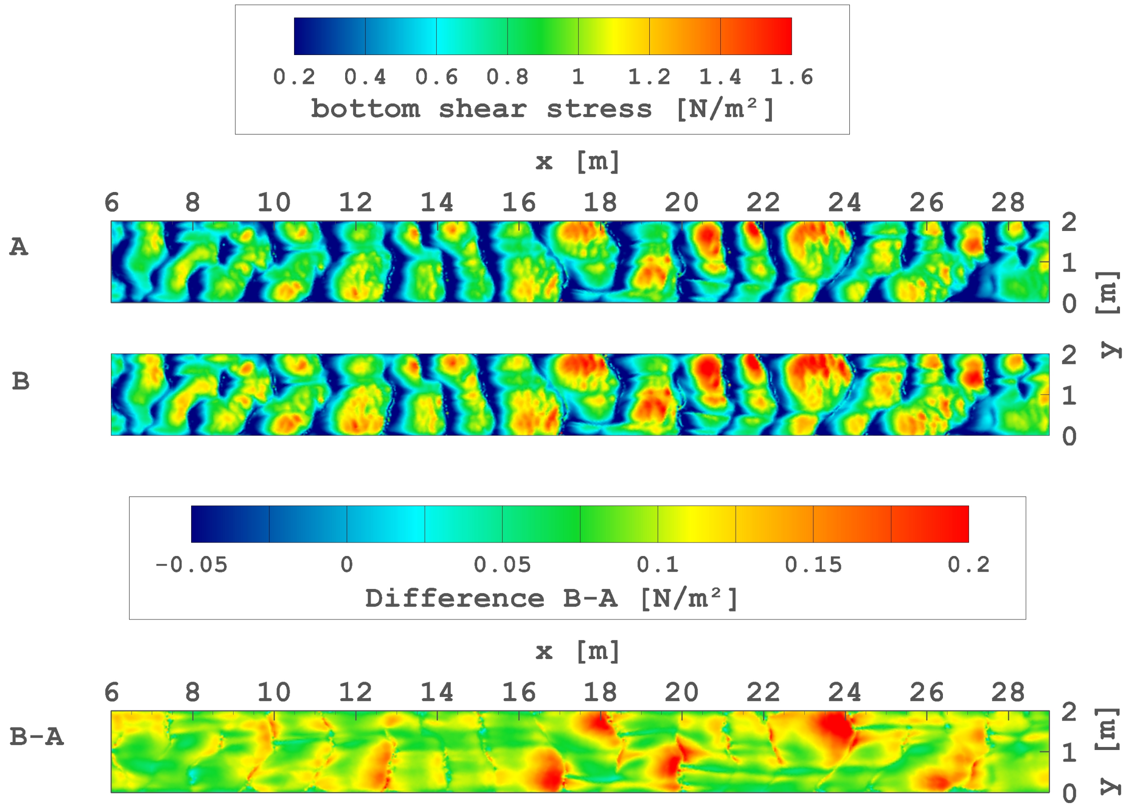

Figure 7.13: Bottom shear stresses [N/m^2] over fixed bed, (A) original calculation, (B) calculated according to Eq. 6.9, below differences in bed shear stresses (B–A) are displayed. Data set No. 7 of Table 7.1

of the flume, where dune forms trace to the free surface (top). Figure 7.14 (bottom) shows a simplified plot where only average free surface levels of the simulations are presented. It is evident, that at the beginning the small, still

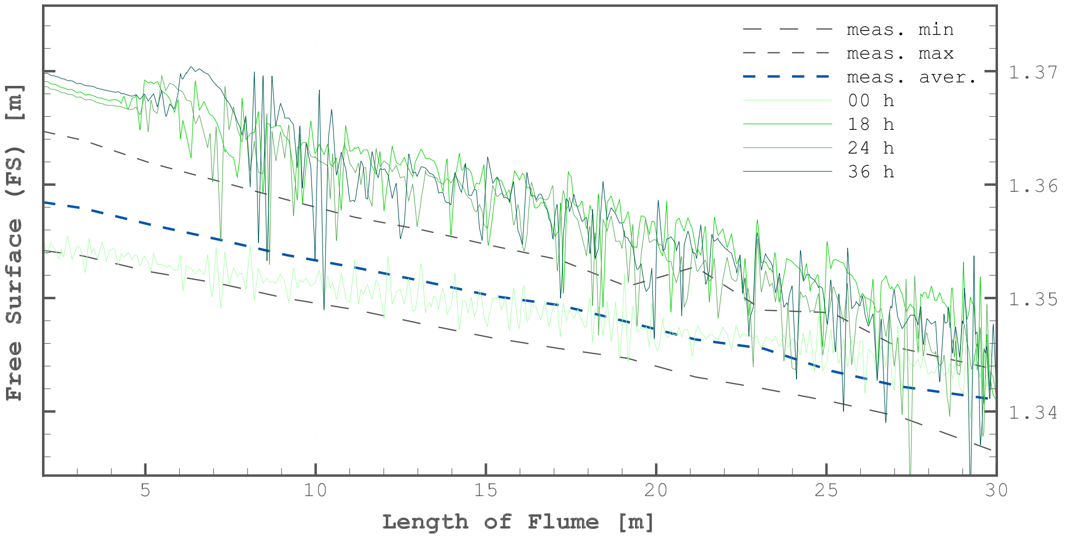

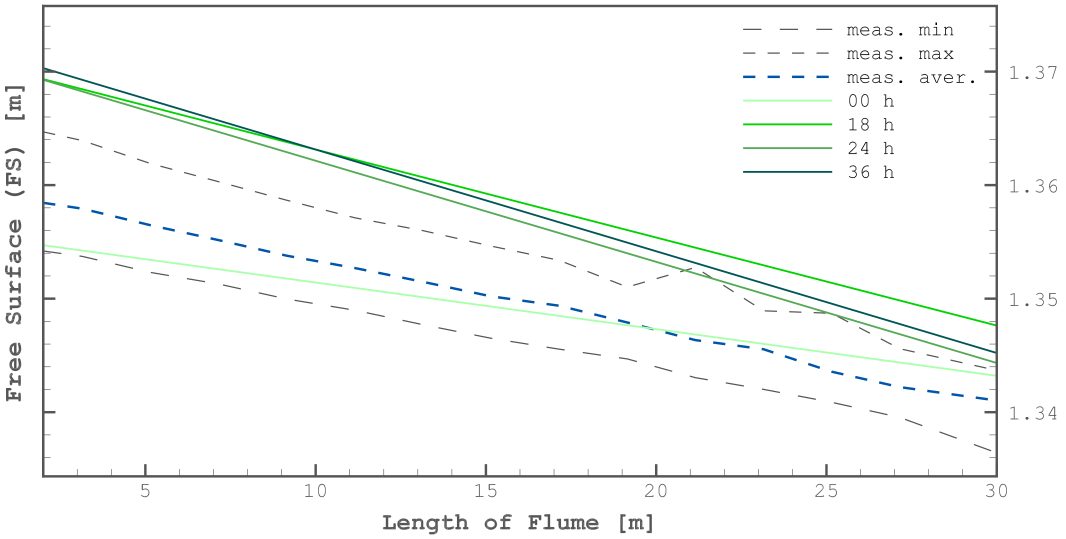

Figure 7.14: Average measured free surface elevation (meas. aver.) and minimal and maximal extents (meas. min/max) [m] of selected measurements of Fig. 7.1 (dashed), in comparison to simulations after 0, 18, 24 and 36 h (no additional bed load factor). Top figure shows non-smoothed free surface levels, where dunes trace to the free surface; bottom figure shows a linear fit of the same results and represent the mean free surface slope. Data set No. 7 of Table 7.1

growing dunes produce a free surface that remains at the same level as the physical experiments. The difference in slope stems from the fact that all of the physical results already contain dunes – whereas the numerical results at 0 h features a smoothened surface.

Free surface levels react in the same way as presented in Figure 7.2. After dune development, the numerical free surface levels are slightly higher than the ones for the physical experiments. The free surface level at the outflow boundary is kept at $1.341\,\mathrm{m}$ and the roughness coefficient is $k_s = 0.003\,95\,\mathrm{m}$. The free surface level at the outflow is the same as in the physical experiments (compare Section 7.1.1).

Figure 7.15 shows the bottom evolution for the above-mentioned morphodynamic simulations in comparison to measurements (S0V6W1T2 after 18 h). The numerical results are shown after 18, 24 and 36 h, with no additional proportionality factor in the bed load transport formulation. Due to this, the numerical results after 36 h should agree with the physical experiments after 18 h for the chosen sediment transport formula. Sediment is introduced through continuous sediment input at the inflow boundary, thus the inflow zone and part of the flume in its proximity offer room for improvement through the use of discontinuous sediment input. In the rest of the flume the bed forms develop continuously and reach a steady state.

The dune parameters of this run are summarised in Table 7.9. Comparing them to the values of the measurements (min, max), the height and length of the simulated dunes remain in very good agreement with their physical counterparts. The form parameters, skewness and kurtosis, fit the natural dunes best after 36 h (which equals the instant of time of the physical experiments after 18 h), when negative skewness and positive kurtosis values are reached. The steepness is also in the range of the measurements. Calculating the steepness of the experimental dunes from the ratio of minimum height over minimum length and maximum height over maximum length values of 0.031 and 0.034 respectively are obtained. The dune steepness of the simulations agree well with the observed values.

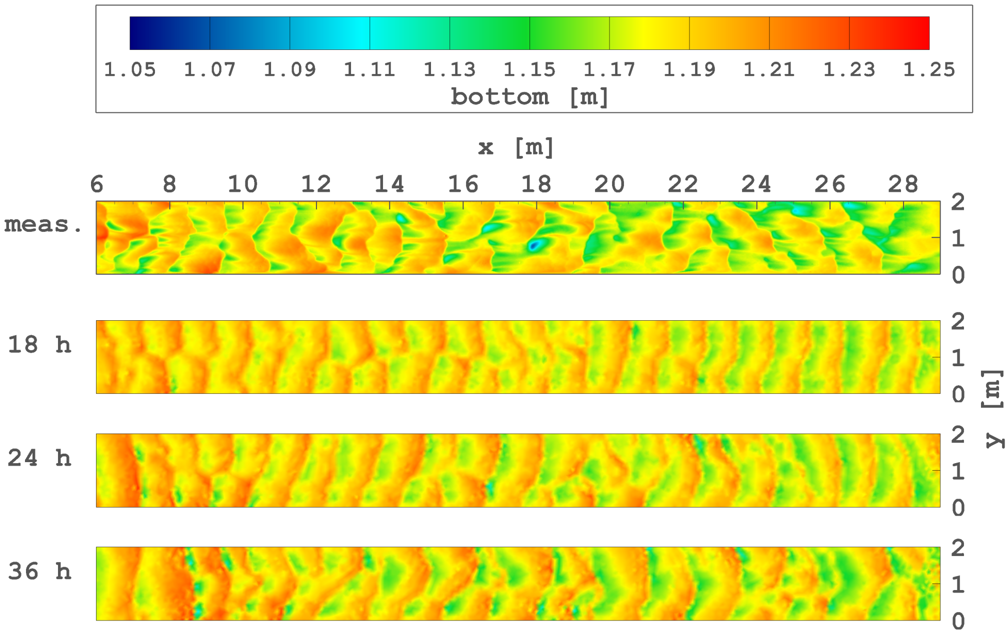

Figure 7.15: Bottom evolution calculated with included turbulence into bed shear stress in comparison to measurements (S0V6W1T2 after 18h). Numerical results after 18, 24, 36 h, no additional bed load proportionality factor. Data set No. 7 of Table 7.1

Table 7.9: Dune parameters of the simulation with included turbulent kinetic energy in bed shear stress calculation (presented in Figure 7.15), in comparison to minimal and maximal results of the physical experiment (min, max)

time	height [m]	length [m]	skewness	kurtosis	steepness
18 h	0.036	1.10	0.183	-0.459	0.033
24 h	0.041	1.17	0.099	-0.423	0.035
36 h	0.043	1.17	-0.207	0.222	0.036
$\min_{EXP}$	0.035	1.03	-0.73	-0.057	0.023*
$\max_{EXP}$	0.047	1.51	-0.445	+1.336	0.046*

*The dune steepness of the experiments is calculated from minimum height over maximum length, maximum height over minimum length respectively

7.6 Discussion

Telemac-3D and Sisyphe offer a wide number of choices of tunable parameters. Selecting the best choice of set up and calibrating the model can be time-consuming and sometimes even unsuccessful. If – like in the case of this work – the configurations should also be applicable to a river scale project, additional restrictions apply compared to a situation, where the work focuses on only laboratory scale. In the following paragraph the main parameters of the numerical morphodynamic system used to simulate dune experiments of the experimental flume of BAW, presented in Chapter 3, are summarised and discussed.

It is found that with the Telemac-3D, the two-equation k-ε turbulence model (Launder and Sharma, 1974; Rodi, 1993) is necessary to reproduce the complex hydrodynamics. This is also the case when coupling the hydrodynamics to the morphodynamic module Sisyphe: only the two-equation k-ε **turbulence model** is able to produce dune-like structures. As high resolution measurements of hydrodynamics over the mobile bed are not available, the bed evolution is the key parameter for assessing the model accuracy of the hydrodynamic model coupled to its morphodynamic counterpart.

The **bed load formulae** of Engelund and Hansen (1967) and Yang and Lim (2003) are successfully applied in the morphodynamic simulations. An implementation of the Engelund and Hansen formula is available in Sisyphe. This total load formula computes bed load and suspended load together and is recommended for rivers with fine sediments ($0.2\,\mathrm{mm} < d_{50} < 1\,\mathrm{mm}$), which can also contain dunes. It applies an energy balance analysis for bed and suspended load. For this calculation, it is assumed that the sediment is transported over bed forms, e.g. ripples and dunes, in a characteristic height Δ and over a certain length λ. Based on this, the energy needed to lift the sediment up to height Δ is calculated (Malcherek, 2009b; Tassi and Villaret, 2014). Being one of the few sediment transport formulae that does not include a critical value for the initiation of sediment transport, it reduces the parametrisation factors required for this calculation. The good results obtained for various dune applications in this work recommend this formula for practical use. The newly implemented formula of Yang and Lim (2003) is also effectively used to simulate the complex three-dimensional dune forms. The total load formula has been developed for river and laboratory applications and further tests with this formula are recommended for a morphological parameter range.

Both formulae do not consider a threshold (fraction) for the start of sediment transport. Thus, this omission of threshold fractions, along with applying gravitational factors as lift-energy and settling velocity, appear necessary when modelling dunes. The successful tests with two different formulations also ensure, that dune emergence, movement and formation are not simply attributable to empirical components or numerical shortcomings in the bed load transport formula.

The applied bed load formulae can be corrected to agree with the sediment output volume of the physical experiments. The formula of Engelund and Hansen (1967) is endued with a proportionality factor of $2.0 \cdot 0.1 = 0.2$ (Eq. 7.2). The total load formula of Yang and Lim (2003) uses a new proportionality factor of $1.75 \cdot 12.5 = 22.0$ (Eq. 7.3). This approach is chosen as it shows, that using the standard proportionality factors of the two total load formulae the results of the simulations do not fit the bottom and sediment discharge measurements of the experimental flume concerning relation of sediment discharge to time period. Using the new proportionality factors, sediment discharge, dune speeds and bottom form parameters can all be fitted. It can be concluded, that the standard proportionality factors are not calibrated for our dune regime in the experimental flume and therefore need adjustment.

The **formulae for slope effect correction** (change of magnitude of bed load transport) **and deviation correction** (change of direction of bed load transport) of Koch and Flokstra (1981) and Apsley and Stansby (2008) profoundly influence the resulting form of the mobile bed and delivered the best results for dune length, height and form parameters such as skewness and kurtosis. With the slope correction method of Koch and Flokstra (1981) the intensity of the solid transport rate is changed by coefficient $c_{\texttt{coef}}$ (Eq. 6.14), depending on the change of bottom slope in flow direction. This is similar to adding a diffusion term to the bed-evolution equation (Sisyphe User Manual, 2014). This smoothens the results and reduces instability. The deviation correction calculated according to the formulation of Apsley and Stansby (2008), which includes the x- and y-components of the bed gradient and the angle of repose (Eq. 6.21), deliver the best results concerning all relevant dune parameters. Although it was developed for steep slopes, neither the avalanching routine of the formula of Apsley and Stansby (2008) nor the one already implemented in the Sispyhe module, influences the results in any apparent way for an angle of repose of 30° for the sediment (data sheet of sediment, see Appendix 1).

Hydro- and morphodynamic **boundary conditions** will influence the results of the simulations. Morphodynamic effects, governed by the applied boundary conditions, have been reported by different authors (Khosronejad and Sotiropoulos, 2014; Mendoza et al., 2015). These effects might be stronger for straight flumes with no installations. The same is valid for the hydrodynamic boundary conditions; if the flow field that establishes over dune forms differs greatly from the parameters presented at the boundary, a stable state might not be reached over the length of the flume. The flow is turbulent when entering the evaluation area (Re > 2300). Thus a turbulent flow field distributed over the water depth is prescribed at the inflow boundary of the numerical model. Two formulae for k and ε can be applied (Burchard, 2002; Nezu and Nakagawa, 1993). Through the hydrodynamic boundary conditions the flow field establishes after about 1/4 of the length of the flume. This proves to be important for dune morphodynamics. Morphodynamic boundary conditions for the inflow boundary need to replicate the physical model in order to establish a dune field throughout the flume. The choice of morphodynamic boundary conditions significantly change the establishing dune field.

The dunes produced during the numerical simulation are insensitive to **mesh resolution**. The position of the dunes calculated with the medium and the coarse mesh (mean edge length $0.065\,\mathrm{m}$ and $0.11\,\mathrm{m}$ respectively) are the same throughout the flume. The mesh resolution influences the results locally, but that the main dune parameters remain the same. The calculations produce no major differences between dune characteristics such as skewness and kurtosis. Three-dimensionality, form and distribution of the dunes are the same for both calculations.

The **inclusion of turbulence parameters** for the calculation of bed shear stress is thoroughly discussed in Section 7.5. Similar to findings by others (e.g. Sumer et al., 2003; Schmeeckle, 2015; Naqshband et al., 2014a) the inclusion of turbulent forces or energy improve the shapes of the calculated dunes. Adding a turbulent term in the form of

$$\tau_{tot} \; = \; \rho u_*^2 \; + \; \rho \, r \, 2 \, k \tag{6.9}$$

where r is calculated according to the log law in the σ-layer most close to the bottom. This approach changed the bed forms, so that it is now possible to match not only height and length of calculated and physically produced dunes, but also the shape parameters like skewness and kurtosis. These parameters give information about the general shape of the dunes (convex/concave stoss-side, steep lee-side and deep troughs) and also describe the dune field in its entirety (orientation towards each other, 2D/3D form and regularity). The new coefficient r includes k, extracted from nodes above the bed, and the factor 2.0 of the turbulent term of Eq. 6.9. Also it includes the found underestimation of k by 2.5

$$r = 2.0\, 2.5\, \kappa^2 \left(\ln \frac{\Delta z}{z_o} \right)^{-2} \tag{7.5}$$

The new formulation allows to fit the dune parameters into the diagram of Friedrich et al. (2006) and makes the results consistent with the measurements (Fig. 7.16 and Fig. 7.17).

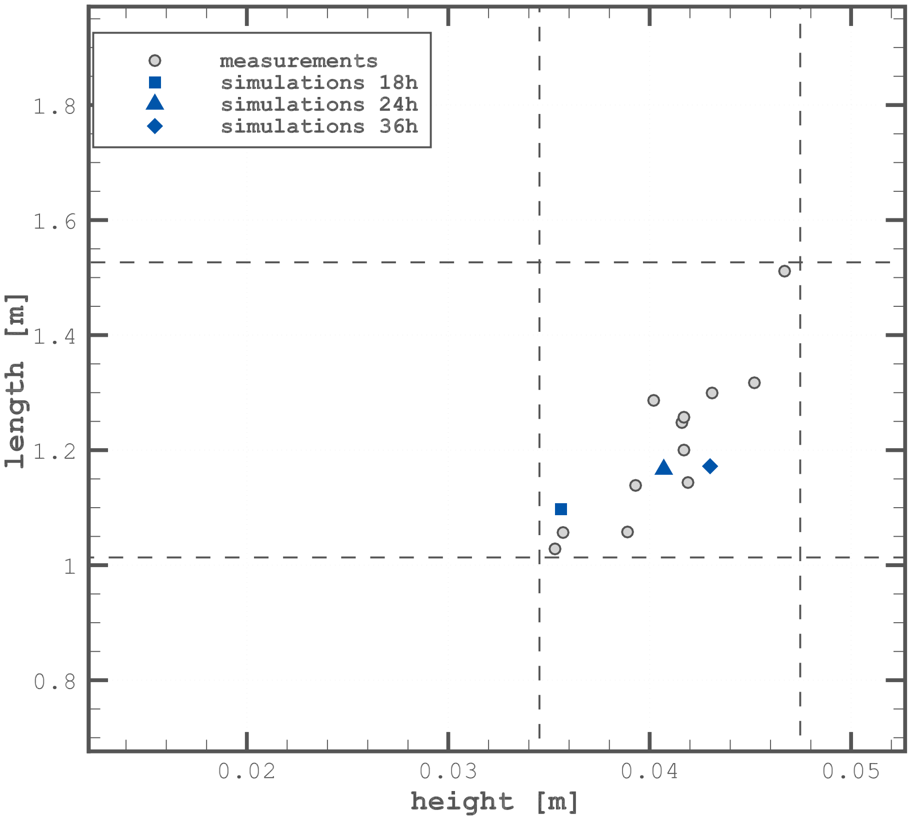

Figure 7.16: Length and height of morphodynamic calculation with turbulent kinetic energy included into bed shear stress, after 18, 24 and 36 h. Data set No. 7 of Table 7.1

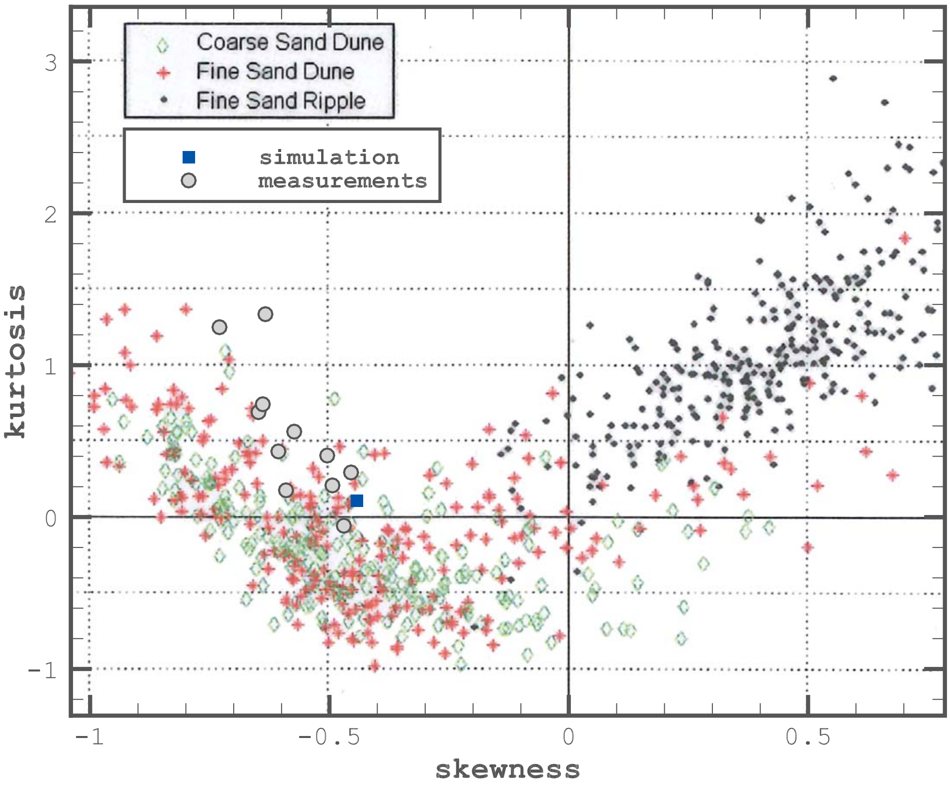

Figure 7.17: Skewness and kurtosis of morphodynamic calculation with turbulent kinetic energy included into bed shear stress, compared to values of the experimental data sets as well as to data sets of coarse and fine sand dunes and ripples by Friedrich et al. (2006; modified). Data set No. 7 of Table 7.1

8

Dunes in Inland Waterways

Contents

In this chapter the results obtained in Chapters 5 and 7 are applied to a model on field-scale. A stretch of the river Elbe in Germany has been selected. The chosen stretch features a pronounced dune regime. Its sediment, a sand-gravel mixture, has the same sedimentological Froude and Reynolds number as the bed load material of the experimental flume, as the material was chosen to correspond with the values of German lowland rivers such as the Elbe or Danube. The Elbe river contains straight stretches in the selected area, thus bends and changes in flow direction can be excluded. The setting provides the maximum possible similarity between the flume experiments and engineering application.

8.1 Elbe river at Lenzen

The city of Lenzen is located in Germany between the mouth of the Havel (Elbe-km 438) and the city of Dömitz (Elbe-km 504), see map in Fig. 8.1. In this reach, the Elbe river has partially retained its hydro- and morphodynamics, even though during the last centuries its flood planes have been reduced and large parts of its banks have been stabilized with groynes and revetments (Faulhaber, 2013). Being dominated by large-amplitude meanders in the lower section, it features long, almost straight stretches further downstream in the chosen river reach.

The Elbe river is an industrial waterway and frequently used by touristic boats. Maintenance and development of the river is needed due to flood control and flood protection of the surrounding infrastructure and especially housing. Figure 8.2 shows the Elbe region upstream of the harbour of Lenzen.

The ordinary width of the main channel (desired pier head line) is $196\,\mathrm{m}$ in the lower stretch of the river (El-km 431.3 to 474.6) and $203\,\mathrm{m}$ in the stretch discussed in this work (El-km 474.6 to 505.8). The groynes are mostly inclined in upstream direction, but their shape varies considerably and they are replaced by revetments at the river bends. Due to the variable width, the velocity at specific cross sections may also change along the reach. In average the mean velocity during mean low water discharge ($297\,\mathrm{m}^3/\mathrm{s}$) is $0.73\,\mathrm{m/s}$, and during mid water discharge ($689\,\mathrm{m}^3/\mathrm{s}$) $0.96\,\mathrm{m/s}$.

The bottom of the river is a sand-gravel mixture, composed of $80\ \%$ medium and coarse sand and $20\ \%$ fine and medium gravel (Table 8.1). It is very mobile, transporting bed forms even at low discharges. The bed forms appear in all sizes, ranging from ripples and dunes to bars. The dunes can be divided into large dunes (length $> 120\,\mathrm{m}$, height $> 1.1\,\mathrm{m}$) and medium dunes (length

Figure 8.1: City of Lenzen (red circle) next to the Elbe river (source: google)

Figure 8.2: Photo of Elbe river, looking upstream from the harbour of Lenzen. Construction phase of the dike relocation. Photograph taken by J.Purps, 2007-04-29

Table 8.1: Bed load and riverbed composition of Elbe river at El-km 438 to 504

sediment characteristics	percentage	range [mm]	d_m [mm]
medium sand	40 %	0.2 - 0.63	0.415
coarse sand	40 %	0.63 - 2	1.315
fine gravel	10 %	2 - 6.3	4.075
medium gravel	10 %	6.3 - 20	13.15
sum	**100 %**	**0.2 - 20**	**2.415**

10 m to 120 m, height up to 1.1 m). The medium dunes, which can be superimposed by ripples, occur on top of the large dunes. After periods with high discharges more large dunes can be found than after low water periods. The average speed of a dune field, of where individual dunes move with different speeds, is about 10 m per day (Faulhaber, 2013). It is found that the form of the bottom is highly dependent on the previous discharge curve (BAW, 2013). The average slope of the river in this section is 0.13 ‰.

8.2 Dune data of Elbe river

As described in Section 3.3.3, there are different methods for dune analysis. The study area needs to satisfy certain criteria to produce reliable results. Technically speaking, the method of zero-crossing (Section 3.3.4), as well as the connection of the statistical moment of the standard deviation (Section 3.3.3) to the dune height require a straight river section. This is the case for the Elbe at El-km 480 to 484. In this area parallel straight profiles can be obtained from high resolution bottom scans that are necessary for zero-crossing analysis, see Figures 8.3 and 8.4.

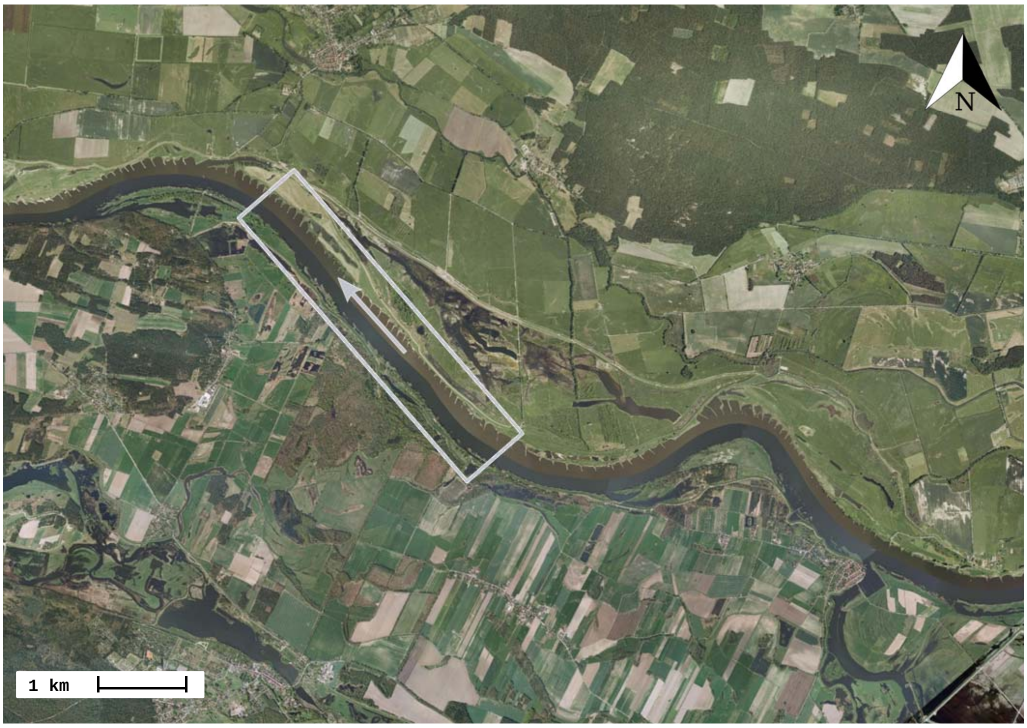

Figure 8.3: Aerial view of evaluated river section of Elbe river; lines mark area of numerical investigation, the arrow indicates the flow direction

Figure 8.4: Elbe river, looking upstream from harbour of Lenzen; lines mark area in which bottom recordings are evaluated, the arrow indicates the flow direction. Photograph taken by J.Purps, 2011-04-30

The physical data sets presented in this work have been analysed by the Leichtweiß Institute for Hydraulic Engineering (LWI) and the results are described in (LWI, 2012a). The technical report explains the relevant work and analysis conducted between 2005 to 2012 in detail and here only a short overview will be given. Not all data discussed in the report will be included in the comparison with the numerical simulation. The data processed by the LWI includes 7 high resolution data sets of the above-mentioned area for different discharges (Q =$368\,\mathrm{m^3/s}$ to $3490\,\mathrm{m^3/s}$), see Table 8.2.

Even though the area of sediment transport between the groynes is about $203\,\mathrm{m}$ in this river section, a measurement corridor of $100\,\mathrm{m}$ in the middle of the stream is chosen, from which 101 longitudinal cross sections of $3\,\mathrm{km}$ length can be extracted during post-processing. This allows to consider a stretch of the river which is completely straight, see Fig. 8.4. In this corridor all 7 bottom scans presented in Table 8.2 cover the complete evaluation area. For further data processing, the bottom scans are orientated in a way that the x-axis follows approximately the flow direction of the river reach. Afterwards the data is rastered on a regular $1\,\mathrm{m} \times 1\,\mathrm{m}$ mesh to extract longitudinal sections. For each section the slope is deducted to ensure the mean value of $\overline{z} = 0$.

A high-pass filter is applied Coleman et al. (2011). This is done by applying a maximum threshold value of $100\,\mathrm{m}$, to exclude long wave forms, which can be classified as bars. Even though the value of $100\,\mathrm{m}$ is called subjective in the LWI report as well, it is based on previous studies and the rule of thumb, that the dune length to be expected would be 6 times the water depth, which would result in a value of $42\,\mathrm{m}$ (LWI, 2012a). A smoothening algorithm also excludes bed forms smaller than $0.05\,\mathrm{m}$, classified as ripples, to reduce their influence on the zero-crossing analysis.

Plots of the recorded bottom heights, with and without applied high-pass filter, can be found in Appendix 7. Key values and results of the data sets evaluated by the LWI can be found in Table 8.2.

Table 8.2: Height (h) and length (l) of bed forms form zero-crossing analysis, with (l_{filt}, h_{filt}) and without 100 m high-pass filter, taken from LWI (2012a)

Year	discharge	100 m high-pass filter (trend adjusted)		no high-pass filter (trend adjusted)	
	Q [m^3/s]	h_{filt} [m]	l_{filt} [m]	h [m]	l [m]
2011	368	0.33	65	0.70	137
2007	417	0.38	56	0.60	97
2004	485	0.36	57	0.53	98
2006	1750	0.33	58	0.74	130
2006	2760	0.32	51	0.64	114
2011	3070	0.38	52	0.83	126
2006	3490	0.31	48	0.61	111

8.3 Morphodynamic simulations

For morphodynamic simulation the data set of 2004 is chosen (Table 8.2). Its discharge of $485\,\mathrm{m^3/s}$ lies between the mean low water discharge ($297\,\mathrm{m^3/s}$) and mid water discharge ($689\,\mathrm{m^3/s}$) of the modelled area, and thus it represents an average value. Additionally, the hydrological discharge curve before the recording date is not dominated by floods or droughts (Faulhaber, 2013). The data was recorded before the substantial dike relocation measure of the year 2009. From 2005 to 2009 the dikes of this area have been moved from the original position in the proximity of the river about $2000\,\mathrm{m}$ inland. Through this measure $420\,\mathrm{ha}$ of retention area were gained (BAW, 2013). At the time of recording the modelled data set, the dikes were still located at their original position close to the water front. The flood planes behind the dikes are not activated at mid water discharge. For the simulations it is therefore possible to reduce the computational grid to the area in between the dikes and to cut off the flood plains. Figure 8.5 shows an aerial view of the computational domain. The computational mesh covers a straight section between El-km 480.0 to 484.0. The edge length of the mesh is $3\,\mathrm{m}$ to $5\,\mathrm{m}$ over the complete domain, thus an average dune is represented by at least 11 nodes in length. The mesh contains $170\,195$ nodes and $337\,944$ elements. With 10 σ-layers this results in roughly 1.7 million nodes in the 3D-mesh.

For the simulations, the numerical configurations developed from the experimental flume of Chapter 5 and 7 are used. The boundary condition for the morphodynamics is set to continuous sediment input (equilibrium boundary condition) at the inflow boundary. In the experimental flume non-equilibrium boundary conditions improved the results, as it enhanced dune formation in the upper third of the experimental flume. But for the Elbe model no recordings of sediment transport volume exists. The introduced sediment will not reach the evaluation area it will not influence the results. The effects of the sediment input method on the bed forms can be basically ruled out for the length of the simulation. Therefore the continuous sediment input is a valid approach. The hydrodynamic boundary conditions are a constant discharge upstream and a fixed elevation downstream. As the model domain proved to be sensitive to drastic flow changes, a 3D hydrodynamic restart file is necessary to start morphodynamic simulations. The morphodynamic simulations start from a pre-formed dune bed, interpolated from high-resolution bottom scans.

Figure 8.6 shows water levels for the 3D hydrodynamic restart calculation after it has reached a steady state, in comparison to the measurements in the Elbe river for discharges of 480 and $489\,\mathrm{m}^3/\mathrm{s}$. The free surface of the restart

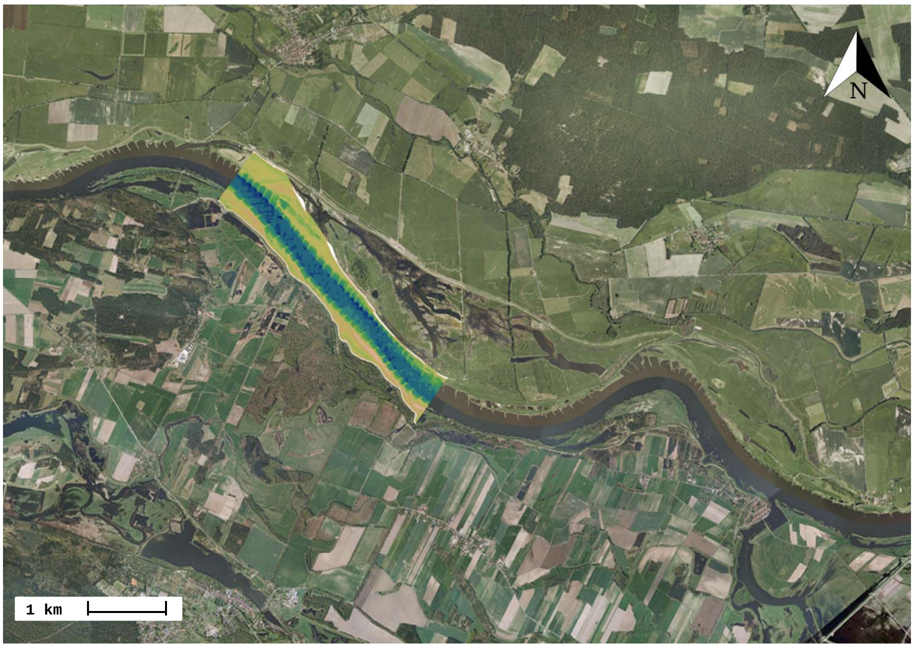

Figure 8.5: Aerial view of the computational domain between El-km 480.0 to 484.0; flood planes behind dikes are not activated at mid water discharge and are therefore not part of computational domain

calculation agrees quantitatively and qualitatively with the measured values, considering that the water levels have been measured at slightly different discharges and over bottoms with different hydrological discharge history. These results are obtained with a roughness height of k_s = 0.07744 m in the river bed, where the mobile bed is present, and k_s = 0.5 m along the groynes and armourstones.

The chosen value for the non-movable bottom of the simulation area, k_s = $0.5\,\mathrm{m}$, is a common value for the size of armourstones. The roughness height k_s = $0.0774\,\mathrm{m}$ for the river bed (moveable sediment) is considerably higher than a roughness height obtained merely from the grain diameter, which would be calculated as

$$k_s^g \;=\; 3\;\cdot d_{50} \;=\; 0.00724\ \mathrm{m}$$

In Section 5.3 the influence of small scale bed forms migrating over larger forms has been discussed. It has also been shown that these small scale forms are not represented in the mesh if they fall below the mesh size, but they will nonetheless influence the flow regime and water levels. Thus, again the form roughness according to van Rijn (1993), which is a combined roughness of bed forms and grain roughness, is applied

$$k_s = k_s^g + k_s^r + k_s^d \tag{1.1}$$

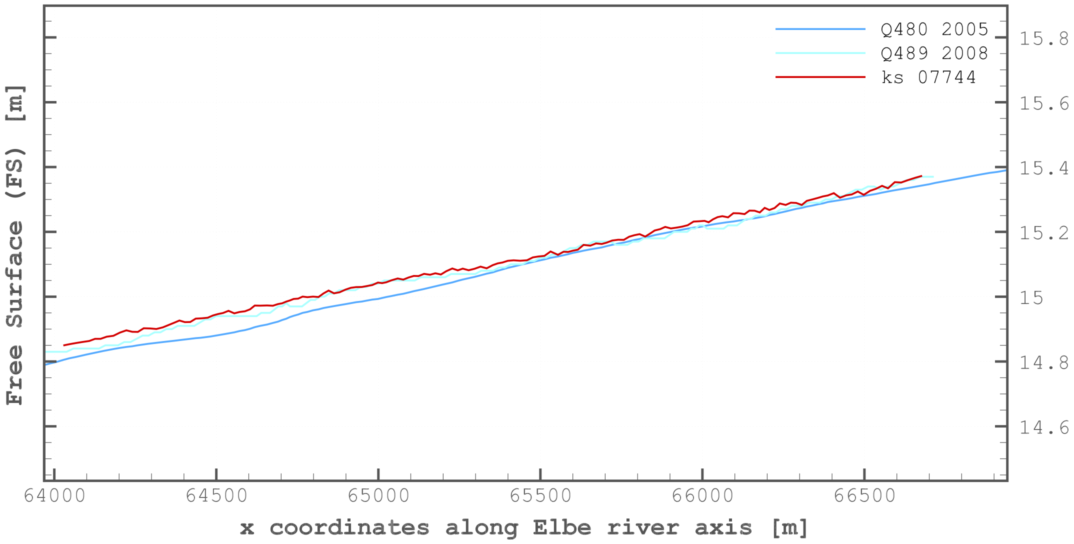

Figure 8.6: Free surface levels of numerical model (with k_s=0.07744 m and discharge of $485\,\mathrm{m}^3/\mathrm{s}$) and measurements (at discharges $480\,\mathrm{m}^3/\mathrm{s}$ and $489\,\mathrm{m}^3/\mathrm{s}$) between El-km 480.0 to 484.0

The form roughness of small, sub-grid bed forms with a length of $4\,\mathrm{m}$ and a height of $0.15\,\mathrm{m}$ (which is an average limit that can not be mapped on the mesh with a mean edge length of $3\,\mathrm{m} \times 5\,\mathrm{m}$) is equivalent to $k_s^d = 0.0702\,\mathrm{m}$, which is almost ten times higher than the grain roughness. The combined roughness sums up to $k_s = 0.0774\,\mathrm{m}$.

With these roughness coefficients morphodynamic simulations are conducted over 288 h (12 days). Computing times on the BAW cluster (bullx bade B510 series) are 54 to 69 h on 96 processors for a simulated time period of 24 h. During the simulations the water levels remain stable and the dunes move throughout the simulation area. Unfortunately the dunes steepen and develop a peaked appearance. No satisfying morphodynamic results are gained, if subgrid dune roughness is added to a model where dunes are already directly represented. Hence, the same run is conducted with the simple grain roughness as roughness height ($k_s = 0.007\,24\,\mathrm{m}$), even though the free surface level of this calibration has some deficits and loses about $0.2\,\mathrm{m}$ towards the inflow boundary, equivalent to 0.05 ‰ (in comparison: the average bed slope of the evaluated area is 0.13 ‰). Morphodynamic simulations with these roughness coefficients coupled to 3D hydrodynamics are done for 126 h (5 days). Calculations have been performed over approx. 8 days on 80 processors on the cluster of BAW.

Using a roughness height of $k_s = 0.007\,24\,\mathrm{m}$ in the river channel the dunes keep their shape and move with the desired speed of 10 meters per day. In Tables 8.3 and 8.4 the dune parameters of these runs with $k_s = 0.007\,24\,\mathrm{m}$, generated with zero-crossing analysis, are summarized. The tables contain the statistical data generated from the bottom scan of the river bed ('bottom scan'). Additionally, the results presented by LWI (2012a) are displayed in the first row, as the interpolation method is sensitive to the geographic orientation of the cross-sections. The rotation point and the location of the spanned area ($100\,\mathrm{m} \times 3000\,\mathrm{m}$), out of which 101 sections are generated, are subject to user input. Secondly the mesh with the interpolated bottom is analysed ('mesh / 0 h'), to categorize the differences that might arise from interpolation of measured bottom heights onto the numerical mesh. Comparison of the values in Table 8.3 shows, that the mesh and the original bottom scan differ only slightly. The bottom scan has a resolution of $2\,\mathrm{m} \times 2\,\mathrm{m}$, whereas the mesh has a resolution of $3\,\mathrm{m}$ to $5\,\mathrm{m}$. Some bottom form information is obviously lost during the interpolation process. Afterwards the time strands of the morphodynamic simulation are analysed (6 to 126 h). The results of the time strands need to be compared to the results of the mesh with the interpolated bottom (0 h). The analysis shows, that the dunes keep all their form parameters, length (L) and height (H) (Table 8.3) and skewness (Sk) and kurtosis (Ku) (Table 8.4). The dunes move with a speed of approximately 10 meters per day and cover a distance of over $50\,\mathrm{m}$ during the simulated period of 126 h. This is about half a dune length. As no flattening and change of form parameters is observed, the dune movement is considered satisfactory. The two tables present additional parameters which give further information generated by the zero-crossing method, such as distance of two subsequent up/down-crossings and stoss/lee-side of dune angle, all of which remain stable during the run.

Figure 8.7 presents longitudinal sections taken along the central axis of the flume, thus following the streamlines of the river. One section is extracted approximately every 6 h to demonstrate the movement of the dunes. It can be seen, that the dune crests and valleys move steadily in the flow direction and that the bed forms maintain their distinct form. The vertical, blue lines shall facilitate the identification of the distance covered by the dune crest in comparison to the initial state. Figure 8.8 shows a three-dimensional plot of a section of the simulation (about $800\,\mathrm{m}$ from the inflow boundary). The bottom at the start (0 h) and end (126 h) of the simulation is shown, flow is from the right hand bottom to the left hand top corner. The vertical exaggeration is 1:10.

Table 8.3: Dune parameters of measured bottom scan (original LWI (2012a) value and own evaluation), numerical mesh with interpolated heights (mesh) and numerical simulations 6 to 126 h

model	l_d [m]	β_d [°]	H [m]	H_+ [m]	H_- [m]	L_{UC} [m]	M [-]	l_u [m]	β_u [°]	L [m]	L_{DC} [m]	h_u [m]	M [-]
LWI 2012a	39.63	0.0172	0.53	0.22	0.30	97.40	2974	58.29	0.0117	98.09	98.05	0.52	2874
bottom scan	39.98	0.0178	0.55	0.23	0.32	98.21	2906	58.67	0.0118	99.14	99.13	0.54	2806
mesh / 0 h	41.12	0.0171	0.54	0.23	0.31	101.92	2800	61.40	0.0112	103.08	103.12	0.54	2700
006 h	41.29	0.0175	0.55	0.23	0.32	104.72	2726	64.08	0.0109	106.04	106.04	0.55	2626
012 h	41.43	0.0175	0.55	0.23	0.32	106.48	2684	65.77	0.0106	107.90	107.91	0.55	2584
018 h	41.76	0.0174	0.55	0.23	0.31	107.64	2658	66.63	0.0103	109.11	109.11	0.55	2558
024 h	41.90	0.0175	0.55	0.23	0.31	108.31	2642	67.22	0.0102	109.85	109.88	0.55	2542
030 h	41.71	0.0175	0.55	0.23	0.31	108.75	2631	67.83	0.0101	110.27	110.30	0.55	2531
036 h	42.15	0.0175	0.55	0.24	0.32	109.54	2612	68.15	0.0101	111.04	111.07	0.55	2512
042 h	42.46	0.0175	0.55	0.24	0.31	110.17	2598	68.49	0.0100	111.67	111.71	0.55	2498
048 h	43.11	0.0175	0.56	0.24	0.32	111.70	2572	69.50	0.0100	113.23	113.41	0.55	2472
054 h	42.96	0.0175	0.56	0.24	0.32	111.75	2580	69.75	0.0099	113.23	113.47	0.55	2480
060 h	42.63	0.0176	0.56	0.24	0.32	111.57	2587	69.86	0.0099	112.96	113.21	0.55	2487
066 h	42.62	0.0177	0.56	0.24	0.32	112.19	2573	70.50	0.0098	113.57	113.85	0.56	2473
072 h	42.48	0.0178	0.56	0.25	0.32	112.92	2557	71.43	0.0098	114.33	114.63	0.56	2457
078 h	42.69	0.0178	0.56	0.25	0.32	112.89	2558	71.16	0.0098	114.23	114.58	0.56	2458
084 h	42.45	0.0178	0.56	0.25	0.32	112.70	2563	71.20	0.0098	113.98	114.38	0.56	2463
090 h	42.34	0.0178	0.56	0.25	0.31	112.57	2566	71.21	0.0098	113.86	114.25	0.56	2466
096 h	42.32	0.0178	0.56	0.25	0.31	112.62	2564	71.29	0.0099	113.87	114.30	0.56	2464
102 h	42.36	0.0178	0.56	0.25	0.31	112.09	2577	70.69	0.0099	113.29	113.74	0.56	2477
108 h	41.76	0.0179	0.56	0.25	0.31	111.85	2583	71.07	0.0099	113.02	113.47	0.56	2483
114 h	41.63	0.0180	0.56	0.25	0.31	111.44	2593	70.82	0.0099	112.65	113.05	0.56	2493
120 h	41.52	0.0180	0.56	0.25	0.31	111.23	2598	70.72	0.0099	112.43	112.84	0.56	2498
126 h	41.81	0.0181	0.57	0.26	0.31	111.64	2589	70.84	0.0099	112.85	113.29	0.57	2489

l_d = distance from dune valley to ridge, β_d = angle of lee side, H = height of bed form, $H_{+/-}$ = distance to absolute max/min of interval, L_{UC} = distance of two subsequent up-crossings, M = number of points of length section, l_u = distance from dune ridge to valley, β_u = angle of stoss-side, L = length of bed form, L_{DC} = distance of two subsequent down-crossings, h_u = height difference between dune ridge and valley of next interval

Table 8.4: Dune parameters of measured bottom scan (original LWI (2012a) value and own evaluation), numerical mesh with interpolated heights (mesh) and numerical simulations 6 h to 126 h

model	σ_s [m]	Sk$_s$ [-]	Ku$_s$ [-]	σ [m]	Sk [-]	Ku [-]
LWI 2012a	0.290	0.210	3.110	0.310	0.100	3.190
bottom scan	0.290	0.179	2.922	0.309	0.075	2.998
mesh / 0 h	0.287	0.195	2.908	0.301	0.099	2.973
006 h	0.288	0.199	2.906	0.302	0.110	2.963
012 h	0.288	0.209	2.908	0.301	0.127	2.958
018 h	0.287	0.218	2.907	0.299	0.140	2.954
024 h	0.287	0.223	2.904	0.299	0.147	2.948
030 h	0.286	0.224	2.902	0.298	0.151	2.943
036 h	0.287	0.225	2.903	0.298	0.156	2.942
042 h	0.287	0.228	2.904	0.298	0.162	2.943
048 h	0.287	0.230	2.907	0.298	0.168	2.945
054 h	0.287	0.232	2.910	0.298	0.173	2.948
060 h	0.287	0.234	2.914	0.299	0.178	2.952
066 h	0.288	0.236	2.923	0.299	0.184	2.965
072 h	0.288	0.237	2.928	0.299	0.187	2.972
078 h	0.288	0.238	2.929	0.299	0.191	2.975
084 h	0.289	0.239	2.932	0.300	0.194	2.981
090 h	0.289	0.241	2.937	0.300	0.198	2.988
096 h	0.289	0.243	2.941	0.300	0.202	2.994
102 h	0.289	0.245	2.943	0.300	0.206	2.999
108 h	0.289	0.246	2.946	0.301	0.209	3.004
114 h	0.290	0.246	2.947	0.301	0.211	3.006
120 h	0.290	0.246	2.949	0.301	0.214	3.011
126 h	0.290	0.245	2.950	0.301	0.216	3.016

σ = deviation, Sk = skewness, Ku = kurtosis, $_s$ = smoothened result

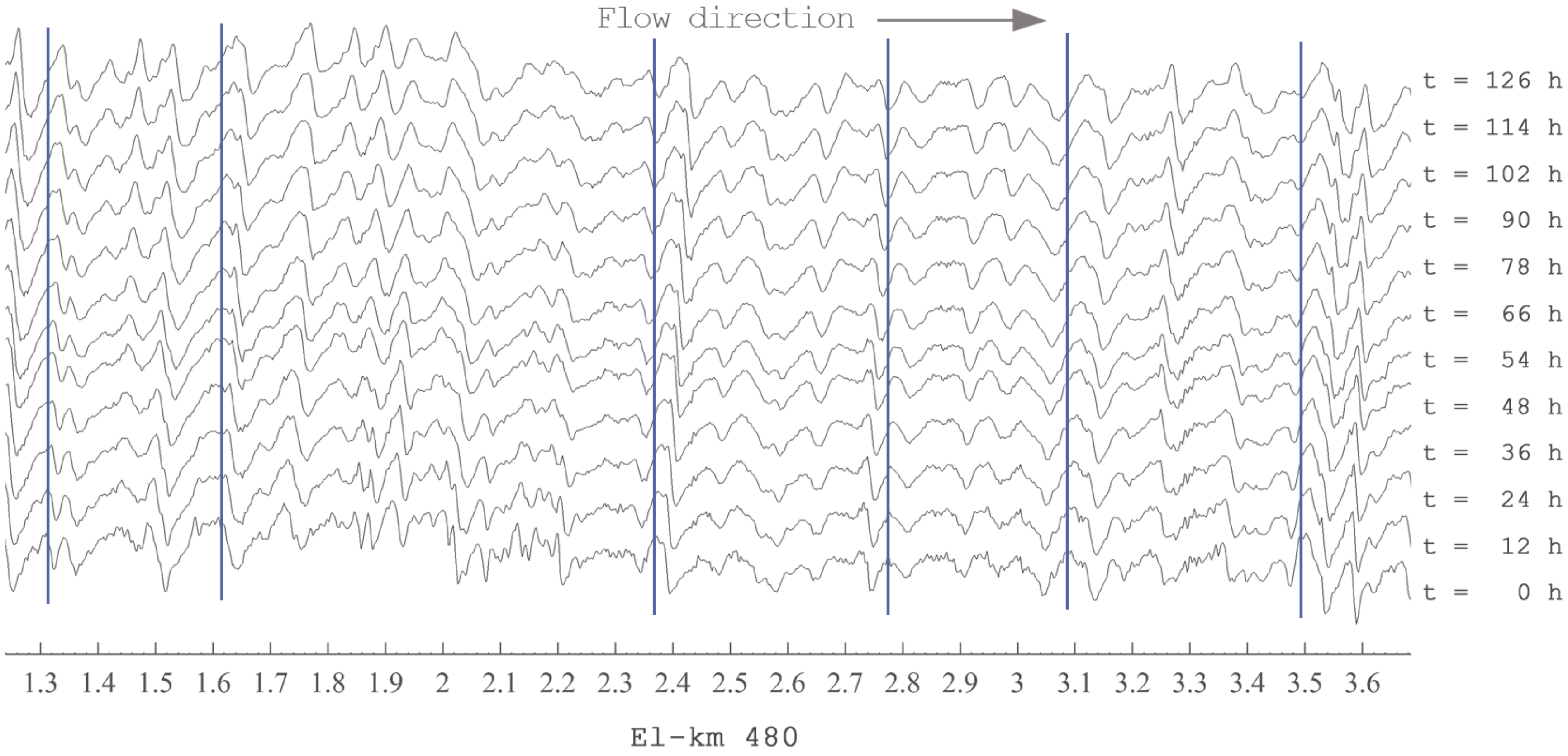

Figure 8.7: Numerical simulation: longitudinal sections from the middle river axis, recorded every 6 h, plotted every 12 h. Vertical, blue lines identify covered distance of dune crest in proportion to initial state

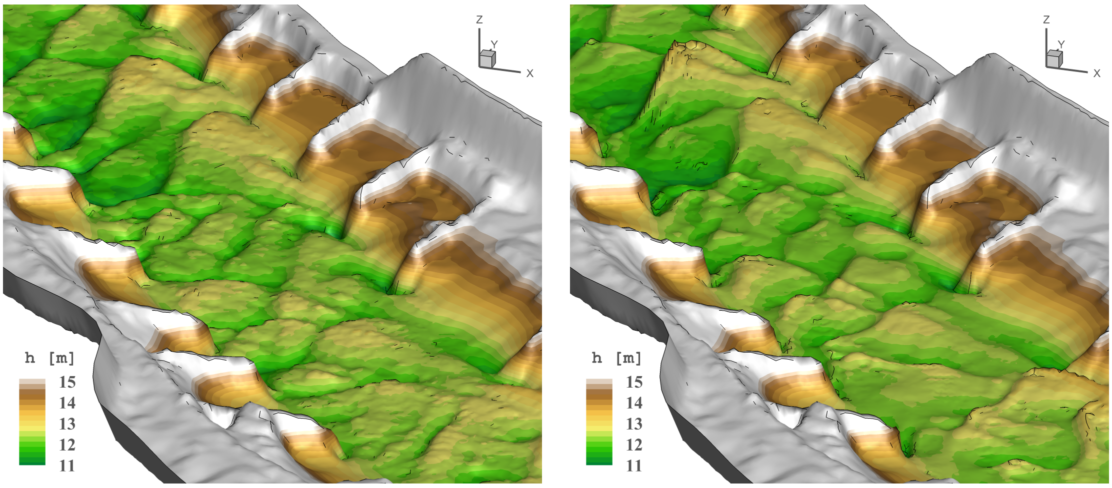

Figure 8.8: Three-dimensional plot, simulated section at 0 h (left) and 126 h (right), flow is from right hand bottom to left hand top corner, vertical deformation is 1:10

Table 8.5: Dune data short

	H [m]	L [m]	Sk [-]	Ku [-]
measurements (0 h)	0.54	103.08	0.199	0.092
24 h	0.55	109.85	0.223	0.096
48 h	0.56	113.23	0.232	0.09
78 h	0.56	114.58	0.238	0.071
102 h	0.56	113.29	0.245	0.057
126 h	0.57	112.85	0.245	0.05

8.4 Discussion

In order to translate the results obtained in the experimental flume to an in situ application, a stretch of the Elbe river has been chosen. The reach features a distinct dune regime, with fine sediments in the range of medium sand ($0.41\,\mathrm{mm}$) to medium gravel (max. $20\,\mathrm{mm}$) with d_{50} of $2.414\,\mathrm{mm}$. The sediment has the same sedimentological Froude and Reynolds numbers as the bed load material used in the experimental flume. The applied transport formula of Engelund and Hansen (1967) is recommended for rivers with fine sediments as well. A straight stretch of $4\,\mathrm{km}$ length is selected to exclude bends and hard changes in flow direction. This is done in order to provide the maximum possible comparability between the flume experiments and field-scale application. Existence of groynes in the waterway makes the simulation more independent of the boundary conditions.

A comparison of key variables of the flume and river simulations is presented in Table 8.6. Dune height in relation to water depth (h/Δ) is similar for the flume and river dunes. The same is true for the relation of dune length to horizontal mesh resolution (λ/Δ_m). The differences in relation of dune length to dune height are taken into account through a different height of the σ-layer most closest to the bottom, which is an adapted vertical resolution. Through this the three-dimensional mesh elements most closest to the bottom of each mesh (flume experiment and in situ application) have the same proportion: $h \cdot \sigma_{min}$ / Δ_m = element-height / element-length. The meshes will therefore produce comparable results similar.

Based on these requisites, the translation of the numerical results obtained in laboratory conditions (Chapter 5 and 7) to field conditions is considered permissible. Main difference between the settings is, that in the flume set-up the experiments and simulations start from a flat bed, whereas in the river model the interest is in the migration of dunes.

Compared to the flume experiments, the simulation time of the in situ application is short – 5 days are simulated. During this time, the dunes move with the desired speed of $10\,\mathrm{m}$ per day, thus covering about half a dune length (1.5 dune lengths). No flattening and change of form parameters is observed during the simulation. All characteristic dune parameters remain stable during the run, as well as additional ones such as distance of two following up/down-crossings and stoss/lee-side of dune angle. Thus the dune movement can be classified as successful. Due to the start from a naturally pre-formed bed, no appearance of bed forms is predicted, but their propagation speed and the preservation of characteristics of the dune field. This ability of the model needs to be further tested for longer simulations in different settings. A dune development from a plane bed would require a very long simulation time. As there is no natural condition of this reach featuring a bottom with no dunes, there would be no data set for validation either. All results from such a configuration must therefore be considered artificial. For a dune development from one dune configuration to an other, e.g. two different bottom scans from Table 8.2, a change in discharge would be required. When considering such a set-up, it is important to keep in mind that the bottom possesses a sort of 'memory' formed by the hydrological previous discharge curve. As a result, a change of discharge from one recording date to another – being months or even years apart – would need to include the complete discharge history to re-create the dunes exactly. Otherwise, only a tendency can be obtained from a simulation. For the foreseeable future, due the required simulation times and mesh resolution, the model will therefore be applicable for short term applications (weeks to months) and local ($10\,\mathrm{km}$ to $50\,\mathrm{km}$) problems and prognoses.

Table 8.6: Key variables of flume and river experiments for permissibility of translation from laboratory experiments to in situ scale

variable		flume	river
water depth $[\mathrm{m}]$	h	0.173	2.41
dune height $[\mathrm{m}]$	Δ	0.04	0.57
dune length $[\mathrm{m}]$	λ	1.17	41.81
lowest σ-layer [-]	σ_{min}	0.0135	0.0312
mesh width $[\mathrm{m}]$	Δ_m	0.11	4.0
h/Δ		4.32	4.23
$(\lambda/\Delta)/\sigma_{min}$		2166	2350
λ/Δ_m		10.63	10.45
$(h \cdot \sigma_{min})/\Delta_m$		0.021	0.019

9

Conclusions and Outlook

Contents

9.1 Hydrodynamic experiments

In this work the possibilities and constraints of modelling bed forms in waterways, using the numerical RANS model Telemac-3D and its morphological module Sisyphe (`www.opentelemac.org`), are highlighted and analysed. The basis for the numerical model is data from an experimental flume of the Federal Waterways Engineering and Research Institute of Germany (BAW). High-resolution measurements have been performed in the laboratory over fixed, naturally formed three-dimensional sand dunes, at equilibrium with the surrounding flow field. The data set includes the mean velocities in all three spatial directions recorded at around 3000 measuring points, and the velocity fluctuations (standard deviations) $u_i'(t)$, from which the turbulent kinetic energy of the flow field can be calculated.

Using the measured data sets, the hydrodynamic model Telemac-3D is calibrated to simulate the complex flow over a train of several three-dimensional dunes. These flow structures can only by model with a two-equation k-ε turbulence model. The numerical set-up further includes a non-hydrostatic pressure approach and an adjusted roughness height considering sub-grid scale bed forms, such as small scale ripples, which might also lie below recording resolution of the bottom scans.

Through extensive tests with the hydrodynamic model Telemac-3D, it is found that it is possible to reproduce the measured turbulent flow field in the wake of three fixed dunes. The water levels can be correctly reproduced for the chosen configuration: differences between simulations and measurements are smaller than 0.18 % of the water depth. For the simulations the two equation k-ε model is applied, being the most appropriate turbulence model for engineering application. It allows a stable, robust solution and is computationally cheap in comparison to other more-equation turbulence models.

The mesh resolution influences the quantity of flow features which is either directly modelled on the mesh or parametrised via a turbulence model. This will also generate differences in the free surface level: smaller directly modelled recirculation zones will result in a lack of supporting flow characteristics behind the dunes. The finest mesh used for this studies produces smaller directly modelled recirculation zones at the lee-side of the dunes than the other two, coarser meshes. The lack is not compensated by the turbulent kinetic energy of the turbulence model, even for the finest mesh, where the turbulent kinetic energy of the turbulence model is the highest. Thus, it must be reasoned that mesh resolutions in the presented range lead to (numerical) effects, that will make the results not scalable anymore and incomparable between two different meshes. The use of the same advection schemes and turbulence models that use a length scale of the mesh – such as the k-ε model – is not feasible in highly three dimensional flows, especially when changing the mesh resolution. Thus, new calibration as well as new considerations become necessary when leaving the range of similar modelled turbulence structures.

The vertical resolution (σ-layers) also influences the amount of calculated turbulent kinetic energy. The finer mesh generates more turbulent kinetic energy through the turbulence model. A different result could be expected: a finer mesh should lead to more flow features represented directly on the mesh, since more details can be mapped onto the mesh, leaving less for the sub-grid scale model to handle.

Appreciable differences of total calculated amount of turbulent kinetic energy of the numerical model compared to the measurements have been observed. For all simulations, the calculated turbulent kinetic energy falls below the amount of measured turbulent kinetic energy in the experimental flume. The measured and simulated values differ by a factor of about 2.5. This is despite the fact that the measured turbulent kinetic energy has to be seen as a minimal level of turbulence that is present in the flume (Kallenberg, 2014). The distribution of the modelled turbulence structures agrees with the measurements, as well as the velocity field distribution and water level.

9.2 Morphodynamic experiments

The aim of this work is to improve the understanding of the processes observed in a hydro- morphological system and to enhance the comprehension of the numerical transport models. Therefore, in addition to the hydrodynamic experiments, morphodynamic studies are conducted in the experimental flume with a mobile bed. The dune bottom that forms from a flat bottom during the experimental runs has been recorded continuously through the water column.

The high resolution bottom scans of the dune forms provide the basis for numerical, morphodynamic studies. From the physical data sets, characteristic dune parameters such as dune height, length, standard deviation, skewness and kurtosis are extracted. The general shape or form of the bed surface can be obtained from the skewness value, whereas the kurtosis will give information about the distribution of the bed forms in relation to each other on the examined bed stretch (Friedrich et al., 2006; Coleman et al., 2011).

Using these morphodynamic data sets, it is possible to validate the findings of the hydro-morphodynamic model. The morphodynamic simulations confirm the findings of the hydrodynamic ones: only with the two-equation k-ε turbulence model it is possible to produce dune like structures. For the morphodynamic simulation it is further essential to pay careful consideration to the choice of transport formula, formulae of slope and deviation, as well as bed shear calculation method.

The findings of this work recommend the bed load formula of Engelund and Hansen (1967) for practical utilisation of direct dune form transport. It falls into the category of energy models. Being one of the few sediment transport formulae that does not include any sort of threshold for the initiation of sediment transport, it relieves the calculation of this parametrisation factor. The use of a second bed load formula, which also delivers the desired dune forms (Yang and Lim, 2003), further frees the formula of Engelund and Hansen of insecurities concerning its applicability - basically that the forming dunes stem from numerical flaws in the formulation. The emergence of bed forms only as a result of numerical characteristics of the bed load transport formulation can be ruled out. Both formulae do not include a threshold fraction for sediment movement but do consider gravitational factors as lift energy and settling velocity. Thus, further investigations of these features should be considered as they might present possible prerequisites when modelling dunes.

For slope effect formula (change of magnitude of bed load transport) and deviation formula (change of direction of bed load transport) the formulae of Koch and Flokstra (1981) and Apsley and Stansby (2008) deliver the best results concerning dune length, height and form parameters such as skewness and kurtosis. The choice of slope and deviation formula profoundly influences the resulting form of the mobile bottom. Against the common expectation that crest displacement plays a crucial role for dune dynamics (Fredsøe and Deigaard, 1992), avalanching routines do not influence the quality of the results in this work.

As a main finding of this work, the inclusion of turbulence into the calculation of bed shear stress is thoroughly discussed and tested. For the presented applications, an inclusion of the turbulent kinetic energy of the flow k in the form of

$$\tau_{tot} \;=\; \rho u_*^2 \;+\; \rho\, r\, 2\, k \qquad (6.9)$$

presents the only way to produce the correct values of skewness and kurtosis of the dune field, where the kurtosis value has the requested, negative algebraic sign. The consideration of turbulent kinetic energy in bed shear stress calculation will provide the dune field with an adequate form: convex dune stoss-sides, steep lee-sides and deep troughs, as well as a three-dimensional form and an irregular distribution on the flume bottom. The coefficient r takes the following form

$$r \;=\; 2.0\; 2.5\, \kappa^2 \left(\ln \frac{\Delta z}{z_o} \right)^{-2} \qquad (7.5)$$

and includes the underestimation of the turbulent kinetic energy k by 2.5 found here.

The dune results are also sensitive to the boundary conditions. This is true for hydrodynamic as well as for morphodynamic boundary conditions. This effect has been noted by other authors (e.g. Khosronejad and Sotiropoulos, 2014; Mendoza et al., 2015) and thus it should be paid special attention to when modelling long-term, morphodynamic situations, especially if the additionally inserted or entering sediment reaches the model area of interest.

Roughness or the representation of roughness elements proves to be essential. Small scale bed forms, which might not only lie below mesh but also recording resolution, will influence the flow field even when larger bed forms such as dunes are present. Their parametrisation in the form of a mesh-dependent roughness coefficient is accepted, as these forms do not interact with the free surface. Dune forms interact strongly with the free surface of a river. Difficulties to provide predictions for water depth and bed movement in dune regimes and the challenge of maintenance measures of waterways that arise as a result are addressed in this work. Therefore, precise predictions of dune forms and their changes are essential and they cannot be parametrised. Ripples do not interact with the free surface and their parametrisation might thus be accepted.

In a last step, the results obtained from the experimental flume are translated to an in situ application. A reach of the river Elbe is chosen, which features a distinct dune regime with coarse sand as sediments and has a straight course over $4\,\mathrm{km}$. Even though the simulation time of the in situ application is short compared to the flume experiment concerning propagated distance in relation to dune length, the movement of the dunes in the in situ application can be classified as successful. The dunes move with the desired speed and no flattening and change of form parameters of the dune field is observed. The success promises operational use of the model in the near future for short term applications and local problems and statements, e.g. maintenance strategies such as changes in flow cross section, groynes and revetments.

9.3 Future research

The applied numerical approach, Reynolds Averaged Navier-Stokes (RANS), provides the possibility to calculate the flow field at small scale application as well as in large, field-scale river models. This transition is only possible with RANS models, as Large Eddy Simulations (LES) and Direct Numerical Simulations (DNS) are so far not applicable on project scale due to high computational costs. In his thesis Nabi (2012) presented successful dune modelling with his LES model, but on a very confined area. The RANS model applied in this work already allows for application on in situ scale, modelling a river reach which is $4\,\mathrm{km}$ in length.

Careful consideration needs to be given to the question, what kind of resolution of a numerical model is necessary. The appropriate resolution for a numerical simulation depends on the addressed question as well as on available resources. This study demonstrated the capabilities of the RANS model using a three-dimensional hydrodynamic model. In practical river engineering, where the calculation of a $50\,\mathrm{km}$ river stretch over 50 years with a three-dimensional hydrodynamic model is planned for the future, a resolution as presented in the last chapter is not yet feasible. For this time frame and spatial extent only two-dimensional models will find application in the next years. But the future will provide engineers and researchers with growing computer capacities. Following Moore's law (1965), these still experience a linear growth. Thus the feasibility of longer and larger three-dimensional simulations is only a matter of time. Also software re-engineering for the use of GPUs is a viable option to reduce calculation costs.

For two-dimensional flow simulations the mesh resolution will not necessarily include individual bed forms. This is legitimate when considering long time effects over long distances, where individual bed forms do not play a significant role. In this case, inclusion of their roughness as shown by Paarlberg (2008), might present itself as more efficient. The single bed form gains its relevance, if spatially confined problems are regarded, for example after a newly built groyne or other constructions which influence the flow regime locally. For these tasks, the Telemac-3D system can already be applied, as shown in this work.

High spatial resolution is needed to represent the bed forms with their steep lee sides, but also small time steps to incorporate the turbulent effects that are able to trigger, build and sustain the bed forms. If bed forms are included directly, the hydrodynamics must provide the flow conditions responsible for the emergence and movement of bed forms. This can be provided by applying a sophisticated turbulence model and the inclusion of turbulent flow movement into bed shear stress. The importance of this link between hydro- and morphodynamics and the effects on form parameters were presented in this thesis.

For possible long term strategies the use of a morphological factor is an option (Wieprecht and Gebler, 2008; Wurms and Schroeder, 2012). With this acceleration technique for morphodynamic simulations the calculated bed load transport is multiplied by a factor and the time scale of the hydrograph is condensed by the same factor. Consideration has to be given to the behaviour of retention areas and flood waves (Wurms and Schroeder, 2012). This approach seems feasible for the presented dune regimes. For long term strategies it should also be discussed, if bed load in numerical models of waterways can be treated statistically, in order to save computation time (see e.g. Audusse et al., 2015).

In their paper Mendoza et al. (2015) included the formula of Wong and Parker (2006), which is based on the formula of Meyer-Peter and Müller (1948), but has been adapted and corrected in their analysis. Mendoza et al. (2015) used it with Telemac-2D and Sisyphe for configurations with dunes and bars in meandering channels. It should be tested if this bed load formula is applicable for three-dimensional hydro-morphodynamics as well. For the simulation of flow over dunes, the k-ω-SST turbulence model (Menter, 1993) might be a valuable option. It possesses the advantages of the k-ε model, which works well for separation and shear zones. Near the wall, the SST-version switches to the k-ω model formulation, thus avoiding the sensitivity problems of the k-ω model in the free flow zone. Tests have been conducted to include the k-ω-SST model (Weilbeer, 2001; Goethel, 2008) and it is recommend to include a permanent version into the Telemac library and conduct further tests. Other flow simulation system (for example the OpenFOAM® library, `www.openfoam.org`) provide an implementation of this package. An initial calculation of the morphological experimental flume has been conducted with OpenFOAM® and the computational mesh and initial result files are available for further studies.

In the scope of the Ph.D. research project the inclusion of a friction parameter, which is automatically calculated from mesh size, has been tested. This would provide the possibility to include sub-grid ripple forms depending on the provided mesh, similar to the approach presented in Section 5.3. Further simulations should be conducted to test this approach, e.g. comparing it to a dynamic friction parameter. The Telemac-Mascaret system provides e.g. the possibility to include a formula for ripples in wave-dominated environments (Wiberg and Harris, 1994), as well as a dynamic ripple (and mega ripple and dune) roughness, presented by Van Rijn (2007).

During the physical flume experiments of the study, tests with installations of different kind were conducted in the experimental flume, e.g. partially fixed bed and groyne variations. High-resolution data sets of the resulting bottom from these experiments are available and offer the possibility to continue the work on understanding dunes and their realisation in numerical models.

Appendix

Appendix 1

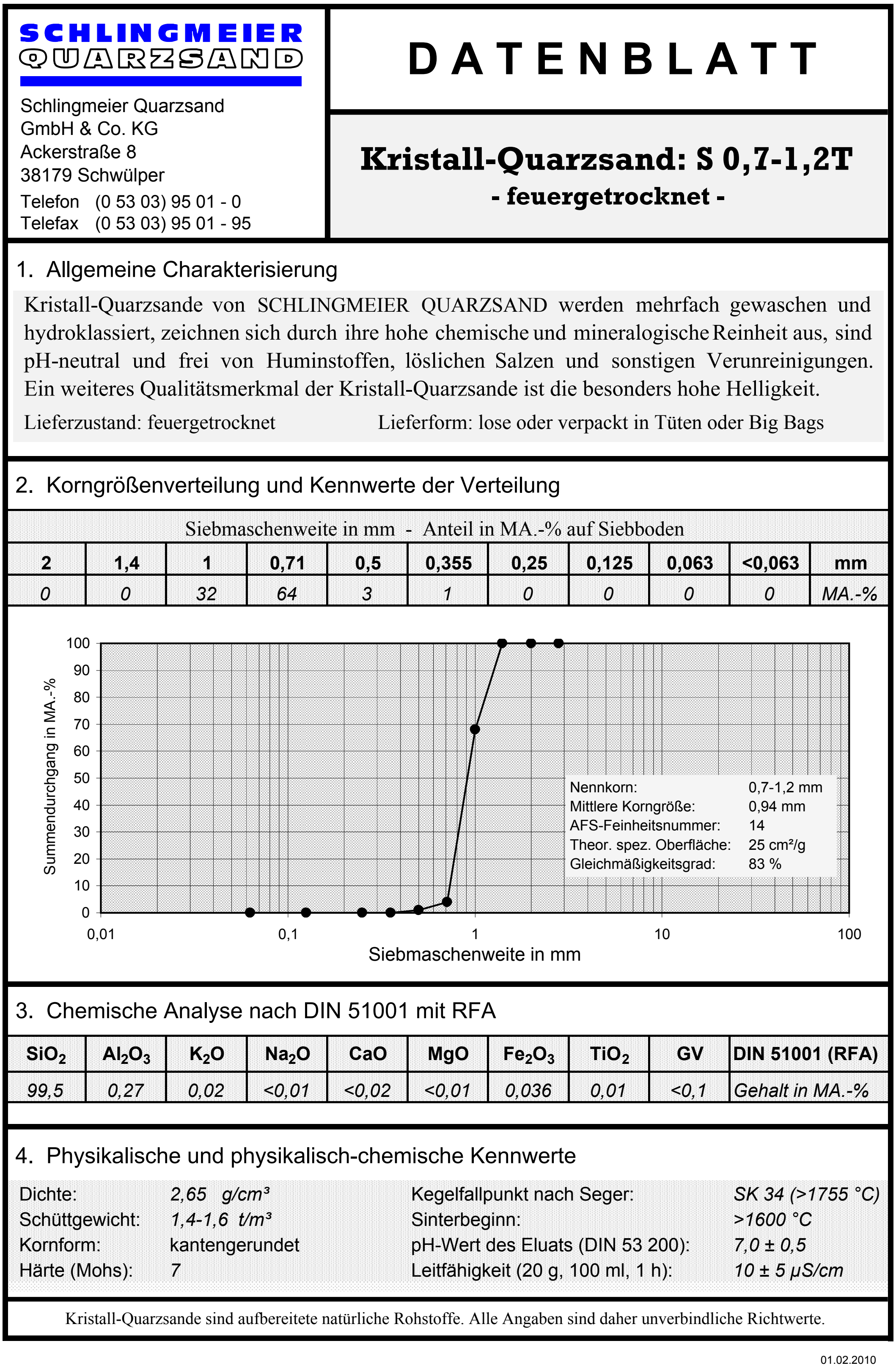

SCHLINGMEIER QUARZSAND

Schlingmeier Quarzsand
GmbH & Co. KG
Ackerstraße 8
38179 Schwülper
Telefon (0 53 03) 95 01 - 0
Telefax (0 53 03) 95 01 - 95

DATENBLATT

Kristall-Quarzsand: S 0,7-1,2T

- feuergetrocknet -

1. Allgemeine Charakterisierung

Kristall-Quarzsande von SCHLINGMEIER QUARZSAND werden mehrfach gewaschen und hydroklassiert, zeichnen sich durch ihre hohe chemische und mineralogische Reinheit aus, sind pH-neutral und frei von Huminstoffen, löslichen Salzen und sonstigen Verunreinigungen. Ein weiteres Qualitätsmerkmal der Kristall-Quarzsande ist die besonders hohe Helligkeit.

Lieferzustand: feuergetrocknet Lieferform: lose oder verpackt in Tüten oder Big Bags

2. Korngrößenverteilung und Kennwerte der Verteilung

Siebmaschenweite in mm - Anteil in MA.-% auf Siebboden

2	**1,4**	**1**	**0,71**	**0,5**	**0,355**	**0,25**	**0,125**	**0,063**	**<0,063**	**mm**
0	*0*	*32*	*64*	*3*	*1*	*0*	*0*	*0*	*0*	*MA.-%*

Nennkorn:	0,7-1,2 mm
Mittlere Korngröße:	0,94 mm
AFS-Feinheitsnummer:	14
Theor. spez. Oberfläche:	25 cm²/g
Gleichmäßigkeitsgrad:	83 %

3. Chemische Analyse nach DIN 51001 mit RFA

SiO_2	**Al_2O_3**	**K_2O**	**Na_2O**	**CaO**	**MgO**	**Fe_2O_3**	**TiO_2**	**GV**	**DIN 51001 (RFA)**
99,5	*0,27*	*0,02*	*<0,01*	*<0,02*	*<0,01*	*0,036*	*0,01*	*<0,1*	*Gehalt in MA.-%*

4. Physikalische und physikalisch-chemische Kennwerte

Dichte:	*2,65 g/cm³*	Kegelfallpunkt nach Seger:	*SK 34 (>1755 °C)*
Schüttgewicht:	*1,4-1,6 t/m³*	Sinterbeginn:	*>1600 °C*
Kornform:	kantengerundet	pH-Wert des Eluats (DIN 53 200):	*7,0 ± 0,5*
Härte (Mohs):	*7*	Leitfähigkeit (20 g, 100 ml, 1 h):	*10 ± 5 µS/cm*

Kristall-Quarzsande sind aufbereitete natürliche Rohstoffe. Alle Angaben sind daher unverbindliche Richtwerte.

01.02.2010

Figure 1: Data sheet crystal silica sand S 0,7-1,2T - Firma Schlingmeier

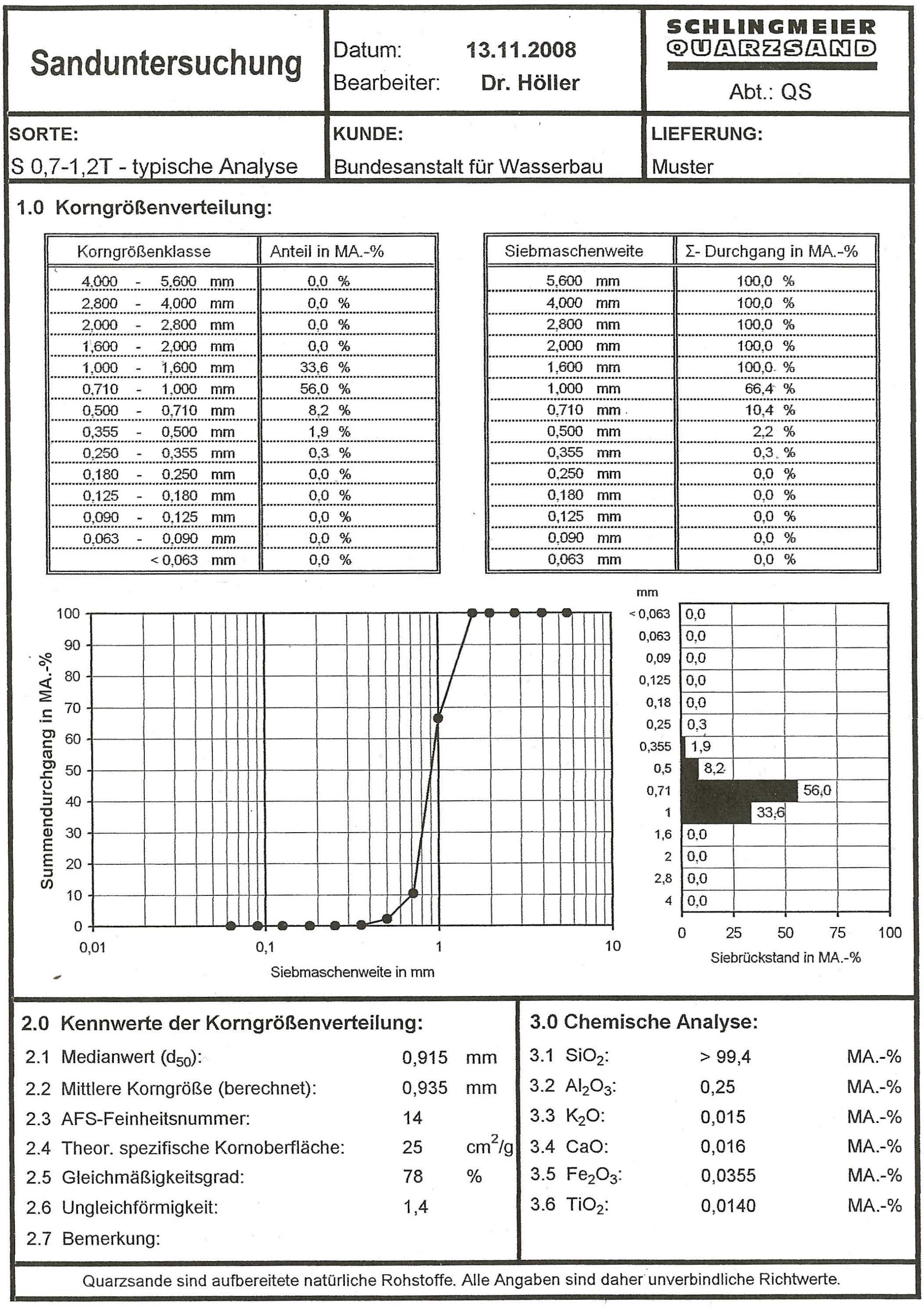

Sandunteruchung

Sanduntersuchung	Datum: **13.11.2008** Bearbeiter: **Dr. Höller**	**SCHLINGMEIER QUARZSAND** Abt.: QS
SORTE: S 0,7-1,2T - typische Analyse	**KUNDE:** Bundesanstalt für Wasserbau	**LIEFERUNG:** Muster

1.0 Korngrößenverteilung:

Korngrößenklasse	Anteil in MA.-%
4,000 - 5,600 mm	0,0 %
2,800 - 4,000 mm	0,0 %
2,000 - 2,800 mm	0,0 %
1,600 - 2,000 mm	0,0 %
1,000 - 1,600 mm	33,6 %
0,710 - 1,000 mm	56,0 %
0,500 - 0,710 mm	8,2 %
0,355 - 0,500 mm	1,9 %
0,250 - 0,355 mm	0,3 %
0,180 - 0,250 mm	0,0 %
0,125 - 0,180 mm	0,0 %
0,090 - 0,125 mm	0,0 %
0,063 - 0,090 mm	0,0 %
< 0,063 mm	0,0 %

Siebmaschenweite	Σ- Durchgang in MA.-%
5,600 mm	100,0 %
4,000 mm	100,0 %
2,800 mm	100,0 %
2,000 mm	100,0 %
1,600 mm	100,0 %
1,000 mm	66,4 %
0,710 mm	10,4 %
0,500 mm	2,2 %
0,355 mm	0,3 %
0,250 mm	0,0 %
0,180 mm	0,0 %
0,125 mm	0,0 %
0,090 mm	0,0 %
0,063 mm	0,0 %

2.0 Kennwerte der Korngrößenverteilung:

2.1 Medianwert (d_{50}):	0,915	mm
2.2 Mittlere Korngröße (berechnet):	0,935	mm
2.3 AFS-Feinheitsnummer:	14	
2.4 Theor. spezifische Kornoberfläche:	25	cm^2/g
2.5 Gleichmäßigkeitsgrad:	78	%
2.6 Ungleichförmigkeit:	1,4	
2.7 Bemerkung:		

3.0 Chemische Analyse:

3.1 SiO_2:	> 99,4	MA.-%
3.2 Al_2O_3:	0,25	MA.-%
3.3 K_2O:	0,015	MA.-%
3.4 CaO:	0,016	MA.-%
3.5 Fe_2O_3:	0,0355	MA.-%
3.6 TiO_2:	0,0140	MA.-%

Quarzsande sind aufbereitete natürliche Rohstoffe. Alle Angaben sind daher unverbindliche Richtwerte.

Figure 2: Data sheet of sand analysis of the same sand, performed by BAW

Appendix 2

Inclusion of turbulence into the numeric code of the Sisyphe in the subroutine `tob_sisyphe.f`

Original formulation

```
         TOB%R(I) = UETCAR%R(I) * XMVE
```

New formulation

```
      IF(CODE(1:9).EQ.'TELEMAC3D') THEN
!AG        CALL OS( 'X=CY     ',X=TOB,Y=UETCAR,C=XMVE)
           do i=1,npoin2
         DIST = MAX((Z(NPOIN2+I)-Z(I))
     &          +3.948D-3/30.D0,1.D-6)
         AUX  = MAX(1.001D0,30.D0*DIST/3.948D-3)
         TOB%R(I)=(UETCAR%R(I)+ 2.5D0*
     &            (2.D0*(KARMAN/LOG(AUX))**2)
     &            * AK%R(I+NPOIN2)) * XMVE
       enddo
!AG
      ELSE
        DO I=1,NPOIN
          TOB%R(I) = XMVE*0.5D0*CF%R(I)*UNORM%R(I)**2
        ENDDO
      ENDIF
```

`TOB` is the total bed shear stress, `UETCAR` is the effective shear velocity u*, `AK` is the turbulent kinetic energy and `XMVE` is the water density ρ. The number 3.948D-3 needs to be equal to `RUGOF`, the roughness height k_s, which is a user input variable.

Appendix 3

Bed load formula of Yang and Lim (2003) – added to the code structure of Sisyphe via the user-subroutine `qsform.f`

```
      ...
      USE DECLARATIONS_SISYPHE, ONLY : VCE, T1
                        ...
      DOUBLE PRECISION :: C1
      DOUBLE PRECISION :: OMEGA, CYANG
!---------------------------------------------------------
! omega = grain fall velocity. need to divide by omega,
! OMEGA is the inverse of omega
      OMEGA = 1.0D0  /(VCE/DM *
     &         (SQRT(25.D0+1.2D0*(DSTAR**2))-5.D0)**1.5D0)
      CYANG = 12.5D0
! kg/s -> m3/s -> /XMVE
! missing gravitation term, make true to dimension -> /GRAV
!   C1 = 1.0D0/XMVE/GRAV/DENS
!   C2 = DM*DENS*GRAV -> taken out, connected with C1:
      C1 = DM/XMVE
      CALL CPSTVC(QSC,T1)
      T1%R = AC
      CALL OS('X=Y-Z␣␣␣', X=QSC, Y=TETAP, Z=T1)
      CALL OS('X=XY␣␣␣␣', X=QSC, Y=TOB)
      CALL OS('X=CX␣␣␣␣', X=QSC, C=OMEGA)
      CALL OS('X=CX␣␣␣␣', X=QSC, C=CYANG)
      CALL OS('X=CX␣␣␣␣', X=QSC, C=C1)
      CALL OS('X=+(Y,C)', X=QSC, Y=QSC , C=0.D0)
!
!---------------------------------------------------------
!
      RETURN
      END
```

Appendix 4

Slope and deviation formula of Apsley and Stansby (2008) – added to the code structure of Sisyphe via the subroutine `bedload_effpnt.f`

Formulation for deviation

```
ELSEIF(DEVIA==3) THEN
DENS  = (XMVS - XMVE )/ XMVE
DSTAR = DM*(GRAV*DENS/1.D-6**2)**(1.D0/3.D0)
   IF (DSTAR <= 4.D0) THEN
      AC1 = 0.24*DSTAR**(-1.0D0)
   ELSEIF (DSTAR <= 10.D0) THEN
      AC1 = 0.14D0*DSTAR**(-0.64D0)
   ELSEIF (DSTAR <= 20.D0) THEN
      AC1 = 0.04D0*DSTAR**(-0.1D0)
   ELSEIF (DSTAR <= 150.D0) THEN
      AC1 = 0.013D0*DSTAR**(0.29D0)
   ELSE
      AC1 = 0.055D0
   ENDIF
C = (XMVS-XMVE)*GRAV*DM
TANPHI = TAN(PHISED*PI/180.D0)
C3 = AC1/TANPHI
DO I = 1 , NPOIN
   INVCBETA=SQRT(1.D0+DZFDX%R(I)**2.D0+DZFDY%R(I)**2.D0)
   TT1 = TOB%R(I) / C
   AA = TT1*STETA%R(I)-C3*DZFDY%R(I)/INVCBETA**2.D0
   BB = TT1*CTETA%R(I)-C3*DZFDX%R(I)/INVCBETA**2.D0
   NORM=SQRT(AA**2.D0+BB**2.D0)
   IF(NORM.GT.1.D-12)THEN
      SALFA%R(I)=AA/NORM
      CALFA%R(I)=BB/NORM
   ELSE
      SALFA%R(I)=0.D0
      CALFA%R(I)=1.D0
   ENDIF
ENDDO
ENDIF
```

Formulation for slope effect

```fortran
      ELSEIF(SLOPEFF.EQ.3) THEN
      DENS  = (XMVS - XMVE )/ XMVE
      DSTAR = DM*(GRAV*DENS/1.D-6**2)**(1.D0/3.D0)
         IF (DSTAR <= 4.D0) THEN
            AC1 = 0.24*DSTAR**(-1.0D0)
         ELSEIF (DSTAR <= 10.D0) THEN
            AC1 = 0.14D0*DSTAR**(-0.64D0)
         ELSEIF (DSTAR <= 20.D0) THEN
            AC1 = 0.04D0*DSTAR**(-0.1D0)
         ELSEIF (DSTAR <= 150.D0) THEN
            AC1 = 0.013D0*DSTAR**(0.29D0)
         ELSE
            AC1 = 0.055D0
         ENDIF
      C = (XMVS-XMVE)*GRAV*DM
      TANPHI = TAN(PHISED*PI/180.D0)
      C3 = AC1/TANPHI
      DO I = 1 , NPOIN
         INVCBETA=SQRT(1.D0+DZFDX%R(I)**2.D0+DZFDY%R(I)**2.D0)
         TT1 = TOB%R(I) / C
         AA = TT1*STETA%R(I)-C3*DZFDY%R(I)/INVCBETA**2.D0
         BB = TT1*CTETA%R(I)-C3*DZFDX%R(I)/INVCBETA**2.D0
         NORM=SQRT(AA**2.D0+BB**2.D0)
! This is the slope-part only:
         TOB%R(I) = C*NORM
         COEF%R(I) = 1.D0/INVCBETA
      ENDDO
      ENDIF
```

Appendix 5

```
/
TITLE = ’blueFlume’
/--------------------------------------------------------------------
/                      FILE DEFINITIONS
/--------------------------------------------------------------------
PARALLEL PROCESSORS = 32
FORTRAN FILE = ’telemac3d_blueFlume.f’
GEOMETRY FILE             = ’mesh.sel’
BOUNDARY CONDITIONS FILE  = ’boundary.cli’
3D RESULT FILE            = ’result3D.res’
2D RESULT FILE            = ’result2D.res’
/--------------------------------------------------------------------
/                   COMPUTATIONAL INFORMATION
/--------------------------------------------------------------------
/Start from 2D
INITIAL TIME SET TO ZERO  = YES
2D CONTINUATION  = YES
FILE FOR 2D CONTINUATION  = ’xxyy.res’
/Start from 3D
/COMPUTATION CONTINUED = YES
/PREVIOUS COMPUTATION FILE = ’xxyy.res’
NUMBER OF HORIZONTAL LEVELS = 10
MESH TRANSFORMATION = 2 / specified in condim.f
NUMBER OF PRIVATE ARRAYS = 2
MASS-BALANCE = YES
INFORMATION ABOUT MASS-BALANCE FOR EACH LISTING PRINTOUT = YES
/--------------------------------------------------------------------
/                        OUTPUT VARIABLES
/--------------------------------------------------------------------
VARIABLES FOR 3D GRAPHIC PRINTOUTS = ’U,V,W,Z,NU*,K,EPS’
VARIABLES FOR 2D GRAPHIC PRINTOUTS =
’PRIVE1,PRIVE2,PRIVE3,PRIVE4,U,V,B,H,KS,S,Q,I,J,M,E,W,F’
/--------------------------------------------------------------------
/                      COUPLING WITH SISYPHE
/--------------------------------------------------------------------
SISYPHE STEERING FILE  = sis.cas
COUPLING WITH  = ’INTER-SISYPHE’
COUPLING PERIOD FOR SISYPHE = 10
/--------------------------------------------------------------------
/                            TIME STEP
/--------------------------------------------------------------------
TIME STEP                = 0.01
NUMBER OF TIME STEPS     = 12960000
GRAPHIC PRINTOUT PERIOD  = 30000
LISTING PRINTOUT PERIOD  = 6000
/--------------------------------------------------------------------
/                           ROUGHNESS
/--------------------------------------------------------------------
LAW OF BOTTOM FRICTION = 5 / Nikuradse
FRICTION COEFFICIENT FOR THE BOTTOM =  0.003984D0
SKIN FRICTION CORRECTION = 1
/--------------------------------------------------------------------
```

```
LAW OF FRICTION ON LATERAL BOUNDARIES = 5
FRICTION COEFFICIENT FOR LATERAL SOLID BOUNDARIES = 0.001
TURBULENCE MODEL FOR LATERAL SOLID BOUNDARIES = 2 / rough
/--------------------------------------------------------------------
VELOCITY VERTICAL PROFILES = 2 / 2;2 logarithmic
/--------------------------------------------------------------------
/                   INITIAL AND BOUNDARY CONDITIONS
/--------------------------------------------------------------------
/                         OUT ; IN
PRESCRIBED ELEVATIONS = 1.341 ; 0.0
PRESCRIBED FLOWRATES  =   0.0 ; 0.145
INITIAL CONDITIONS = 'CONSTANT ELEVATION'
INITIAL ELEVATION  = 1.35
VELOCITY PROFILES  = 4;5
TREATMENT OF FLUXES AT THE BOUNDARIES = 2;2
/--------------------------------------------------------------------
/                           CONSTANTS
/--------------------------------------------------------------------
AVERAGE WATER DENSITY = 999.5
/--------------------------------------------------------------------
/                       NUMERICAL OPTIONS
/--------------------------------------------------------------------
FREE SURFACE GRADIENT COMPATIBILITY = 0.8
/--------------------------------------------------------------------
NON-HYDROSTATIC VERSION = NO
/CONSISTENT PROJECTION  = YES /YES for non-hydrostatic version
MATRIX STORAGE = 3 / edge-based storage
/--------------------------------------------------------------------
TIDAL FLATS = NO
TREATMENT OF NEGATIVE DEPTHS = 2 / smoothing
OPTION FOR THE TREATMENT OF TIDAL FLATS = 1
/--------------------------------------------------------------------
MAXIMUM NUMBER OF ITERATIONS FOR DIFFUSION OF VELOCITIES = 100
SOLVER FOR DIFFUSION OF VELOCITIES = 7 /default=1
MASS-LUMPING FOR DEPTH = 1 /default=0
IMPLICITATION FOR DEPTH = 0.55 / default
IMPLICITATION FOR VELOCITIES = 0.55 / default
/--------------------------------------------------------------------
VERTICAL TURBULENCE MODEL = 3 /k-epsilon
HORIZONTAL TURBULENCE MODEL = 3 / k-epsilon
COEFFICIENT FOR VERTICAL DIFFUSION OF VELOCITIES = 1.D-6
COEFFICIENT FOR HORIZONTAL DIFFUSION OF VELOCITIES = 1.D-6
DIFFUSION STEP = YES /default
SCHEME FOR ADVECTION OF VELOCITIES = 2 /explizit + SUPG
SCHEME FOR ADVECTION OF K-EPSILON = 4 /explizit + MURD schema N
/--------------------------------------------------------------------
OPTION FOR THE HYDROSTATIC STEP = 2 /wave equation
PRECONDITIONING FOR PROPAGATION = 2 /for wave equation default=2
/--------------------------------------------------------------------
PRECONDITIONING FOR PROJECTION = 2
SOLVER FOR PROJECTION = 7
ACCURACY FOR PROJECTION = 1.E-6
SOLVER FOR PPE = 6
ACCURACY FOR PPE = 1.E-4
PRECONDITIONING FOR PPE = 2
```

```
SOLVER FOR PROPAGATION  = 7
SOLVER FOR DIFFUSION OF K-EPSILON = 7
MAXIMUM NUMBER OF ITERATIONS FOR PROJECTION = 101
MAXIMUM NUMBER OF ITERATIONS FOR PPE = 100
MAXIMUM NUMBER OF ITERATIONS FOR PROPAGATION = 199
MAXIMUM NUMBER OF ITERATIONS FOR DIFFUSION OF K-EPSILON = 198
/
&ETA
&FIN
```

Appendix 6

```
/
TITLE = ’blueFlume’
/-----------------------------------------------------------------------
/                      FILE DEFINITIONS
/-----------------------------------------------------------------------
PARALLEL PROCESSORS = 32
FORTRAN FILE = ’sisyphe_blueFlume.f’
GEOMETRY FILE             = ’mesh.sel’
BOUNDARY CONDITIONS FILE  = ’boundary.cli’
RESULT FILE               = ’resultSis.res’
/COMPUTATION CONTINUED    = YES
/PREVIOUS SEDIMENTOLOGICAL COMPUTATION FILE = ’xxyy.res’
/-----------------------------------------------------------------------
/                        OUTPUT VARIABLES
/-----------------------------------------------------------------------
VARIABLES FOR GRAPHIC PRINTOUTS =
’R,M,E,H,B,S,U,V,KS,TOB,MU,P,QS*,N,1A*,*ES’
/-----------------------------------------------------------------------
/                   SISYPHE NUMERICAL ALGORITHMS
/-----------------------------------------------------------------------
STEADY CASE   = NO
MASS-BALANCE  = YES
TIDAL FLATS   = NO
ZERO          = 1e-12
TETA          = 0.5
MASS-LUMPING  = YES
SOLVER ACCURACY = 1e-8
MINIMAL VALUE OF THE WATER HEIGHT  = 0.01
OPTION FOR THE TREATMENT OF TIDAL FLATS  = 1 / 3
/-----------------------------------------------------------------------
/                           ROUGHNESS
/-----------------------------------------------------------------------
%LAW OF BOTTOM FRICTION = 5 / Nikuradse
%FRICTION COEFFICIENT  = 0.003984D0
RATIO BETWEEN SKIN FRICTION AND MEAN DIAMETER = 3
/-----------------------------------------------------------------------
/                            BED LOAD
/-----------------------------------------------------------------------
BED-LOAD TRANSPORT FORMULA  = 30 \ ENGELUND-HANSEN (total)
CRITICAL EVOLUTION RATIO  = 1000.0
NON COHESIVE BED POROSITY = 0.375
SEDIMENT DENSITY  = 2650.D0
OPTION FOR THE TREATMENT OF NON ERODABLE BEDS  = 3
/HIDING FACTOR FORMULA  = 4 / Karim, Holly & Jang
NUMBER OF SIZE-CLASSES OF BED MATERIAL = 4
NUMBER OF BED LOAD MODEL LAYERS = 2
/HIDING FACTOR FOR PARTICULAR SIZE CLASS = 0.85;0.85;0.85;0.85
D90 = 0.000486; 0.000689; 0.000971; 0.00136
MEAN DIAMETER OF THE SEDIMENT = 0.0004275; 0.000605; 0.000855; 0.0012
/
INITIAL FRACTION FOR PARTICULAR SIZE CLASS  = 0.01; 0.03; 0.64; 0.32
CONSTANT ACTIVE LAYER THICKNESS = YES
```

```
ACTIVE LAYER THICKNESS = 0.05D0
%GRAIN-FEEDING = NO
/----------------------------------------------------------------------
/                             SLOPE EFFECT
/----------------------------------------------------------------------
SLOPE EFFECT                     = YES
FORMULA FOR SLOPE EFFECT         = 1
/1: Koch & Flokstra, 2: Soulsby, 3: Apsley & Stansby
BETA                             = 1.3 / Default
FORMULA FOR DEVIATION            = 3
/1: Koch & Flokstra, 2: Talmon, 3: Apsley & Stansby
PARAMETER FOR DEVIATION          = 2 /Default = 0.85, for Talmon
SEDIMENT SLIDE                   = NO / YES
FRICTION ANGLE OF THE SEDIMENT   = 35

&ETA
&FIN
```

Appendix 7

Bottom scans LWI (2012a), showing the evaluated area at Lenzen presented in Chapter 8. 2 km between El-km 480 and 483 are shown.

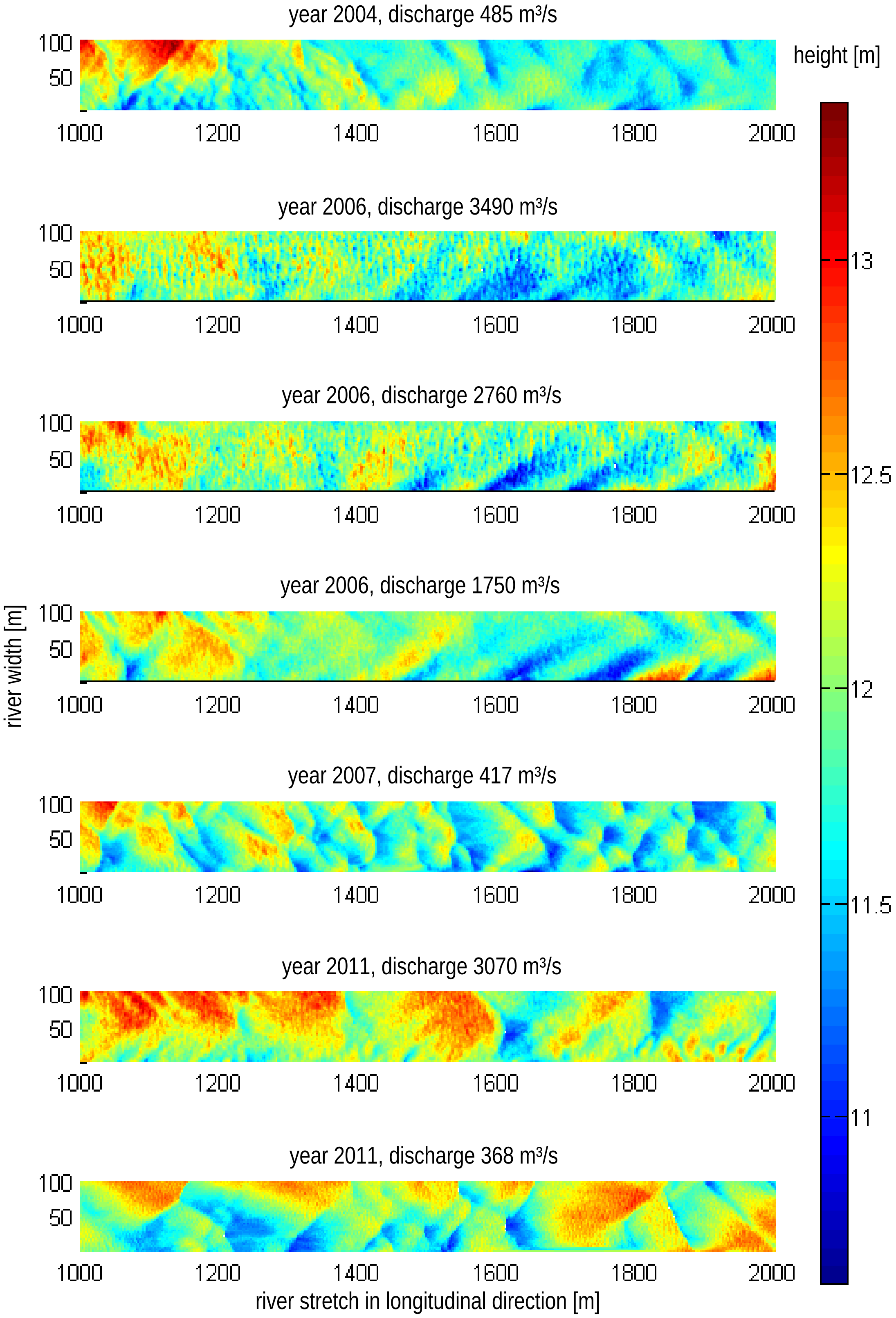

Figure 3: Bottom scans of the evaluated area at Lenzen, 2 km between El-km 480 and 483, changed after LWI (2012a). Flow is from left to right

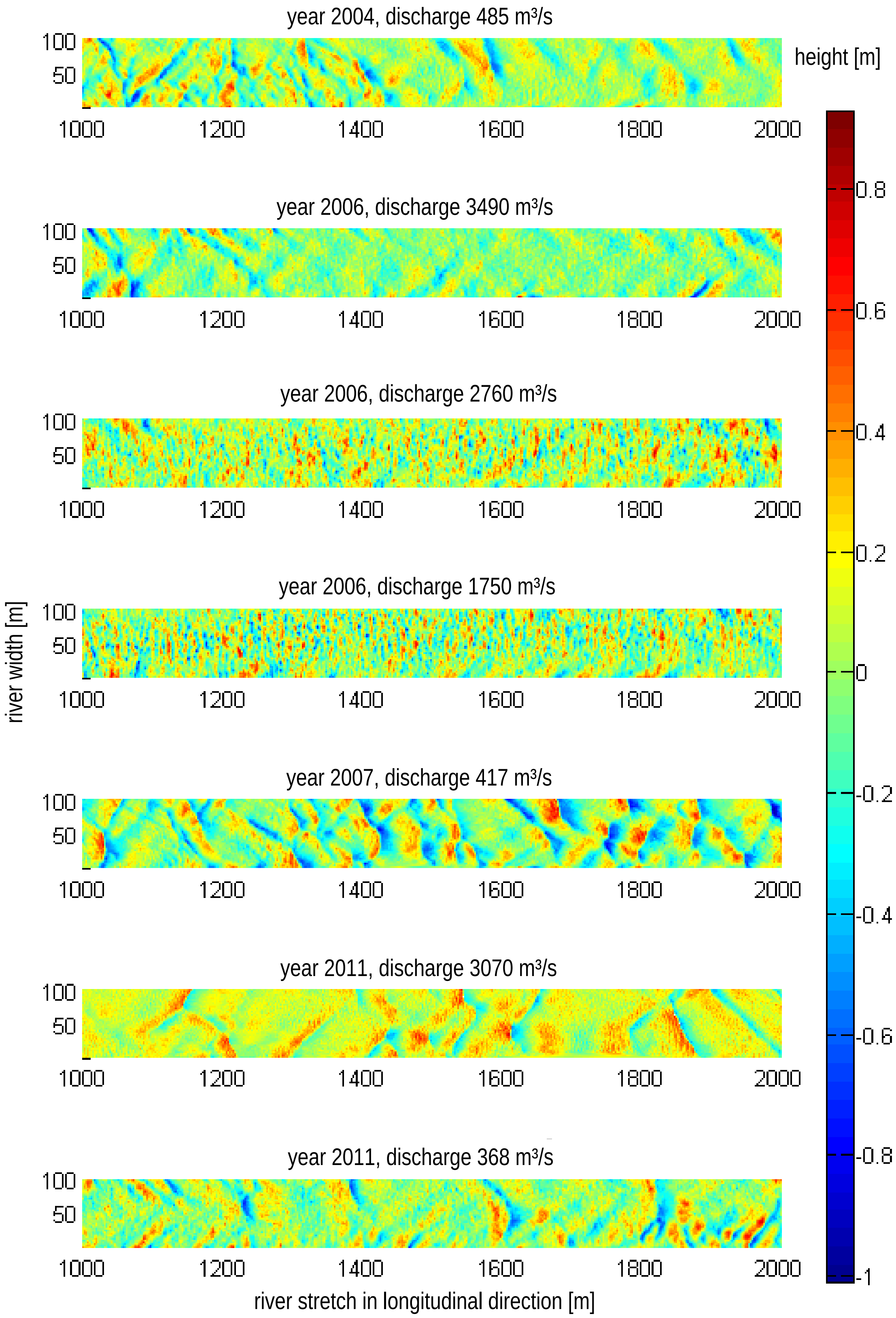

Figure 4: Bottom scans of the evaluated area Lenzen, filtered with 100 m high-pass filter, changed after LWI (2012a). Flow is from left to right

Appendix 8

The results of this thesis are partially based on results published during the project. These include the following:

- Numerical modelling of bed forms (dunes) with Telemac-3D and Sisyphe. Proceedings of the 18th Telemac and Mascaret User Conference. EDF Corporate University, Paris, 2011, pp. 16–21 *(Goll et al., 2011)*
- Numerical simulations of groyne influenced dunes. Proceedings of River Flow 2012. Costa Rica, 2012 *(Goll and Kopmann, 2012a)*
- Dune simulation with Telemac-3D and Sisyphe: A parameter study. Proceedings of the 19th Telemac and Mascaret User Conference. Oxford, 2012 *(Goll and Kopmann, 2012b)*
- Numerical modelling of flumes with moving dunes – Telemac3D and Sisyphe. Proceedings of 4th International Conference on Marine and River Dune Dynamics (MARID). Bruges, Belgium, 2013, VLIZ Special Publication *(Goll et al., 2013b)*
- Kontinuierliche Validierung hydrodynamischer und morphodynamischer Modelle mit physikalischen Modellversuchen. *Wasserwirtschaft*, 2013 (12) *(Goll et al., 2013a)*
- Direct Simulations of Bed forms in the River Elbe, Germany. Proceedings of the 21th Telemac and Mascaret User Conference. Grenoble, 2014 *(Goll, 2014a)*
- Numerische Simulation von Dünen. Kolloquium Herausforderung Sedimenttransport – Methoden und Konzepte im Flussbau, Karlsruhe, Germany, 2014 *(Goll, 2014b)*

Bibliography

Aberle, J. and G. M. Smart. The influence of roughness structure on flow resistance on steep slopes. *Journal of Hydraulic Research*, 41(3):259–269, 2003.

Allen, J. R. L. *Current ripples : their relation to patterns of water and sediment motion*. North-Holland Publ., Amsterdam, 1968.

Amoudry, L. O. and A. J. Souza. Impact of sediment-induced stratification and turbulence closures on sediment transport and morphological modelling. *Continental Shelf Research*, 31(9):912–928, 2011.

Apsley, D. D. and P. K. Stansby. Bed-load sediment transport on large slopes: Model formulation and implementation within a rans solver. *Journal of Hydraulic Engineering*, 134(10):1440–1451, 2008.

ASCE. Flow and transport over dunes. *Journal of Hydraulic Engineering*, 128(8):726–728, 2002.

Audusse, E., S. Boyaval, N. Goutal, M. Jodeau, and P. Ung. Numerical simulation of the dynamics of sedimentary river beds with a stochastic exner equation. *ESAIM: Proceedings and Surveys*, pages 1–10, 2015.

Baas, J. H. A flume study on the development and equilibrium morphology of current ripples in very fine sand. *Sedimentology*, 41(2):185–209, 1994.

Baas, J. H., A. P. Oost, O. K. Sztano, P. L. de Boer, and G. Postma. Time as an independent variable for current ripples developing towards linguoid equilibrium morphology. *Terra Nova*, 5(1):29–35, 1993.

Bailard, J. A. A simplified model for longshore sediment transport. *Proceedings of the 19th International Conference on Coastal Engineering, ASCE*, 1: 1454–1470, 1984.

Balachandar, R. and H. P. Reddy. Bed forms and flow mechanisms associated with dunes. In *Sediment Transport - Flow and Morphological Processes*, volume 1, pages 35–69. InTech, October 26 2011.

Balachandar, R., B.-S.Hyun, and V. C.Patel. Effect of depth on flow over a fixed dune. *Canadian Journal of Civil Engineering*, 34(12):1587–1599, 2007.

Bastian, P. *Numerische Lösung partieller Differenzengleichungen*. Instiut für Parallele und Verteiler Systeme, Universität Stuttgart, 2008.

BAW. *BAWMitteilungen Nr. 97, Die Deichrückverlegung bei Lenzen an der Elbe*. Bundesanstalt für Wasserbau (BAW), 2013.

Bennett, S. J. and J. L. Best. Mean flow and turbulence structure over fixed, two-dimensional dunes: Implications for sediment transport and bedform stability. *Sedimentology*, 42(3):491–513, 1995.

Best, J. The fluid dynamics of river dunes: A review and some future research directions. *Journal of Geophysical Research (Earth Surface)*, 110(9), December 2005.

Best, J., R. Kostaschuk, and R. Hardy. The fluid dynamics of low-angle river dunes: results from integrated field monitoring, laboratory experimentation and numerical modelling. *Proceedings of the Marine Sandwave and River Dune Dynamics Conference*, 1:17–23, 2004.

Bhaganagar, K. and T.-J. Hsu. Direct numerical simulations of flow over two-dimensional and three-dimensional ripples and implication to sediment transport: Steady flow. *Coastal Engineering*, 56(3):320–331, 2009.

Bijker, E. Littoral dirft as function of waves and current. *Proceedings of the 11th International Conference on Coastal Engineering, ASCE*, 1:415–435, 1968.

Biron, P. M., C. Robson, M. F. Lapointe, and S. J. Gaskin. Comparing different methods of bed shear stress estimates in simple and complex flow fields. *Earth Surface Processes and Landforms*, 29(11):1403–1415, 2004.

BMVI - Bundesministerium für Verkehr und digitale Infrastruktur. KLIWAS Abschlussbericht des BMVI, 2015.

Boussinesq, J. *Essai sur la théorie des eaux courantes*. Mémoires présentées par divers savants à l'Académie des Sciences. Imprimerie Nationale, 1877.

Boussinesq, J. *Théorie analytique de la chaleur*. Gauthier-Villars, Paris, 1903.

Burchard, H. *Applied Turbulence Modelling in Marine Waters*, volume 100 of Lecture Notes in Earth Sciences. Springer, Berlin, 2002.

Carling, P., E. Gölz, H. Orr, and A. Radecki-Pawlik. The morphodynamics of fluvial sand dunes in the River Rhine, near Mainz, Germany. I. Sedimentology and morphology. *Sedimentology*, 47(1):227–252, 2000a.

Carling, P., J. Williams, E. Gölz, and A. Kelsey. The morphodynamics of fluvial sand dunes in the River Rhine, near Mainz, Germany. II. Hydrodynamics and sediment transport. *Sedimentology*, 47(1):253–278, 2000b.

Casulli, V. and G. Lang. Mathmetical model UnTRIM, validation document. Technical Report 1.0, Bundesanstalt für Wasserbau, Hamburg, June 2004.

Chabert, J. and J. Chauvin. Dune and ripple formation in river models. *Bulletin du Centre de Recherches et d'essais de Chatou*, 4:31–51, 1963.

Charru, F., B. Andreotti, and P. Claudin. Sand ripples and dunes. *Annual Review of Fluid Mechanics*, 45(1):469–493, 2013.

Cheng, N.-S. Simplified settling velocity formula for sediment particle. *Journal of Hydraulic Engineering*, 123(2):149–152, 1997.

Chini, N. Sloping bed effects on the evolution of submerged mounds in an oscillatory flow. *Proceedings of the 16th Telemac User Conference 2009*, 1: 1–26, 2009.

Chollet, J. and J. Cunge. New interpretation of some head loss - flow velocity relationship for deformable movable beds. *Journal of Hydraulic Research*, 17:1–13, 1979.

Claude, N. *Processus et flux hydro-sédimentaires en rivière sablo-graveleuse: influence de la largeur de section et des bifurcations en Loire moyenne (France)*. PhD thesis, Université François - Rabelais de Tours, 2012.

Coleman, S. E. and V. I. Nikora. Initiation and growth of fluvial dunes. *Proceedings of Marine and River Dune Dynamics Conference*, 1:43–49, 2008.

Coleman, S. E. and V. I. Nikora. Exner equation: A continuum approximation of a discrete granular system. *Water Resources Research*, 45(9):1–8, 2009.

Coleman, S. E. and V. I. Nikora. Fluvial dunes: initiation, characterization, flow structure. *Earth Surface Processes and Landforms*, 36:39–57, October 2010.

Coleman, S. E., V. I. Nikora, and J. Aberle. Interpretation of alluvial beds through bed-elevation distribution moments. *Water Resources Research*, 47:W11505, November 2011.

Coleman, S. E., M. H. Zhang, and T. M. Clunie. Sediment-wave development in subcritical water flow. *Journal of Hydraulic Engineering*, 131(2):106–111, 2005.

Colombini, M. Revisiting the linear theory of sand dune formation. *Journal of Fluid Mechanics*, 502:1–16, 2004.

Decoene, A. and J.-F. Gerbeau. Sigma transformation and ALE formulation for three-dimensional free surface flows. *International Journal for Numerical Methods in Fluids*, pages 357–386, 2008.

Dibajnia, M. and A. Watanabe. Sheet flow under nonlinear waves and currents. *Proceedings of the 23rd Coastal Engineering Conference, ASCE*, 1: 2015–2028, 1992.

Dimas, A. A., N. T. Fourniotis, A. P. Vouros, and A. C. Demetracopoulos. Effect of bed dunes on spatial development of open-channel flow. *Journal of Hydraulic Research*, 46(6):802–813, 2008.

DVWK. *Merkblatt 220/1991 - Hydraulische Berechnung von Fließgewässern*, 1991.

TELEMAC Modelling System - 3D hydrodynamics TELEMAC-3D Software - Operating Manual. EDF R&D, Release 6.2, March 2013.

Einstein, H. A. The bed load function for sediment transportation in open channel flows. *Technical Bulletin*, 1026:78, 1950.

el Kheiashy, K., J. McCorquodale, I. Georgiou, and E. Meselhe. Three dimensional hydrodynamic modeling over bed forms in open channels. *International Journal of Sediment Research*, 25(4):431–440, 2010.

Engel, P. Length of flow separation over dunes. *Journal of the Hydraulics Division, ASCE*, 107:1133–1143, 1981.

Engelund, F. and E. Hansen. *A monograph on sediment transport in alluvial streams*. Technical University of Denmark, Denmark, 3 edition, 1967.

Engelund, F. and J. Fredsøe. Sediment ripples and dunes. *Annual Review of Fluid Mechanics*, 14:13–37, 1982.

Exner, F. M. Über die Welchselwirkung zwischen Wasser und Geschiebe in Flüssen. *Sitzungsbericht der Akademie der Wissenschaften, Wien*, 134(Abt. IIa), 1925.

Faulhaber, P. Characteristics of the Elbe between the mouth of the Havel and Doemitz. In *BAWMitteilungen Nr. 97*, pages 7–22. Bundesanstalt für Wasserbau (BAW), 2013.

Federal Statistical Office. Verkehr, Fachserie 8 Reihe 1.1, 08 2015.

Flemming, B. Zur klassifikation subaquatischer stroemungstransversaler transportkoerper. *Bochumer geologische und geotechnische Arbeiten*, 29:44–47, 1988.

Fredsøe, J. and R. Deigaard. *Mechanics of Coastal Sediment Transport*. Advanced series on ocean engineering. World Scientific, 1992.

Fredsøe, J. On the development of dunes in erodible channels. *Journal of Fluid Mechanics*, 64:1–16, 1974.

Fredsøe, J. Unsteady flow in straight alluvial streams: modification of individual dunes. *Journal of Fluid Mechanics*, 91:497–512, 4 1979.

Friedrich, H., V. Nikora, B. W. Melville, and S. E. Coleman. Statistical interpretation of geometric differences in ripple and dune shapes. *Proceedings of the Seventh International Conference on Hydroscience and Engineering*, 2006.

Gill, M. A. Height of sand dunes in open channel flows. *Journal of the Hydraulics Division*, 97(12):2067–2074, 1971.

Giri, S. and Y. Shimizu. Numerical computation of sand dune migration with free surface flow. *Water Resources Research*, 42:19, October 2006.

Goethel, O. *Numerical modelling of flow and wave induced scour around veritcal circular piles*. PhD thesis, Institut für Strömungsmechanik und Elektronisches Rechnen im Bauwesen, Leibniz Universität Hannover, 2008.

Goll, A., R. Kopmann, and T. Brudy-Zippelius. Numerical modelling of bed formes (dunes) with TELEMAC3D and SISYPHE. *Proceedings of the 18th Telemac and Mascaret User Conference, 19-21 October 2011, EDF Corporate University*, 1:16 – 21, 2011.

Goll, A. Numerische Modellierung von Geschiebetransport durch Dünen. Master's thesis, Universität Stuttgart, 2011.

Goll, A. Direct Simulations of Bed Forms of the River Elbe, Germany. *Proceedings of the 21th Telemac and Mascaret User Conference, 15-17 October 2014, Grenoble*, 1, 2014a.

Goll, A. Numerische Simulation von Dünen. *Kolloquium Herausforderung Sedimenttransport - Methoden und Konzepte im Flussbau*, 1:71–76, 2014b.

Goll, A. and R. Kopmann. Numerical simulations of groyne influenced dunes. *Proceedings of River Flow 2012, Costa Rica*, 1:635–642, 2012a.

Goll, A. and R. Kopmann. Dune simulation with Telemac3D and Sisyphe: A parameter study. *Proceedings of the 19th Telemac and Mascaret User Conference, 17-19 October 2012, Oxford*, 1:19–25, 2012b.

Goll, A., R. Kopmann, and M. Baronjac. Kontinuierliche Validierung hydrodynamischer und morphodynamischer Modelle mit physikalischen Modellversuchen. *Wasserwirtschaft*, 12:28–33, December 2013a.

Goll, A., R. Kopmann, and C. Villaret. Numerical modelling of flumes with moving dunes - Telemac3D and Sisyphe. *Proceedings of Fourth International Conference on Marine and River Dune Dynamics (MARID)*, 65:127–128, May 2013b.

Haber, B., T. Hüsener, S.-C. Mietz, and P. Faulhaber. Versuche an der 5-m-Rinne (linke Seite) Dokumentation der Versuchsvarianten und Zusammenstellung der Messdaten 2010 bis 2014. Technical report, Bundesanstalt für Wasserbau (BAW), 2014.

Henning, M., B. Hentschel, and T. Hüsener. Photogrammetric system for measurement and analysis of dune movement. *Proceedings of 33rd IAHR Congress: Water Engineering for a Sustainable Environment*, 1:4965–4972, 2009.

Henning, M. Bericht Nr. 966 - Literaturrecherche zum Geschiebetransport und Morphologie alluvialer Gewässer unter besonderer Berücksichtigung von Transportkörpern. Bericht 966, Leichtweiß-Institut für Wasserbau (LWI), Braunschweig, July 2008.

Henning, M. *Mehrdimensionale statistische Analyse räumlich und zeitlich hoch aufgelöster Oberflächen von Dünenfeldern*. PhD thesis, TU Braunschweig, Leichtweiss-Institut für Wasserbau, 2013.

Hervouet, J.-M. *Hydrodynamics of free surface flows: modelling with the finite element method*. Wiley, Chichester, 2007. Formerly CIP.

Hirt, C. and B. Nichols. Volume of fluid (vof) method for the dynamics of free boundaries. *Journal of Computational Physics*, 39(1):201–225, 1981.

Hoan, N., M. Stive, R. Booij, B. Hofland, and H. Verhagen. Stone stability in nonuniform flow. *Journal of Hydraulic Engineering*, 137(9):884–893, 2011.

Hofland, B. *Rock and roll: turbulence-induced damage to granular bed protections*. PhD thesis, TU Delft, Faculty of Civil Engineering and Geosciences, 2005.

Hunziker, R. *Fraktionsweiser Geschiebetransport*. Mitteilungen der Versuchsanstalt für Wasserbau, Hydrologie und Glaziologie an der Eidgenössischen Technischen Hochschule Zürich ; 138. Versuchsanstalt für Wasserbau, Hydrologie und Glaziologie der ETH, Zürich, 1995.

Jackson, R. G. Sedimentological and fluid-dynamic implications of the turbulent bursting phenomenon in geophysical flows. *Journal of Fluid Mechanics*, 77(3):531–560, 1976.

Jankowski, J. A. *A non-hydrostatic model for free surface flows*. PhD thesis, Institut für Strömungsmechanik und Elektronisches Rechnen im Bauwesen der Universität Hannover, Hannover, 1999.

Jongeling, T., A. Blom, H. Jagers, C. Stolker, and H. Verheij. Design method granular protections (in dutch). Technical report, WL | Delft Hydraulics, 2003.

Kallenberg, M. Turbulenzauswertungen an der blauen Rinne (intern). Technical report, Bundesanstalt für Wasserbau, 2014.

Karim, F. Bed material discharge prediction for nonuniform bed sediments. *Journal of Hydraulic Engineering*, 124(6):579–604, 1998.

Kennedy, J. F. The formation of sediment ripples, dunes, and antidunes. *Annual Review of Fluid Mechanics*, 1(1):147–168, 1969.

Kennedy, J. F. The mechanics of dunes and antidunes in erodible-bed channels. *Journal of Fluid Mechanics*, 16:521–544, 8 1963.

Khosronejad, A. and F. Sotiropoulos. Numerical simulation of sand waves in a turbulent open channel flow. *Journal of Fluid Mechanics*, 753:150–216, 8 2014.

Khosronejad, A., J. L. Kozarek, M. L. Palmsten, and F. Sotiropoulos. Numerical simulation of large dunes in meandering streams and rivers with in-stream rock structures. *Advances in Water Resources*, pages 45–61, 2015.

Kidanemariam, A. and M. Uhlmann. Direct numerical simulation of pattern formation in subaqueous sediment. *Journal of Fluid Mechanics*, 750:R2 1–13, 7 2014.

Kim, S., C. Friedrichs, J. Maa, and L. Wright. Estimating bottom stress in tidal boundary layer from acoustic doppler velocimeter data. *Journal of Hydraulic Engineering*, 126(6):399–406, 2000.

Koch, F. and C. Flokstra. Bed level computations for curved alluvial channels. In *Proceedings of 19th IAHR congress*, volume 2, New Delhi, India, 1981.

Kostaschuk, R., D. Shugar, J. Best, D. Parsons, S. Lane, R. Hardy, and O. Orfeo. Suspended sediment transport and deposition over a dune: Rio Parana, Argentina. *Earth Surface Processes and Landforms*, 34(12):1605–1611, 2009.

Kubatko, E. J. and J. J. Westerink. Exact discontinuous solutions of exner's bed evolution model: Simple theory for sediment bores. *Journal of Hydraulic Engineering*, 133(3):305–311, 2007.

Launder, B. E. and B. I. Sharma. Application of the energy dissipation model of turbulence to the calculation of flow near a spinning disc. *Letters in Heat and Mass Transfer*, 1(2):131–138, 1974.

Lesser, G., J. Roelvink, J. van Kester, and G. Stelling. Development and validation of a three-dimensional morphological model. *Coastal Engineering*, 51(8-9):883–915, 2004. Coastal Morphodynamic Modeling.

LWI. Bericht Nr. 924 - Konzipierung eines flussbaulichen Systemmodells für die Bundesanstalt für Wasserbau. Technical report, Leichtweiß-Institut der Universität Braunschweig, 2004.

LWI. Bericht Nr. 903 - Entwicklung eines Ansatzes zur Parametrisierung von turbulenzinduziertem Geschiebetransport in 2D-Modellen. Technical report, Leichtweiß-Institut der Universität Braunschweig, 2006.

LWI. Bericht Nr. 1030 - Bestimmung von Dünenparametern aus Naturmessungen im Bereich der Deichrückverlegung Lenzen/Elbe. Technical report, Leichtweiß-Institut der Universität Braunschweig, 2012a.

LWI. Bericht Nr. 2025 - Durchführung der dauerhaften Befestigung der Sanddünensohle in einer Versuchsrinne. Technical report, Leichtweiß-Institut der Universität Braunschweig, 2012b.

Lyn, D. Turbulence models for sediment transport engineering. In Garcia, M., editor, *Sedimentation Engineering - Processes, Measurements, Modeling and Practice*, pages 763–825. ASCE manuals and reports, 2008.

Maddux, T. B., S. R. McLean, and J. M. Nelson. Turbulent flow over three-dimensional dunes: 2. Fluid and bed stresses. *Journal of Geophysical Research (Earth Surface)*, 108:17, December 2003a.

Maddux, T. B., J. M. Nelson, and S. R. McLean. Turbulent flow over three-dimensional dunes: 1. Free surface and flow response. *Journal of Geophysical Research (Earth Surface)*, 108:20, December 2003b.

Malcherek, A. *Fliessgewässer - Hydromechanik und Wasserbau*. Universität der Bundeswehr - München, 2009a.

Malcherek, A. *Sedimenttransport und Morphodynamik*. Universität der Bundeswehr - München, 2009b.

Malcherek, A. *Numerische Methoden in der Strömungsmechanik*. Universität der Bundeswehr - München, 6.3 edition, 2013.

Marburger, M. *Entwicklung eines tiefengemittelten morphodynamischen Fließgewässermodells: ein Beitrag zur zweidimensionalen numerischen Simulation bettbildender Prozesse*. PhD thesis, Universität Kassel, Kassel, 1999.

McLean, S. The stability of ripples and dunes. *Earth Science Reviews*, 29: 131–144, 1990.

McLean, S., J. Nelson, and L. Gary. Suspended sediment in the presence of dunes. In Dohmen-Janssen and Hulscher, editors, *River, Coastal and Estuarine Morphodynamics: RCEM 2007*, pages 611–618. Taylor & Francis Group, London, 2008.

McLelland, S. J. and A. P. Nicholas. A new method for evaluating errors in high-frequency ADV measurements. *Hydrological Processes*, 14(2):351–366, 2000.

Mendoza, A., J. D. Abad, E. J. Langendoen, D. Wang, P. Tassi, and K. E. K. Abderrezzak. Effect of sediment transport boundary conditions on the numerical modeling of bed morphodynamics. unpublished, 2015.

Menter, F. R. Zonal two equation k-omega turbulence models for aerodynamic flows. *AIAA Journal, 24th Fluid Dynamics Conference*, AIAA 93·2906:1–22, 1993.

Menter, F. R. Two-equation eddy-viscosity turbulence models for engineering applications. *AIAA Journal*, 32(8):1598–1605, August 1994.

Mertens, W. Zur Wahl geeigneter Sedimenttransport-Formeln. *Wasserwirtschaft*, 85(10):486–490, 1995.

Meyer-Peter, E. and R. Müller. Formulas for bed-load transport. *Proceedings of the 2nd Meeting of the International Association for Hydraulic Structures Research*, 1:39–64, 1948.

Moore, G. E. Cramming more components onto integrated circuits. *Electronics*, 1:114–117, 1965.

Motamedi, A., H. Afzalimehr, G. Zenz, and M. Galoie. RANS simulations of flow over dunes with low lee and sharp lee angles. In *Advances in Hydroinformatics*, Springer Hydrogeology, pages 525–533. Springer Singapore, 2014.

Nabi, M., H. J. de Vriend, E. Mosselman, C. J. Sloff, and Y. Shimizu. Detailed simulation of morphodynamics: 1. hydrodynamic model. *Water Resources Research*, 48(12):n/a–n/a, 2012. W12523.

Nabi, M., H. J. de Vriend, E. Mosselman, C. J. Sloff, and Y. Shimizu. Detailed simulation of morphodynamics: 2. sediment pickup, transport, and deposition. *Water Resources Research*, 49(8):4775–4791, 2013a.

Nabi, M., H. J. de Vriend, E. Mosselman, C. J. Sloff, and Y. Shimizu. Detailed simulation of morphodynamics: 3. ripples and dunes. *Water Resources Research*, 49(9):5930–5943, 2013b.

Nabi, M. *Computational modelling of small-scale river morphodynamics*. PhD thesis, Delft University, Faculty of Civil Engineering and Geosciences, Department of Hydraulic Engineering, June 2012.

Naqshband, S., J. S. Ribberink, and S. J. M. H. Hulscher. Using both free surface effect and sediment transport mode parameters in defining the morphology of river dunes and their evolution to upper stage plane beds. *Journal of Hydraulic Engineering*, 140:1–6, 2014a.

Naqshband, S., J. S. Ribberink, D. Hurther, and S. J. M. H. Hulscher. Bed load and suspended load contributions to migrating sand dunes in equilibrium. *Journal of Geophysical Research: Earth Surface*, 119(5):1043–1063, 2014b.

Naudascher, E. *Grundlagen der Gerinnehydraulik*. Springer Vienna, Vienna, 1992.

Nelson, J. M., S. R. McLean, and S. R. Wolfe. Mean flow and turbulence fields over two-dimensional bed forms. *Water Resources Research*, 29(12):3935–3953, 1993.

Nelson, J. M., R. L. Shreve, S. R. McLean, and T. G. Drake. Role of near-bed turbulence structure in bed load transport and bed form mechanics. *Water Resources Research*, 31(8):2071–2086, 1995.

Nezu, I. and H. Nakagawa. *Turbulence in open channel flows*. IAHR AIRH monograph series. Balkema, Rotterdam [u.a.], 1993.

Niemann, S., J. Fredsøe, and N. Jacobsen. Sand dunes in steady flow at low froude numbers: Dune height evolution and flow resistance. *Journal of Hydraulic Engineering*, 137(1):5–14, 2011.

Nikuradse, J. *Strömungsgesetze in rauhen Rohren*. Forschungsheft auf dem Gebiete des Ingenieurwesens. VDI-Verlag, 1933.

Nordin, C. F. *Statistical properties of dune profiles*. Washington : U.S. Govt. Print. Off, 1971.

Omidyeganeh, M. and U. Piomelli. Large-eddy simulation of three-dimensional dunes in a steady, unidirectional flow. Part 1. Turbulence statistics. *Journal of Fluid Mechanics*, 721:454–483, 4 2013a.

Omidyeganeh, M. and U. Piomelli. Large-eddy simulation of three-dimensional dunes in a steady, unidirectional flow. Part 2. Flow structures. *Journal of Fluid Mechanics*, 734:509–534, 11 2013b.

Paarlberg, A. *Modelling dune evolution and dynamic roughness in rivers*. PhD thesis, University of Twente, 2008.

Paarlberg, A. J., C. M. Dohmen-Janssen, S. J. Hulscher, and P. Termes. Modeling river dune evolution using a parameterization of flow separation. *Journal of Geophysical Research: Earth Surface (2003–2012)*, 114(F1), 2009.

Patel, B. R. *Internal Flows (In: Fundamentals of Fluid Dynamics)*. John Wiley & Sons, Inc., 2007.

Platzek, F. W., G. S. Stelling, J. A. Jankowski, R. Patzwahl, and J. D. Pietrzak. An efficient semi-implicit subgrid method for free-surface flows on hierarchical grids. *International Journal for Numerical Methods in Fluids*, 80(12): 715–741, 2016. fld.4172.

Pope, S. B. Ten questions concerning the large-eddy simulation of turbulent flows. *New Journal of Physics*, 6(35):35, March 2004.

Pope, S. B. *Turbulent flows*. Cambridge Univ. Pr., Cambridge [u.a.], 1. publ., 6. print edition, 2000.

Prandtl, L. Bericht über Untersuchungen zur ausgebildeten Turbulenz. *Z. Angew. Math. Meth.*, 5(1):136–139, 1925.

Raudkivi, A. J. Bed forms in alluvial channels. *Journal of Fluid Mechanics*, 26:507–514, 11 1966.

Raudkivi, A. J. *Loose boundary hydraulics*. The Commonwealth and international Library : Civil engineering division. Pergamon Pr., Oxford [u.a.], 1967.

Reynolds, A. J. Waves on the erodible bed of an open channel. *Journal of Fluid Mechanics*, 22:113–133, 1965.

Rodi, W. On the simulation of turbulent flow past bluff bodies. *Journal of Wind Engineering and Industrial Aerodynamics*, 46-47:3–19, 1993. Proceedings of the 1st International on Computational Wind Engineering.

Schindler, R. J. and A. Robert. Flow and turbulence structure across the ripple-dune transition: an experiment under mobile bed conditions. *Sedimentology*, 52(3):627–649, 2005.

Schmeeckle, M. W. The role of velocity, pressure, and bed stress fluctuations in bed load transport over bed forms: numerical simulation downstream of a backward-facing step. *Earth Surface Dynamics Discussions*, 2(2):715–732, 2015.

Schmeeckle, M. W. Numerical simulation of turbulence and sediment transport of medium sand. *Journal of Geophysical Research: Earth Surface*, 119 (6):1240–1262, 2014.

Shen, H. W. *River mechanics*. H. W. Shen Fort Collins, Colorado, 1970.

Shields, A. Anwendung der Ähnlichkeitsmechanik und der Turbulenz Forschung auf die Geschiebebewegung. *Mitteilungen der Preußische Versuchanstalt für Wasserbau und Schiffbau, Berlin, Germany*, 26:1–42, 1936.

Singh, A. and E. Foufoula-Georgiou. *Effect of Migrating Bed Topography on Flow Turbulence: Implications for Modelling Sediment Transport*, chapter 21, pages 323–339. John Wiley & Sons, Ltd, 2013.

Smagorinsky, J. General circulation experiments with the primitive equations, part i: The basic experiment. *Monthly Weather Review*, 91:99–152, 1963.

Soulsby, R. The bottom boundary layer of shelf seas. In *Physical Oceanography of Coastal and Shelf Seas*. Elsevier, Amsterdam, 1983.

Soulsby, R. *Dynamics of Marine Sands*. Thomas Telford, 1997.

Soulsby, R., R. Whitehouse, and K. Marten. Prediction of time-evolving sand ripples in shelf seas. *Continental Shelf Research*, 38:47 – 62, 2012.

Southard, J. B. Experimental determination of bed-form stability. *Annual Review of Earth and Planetary Science*, 19:423–455, 1991.

Spiegel, E. A. and G. Veronis. On the boussinesq approximation for a compressible fluid. *apj*, 131:442, March 1960.

Stansby, P., N. Chini, and P. Lloyd. Oscillatory flows around a headland by 3d modelling with hydrostatic pressure and implicit bed shear stress comparing with experiment and depth-averaged modelling. *Coastal Engineering*, 116:1–14, 2016.

Stansby, P. K. and J. G. Zhou. Shallow-water flow solver with non-hydrostatic pressure: 2d vertical plane problems. *International Journal for Numerical Methods in Fluids*, 28(3):541–563, 1998.

Stansby, P., J. Huang, D. Apsley, M. García-Hermosa, A. Borthwick, P. Taylor, and R. Soulsby. Fundamental study for morphodynamic modelling: Sand mounds in oscillatory flows. *Coastal Engineering*, 56(4):408–418, 2009.

Stoesser, T., C. Braun, M. García-Villalba, and W. Rodi. Turbulence structures in flow over two-dimensional dunes. *Journal of Hydraulic Engineering*, 42: 14, 2008.

Sumer, B., L. Chua, N. Cheng, and J. Fredsøe. Influence of turbulence on bed load sediment transport. *Journal of Hydraulic Engineering*, 129(8): 585–596, 2003.

Talmon, A. *Bed topography of river bends with suspended sediment transport*. PhD thesis, Technische Hogeschool Delft, 1992.

Tassi, P. and C. Villaret. *Sisyphe User Manual*. EDF, Release 6.3, January 2014.

Taylor, G. I. Tidal friction in the irish sea. *Philosophical Transactions of the Royal Society of London A: Mathematical, Physical and Engineering Sciences*, 220(571-581):1–33, 1920.

Thielmann, S. Messung und Auswertung punktueller Geschwindigkeiten über fixierten Sanddünen. Master's thesis, Universität Kassel, 2013.

Tjerry, S. and J. Fredsøe. Calculation of dune morphology. *Journal of Geophysical Research (Earth Surface)*, 110:F04013, 2005.

van den Berg, J. H. Bedform migration and bed-load transport in some rivers and tidal environments. *Sedimentology*, 34(4):681–698, 1987.

van Rijn, L. Unified view of sediment transport by currents and waves. i: Initiation of motion, bed roughness, and bed-load transport. *Journal of Hydraulic Engineering*, 133(6):649–667, 2007.

van Rijn, L. C. Sediment Transport, Part I: Bed load transport. *ASCE Journal of Hydraulic Engineering*, 110:1431–1456, 1984a.

van Rijn, L. C. Sediment Transport, Part III: Bed forms and alluvial roughness. *ASCE Journal of Hydraulic Engineering*, 110(12):1733–1755, 1984b.

van Rijn, L. C. *Principles of sediment transport in rivers, estuaries and coastal seas: Part 1.* Aqua Publ., Amsterdam, ed. 1993 edition, 1993.

Venditti, J. G. Turbulent flow and drag over fixed two- and three-dimensional dunes. *Journal of Geophysical Research (Earth Surface)*, 112(11):21, November 2007.

Venditti, J. G., M. A. Church, and S. J. Bennett. Bed form initiation from a flat sand bed. *Journal of Geophysical Research (Earth Surface)*, 110(9):19, February 2005.

Villaret, C., J. Hervouet, N. Huybrechts, L. Van, and A. Davies. Effect of bed friction on morphodynamic modelling: Application to the central part of the Gironde estuary. *Proceedings of RCEM 2009 - River, Coastal and Estuarine Morphodynamics*, 1:899–905, 2009.

Villaret, C., J.-M. Hervouet, R. Kopmann, U. Merkel, and A. G. Davies. Morphodynamic modeling using the Telemac finite-element system. *Computers & Geosciences*, 5(0):105–113, 2013.

von Kármán, T. Mechanical similitude and turbulence. *Reprint from Nachrichten von der Gesellschaft der Wissenschaften zu Goettingen*, 1930.

Weilbeer, H. *Numerische Simulation von Strömung und Kolkung an Wasserbauwerken.* PhD thesis, Institut für Stroemungsmechanik und Elektronisches Rechnen im Bauwesen, Leibniz Universität Hannover, 2001.

Wenka, T. and P. Schröder. Unsicherheiten bei der Abbildung von 3D-Effekten in der Hochwasserabschätzung mit 2D-tiefengemittelten Berechnungsverfahren. *Wasserbauliche Mitteilungen, Institut für Wasserbau und THM der TU Dresden*, 27:297–306, 2004.

Wiberg, P. L. and C. K. Harris. Ripple geometry in wave-dominated environments. *Journal of Geophysical Research: Oceans*, 99(C1):775–789, 1994.

Wieprecht, S. and T. Gebler. Literaturstudie zu Langzeitstrategien für morphodynamische Modelle. Technical report, Institute for Modelling Hydraulic and Environmental Syystems - University of Stuttgart, 2008.

Wilbers, A. *The development and hydraulic roughness of subaqueus dunes*. PhD thesis, Faculty of Geosciences, Utrecht University, Utrecht, Netherlands, 2004.

Wilcox, D. *Turbulence Modeling for CFD*. DCW Industries Inc., California, USA, 2 edition, 1993.

Wong, M. and G. Parker. Reanalysis and correction of bed-load relation of Meyer-Peter and Müller using their own database. *Journal of Hydraulic Engineering*, 132(11):1159–1168, November 2006.

Wurms, S. and P. M. Schroeder. Evaluation of strategies for the acceleration of morphodynamic simulations against the background of waterways maintenance. *Proceedings of River Flow 2012, Costa Rica*, 2:1235–1241, 2012.

Yalin, M. S. Geometrical properties of sand waves. *Journal of the Hydraulics Division, ASCE*, 90:105–119, 1964.

Yalin, M. S. On the geometrically similar reproduction of dunes in a tidal model with movable bed. *Proceedings of the 13th Coastal Engineering Conference*, II:1143–1154, 1972.

Yalin, M. S. *River mechanics*. Pergamon Pr., Oxford [u.a.], 1 edition, 1992.

Yalin, M. S. and A. M. Ferreira da Silva. *Fluvial processes*. IAHR, International Association for Hydraulic Research, Delft, 2001.

Yang, S.-Q. and S.-Y. Lim. Total load transport formula for flow in alluvial channels. *Journal of Hydraulic Engineering*, 129(1):68–72, 2003.

Yue, W., C.-L. Lin, and V. C. Patel. Large-eddy simulation of turbulent flow over a fixed two-dimensional dune. *Journal of Hydraulic Engineering*, 132 (7):643–651, July 2006.

Zanke, U. *Grundlagen der Sedimentbewegung*, volume XII. Springer, Berlin, 1982.